Fault families around salt structures: Implications for fluid flow, storage and production

Qiang Zhang

Thesis submitted in partial fulfilment of the requirements for the degree of Doctor of Philosophy (Ph.D.)

School of Earth and Environmental Sciences

Cardiff University

September 2023

Fault families around salt structures: Implications for fluid flow, storage and production

Ph.D. project sponsored by China Scholarship Council
(File No. 201906450047)

Qiang Zhang

Dedicated to my parents, Yuxiang Huang and Shaolin Zhang.

“What doesn’t kill you, makes you stronger”.

(Friedrich Nietzsche)

Abstract

This thesis uses high-quality 3D seismic reflection volumes and well data from offshore Espírito Santo Basin (SE Brazil) and the Cleaver Bank High (Southern North Sea) to investigate fault families around salt structures and their implications for fluid flow, storage and production. The main aims are to understand: a) the distribution, geometry, scale and type of fault families around salt structures; b) the growth and development of fault families around salt structures and their relationship with halokinesis; c) the stress states necessary for the formation of fault families around salt structures; d) the role of fault families around salt structures in controlling fluid flow; e) the influence of salt structures and faults on the geothermal potential of surrounding strata. Hence, analyses were completed for fault families recognised in the two study areas, and such analyses included the mapping of plane and profile geometry, the mapping of faults' spatial distribution, and the gathering of maximum displacement/throw-length (D_{max}/T_{max}-L) and displacement/throw-depth (D/T-Z) data for selected faults. Stress analyses were applied to the interpreted fault families, providing important insights into the palaeostress states around salt structures. Multiple bottom-hole temperatures (BHTs) around salt structures and faults were utilised to reveal the influence of the latter on geothermal potential. In addition, fluid flow features and geothermal gradient anomalies were studied to address the role of distinct fault families in fluid flow and trapping around salt structures.

In a first stage, the distribution, evolution history and significance of tectonic faulting were investigated in a salt minibasin from offshore Espírito Santo Basin (SE Brazil). Interpreted faults include crestal, corridor, listric and keystone faults, all showing different geometries, orientations and distributions. Maximum displacement-length (D_{max}-L) and displacement-depth (D-Z) plots for selected eight (8) faults from four (4) fault families were compiled - together with eight (8) key structural maps - to understand their growth history. The results show that listric faults in minibasins can point out the presence of ductile, highly likely organic-rich shales and marls, which have similar seismic, lithological and petrophysical characters to known Cenomanian to Turonian source rocks. Three distinct evolutionary stages can be identified in the study area during the Cenozoic, and these reveal the control of halokinesis on the growth and development of faults around salt structures. Normalised leakage factor analyses for all fault families indicate that keystone faults are the most favourable paths for fluid migration in salt minibasins. Conversely, listric faults are likely to form barriers and baffles to fluid in their lower parts.

In a second stage, the palaeostress state around a rising salt diapir developing on the Cleaver Bank High, Southern North Sea, was investigated. Fault families around salt structures, including radial, polygonal and keystone faults, were separated into eight zones. Stress inversions were applied to a total of 10,401 interpreted faults to reveal the palaeostress state around the diapir of interest (diapir K09). The results show that diapir K09 experienced multiple phases of growth during the Cenozoic and two of these phases were associated with discrete episodes of tectonic inversion. Halokinesis controlled the formation and growth of fault families around diapir K09 following three structural stages. Palaeostresses in the flanking zones of the salt diapir show marked differences when compared with its corner zones, but the combination of minimum principal palaeostresses from all flanking and corner zones forms a triangular stress ring around the salt diapir. The width of this stress ring was not only associated with the growth of salt diapir but was also strongly influenced by adjacent salt structures.

The influence of salt structures and faults on the geothermal potential were investigated, in a third stage, over the Cleaver Bank High, Southern North Sea. The results of this part show that strata deposited above the Zechstein Group record geothermal gradients increasing proportionally to the thickness of this evaporite unit. Conversely, strata buried below the Zechstein Group reveal a moderate decreasing trend in geothermal gradients with increasingly thick salt. In parallel, large supra-salt faults can act as fluid paths to deep and hot fluid, a factor that results in the presence of high geothermal gradients in shallow strata around these same faults. In detail, geothermal gradients on the footwall of supra-salt faults are higher than that in their corresponding hanging-wall, but decrease markedly with distance away from these faults. Sub-salt faults influence the geothermal gradient of supra-salt strata in parts of the study area where there is very thin, or even absent, salt (<100 ms; or ~230 m), forming distinct low-amplitude trails of fluid above these same faults. They also indirectly influence geothermal gradient by controlling the position, geometry and distribution pattern of salt structures. As a corollary, three potential geothermal exploration targets are suggested in the study area; one located on the footwall of a large supra-salt fault, one above thick salt, and a third target above very thin Zechstein strata, where low-amplitude fluid chimneys are found in seismic data.

In conclusion, fault families around salt structures are divided in this thesis into clustered salt-related faults and scattered sub-salt and listric faults based on their scales and geometries. They can act as effective paths to deep and hot fluid into shallow strata, as indicated by the fluid flow features and geothermal gradient anomalies recorded around them. The growth or reactivation of steep faults propagating into sources of fluid (hydrocarbon) or heat (hot water

and gas) are the most favourable migration paths in the two study areas considered. Salt-related faults can also provide a relatively accurate record of stress states associated with halokinesis, a character that has important implications to hydrocarbon exploration, carbon and energy storage around salt structures. The results in this thesis can thus be extrapolated to fault families formed in salt-rich basins worldwide.

Author note and status of publications

The results chapters presented in this thesis have been prepared as scientific papers for publication in international journals. Their present status is as follow:

Chapter 4 was published in 2022 as Zhang, Q., Alves, T.M. and Martins-Ferreira, M.A.C. (2022). Fault analysis of a salt minibasin offshore Espírito Santo, SE Brazil: Implications for fluid flow, carbon and energy storage in regions dominated by salt tectonics. Marine and Petroleum Geology, 143, p.105805.

Chapter 5 was published in 2023 as Zhang, Q. and Alves, T.M. (2023). Palaeostress state around a rising salt diapir inferred from seismic reflection data. Marine and Petroleum Geology, p.106385.

Chapter 6 was published in 2024 as Zhang, Q. and Alves, T.M. Contrasting influence of salt structures and faults on the geothermal potential of regional structural highs: The Cleaver Bank High, Southern North Sea. Geothermics, 116, p.102842.

Although the articles are jointly co-authored with the project supervisor and another author, the work presented in the publications is that of the lead author, Qiang Zhang. Editorial work was provided by the project supervisor in accordance with a normal thesis chapter.

Acknowledgements

I would like to sincerely thank all the people who have directly or indirectly helped me during my Ph.D. studies at Cardiff University.

First and foremost, I am deeply grateful to my Ph.D. supervisor Tiago M. Alves for all his encouragement, guidance and support I received since applying for my Ph.D. programme, back in December 2018. I greatly acknowledge him for offering valuable suggestions about my research ideas, for reviewing drafts of my research papers and giving constructive comments promptly, all in all for boosting my confidence as my research progressed, helping me to become a qualified researcher in geosciences. Thank you sincerely for caring for me when I was going through hard times, especially during the Covid-19 pandemic in 2020 and 2021. Thank you also for sharing job opportunities when I was looking for post-doctoral positions.

I would like to acknowledge my pastoral supervisor, Ernest Chi Fru, for all the help and support provided. Co-author Marco Antonio Caçador Martins-Ferreira is acknowledged for his constructive comments, which improved our first published paper. A sincere thanks goes to Gwen Pettigrew for providing the indispensable IT supports and for maintaining computer equipment in the 3D Seismic Lab. Also to my fellow 3D seismic labbers, past and present, particularly Song, Roberto, Cerys, Nathalia, Abubakar, Chantelle, Lilly, Lizan and Ahmed, for all the fun time and interesting talks during lunchtime, Christmas dinners, etc.

I am thankful for CSC (China Scholarship Council), which granted me four years of funding during my Ph.D. studies at Cardiff University. CGG and Rock Rose NL CS5 BV are acknowledged for the provision of the high-quality 3D seismic reflection volumes. Brazilian National Petroleum Agency (ANP) and Dutch Oil and Gas portal (NLOG) are thanked for providing well data. Schlumberger (Petrel® and PetroMod®) and Petroleum Experts (Move®) are appreciated for providing academic licences to Cardiff University's 3D Seismic Lab. Furthermore, I thank all editors and reviewers of the published manuscripts included in this thesis for their constructive comments: Bernard Colletta, Kamaldeen O. Omosanya, Daniel Roberts, Christopher Bromley, Gioia Falcone and four anonymous reviewers.

All my good friends and flatmates I have met in Cardiff are much appreciated, especially Song Jing, Duo Zhang, Ying Deng, Yuanqiao Cen, Zhengyang Qiu, Zhibing Lei, Dr. Chang, Yun Zhang, Qi Liu, Sicheng Chen, Jianmin Feng, Mingcan Xu, Freda, Dennis, Marilyn,

Ann, Usman, Michal, Fadi, Sethu, Rachelle, Niger, Andrej and Afrah. Thank you for all the help and support you have given me, and thank you for the good times together in Cardiff.

A special thanks to my girlfriend Xingxing Wei, for always giving me positive encouragement to complete my thesis, for supporting me by doing plenty of routine housework, and for waiting for me to get married with you in the future. Your companion has brought much happiness during my Ph.D. studies; thank you very much for your presence in my life.

Last but not the least, I would like to give the greatest gratitude to my parents, Yuxiang Huang and Shaolin Zhang, for your unconditional love and care, for your precious encouragement, support and trust, and for always being there for me.

Table of Contents

List of Figures

List of Tables

List of Equations

Chapter 1

Introduction and literature review

1 Introduction and literature review

1.1 Rationale and research aims

1.1.1 Rationale

Salt structures are common and important geological structures in evaporite basins around the world, and have gathered the interest of multiple scientists, especially practicing geologists, for decades (e.g. Murray, 1966; Jackson and Seni, 1983; Seni and Jackson, 1983; Jackson and Talbot, 1986). The prime interest in salt structures comes from industry as large hydrocarbon discoveries are often found close to salt structures, such as in the case of the Gulf of Mexico, North Sea, Campos Basin and Tarim Basin (e.g. Ratcliff et al., 1992; Volozh et al., 2003; Fiduk et al., 2004; Yu et al., 2014). Salt structures are also of great interest to mineral exploration (e.g. Davison et al., 1996; Behlau and Mingerzahn, 2001; Van Gent et al., 2011), carbon sequestration (e.g. Chiaramonte et al., 2008; Chang et al., 2011) and gas storage (e.g. Warren, 2017; Gasanzade et al., 2021) within or near salt bodies. In addition, salt structures are important to geothermal exploration projects as salt has high geothermal conductivity, effectively heating up the rocks placed above salt structures but cooling the rocks below or adjacent to salt bodies (Wilson and Ruppel, 2007; Canova et al., 2018; Nolan, 2021).

Multiple fault families are usually observed in salt-rich basins, and their growth and development are naturally associated with halokinesis (e.g. Rowan et al., 1999; Stewart, 2006; Stewart, 2007). These faults can act as baffles or conduits to fluid flow depending on their seal competence, a property that is controlled by multiple factors (Caine et al., 1996; Fisher and Knipe, 2001; Koledoye et al., 2003; Manzocchi et al., 2010). The magnitude of fault displacement, fault geometry in relation to local stress, rock lithology crossed by faults, etc. are known factors controlling the seal potential of faults. More importantly, many structural traps identified around salt structures relate to these faults, as summarised by previous research (e.g. Halbouty, 1979; Stewart, 2006; Despinois, 2013). Therefore, understanding fault families around salt structures is important to reduce the risks for effective hydrocarbon exploration. It has also implications for seal competence analyses around salt structures, and their potential as feasible storage sites for carbon sequestration and gas storage.

The Espírito Santo Basin (SE Brazil) and the Cleaver Bank High (Southern North Sea) are typical salt-rich areas, with abundant salt structures (e.g. Taylor, 1998; Peryt et al., 2010;

Davison et al., 2012). They were respectively developed in a divergent ('passive') continental margin and in an inter-cratonic basin, and both comprise important hydrocarbon resources (e.g. Fiduk et al., 2004; Fattah et al., 2012b). They can be regarded as ideal study areas to investigate fault families around salt structures. High-quality three-dimensional (3D) seismic reflection volumes and well data are available in these two areas, providing the conditions for a detailed visualisation, mapping and analysis of geological structures. These data are useful to study the relationship between fault families and salt structures, helping to better understand fault growth and development. The palaeostress state around salt structures can also be investigated by stress inversion for interpreted faults as the seismic data are of high resolution, providing insights into the feasibility of carbon sequestration, gas storage and hydrocarbon production around or within salt structures. Many fluid flow features, including pockmarks, bright spots and gas pipes, preserved around faults are well imaged in the two study areas, providing direct evidence for fluid flow along faults. Finally, the geothermal data (448 Bottom-hole temperatures, BHTs) gathered from 48 drilling wells on the Cleaver Bank High are useful to investigate the influence of salt structures and faults on geothermal potential.

1.1.2 Research aims

This research aims at improving the current understanding of fault families around salt structures and their implications for fluid flow, storage and production in salt-rich basins. The three case studies considered in this thesis are used to explore the relationship between fault families and salt structures in different tectonic settings, and their significance for fluid flow, storage and production. In summary, this thesis aims to address the following research questions:

- What is the importance of listric faults and their soling out intervals as structures signing the presence of rheologically weak, muddy successions in salt minibasins, Espírito Santo Basin?
- What is the chronology of faulting around salt structures when comparing them to other fault families in the Espírito Santo Basin?
- Which of the interpreted fault families around salt structures is more favourable to form fluid flow pathways in the Espírito Santo Basin?
- What is the structural evolution of irregularly shaped salt structures in the Cleaver Bank High?

- How does halokinesis control the formation and development of fault families surrounding the salt structures of interest in the Cleaver Bank High?
- What are the differences in stress state amongst the different zones surrounding irregularly shaped salt diapirs in the Cleaver Bank High?
- Is there an influence of salt structures on the geothermal potential of regional structural highs, such as the Cleaver Bank High?
- How do faults developed on structural highs control the geothermal potential of sub- and supra-salt strata in the Cleaver Bank High?
- What potential geothermal exploration targets can be identified on the Cleaver Bank High?

The following section includes a relevant background literature review covering the main themes studied in this thesis. This thesis starts by introducing elemental fault terminology, displacement-distance relationships, scaling laws and fault-growth models, which are the main themes addressed in Chapters 4-6. The role of mechanical stratigraphy in controlling deformation is summarised, an important theme mentioned in Chapters 4 and 5. The thesis continues by summarising the importance of salt tectonics, especially the mechanisms promoting salt diapirism and diapir-related faults, the main theme of Chapters 4-6. The final topic of this literature review relates to fluid flow features, an important theme explored in Chapters 4 and 6.

1.2 Fault growth and propagation

1.2.1 Elemental fault terminology

The fault terminology used in this thesis is summarised in Fig. 1.1. Fault length (L) represents the longest along-strike dimension of a fault plane between their lateral tips, and fault trace length (L') indicates the arbitrary along-strike length of a fault plane (Fig. 1.1a). Fault height (H) represents the longest dimension of a fault plane in the direction normal to the strike, while fault trace height (H') indicates the arbitrary length of a fault plane measured in the direction normal to the strike. Fault length and height are independent of the orientation of the fault's slip vector and, most importantly, can be measured at outcrop or in 3D seismic data (Kim and Sanderson, 2005). When fault characteristics are compared for different fault populations, their maximum values can be used to express the overall dimensions of faults. A sig-

nificant aspect of fault growth and propagation is that, theoretically, fault displacement decreases to zero towards the lateral tip loops of an ellipse (fault surface) but increases towards a maximum (D_{max}) point within a fault surface (Walsh and Watterson, 1988; Cowie and Scholz, 1992a; Childs et al., 2003; Kim and Sanderson, 2005) (Fig. 1.1). This point of maximum displacement is considered to be the position of a fault in which rupture was first initiated, with this same fault growing and propagating vertically and laterally from such a position of initial rupture in subsequent stages (Childs et al., 1995; Childs et al., 2003).

1.2.2 Displacement-distance relationships

The displacement-distance (D_{max}-x) relationships of faults are studied via detailed measurements of displacement-length, displacement-height and displacement-width along fault traces. These are key parameters that indicate the modes of initiation and growth of faults (e.g. Chapman and Williams, 1984; Rippon, 1984; Walsh and Watterson, 1988; Cowie and Scholz, 1992a; Cowie and Scholz, 1992b; Kim and Sanderson, 2005; Torabi and Berg, 2011). Measurements of displacement-distance are often acquired from fault surfaces on seismic cross-sections, geological outcrops and topographic surfaces (Kim and Sanderson, 2005).

Displacement-length (D_{max}-L) data usually reflect the relationship between a fault's maximum displacement (D_{max}) and its length (L), providing an interpreted three-dimensional views of fault geometries (Cowie and Scholz, 1992a; Cowie and Scholz, 1992b). These data can be useful to estimate total strain in faulted rocks (Scholz and Cowie, 1990) and to assess kinematic relationships between faulting and folding (Chapman and Williams, 1984). The most important use of displacement-length measurements is to provide insights into the mechanisms of fault initiation, growth and evolution through time, eventually assisting the interpretation of distinct fault growth models (e.g. Watterson, 1986; Walsh and Watterson, 1988; Cowie and Scholz, 1992a; Cowie and Scholz, 1992b; Kim et al., 2001; Kim and Sanderson, 2005; Nicol et al., 2005; Roche et al., 2012; Durogbitan, 2016; Nicol et al., 2017; Tao, 2018; Rotevatn et al., 2019) (Fig. 1.2).

Displacement-height (D_{max}-H) measurements consider the relationship between a fault's maximum displacement (D_{max}) and its height (H) in a seismic or outcrop section that is normal to the fault strike. Such measurements reflect the true dip-slip values for normal faults, thrust faults, thrust fold zones and linked-fault systems (Muraoka and Kamata, 1983; Chapman and Williams, 1984; Baudon and Cartwright, 2008a; Torabi et al., 2019).

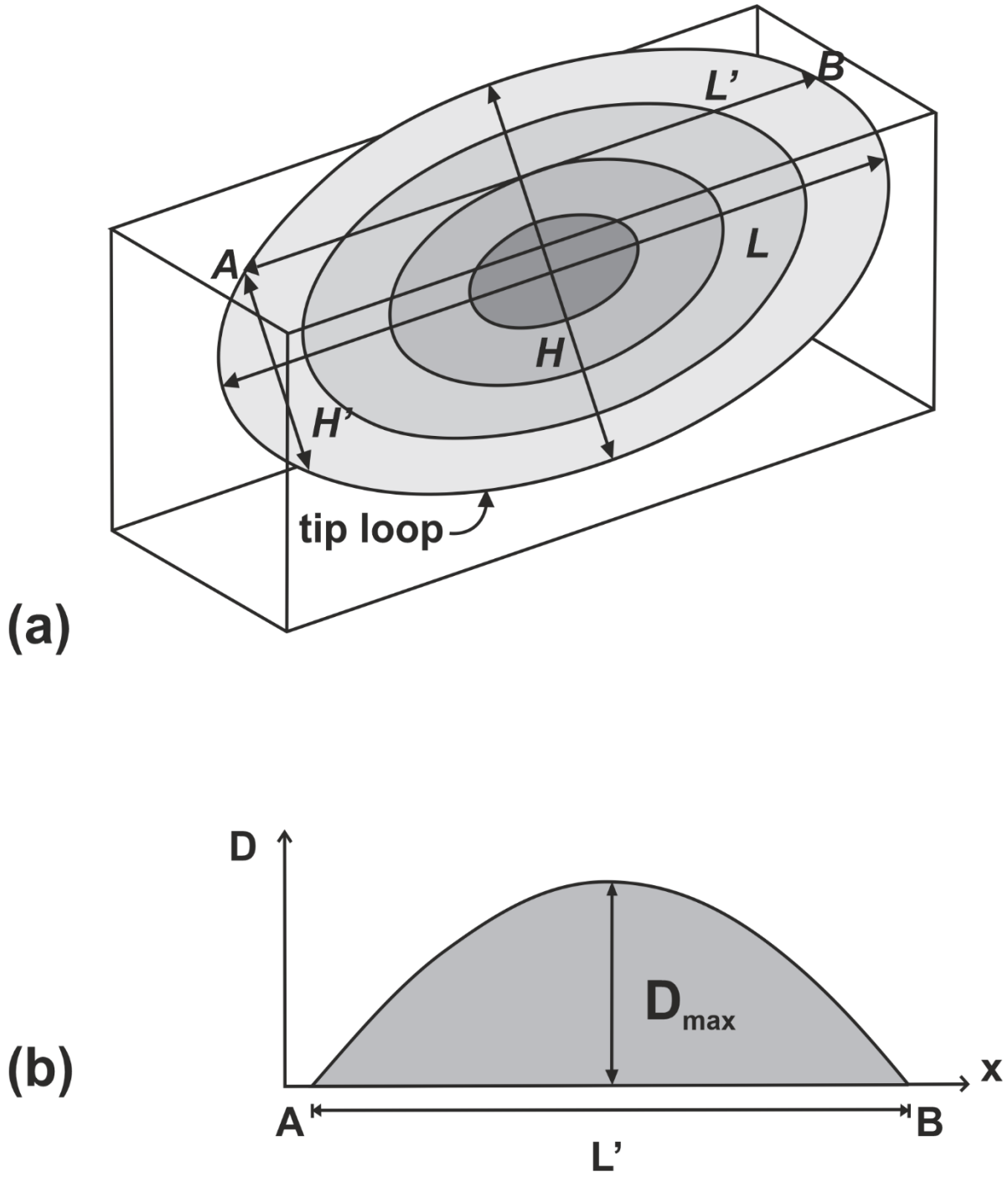

Fig. 1.1. Schematic illustration of the elemental fault terminology used in this thesis. (a) Diagram showing the ideal displacement, length and height distributions of an elliptical fault surface. (b) Diagram showing a typical displacement (D) vs. distance (x) plot of a fault trace along line A–B in Fig. 1.1a. Figure modified from Kim and Sanderson (2005).

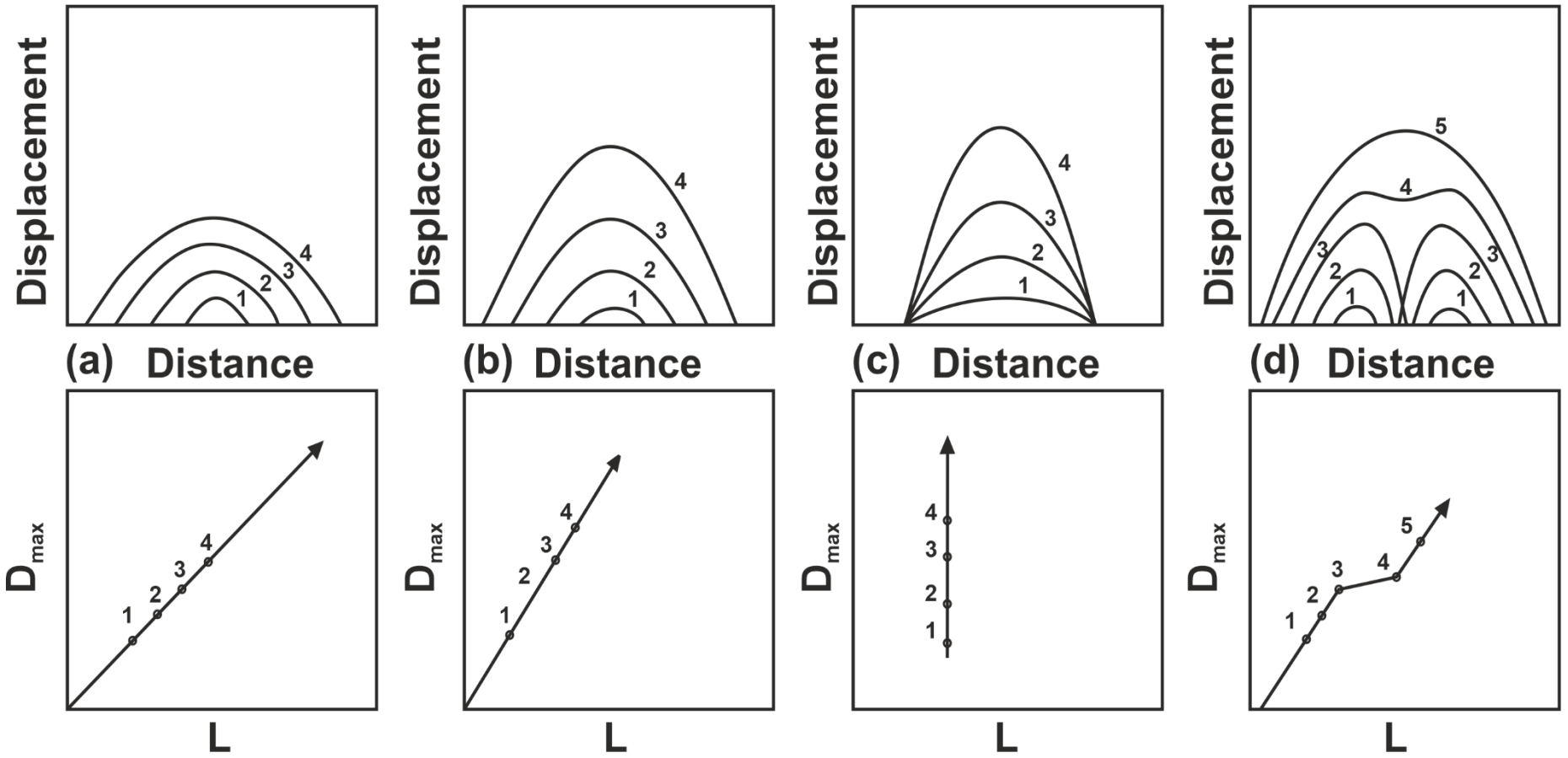

Fig. 1.2. Four principal fault growth models based on the displacement-length (D_{max}-L) relationships. a) 'Constant D/L ratio model', with a constant D/L ratio recorded during fault growth; b) 'Increasing D/L ratio model', where the D/L ratio increases as fault grow; c) 'Constant length model' provided by Walsh et al. (2002), with a rapid increase in fault length at an early stage being followed by a gradual increase in displacement with no significant increases in length; d) 'Fault linkage model', in which faults grow as isolated structures in their early stages to later link and increase total fault length (Peacock and Sanderson, 1991; Cartwright et al., 1995; Kim et al., 2000). Figure modified from Kim and Sanderson (2005).

Displacement-width (D_{max}-W) data reflect the correlation between a fault's maximum displacement (D_{max}) and its damage zone width (W), as multiple studies have identified that damage-zone width increases semi-proportionally to fault displacement (e.g. Evans, 1990; Shipton and Cowie, 2003; Manighetti et al., 2004; Mitchell and Faulkner, 2009; Savage and Brodsky, 2011; Mitchell and Faulkner, 2012; Alaei and Torabi, 2017; Mayolle et al., 2019). Previous research has shown that a proportional relationship exists between damage-zone width and maximum displacement when maximum displacement is less than 2400 m. However, such a relationship is less clear when maximum displacement exceeds 2400 m as damage-zone width seems to stabilize near a value of a few hundred metres in these cases (Shipton and Cowie, 2003; Mitchell and Faulkner, 2009; Savage and Brodsky, 2011; Mitchell and Faulkner, 2012; Johri et al., 2014) (Fig. 1.3).

1.2.3 Scaling laws

The scaling laws for faults formed in different settings and with varied geometries have been widely considered in the literature over the past few decades (e.g. Gillespie et al., 1992; Dawers et al., 1993; Dawers and Anders, 1995; Gross et al., 1997; Bonnet et al., 2001; Kim and Sanderson, 2005; Schultz et al., 2008; Childs et al., 2009). Understanding the scaling laws of fault attributes can be useful for a range of purposes, as they can help estimating the distribution of strain in a region (Marrett and Allmendinger, 1991; Cowie and Scholz, 1992a), explaining fault growth models (Cowie and Scholz, 1992a; Gudmundsson, 1992; Cartwright et al., 1995; Walsh et al., 2002; Kim and Sanderson, 2005; Gudmundsson et al., 2013), and forecasting the spatial distribution of sub-seismic (under seismic resolution) faults from seismically resolvable faults (Torabi and Berg, 2011; Johri et al., 2014). In practical terms, understanding fault scaling laws contributes to the compilation of accurate geological models, thus reducing uncertainties and risks involved in the exploration of faulted hydrocarbon reservoirs (Knai and Knipe, 1998; Kim and Sanderson, 2005; Torabi and Berg, 2011; Tao and Alves, 2017; Stanton-Yonge et al., 2020).

Multiple work has been carried out to reveal the relationship between maximum displacement and length of faults in different lithologies and in distinct tectonic settings (Walsh et al., 2002; Kim and Sanderson, 2005; Ferrill and Morris, 2008; Schultz et al., 2008; Ferrill et al., 2017). In fact, it is generally assumed that the relationship between the maximum displacement (D_{max}) and its length (L) is expressed as (Equation 1.1):

$$D_{max} = c*L^{n} \qquad \text{Equation 1.1}$$

Where the parameter c is a constant related to rock mechanical properties, chiefly the shear strength and elasticity of rocks offset by faults (Cowie and Scholz, 1992a; Gillespie et al., 1992; Ackermann et al., 2001; Kim and Sanderson, 2005; Schultz et al., 2008). For a linear scaling (i.e. n=1), c is the constant ratio D_{max}/L. The parameter n ranges from 0.5 to 2 in the literature (Watterson, 1986; Walsh and Watterson, 1988; Marrett and Allmendinger, 1991; Cowie and Scholz, 1992a; Gillespie et al., 1992; Dawers et al., 1993; Scholz et al., 1993; Schlische et al., 1996; Fossen and Hesthammer, 1997; Kim and Sanderson, 2005; Schultz et al., 2008; Nicol et al., 2010; Torabi and Berg, 2011; Nicol et al., 2020). An exponential value of n=1 defines a linear scaling law (i.e. self-similarity), implying that faults grow under constant driving stresses and act similarly at different scales. Values of $n \neq 1$ suggest a scale-dependent geometry (Kim and Sanderson, 2005; Schultz et al., 2008; Torabi and Berg, 2011). This implies that the difference between consecutive slip events on a fault is not a constant, but related to the number of slip events that occurred along the fault (Cowie and Scholz, 1992a).

In order to have a better understanding of the relationship between maximum displacement and length of faults, plots of maximum displacement vs. length (D_{max}/L) for faults formed in different tectonic settings have been systematically compiled using vast datasets (Cowie and Scholz, 1992a; Kim and Sanderson, 2005; Torabi and Berg, 2011; Kolyukhin and Torabi, 2012) (Fig. 1.4). From log-log plots of these two properties, one can observe there is a positive correlation (Fig. 1.4). There are also breaks in the D_{max}/L plot in Fig. 1.4, one between fault populations of small and medium scales (with displacements of ~1 m), and the second between fault populations of medium and large scales (with displacements of ~ 1000 m). Such breaks may be ascribed either to the lack of sufficient data or to the presence of a possible hierarchy in fault systems (Torabi and Berg, 2011). In addition, both small and large size faults show D_{max}/L ratios that are higher than the ratios of medium size faults, a character that is likely due to different fault growth mechanisms at different scales (Cowie and Scholz, 1992a; Willemse et al., 1996; Walsh et al., 2002; Walsh et al., 2003). The D_{max}/L ratios of strike-slip faults are slightly higher than for normal and reverse faults, a result of measuring fault length in a direction parallel to the slip direction (Kim and Sanderson, 2005; Torabi and Berg, 2011).

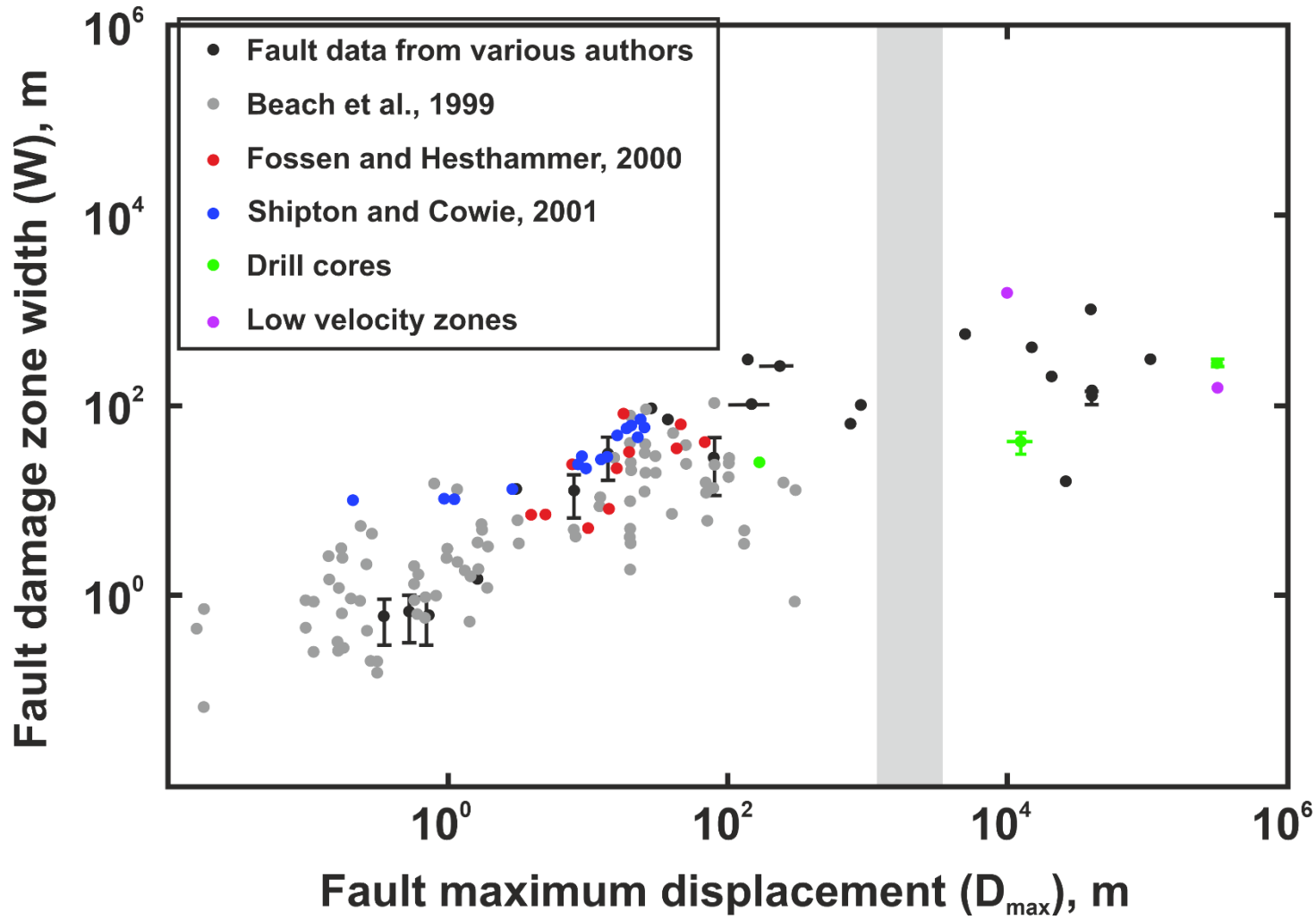

Fig. 1.3. Plot of fault damage-zone width (W) against maximum displacement (D_{max}). The figure shows that W is nearly proportional to D_{max} until a maximum displacement of ~2400 m is reached. In contrast, W stabilizes close to a value of a few hundred metres when maximum displacement exceeds 2400 m. Figure modified from Savage and Brodsky (2011).

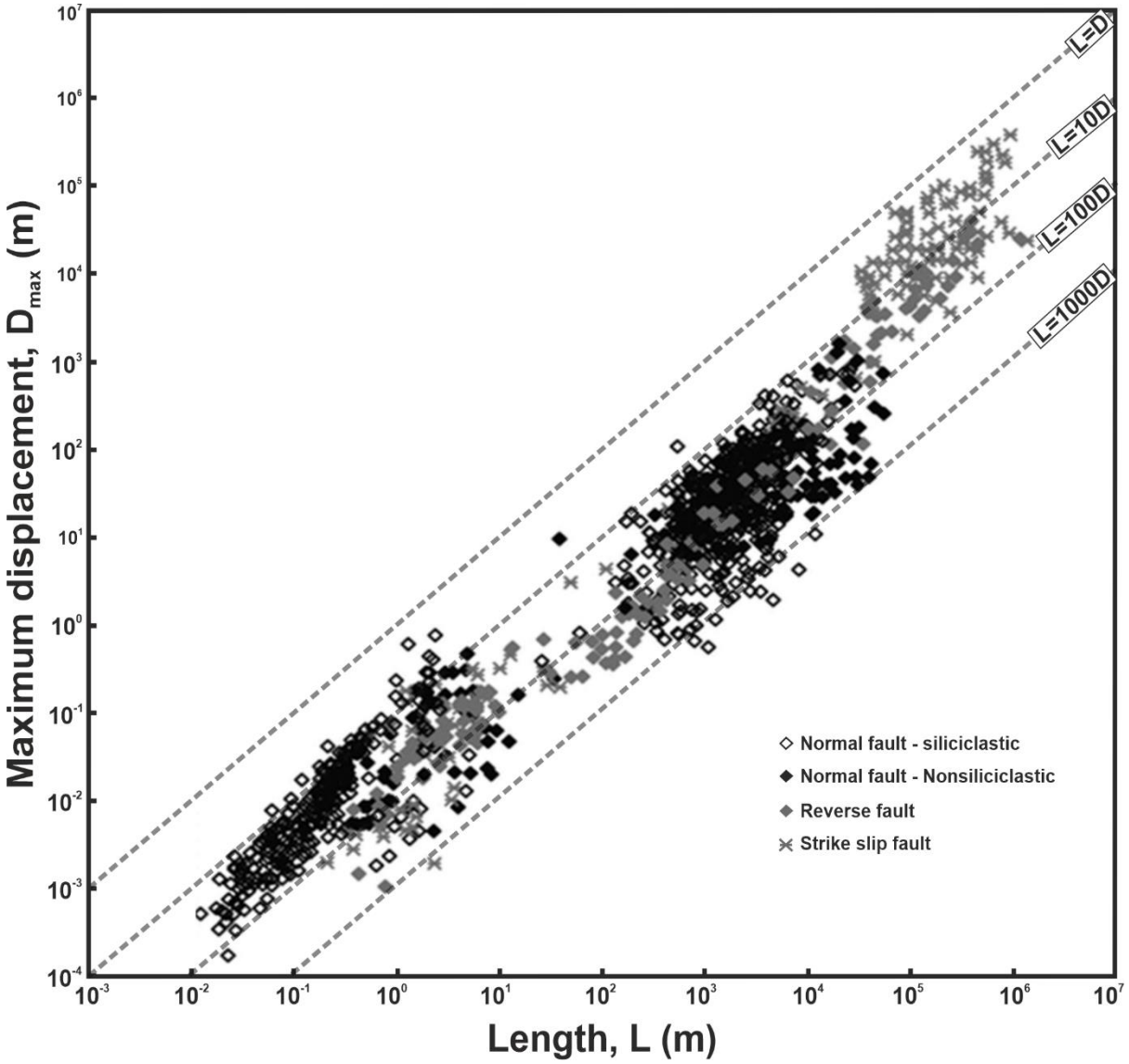

Fig. 1.4. Plot of fault maximum displacement (D_{max}) vs. length (L) for different types of faults, including normal, reverse and strike-slip faults. Normal faults offsetting siliciclastic and non-siliciclastic rocks are highlighted by different symbols in this plot. Figure modified from Torabi and Berg (2011).

When considering data from different tectonic settings, lithology changes and fault growth models reflecting disparate deformation styles will add to significant scatter in D_{max}/L plots, eventually resulting in the misinterpretation of scale relationships between faults (Cowie and Scholz, 1992a; Kim and Sanderson, 2005; Torabi and Berg, 2011). In detail, the key factors leading to scattering in D_{max}/L plots include:

a) Sampling and measurement errors (Walsh and Watterson, 1988; Gillespie et al., 1992; Kim and Sanderson, 2005; Torabi and Berg, 2011; Tao and Alves, 2019);

b) Variation in tectonic setting (Cowie and Scholz, 1992a; Kim and Sanderson, 2005; Kolyukhin and Torabi, 2012);

c) Mechanical stratigraphy in rocks intersected by the analysed faults (Scholz et al., 1993; Bürgmann et al., 1994; Schultz and Fossen, 2002; Wilkins and Gross, 2002; Kim and Sanderson, 2005; Ferrill and Morris, 2008; Ferrill et al., 2017);

d) Fault kinematics and kinematic interactions in linking faults (Peacock and Sanderson, 1991; Peacock, 1991; Bürgmann et al., 1994; Cartwright et al., 1995; Willemse et al., 1996; Wojtal, 1996; Willemse, 1997);

e) Different propagation and reactivation histories in faults (Peacock and Sanderson, 1996; Kim et al., 2001; Kim and Sanderson, 2005);

f) Intrinsic scale variations when analysing faults of different sizes (Watterson, 1986; Wojtal, 1994; Wojtal, 1996; Gross et al., 1997; Torabi and Berg, 2011).

1.2.4 Fault-growth models

Multiple work has been presented over the past few decades to better understand fault growth (e.g. Ellis and Dunlap, 1988; Cowie and Scholz, 1992a; Cartwright et al., 1996; Walsh et al., 2002; Nicol et al., 2005; Jackson and Rotevatn, 2013; Rotevatn and Jackson, 2014; Childs et al., 2017; Nicol et al., 2017; Rotevatn et al., 2019; Nicol et al., 2020). Understanding how faults grow in 3D dimensions has important applications in science disciplines. For example, fault styles and tip propagation rates control the tectono-stratigraphic development of sedimentary basins (Henstra et al., 2017; Jackson et al., 2017; Gawthorpe et al., 2018; Ge et al., 2018), and the location, magnitude and recurrence interval of potentially hazardous earthquakes (Walsh et al., 2003; Nicol et al., 2005; Schultz et al., 2008). In essence, four key models have

been established to describe fault growth: isolated, coherent, constant-length and segment linkage fault models (e.g. Mansfield and Cartwright, 1996; Walsh et al., 2002; Walsh et al., 2003; Nicol et al., 2005; Jackson and Rotevatn, 2013; Henstra et al., 2015; Fossen and Rotevatn, 2016; Childs et al., 2017; Jackson et al., 2017; Rotevatn et al., 2019).

1.2.4.1 Isolated fault model

The isolated fault model (also referred to as 'propagating fault model'; see Rotevatn et al., 2019) refers to those faults that grow via a synchronous increase in their length and displacement, i.e. the view is that when faults accrue displacement they also lengthen by tip propagation (Walsh and Watterson, 1988; Dawers et al., 1993; Cartwright et al., 1995; Walsh et al., 2003; Kim and Sanderson, 2005; Bergen and Shaw, 2010; Jackson et al., 2017; Rotevatn et al., 2019) (Fig. 1.5a). The isolated fault model is largely based on the obvious positive correlation between faults' maximum displacement and length (D_{max}-L) across several orders of magnitude (Kim and Sanderson, 2005; Torabi and Berg, 2011; Rotevatn et al., 2019). Due to this positive correlation, the isolated fault model implies that an increase in fault displacement results in a corresponding increase in length (Watterson, 1986; Peacock and Sanderson, 1991; Cartwright et al., 1995; Morley, 1999; Mansfield and Cartwright, 2001; Kim and Sanderson, 2005; Baudon and Cartwright, 2008a; Torabi and Berg, 2011; Rotevatn et al., 2019). For a given rock shear strength, displacement and length must increase linearly according to the theoretical fracture mechanisms, a character supporting the predominance of the isolated fault model in nature (e.g. Cowie and Scholz, 1992a). The isolated fault model has thus dominated the structural geology and tectonics literature for decades, providing the basis for descriptions of fault growth in textbooks (e.g. Kim and Sanderson, 2005; Torabi and Berg, 2011; Fossen and Rotevatn, 2016; Rotevatn et al., 2019). However, there is a range of challenges in applying the isolated fault model to all faults in nature, though it provides a relatively simple and appealing explanation of global D_{max}-L scaling relationships (e.g. Jackson et al., 2017; Rotevatn et al., 2019). For example, isolated fault models show incompatibility with displacement-length ratios of faults reactivated in individual earthquakes (e.g. Wells and Coppersmith, 1994; Walsh et al., 2002; Nicol et al., 2005).

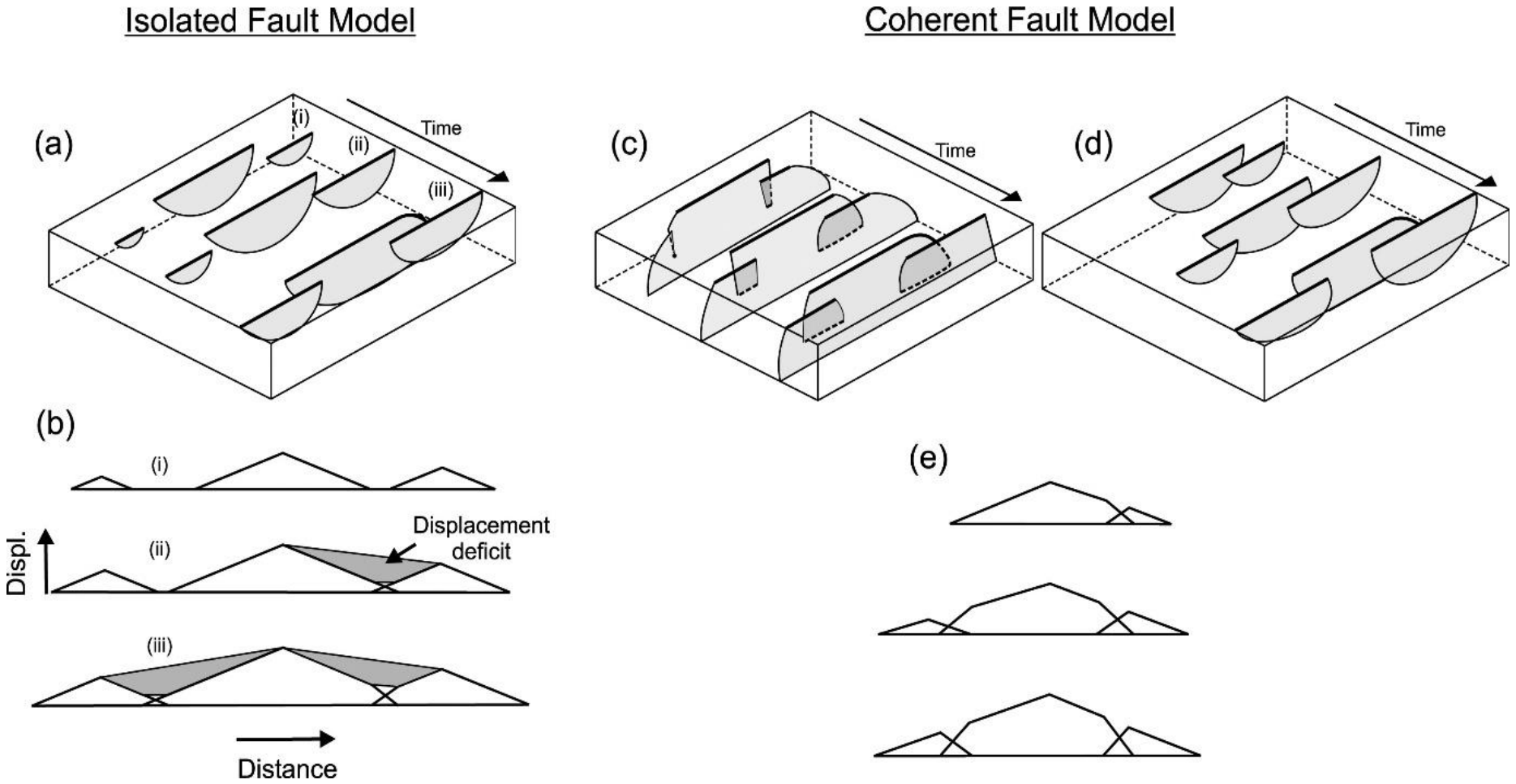

Fig. 1.5. Schematic illustration of the isolated and coherent fault models. The block diagrams a, c and d show three growth stages of a segmented fault array (i-iii). The displacement-distance plots b and e are for the fault traces on the upper surfaces (bold lines) of the block diagrams. The coherent fault model is explained for segmented fault traces that are (c) hard-linked and formed by fault surface bifurcation and (d) soft-linked and formed by 3D segmentation. Figure from Walsh et al. (2003).

1.2.4.2 Coherent fault model

The coherent fault model refers to that individual fault segments initiate, propagate and develop as part of a spatially and kinematically related components of a fault array (Childs et al., 1995; Childs et al., 1996b; Walsh et al., 2002; Walsh et al., 2003) (Figs. 1.5 and 1.6). In the coherent fault model, fault segments that are hard- or soft-linked may be formed due to fault surface bifurcation, i.e. splaying or stepping (Walsh et al., 2003) (Figs. 1.5c and d). Fault propagation in the coherent fault model is closely associated with interactions of adjacent fault segments, in contrast with the isolated fault model in which fault propagation is not influenced by other faults (Figs. 1.5 and 1.6). In the coherent model, fault segments do not have significant displacement deficits between their overlapping areas (Figs. 1.5b and e), implying these fault segments behave as one kinematically coherent structure. Nevertheless, elastic deformation is still likely to occur between the overlapping areas of fault segments in coherent fault model, resulting in the presence of displacement deficits (Walsh et al., 2003) (Fig. 1.6b). Measurement errors, especially sampling interval, can also lead to the recognition of erroneous displacement deficits, causing an inaccurate interpretation of a coherent fault model (Tao and Alves, 2019). Distinct field examples of fault growth have nonetheless been observed in accordance with the coherent fault model (Fig. 1.6a).

1.2.4.3 Constant-length fault model

The constant-length model suggests that faults grow by the rapid establishment of their near-final length, after which they mainly grow by displacement accrual (Walsh et al., 2002; Walsh et al., 2003; Nicol et al., 2005; Jackson and Rotevatn, 2013; Nicol et al., 2017; Rotevatn et al., 2019) (Fig. 1.7). The constant-length fault model was first proposed and developed in series of papers published from 2002 onwards, partly motivated by the incompatibility between fault and earthquake D-L scaling properties. Initially, Walsh et al. (2002) put forward the term 'alternative model' to describe a fault growth that is achieved mainly by increase in cumulative displacement but with near constant length in an early stage. This term was later coined the 'constant-length model' by Nicol et al. (2005) to describe the fact that faults experience displacement accumulation rather than lengthening for much of their development. The constant-length fault model is based on the premise that faults propagate to their near-full length relatively rapidly (Walsh et al., 2002; Nicol et al., 2017), because further lengthening is typically inhibited due to mechanical fault interactions between adjacent faults and an

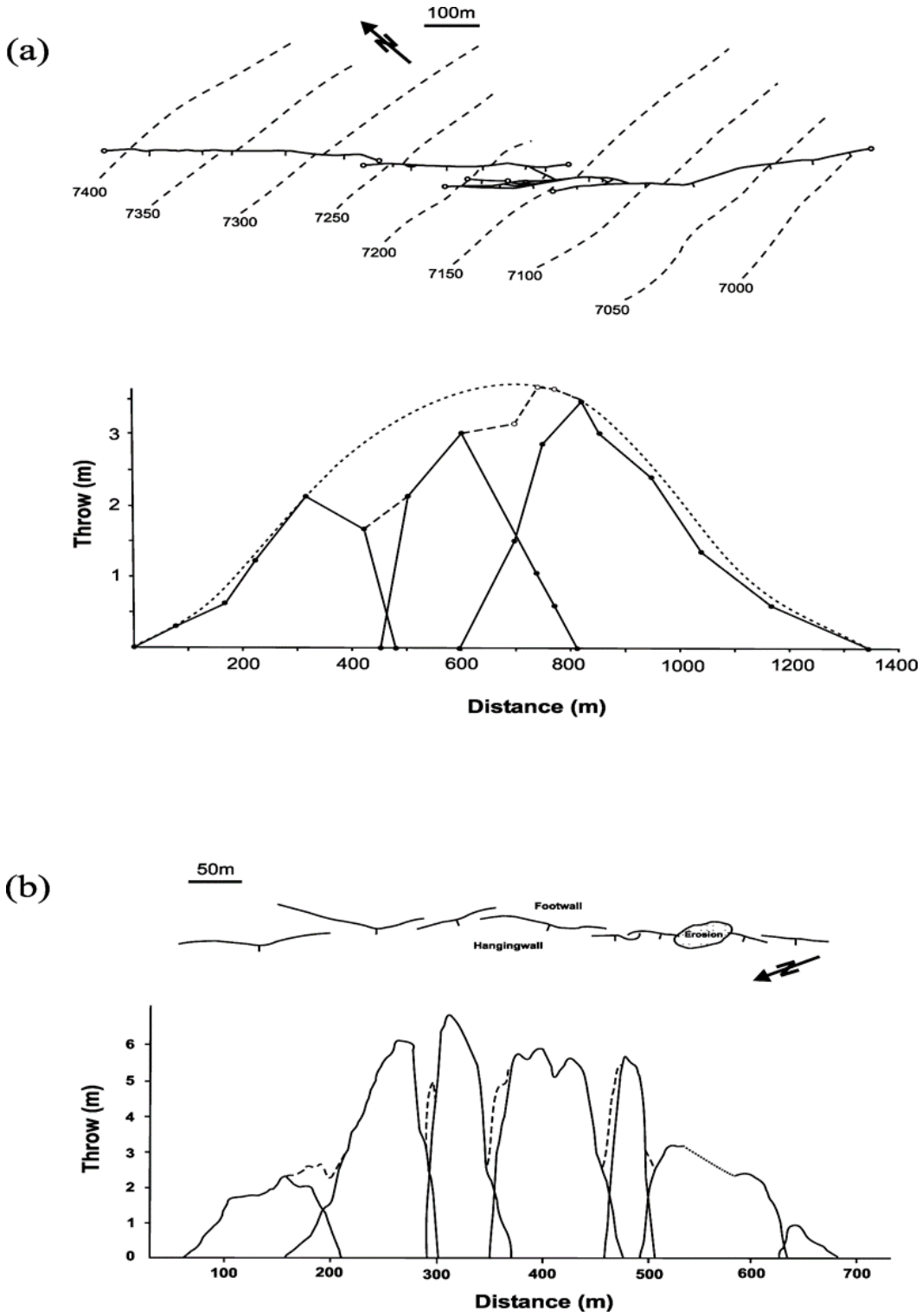

Fig. 1.6. (a) A segmented normal fault with its throw profile measured along the segmented fault array (solid lines), indicating fault segments behave as a kinematically coherent structure, highlighted by the idealised envelope plotted through summed throws (dashed line). (b) Segmented fault array showing a systematic distribution of throw along seven fault segments (solid lines). The aggregate throw profile is shown as dashed lines, but it does not include the strain accommodated by bedding rotation in the relays zones. Figure from Walsh et al. (2003).

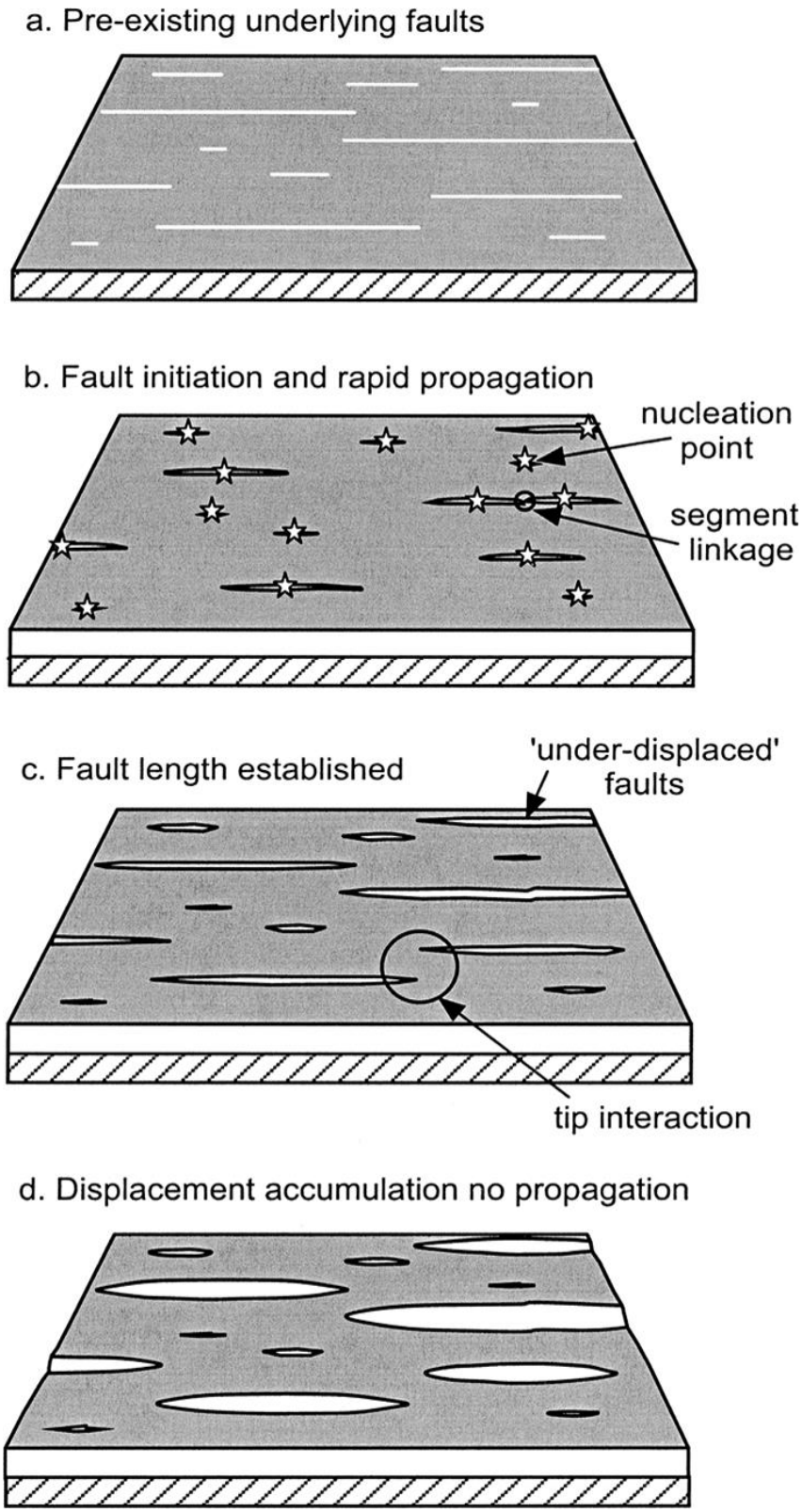

Fig. 1.7. Schematic illustration focusing on the constant-length model. The figure shows that faults grow by rapid establishment of their near-final length in their early slip history, after which they grow mainly by displacement accrual. Figure from Walsh et al. (2002).

associated reduction of tip stresses (Cowie, 1998; Gupta and Scholz, 2000; Walsh et al., 2002). The constant-length fault model offers a more dynamic view of displacement-length (D-L) scaling relationships and helps to understand the incompatibility between fault and earthquake-rupture scaling relationships (Cladouhos and Marrett, 1996; Nicol et al., 2005; Torabi and Berg, 2011; Nicol et al., 2017). However, the constant-length fault model cannot explain the observation that relatively few ancient faults plot below the regression trend line in global D_{max}-L compilations (Rotevatn et al., 2019).

1.2.4.4 Fault growth by segment linkage

Fault growth by segment linkage is one of the most important mechanisms for fault growth (Peacock and Sanderson, 1991; Peacock, 1991; Cartwright et al., 1995; Wilkins and Gross, 2002; Kim and Sanderson, 2005; Torabi and Berg, 2011; Nicol et al., 2017; Peacock et al., 2017). Mature faults are often a result of fault-segment linkage (e.g. Cartwright et al., 1995; Walsh et al., 2003; Lohr et al., 2008), with two modes being recognised in the literature based on the observed linkage directions: lateral tip linkage and dip linkage (Mansfield and Cartwright, 1996; Baudon and Cartwright, 2008a, b) (Figs. 1.8 to 1.10).

When dealing with segment linkage at the lateral tips of faults, maximum and minimum displacement points represent the loci of nucleation and linkage of fault segments, respectively (e.g. Ellis and Dunlap, 1988; Kim and Sanderson, 2005). Three stages elucidate the way the lateral tips may link in segmented faults (Peacock and Sanderson, 1991; Peacock, 1991; Kim and Sanderson, 2005) (Fig. 1.8). In the first stage (stage 1), isolated faults are formed without interacting. These isolated faults propagate to each other resulting in overlaps, or relay structures developing without an obvious connection (soft linkage - stage 2). Eventually, a through-going fault develops and connects the overlapping faults (hard-linkage - stage 3) (Fig. 1.8). Due to through-going fault connections tending to form either at the hanging-wall end of the ramp, or at the footwall, the overlapping area can be classified into hanging-wall breached and footwall breached (Cartwright et al., 1996). With further propagation of the linked fault, the breached ramp (overlapping area) will either be locked into further movement with the footwall or, instead, with the hanging wall (Cartwright et al., 1996) (Fig. 1.9). Lateral tip linkage also influences the final displacement-length (D_{max}-L) values for a fault, as the interaction between segment faults acts as a 'barrier' that inhibits propagation in overlapping fault tips. Thus, segmented faults can cause a significant scattering in displacement-length data, causing any single

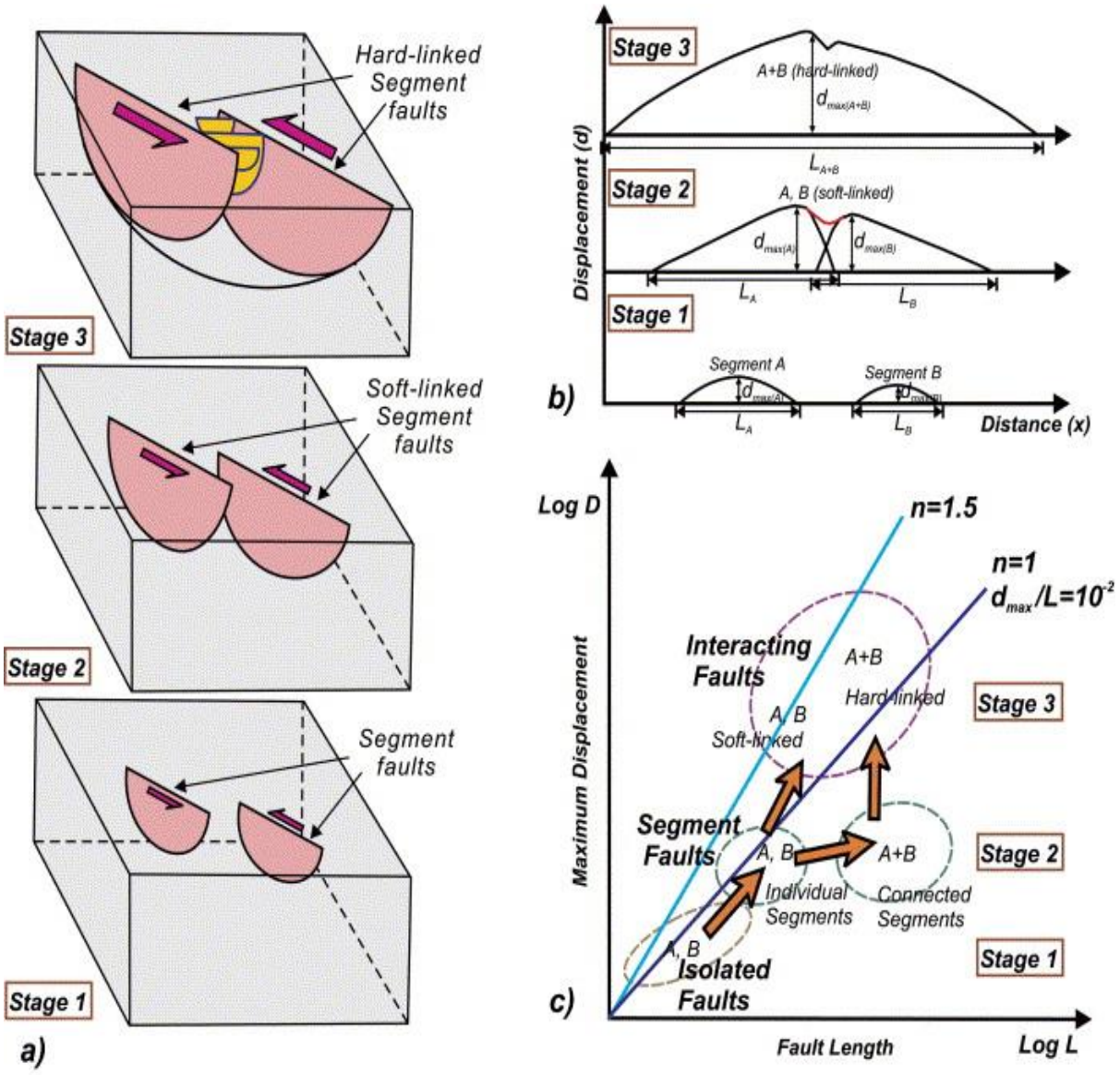

Fig. 1.8. Schematic illustration for fault segmentation and linkage. a) Faults evolve from isolated faults to interacting faults through segment linkage in three different stages. b) Plot of displacement (D) vs. distance (x) showing how fault displacement varies with segment linkage in three different stages. c) Maximum displacement (D_{max}) vs. length (L) shown as a log-log plot indicating different evolution paths for segment faults due to hard- and soft-lonkages in three different stages. Figure from Kim and Sanderson (2005).

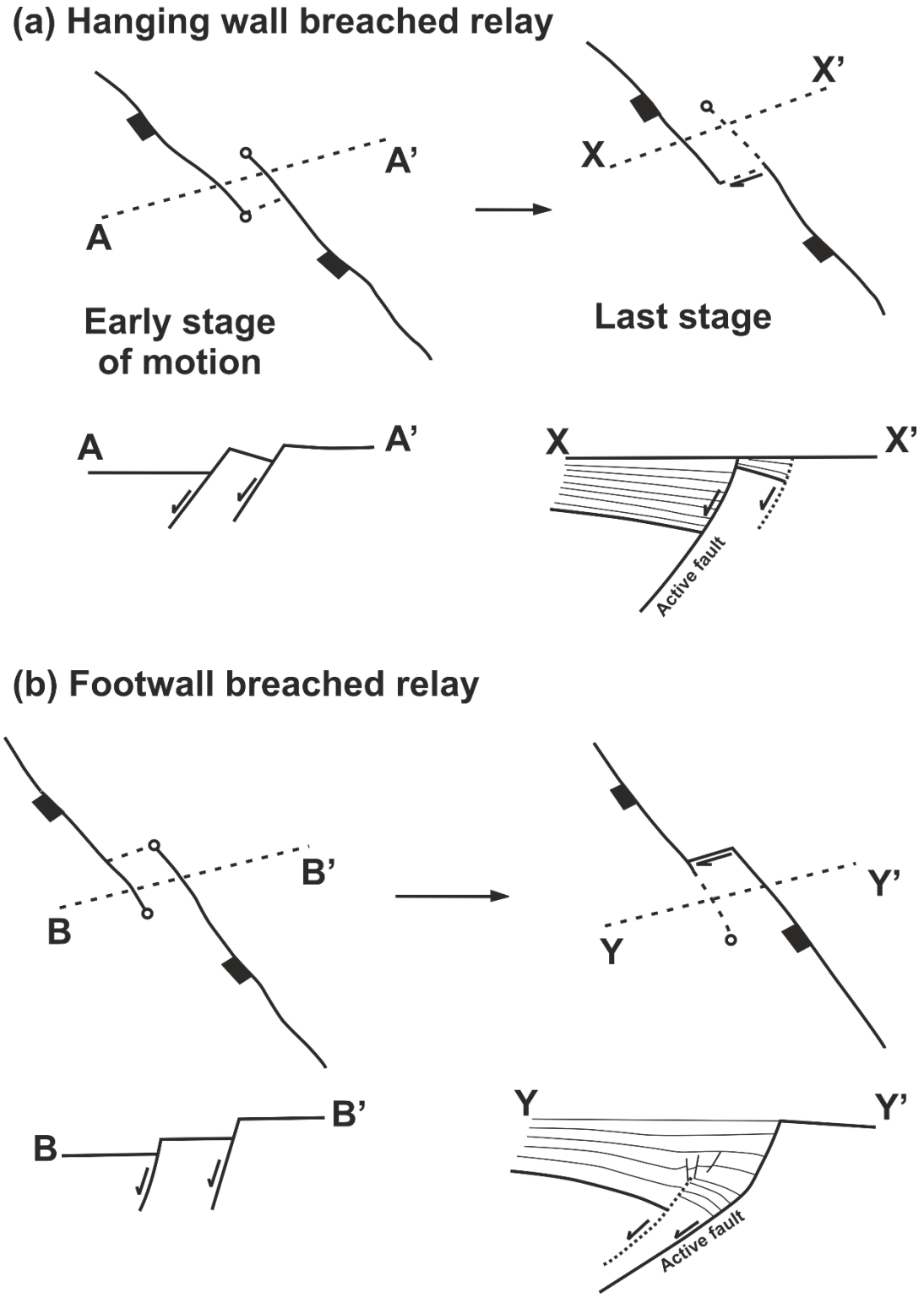

Fig. 1.9. Schematic map illustrating two types of breached relay structures. (a) Hanging wall breached relay, characterised by an inactive splay fault and ramps attached to the footwall. (b) Footwall breached relay, characterised by the ramp and splay fault being coupled to the motion of the hanging wall. Figure modified from Cartwright et al. (1996).

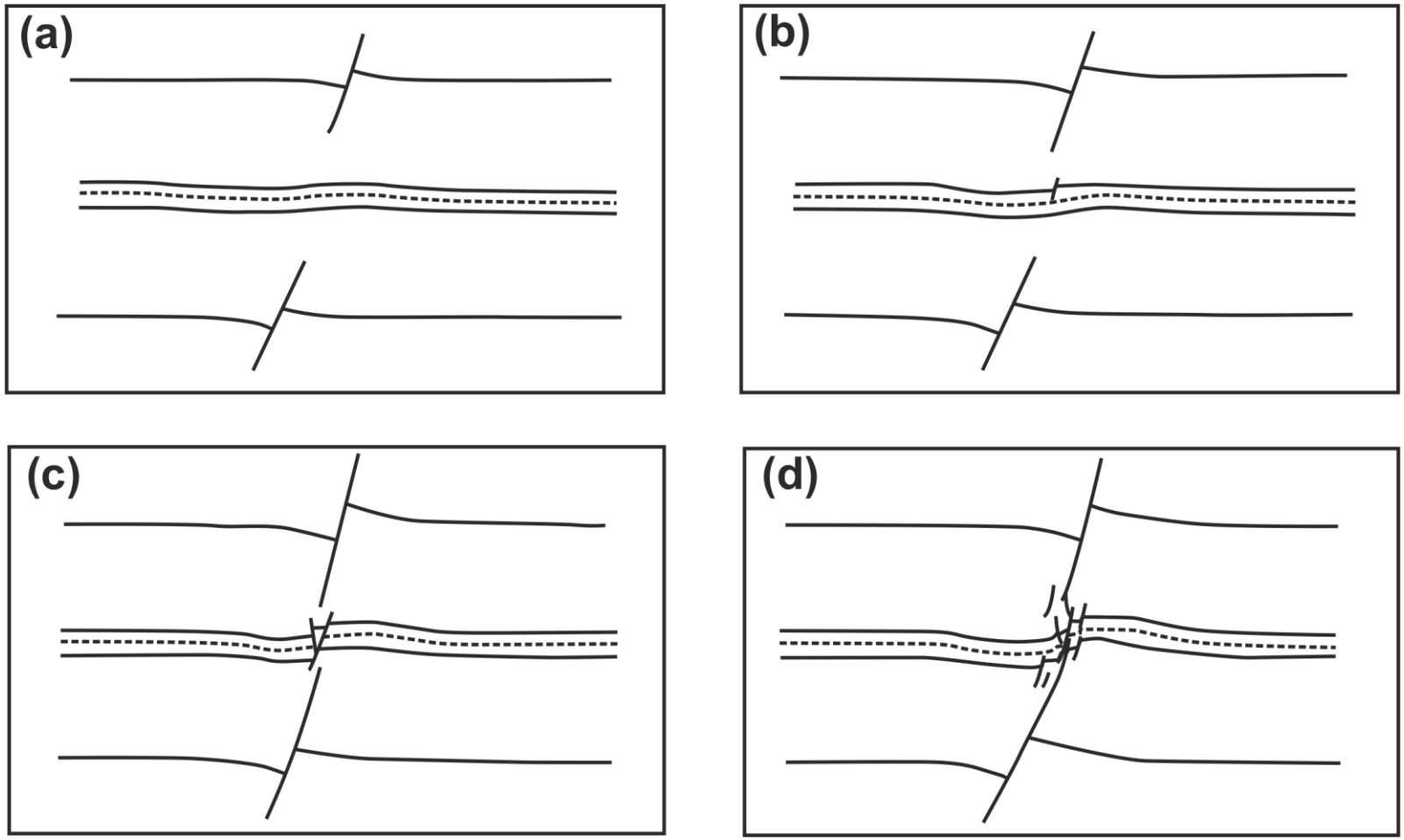

Fig. 1.10. Schematic illustration for dip linkage of fault segments on cross sections. (a) Isolated and precursor fault segments with a similar strike and dip grow by tip-line propagation. (b) and (c) As the neighbouring fault tips approach one another, a mix of brittle and ductile deformation occurs in the region between the two tips. (d) Segment faults link to form a single, coherent structure. Figure modified from Mansfield and Cartwright (1996).

scaling law to be hardly valid for a specific area, or when comparing distinct regions (Peacock and Sanderson, 1991; Cartwright et al., 1996; Mansfield and Cartwright, 1996; Cowie and Roberts, 2001; Walsh et al., 2003; Kim and Sanderson, 2005; Torabi and Berg, 2011).

Fault dip linkage refers to the linkage of the lower tips of shallower faults to the upper tips of faults developed in lower strata (Mansfield and Cartwright, 1996) (Fig. 1.10). Several stages can be identified during the evolution of fault dip linkage in nature. Initially, independent fault segments develop with similar strikes at different depths, and the tips of these faults propagate to approach each other causing brittle and ductile deformation in the region between them. With continuing fault propagation, the segments can link to form a single, coherent structure (Mansfield and Cartwright, 1996) (Fig. 1.10). With full linkage of fault segments, brittle and ductile deformation zones will develop between them, causing scattering in displacement-length (D_{max}-L) plots (Peacock and Sanderson, 1991; Cartwright et al., 1995; Childs et al., 1996a; Cowie and Roberts, 2001). By using high resolution data, fault displacement minima can be identified to accurately differentiate fault dip linkage (Tao and Alves, 2019).

1.3 Mechanical stratigraphy

Mechanical stratigraphy is an overarching term referring to the mechanical properties, layer thickness, and frictional properties of mechanical boundaries that constitute a rock sequence (e.g. Young et al., 1982; Erickson, 1996; Di Naccio et al., 2005; Peacock and Mann, 2005; Ferrill and Morris, 2008; Laubach et al., 2009; Morris et al., 2009; McGinnis et al., 2016; Ferrill et al., 2017). Mechanical stratigraphy must be considered when interpreting geological structures correctly (McGinnis et al., 2016), as it greatly affects fault initiation and growth (Ferrill and Morris, 2008; Roche et al., 2012; Roche et al., 2013), fault zone processes (Jamison, 1979; Young et al., 1982), and also fault geometry and network characteristics (Ferrill and Morris, 2003; Morris et al., 2009). In previous research work, a range of terms have been used to describe the ability for individual layers to resist deformation, such as strong vs. weak or very weak (e.g. Wiltschko and Chapple, 1977), stiff vs. soft (e.g. Ferrill and Groshong Jr, 1993), or competent vs. incompetent (e.g. Ferrill and Morris, 2008). Commonly, strong, stiff or competent intervals tend to resist deformation, keeping bed length and thickness when compared to weak, soft or incompetent intervals. Conversely, weak, soft or incompetent intervals tend to accommodate a greater degree of deformation before reaching brittle failure; they are more ductile than strong, stiff or competent intervals (e.g. Young et al., 1982; Erickson,

1996; Ferrill and Morris, 2001; Di Naccio et al., 2005; Ferrill et al., 2005; Ferrill and Morris, 2008; Laubach et al., 2009; Morris et al., 2009; Ferrill et al., 2014; Ferrill et al., 2017). In nature, a vertical section the strata that constitute brittle material is sometimes broken to form a fault, whereas relatively ductile strata above or below are bent to form a fold (Powell, 1875) (Fig. 1.11). In summary, the term 'mechanical stratigraphy' includes three different aspects: (1) the different material properties of rock strata; (2) the thickness of mechanical layers in nature; (3) the character and frictional properties of the transitions or boundaries between mechanical layers, which cause variations of stiffness and strength in heterolithic intervals (Groshong and Groshong, 2006; Ferrill and Morris, 2008; Laubach et al., 2009; Morris et al., 2009; Ferrill et al., 2014; Ferrill et al., 2017).

1.3.1 Material properties of rock and strata

The material properties of rock and strata are mainly associated with their mineralogy and texture, especially porosity (e.g. Donath, 1970; Hanks et al., 1997; Wilkins and Gross, 2002; Underwood et al., 2003; Peacock and Mann, 2005; Schopfer et al., 2006; Ferrill and Morris, 2008; Laubach et al., 2009; Morris et al., 2009; Gale et al., 2010; Ferrill et al., 2017; Rowan et al., 2019). As rock strength usually relates to its mineral constituents, competent lithologies generally consist of strong minerals such as calcite, dolomite and quartz, whereas incompetent lithologies likely consist of weak constituents such as clay minerals, organic carbon, and/or evaporite minerals (e.g. Donath, 1970). In particular, the proportion and distribution of clay minerals in a rock can greatly influence the strength of rock (e.g. Laubach et al., 2009). Hence, competent lithologies (e.g., clay-poor limestone or dolomite) cannot accommodate great amounts of pre-failure strain when compared to incompetent lithologies (e.g., clay-rich shale, argillaceous limestone) (Ferrill et al., 2017). In addition, pre-failure strain is usually accommodated by grain rearrangement, pore collapse, and a variety of crystal plastic deformation mechanisms, pressure solution, and transitions to dynamic recrystallisation at higher temperatures (Rutter, 1976; Groshong Jr, 1988; Burkhard, 1993). These phenomena have been proven by experimental studies, and explain why brittle strata will fault first with the accumulation of strain, whereas ductile strata accommodate greater pre-failure strain before faulting (Donath, 1970; Ferrill and Morris, 2003; Welch et al., 2009; Ferrill et al., 2012; Ferrill et al., 2017) (Fig. 1.12). In parallel, faults cross-cutting multiple layers are likely to be steeper in

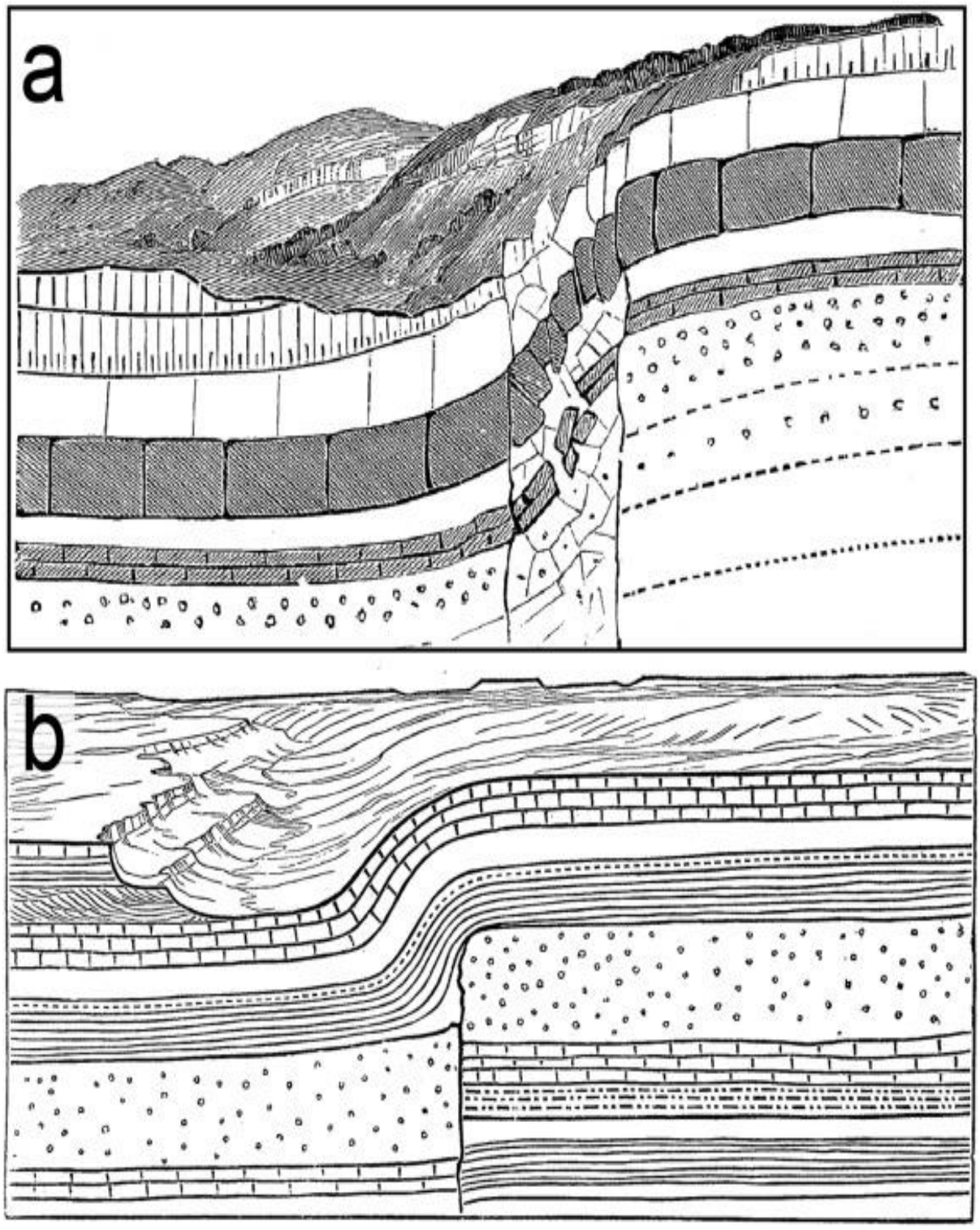

Fig. 1.11. Schematic illustration for the influence of mechanical stratigraphy on deformation. (a) A monocline with brittle deformation in the monocline limb. (b) A fault dying upwards into a fold. Figure from Ferrill et al. (2017) who adapted it from Powell (1875).

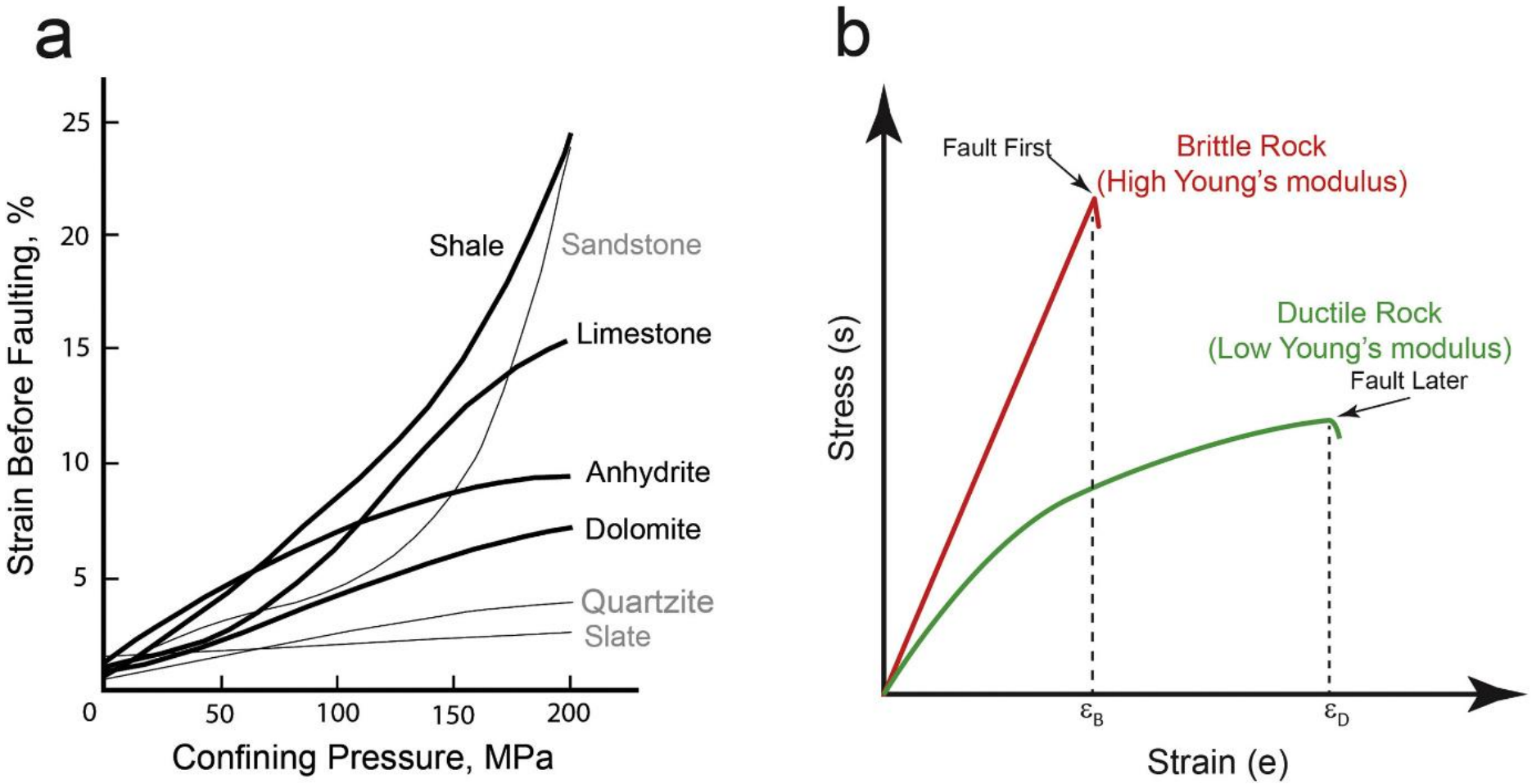

Fig. 1.12. (a) Plot of strain before faulting vs. confining pressure for multiple common rock types. (b) Plot of stress vs. strain for brittle and ductile rocks highlighting that brittle rock is faulted before ductile rock with increasing strain. Figs. 1.12a and 1.12b are from Ferrill and Morris (2008) and Ferrill et al. (2017), respectively.

brittle strata than in ductile strata (Jackson et al., 1987; Westaway, 1999; Collettini and Sibson, 2001; Laubach et al., 2009; Ferrill et al., 2017) (Fig. 1.13). Finally, the diagenetic history of a rock can significantly affect its strength, causing changes of rock mass by mechanic compaction and cementation (e.g. Laubach et al., 2009). Rock strength is likely to increase with increasing cementation, compaction and/or welding, and also with decreasing porosity (e.g. Dunn et al., 1973; Chang et al., 2006; Sone and Zoback, 2010).

1.3.2 Thickness of mechanical layers

The thickness of mechanical layers has an important effect on the structural deformation mechanisms and styles (e.g. Erickson, 1996; Gross et al., 1997; Di Naccio et al., 2005; Peacock and Mann, 2005; Laubach et al., 2009; Morris et al., 2009; Welch et al., 2009; Ferrill et al., 2014; Ferrill et al., 2017) (Fig. 1.14). As stratigraphic sequences usually constitute both competent and incompetent strata, the thickness ratio of incompetent vs. competent strata can be regarded as an important and useful parameter to explain variations in the relative rates of fault displacement and propagation in nature (e.g. Ferrill and Morris, 2008; Morris et al., 2009; Ferrill et al., 2017) (Fig. 1.14). For low thickness ratios of incompetent to competent strata (e.g. 0.07), the displacement to propagation ratios and displacement gradients in faults are low. Comparatively, for high thickness ratios (e.g. about 1.4), the displacement to propagation ratios and displacement gradients in faults are high. The thickness ratio of incompetent vs. competent strata can also indicate which types of strata are the dominant in mechanical layers (e.g. Ferrill et al., 2017) (Fig. 1.14).

1.3.3 Properties of transitions or boundaries between mechanical layers

The transitions or boundaries between mechanical layers are important to the detailed characterisation of mechanical stratigraphy (e.g. Ferrill et al., 2017). Frictional properties of bed boundaries or weak inter-beds usually influence the deformation behaviour (e.g. Peacock and Mann, 2005; Laubach et al., 2009; Ferrill et al., 2017; Rowan et al., 2019). An increasing content of insoluble clay minerals and organic particles usually decrease the frictional strength and interface cohesion along bedding surfaces, or in zones between competent beds (e.g. Ferrill et al., 2017). Conversely, rugose or sutured boundaries, such as those formed by the karstic

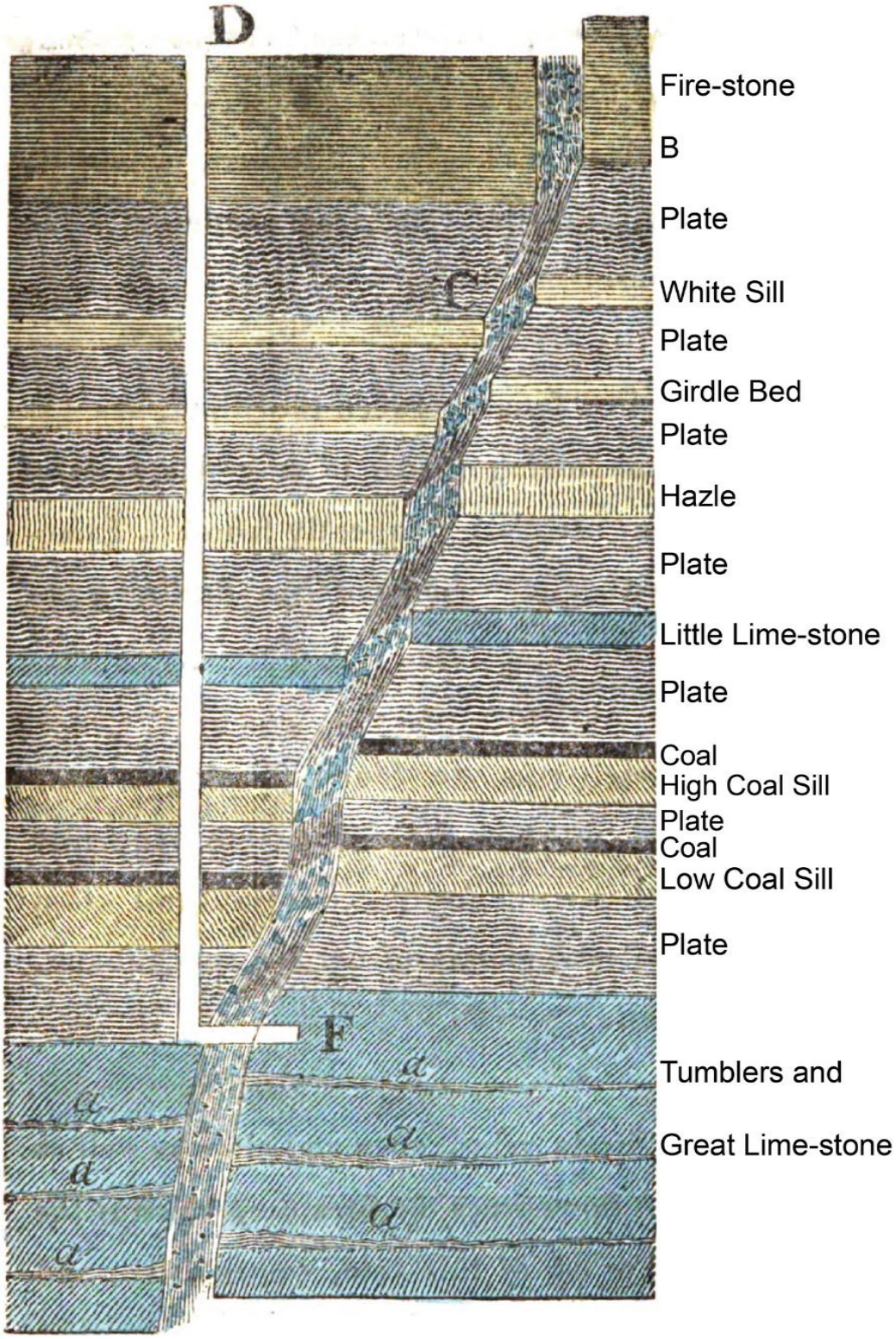

Fig. 1.13. An approximate 70 m thick cross-section through the Northern Pennine Orefield fissure vein, showing how fault dips change in strata with different lithology. Near vertical fault segments through limestones (blue) and sandstones (yellow) are linked by moderate dipping fault segments through shale (grey) and coal (horizontal black layers). Figure from Ferrill et al. (2017) who adapted it from Forster (1821).

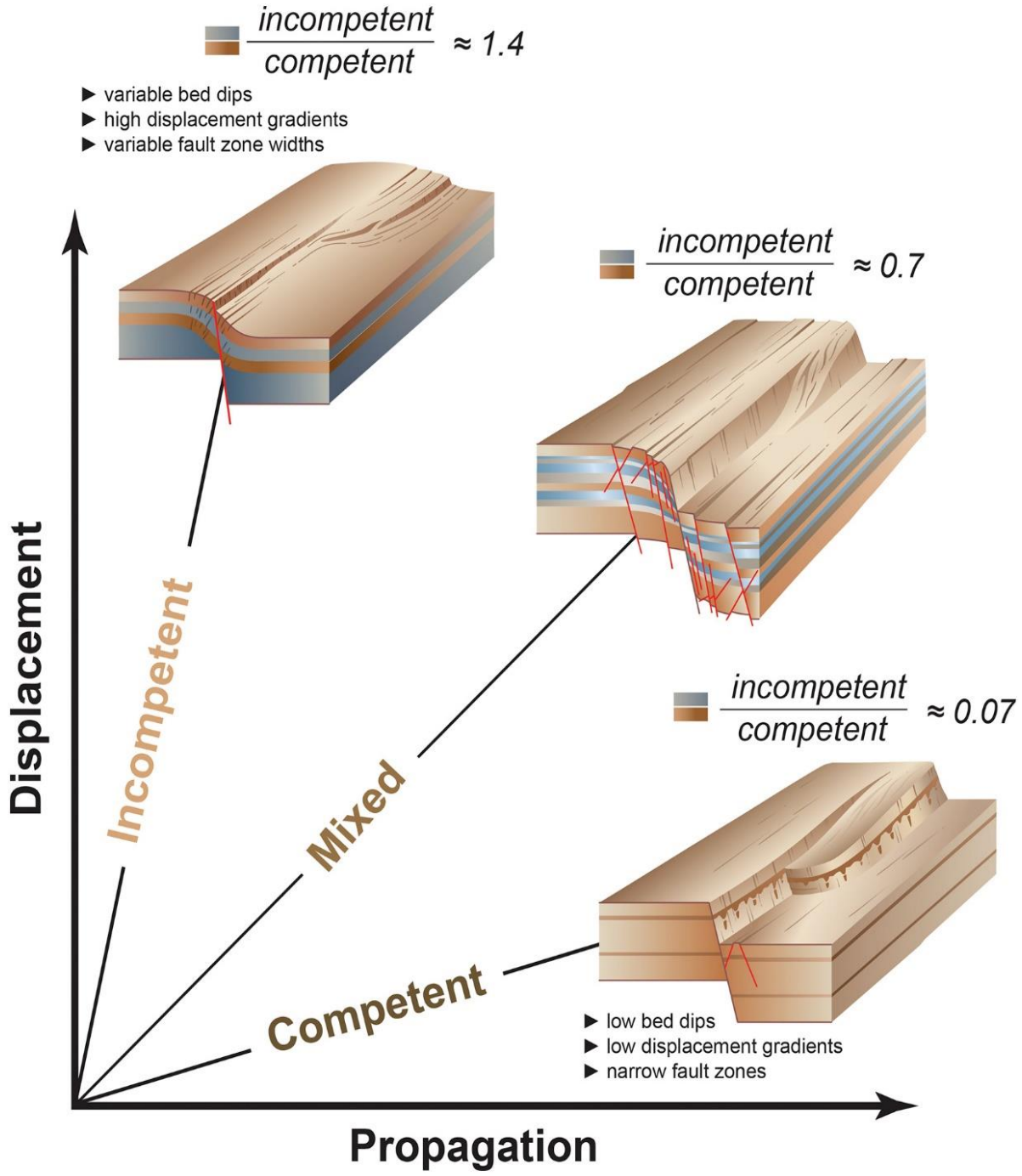

Fig. 1.14. Schematic illustration for the influence of mechanical stratigraphy on fault propagation vs. displacement for mechanical stratigraphic units with different incompetent to competent thickness ratios. Volumes of rock with low incompetent to competent thickness ratios (0.07) have has low bed dips, displacement gradients and narrow fault zones. In contrast, high incompetent to competent thickness ratios (e.g., 1.4) result in variable bed dips, high displacement gradients and variable fault zone widths. Mechanical stratigraphy with intermediate incompetent to competent thickness ratios show behaviours depending on the local conditions. Figure from Ferrill et al. (2017) who adapted it from Ferrill and Morris (2008).

dissolution of marine-cemented hardgrounds in carbonate sections, or irregular lava flow surfaces in volcanic sections, increase the resistance to frictional sliding between layers (e.g. Ferrill et al., 2017). Bedding-parallel stylolites with vertical 'teeth' can be formed due to carbonate dissolution during burial and compaction, and are likely to lock bedding planes so that they are not disposed to slip (e.g. Ferrill et al., 2017). Additionally, distinct mechanical contrasts and weak beds or laminae may localize bedding plane slip or, instead, result in abrupt changes in deformation behaviour (Higgs, 1991; Ferrill, 1998; Cooke and Underwood, 2001; Ferrill and Morris, 2008; Ferrill et al., 2012; Ferrill et al., 2017).

1.4 Salt tectonics

Salt tectonics is the study of geologic deformation involving sub-surface salt, i.e. how and why salt structures evolve, the three-dimensional forms that result from salt tectonics, and the interactions of local salt and more regional tectonics (e.g. Jackson and Hudec, 2017). Salt tectonics has radically influenced more than 130 sedimentary basins around the world, especially sedimentary basins developed in three important geological settings: (1) inter-cratonic basins such as the Zechstein Group of the North Sea (e.g. Remmelts, 1995; Stewart and Coward, 1995; Remmelts, 1996; Taylor, 1998); (2) syn-rift and post-rift passive margins such as those developed along East Brazil and its conjugate West African margin (e.g. Chang et al., 1992; Mohriak et al., 2008; Mohriak et al., 2012); (3) continental collision zones and foreland basins such as the Tarim Basin in Northwest China (e.g. Jianfeng et al., 2004; Yixin et al., 2008; Yu et al., 2014). Significantly, the control of salt tectonics on structural deformation and sedimentation is of vital importance to hydrocarbon exploration (e.g. Jackson and Vendeville, 1990; Ge and Jackson, 1996; Yao et al., 2003; Hudec and Jackson, 2007; Yu et al., 2011; Nikolinakou et al., 2014; Thigpen et al., 2019), the mining industry (e.g. Davison et al., 1996; Behlau and Mingerzahn, 2001; Van Gent et al., 2011), carbon sequestration (e.g. Chiaramonte et al., 2008; Chang et al., 2011; Maia da Costa et al., 2019) and gas storage (e.g. Warren, 2017; Gasanzade et al., 2021).

1.4.1 Elemental concepts in salt tectonics

A range of terms has been used in the past to characterise salt tectonics (e.g. Hudec and Jackson, 2007; Jackson and Hudec, 2017). This section will first introduce key salt properties

such as its composition, colour, solubility, density, etc., as salt is distinctly different from the most common sedimentary rock types. Later, the types of salt structure and the relationship between salt and host rock will be presented as important background knowledge.

1.4.1.1 Salt properties

Salt generally refers to the rocks largely composed of evaporite minerals, especially halite – the mineral form of sodium chloride that is the most common salt mineral (e.g. Talbot and Jackson, 1987b; Jackson, 1997; Hudec and Jackson, 2007; Jackson and Hudec, 2017). In general, twelve evaporite minerals can compose an evaporite sequence, but only a few are important to salt tectonics, namely halite, anhydrite and gypsum (e.g. Jackson and Hudec, 2017). Evaporites are usually coloured due to the presence of impurities, especially iron compounds and clay, so it is not likely to recognise them through colour. Comparatively, hardness and density are relatively reliable to identify different types of evaporite minerals, and taste is especially useful in the field. Finally, evaporites have significant solubility differences, associated with variations in the composition of layered sequences when brine concentrations fluctuate (Jackson and Hudec, 2017).

Rock salt density is greatly different from siliciclastic sediments, a fundamental property in driving salt tectonics (Gevantman and Lorenz, 1981; Weijermars et al., 1993). Rock salt is denser than uncompacted siliciclastic sediments near the surface, but these latter become denser than salt after early burial and dewatering processes start. In fact, rock salt density does not record obvious changes during its burial. Increasing confining pressure and temperature during burial have opposite effects in changing density within salt units (Talbot and Jackson, 1987a; Talbot and Jackson, 1987b). Although increasing pressure makes salt denser, increasing temperature makes salt expand and become less dense (Gevantman and Lorenz, 1981; Jackson and Talbot, 1986). Hence, with increasing depth, the net result due to increased compression and increased temperature is that rock salt becomes slightly less dense (Jackson and Talbot, 1986).

The elastic moduli (bulk modulus, rigidity modulus, and Young's modulus) and Poisson's ratio represent the stress-strain properties (stiffness) of elastic, instantly recoverable deformation (Jackson and Hudec, 2017). These moduli control the velocities of pressure (P) and shear (S) waves through pure salt, which do not usually vary greatly except when in the presence of impure salt (Jackson and Hudec, 2017). In essence, halite is stiffer than ice but less stiff

than quartz, and its stiffness decreases linearly with rising temperature (Fossum and Fredrich, 2002). Similarly, the brittle strength of halite is placed between that of ice and quartz, with its brittle strength increasing proportionally to confining pressure. The brittle strength of halite indicates its response to short-term differential stress, such as a hammer blow, an explosion, or a brief experiment. The yield strength of halite involved in salt tectonics in the long time scales decreases to the level of creep, i.e. approximately zero on geological time scales (Jackson and Hudec, 2017).

Thermal conductivity and thermal diffusivity are properties that measure how effectively salt conducts heat. Halite has extremely high conductivity and diffusivity, so strata above it are relatively warmer than expected at a particular depth, and are able to accelerate hydrocarbon source-rock maturation (e.g. Zhuo et al., 2016; Jackson and Hudec, 2017; Raymond et al., 2022). Conversely, strata below thick salt intervals are relatively cooled, and source-rock maturation will be relatively slowed downed (Wilson and Ruppel, 2007; Canova et al., 2018; Nolan, 2021). Thermal expansivity measures how much salt expands when heated, a property that controls whether thermal convection occurs at depth. The thermal expansivity of salt is usually higher when compared to other sediments and rocks (Jackson and Hudec, 2017).

1.4.1.2 Types of salt structures

Salt structures generally describe an evaporite body that is large enough to be imaged on seismic reflection profiles from a salt-rich basin. A salt structure can be described by specifying the shape of the salt body itself as in the case of salt anticlines, walls and rollers (Fig. 1.15). Other salt structures have more equant planforms, such as salt pillows and stocks. Some salt stocks are narrower upwards; others widen towards the surface to form a deep narrow stem and a shallow, swollen bulb. Other salt structures, such as salt sheets, canopies and massifs, are irregular (e.g. Jackson and Talbot, 1986; Hudec and Jackson, 2007; Jackson and Hudec, 2017) (Fig. 1.15).

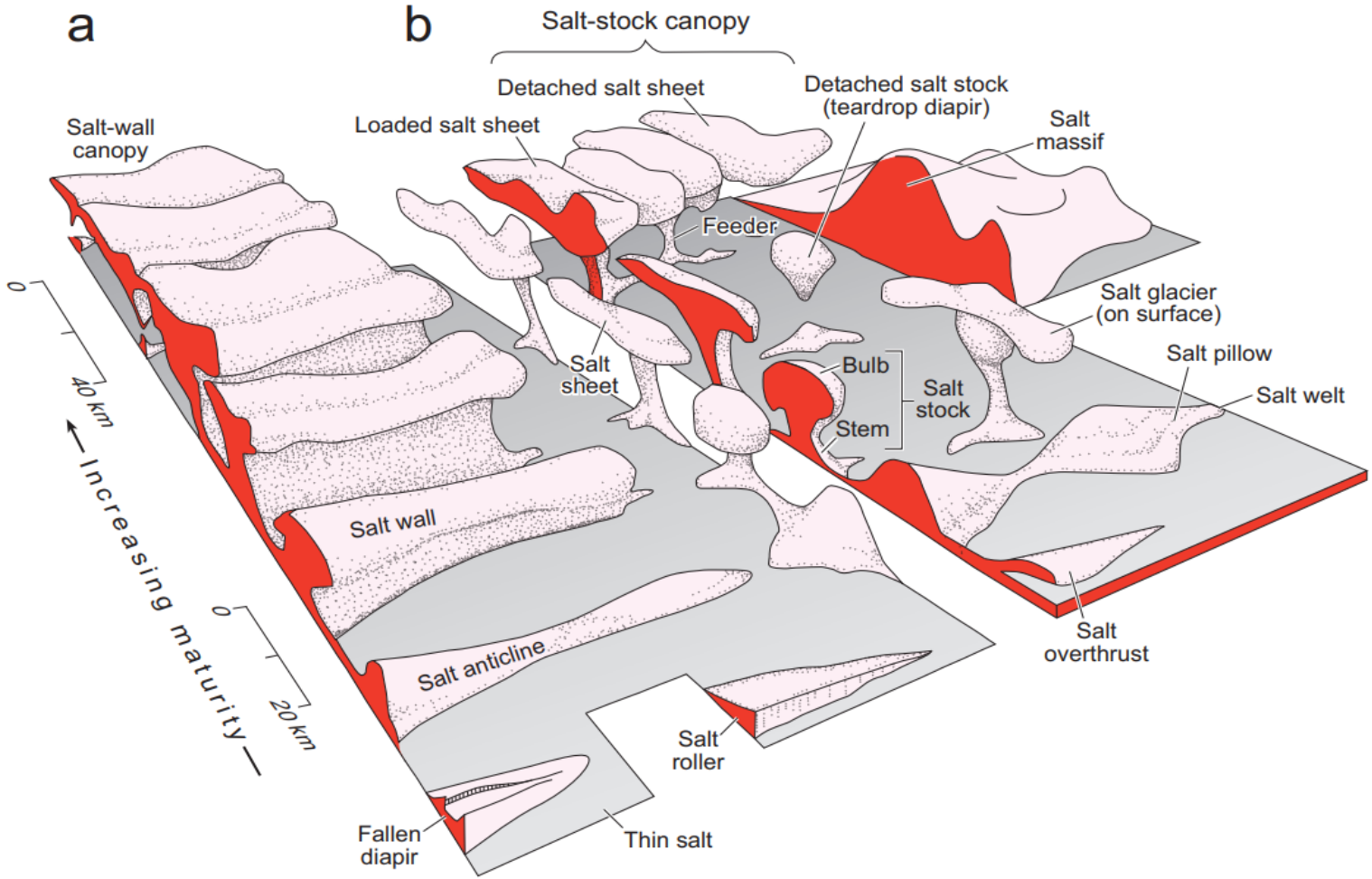

Fig. 1.15. Block diagram showing typical shapes of salt structures in nature. Structural maturity and size increase toward the composite, coalesced structures at the top of the figure. (a) Elongated structures rising from line sources. (b) Structures rising from point sources. Figure from Jackson and Hudec (2017) who adapted it from Jackson and Talbot (1986).

When considering the contact between the salt and its overburden, the diverse salt geometries can be grouped into diapiric and non-diapiric structures (Jackson and Talbot, 1986). Diapiric structures refer to the presence of a discordant contact between the salt body and its overburden indicating that salt body has pierced, or appears to have pierced, its confining strata or rocks. Conversely, non-diapiric structures relate to the presence of a concordant contact between the salt body and its overburden. Salt structures generally evolve from concordant, low-amplitude structures to discordant, high-amplitude intrusions and thence to extrusion, but they can stop growing at any stage (Jackson and Talbot, 1986; Hudec and Jackson, 2007) (Fig. 1.15). Thus, immature salt structures are concordant with its overburden to include salt anticlines, rollers and pillows, whereas intrusive types of salt structures include salt diapirs, walls, stocks and nappes (Jackson and Talbot, 1986; Ge and Jackson, 1996; Hudec and Jackson, 2007). In addition, there are extrusive salt structures that evolve from the concordant and intrusive types, often forming the exposed crests of diapiric stocks. Extrusive sheets are known as 'salt glaciers' or 'namakier', the latter of which can be confined to valleys or spread over alluvial plains as piedmont namakiers (Jackson and Talbot, 1986) (Fig. 1.16).

1.4.1.3 Overburden geometry as a record of salt tectonics

The strata surrounding a salt body provide a better record about its growth history than the salt body itself. The surrounding sediments provide a tectonostratigraphic context for salt movement, a term generally coined as 'halokinesis' (Jackson and Hudec, 2017) (Fig. 1.17). An originally autochthonous salt layer is usually the source layer, or mother salt, and the strata below the salt layer are stratigraphically older sub-salt and basement units. The supra-salt strata above the salt layer are considered as part of the overburden. In contrast, allochthonous salt has moved from its original place and overlies younger sub-salt strata, which may or may not connected to an autochthonous salt volume via a salt feeder. Sediment cover is the entire sedimentary-volcanic pile in a basin, including the autochthonous and allochthonous salt, and all of these components above and below the salt - plus the salt itself - make up the salt system (Jackson and Hudec, 2017) (Fig. 1.17).

The geometric relationship between overburden strata and underlying salt bodies is important for interpreting salt tectonics and often take in consideration the thickness, contact, age and regional setting in any interpretation (Jackson and Hudec, 2017). Thickness refers to lateral variations in overburden thickness, which effectively reflect (and promote) salt flow,

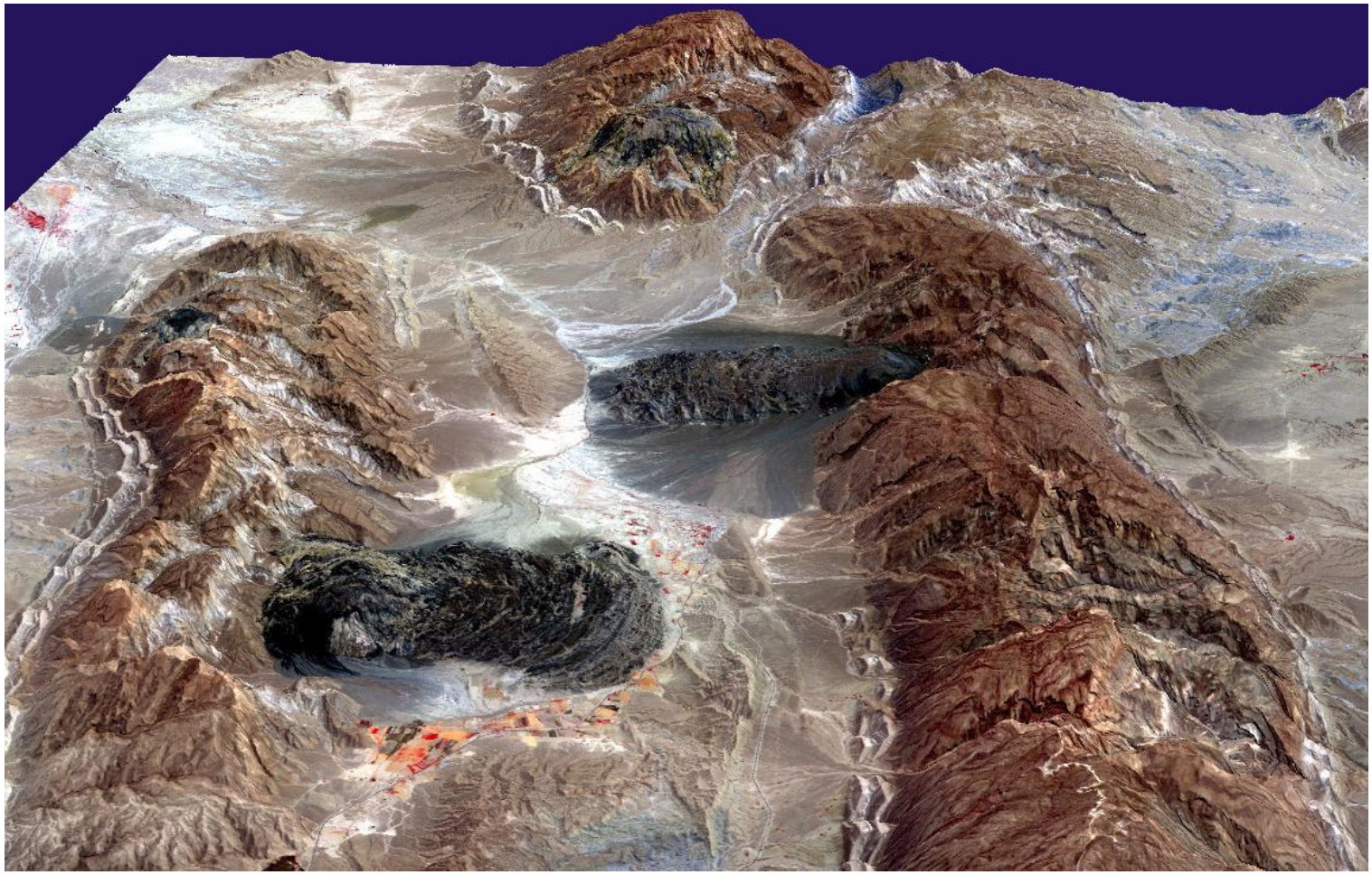

Fig. 1.16. Satellite image of salt domes (brown hills) and salt glaciers (dark areas), Zagros Mountains, Southern Iran. In this region, salt flows like glaciers into adjacent valleys due to the gravity. Figure from the website of NASA (2001): https://earthobservatory.nasa.gov/images/4168/irans-salt-glaciers.

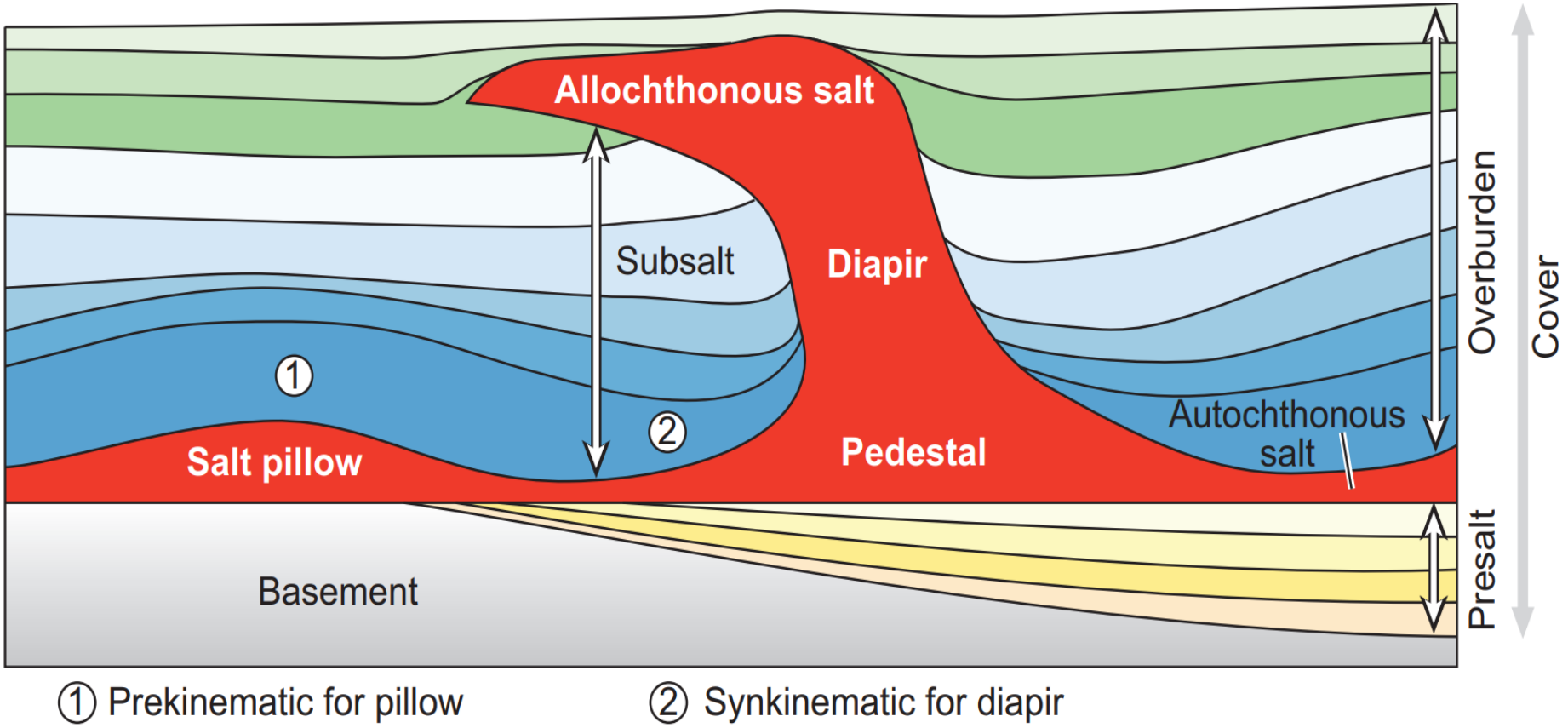

Fig. 1.17. Basic tectonostratigraphic elements of a salt system highlighting the basement, pre-salt strata, salt structures, sub-salt strata and the overburden. Allochthonous salt was formed due to the salt movement from the autochthonous salt. Figure from Jackson and Hudec (2017).

and is measured via isopach analyses of overburden strata. Contacts indicate the relationship of the boundary formed between salt and the overburden, including concordant and discordant contacts. The age refers to any hiatuses between the time of overburden deposition and the time of salt flow, while the regional setting considers those relationships between a given key horizon in the overburden and a regional datum (Jackson and Hudec, 2017).

1.4.2 Salt-flow mechanisms

A salt body has fundamentally different physical and rheological properties when compared to other sedimentary rocks (Weijermars et al., 1993). Salt density decreases slightly with increasing depth, whereas its surrounding rocks record a significant increase in density (Gevantman and Lorenz, 1981). This results in a density inversion between the salt body and its overburden, triggering tectonic instability in salt-bearing basins. With increasing depth salt strength decreases significantly to near zero, whereas its overburden strength increases steadily. Thus, salt flows like a fluid with increasing depth, but its overburden is brittle and far stronger than salt (Jackson and Hudec, 2017). In summary, there are several different forces that drive or resist salt flow, determining whether or not salt remain stable.

1.4.2.1 Forces driving salt flow

Differential loading is recognised as the dominant process driving salt flow, and results from three main processes: gravitational (‘vertical’) loading, displacement (‘tectonic’) loading and thermal loading. These three processes may jointly act on a salt interval (Jackson and Hudec, 2017). Which of these three types of loading is the most important depends on the depth of the salt, the geometry of the salt body, the tectonic setting, and thermal conditions of the salt (Jackson and Talbot, 1986; Hudec and Jackson, 2007; Jackson and Hudec, 2017).

Gravitational loading relates to the weight of the rocks above the salt, as well as the gravitational body forces within this same salt, both of which drive salt to flow laterally with the downward force. The direction of salt flow is from high to low pressure zones and, therefore, is determined by the pressure heads and elevation heads imposed on a volume of salt (Hudec and Jackson, 2007; Jackson and Hudec, 2017) (Fig. 1.18). As a result, the displaced salt can feed a nearby diapir or merely inflate the salt layers – the process driving the flow of salt away from the gravitational load is termed salt withdrawal or salt expulsion (Fig. 1.18).

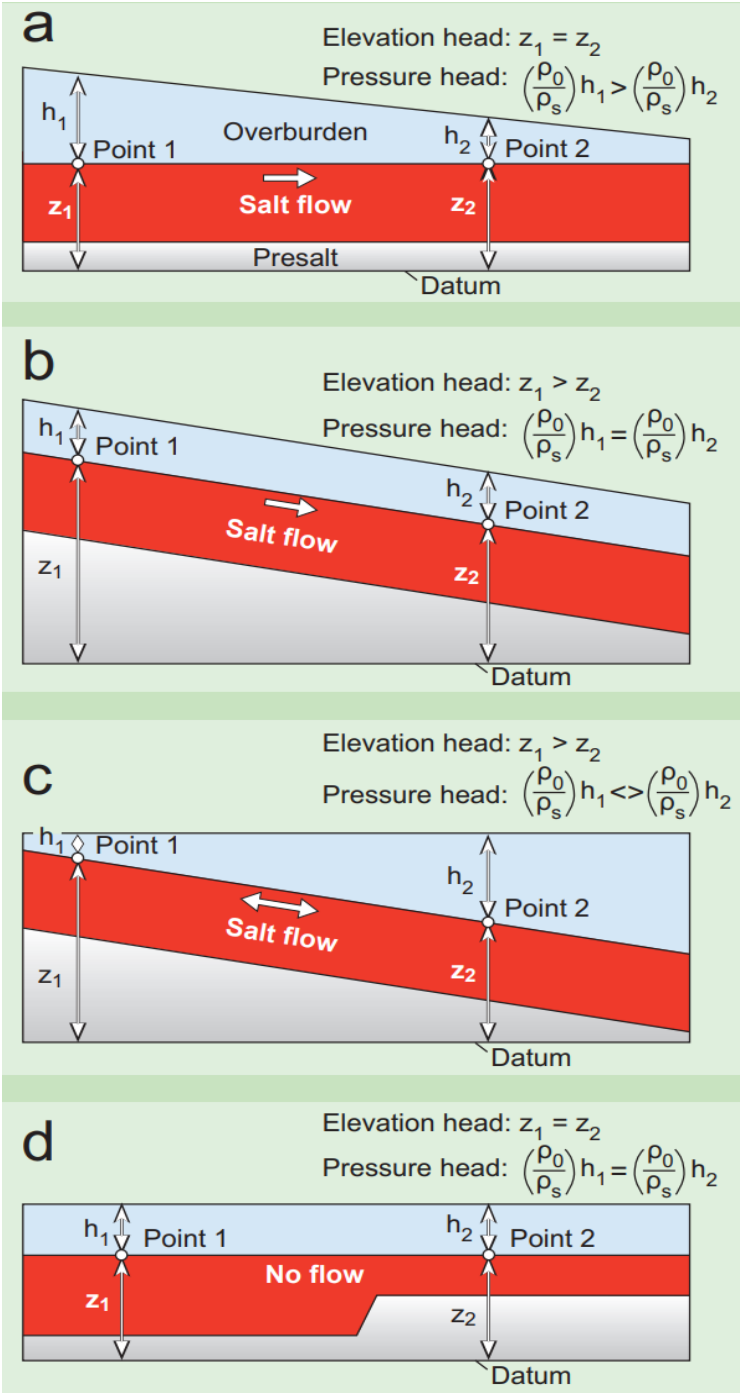

Fig. 1.18. Schematic illustration for the initial direction of salt flow inferred from elevation and pressure heads. (a) Salt driven by pressure head whether or not the overburden is denser than salt. (b) Salt driven by elevation head whether or not the overburden is denser than salt. (c) Salt driven either way, depending on whether the elevation head gradients is more or less than the pressure head gradient. (d) No flow because the irregular base of salt does not create any hydraulic head gradient. Figure from Jackson and Hudec (2017) who adapted it from Hudec and Jackson (2007). h=Vertical thickness of material above the point; z=Elevation head; ρ_o=Density of the overburden; ρ_s=Density of salt.

Displacement loading results from the forced displacement of one boundary of a rock body relative to another boundary (Suppe, 1985). Displacement loading takes place when the flanks of a salt body move towards, or away from, one another due to the lateral forces imposed during regional shortening or extension (Hudec and Jackson, 2007; Jackson and Hudec, 2017) (Fig. 1.19). Displacement loading typically shows distinct pulses over geologic time scales, in a process that is markedly different from the more continuous, progressive gravitational loading (Hudec and Jackson, 2007; Jackson and Hudec, 2017).

Thermal loading occurs when volume changes of salt due to the changes of temperature. It is because salt is sensitive to the change in confining temperature in comparison with other sedimentary rocks. With an increase in temperature, salt tends to expand generating vertical stresses on the surrounding rock. The expanding salt decreases in density and increases in buoyancy, a phenomenon that eventually results in thermal convection. Thermal convection is enhanced by: (1) increases in the temperature gradient, thermal expansivity, and layer thickness, or (2) decreases in the thermal diffusivity or kinematic viscosity of salt (Jackson and Hudec, 2017).

1.4.2.2 Forces resisting salt flow

In nature most salt bodies are subject to certain driving forces, but not all salt bodies deform at tectonic scales. This is because there are two types of forces capable of resisting salt flow: frictional and viscous forces. Frictional forces represent the strength of the overburden rocks, or strata, whilst viscous forces reflect the existence of boundary drag within the salt layer itself (Jackson and Hudec, 2017).

With increasing burial depth and confining pressure, sedimentary rocks increase their shear and frictional strengths. Thick sedimentary roofs become more difficult to deform than thin roofs with the same lithology because the pressure forces generated purely by gravity within salt are relatively small (Jackson and Hudec, 2017). Thus, the salt is confined above and below by stronger rocks, though it is intrinsically highly mobile. Even buoyant buried salt can remain stable under a thick overburden, unless extension or shortening causes a reasonable amount of displacement loading, generating faults in the overburden and stretching or squeezing within the salt (Jackson and Hudec, 2017).

Flow within buried salt is also restricted by boundary drag along the top and bottom surfaces of a relatively thin salt layer (Jackson and Hudec, 2017). The margins of most salt

bodies have a zone of restricted flow, where the salt shears pass static country rocks. Resistance by viscous shear forces is less important in thick salt layers than in thin layers, because only a small proportion of thick salt is intensely sheared along the boundary. Thus, in thin salt layers, the boundary drag can effectively immobilize the salt. Drag dominates when the salt layer is thinner than a few hundred meters (Waltham, 1997).

1.4.3 Salt diapirism mechanisms

Salt diapirs are the most typical structures reflecting the piercing of ductile salt that through their overburden rocks or strata (e.g. Jackson and Talbot, 1986; Talbot and Jackson, 1987b; Vendeville and Jackson, 1992b; Schultzela et al., 1993; Hudec and Jackson, 2007; Jackson and Hudec, 2017). Diapirs are discordant relative to their overburden, as upper contacts cut across bedding. In map and depth slices, diapiric salt has an anomalous stratigraphic position; the salt is discordant with strata younger than the units that stratigraphically overlie the autochthonous salt. Hence, for buried salt to be diapirically emplaced, the overburden occupying the intruded space must be removed or displaced (Jackson and Hudec, 2017).

There are three diapirism modes involving the piercement of salt into the overburden (Jackson and Hudec, 2017) (Figs. 1.21a, b and c). Firstly, regional extension may stretch the overburden, creating space for a reactive diapir to rise between fault blocks (Fig. 1.20a). Secondly, flaps of the overburden rocks, or strata, may tilt outwards as the diapir rises by active diapirism (Fig. 1.20b). Third, salt may pierce its overburden in the hanging wall of thrust faults (Fig. 1.20c). In addition, three other modes of diapirism may occur in nature: 1) the roof of a salt pillow or salt unit may be removed by erosion, exposing the salt, which is free to spread discordantly across the resulting unconformity (Fig. 1.20d), 2) a diapir with a weak overburden may thin its roof (e.g. Talbot and Jackson, 1987b; Hudec and Jackson, 2007; Jackson and Hudec, 2017) (Fig. 1.20e), 3) when diapirs apparently pierce their overburden, the term to define such process is passive diapirism, or downbuilding where the diapir remains at or near the surface while surrounding sediments accumulate (Giles and Lawton, 2002; Hudec and Jackson, 2007) (Fig. 1.20f). However, these diapiric mechanisms are not mutually exclusive, and most salt diapirs grow by mixed processes.

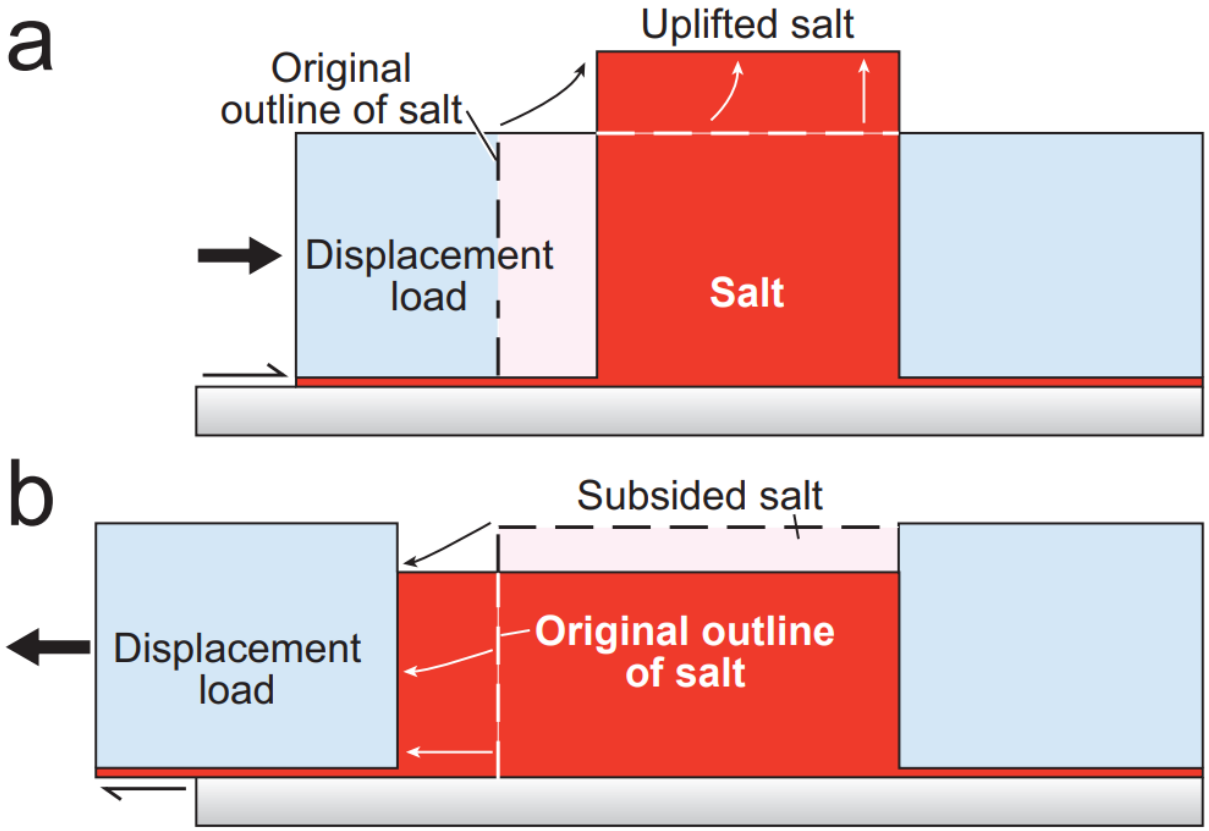

Fig. 1.19. Schematic illustration for the effects of displacement loading on salt. (a) During shortening, salt is loaded horizontally by inward movement of one or both sidewalls. The horizontal displacement load then exceeds the vertical gravitational load, forcing salt to rise. In a natural example, the salt would flow out over the sediment surface rather than form a vertical column. (b) During extension, salt is unloaded horizontally by the outward movement of one or both sidewalls. The vertical gravitational load then exceeds the horizontal displacement load, so salt subsides. Figure from Jackson and Hudec (2017) who adapted it from Hudec and Jackson (2007).

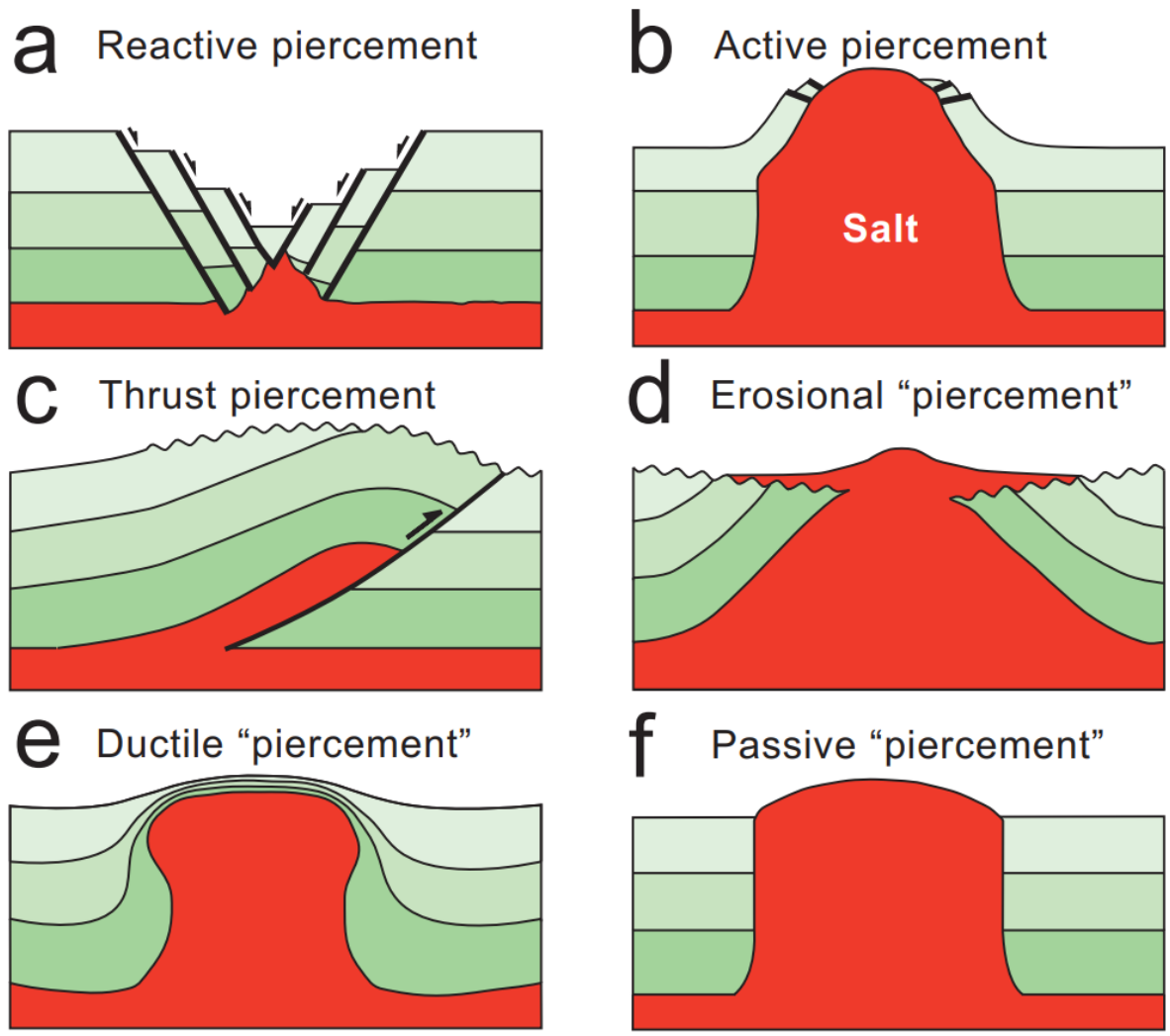

Fig. 1.20. Schematic diagram showing the modes of diapir piercement in cross sections. (a) Reactive piercement associated with the weakening of the overburden. (b) Active piercement associated with the overburden loading and/or shortening. (c) Thrust piercement associated with the movement of a thrust fault. (d), (e) and (f) Three other diapirism modes that are apparent rather than actual piercement of the overburden. The overburden is brittle in all these examples, except in (e). Figure from Jackson and Hudec (2017) who adapted it from Hudec and Jackson (2007).

1.4.3.1 Reactive diapirism

Differential loading and overburden thinning are caused by fracturing and faulting of overburden rocks due to regional extension, a phenomenon that results in the upwelling of salt below the (now) thinned overburden (Fig. 1.21). Salt fills the space created by the extensional thinning and separation of overlying fault blocks. This type of salt upwelling is termed reactive diapirism as salt rises in reaction to extension (e.g. Vendeville and Jackson, 1992b). In physical models, reactive diapirism depends on the occurrence of extension, which explains why salt diapirs begin to rise when salt layer first extends in many basins around the world (Jackson and Vendeville, 1994; Jackson et al., 1994). It also explains why there are no salt diapirs in many cratonic basins though many of these basins have thick salt and a dense overburden. That is because sedimentary loading is too uniform in these regions and there is no regional extension to differentially load the salt (Jackson and Hudec, 2017).

Reactive diapirs formed during synkinematic deposition, or formed from prekinematic overburden rocks are similar and usually triangular, with their sharp apexes overlain by a graben (Fig. 1.21). These diapirs are also flanked by a fan of inward dipping normal faults that terminate at the salt contact; these faults will be growth faults if reactive diapirs are formed through synkinematic overburdens. In addition, the width of a reactive diapir's base records the amount of extension, as this is accommodated entirely by flow of salt at the base. Midway up the diapir, extension is partly due to the flow of salt, and partly by faulting. Above the diapir, extension is entirely by faulting. When in the presence of entirely prekinematic overburdens, extension is equal at these three levels, despite taking different forms. With synkinematic overburdens, extension declines upwards (Hudec and Jackson, 2007).

There are also highly asymmetric diapirs in reactive diapirs, known as salt rollers. These diapirs have asymmetric profiles similar to scalene triangles, with a long sloping side that is concordant to the overburden and a short sloping side that is a normal fault (Jackson and Hudec, 2017). Salt rollers form whenever one crestal fault orientation is favoured over another, as it might happen if stress axes were rotated from the vertical. Stress axes rotate above dipping detachments, so rollers are particularly common above seaward-dipping salt detachments near the landward ends of divergent margins (Jackson and Hudec, 2017).

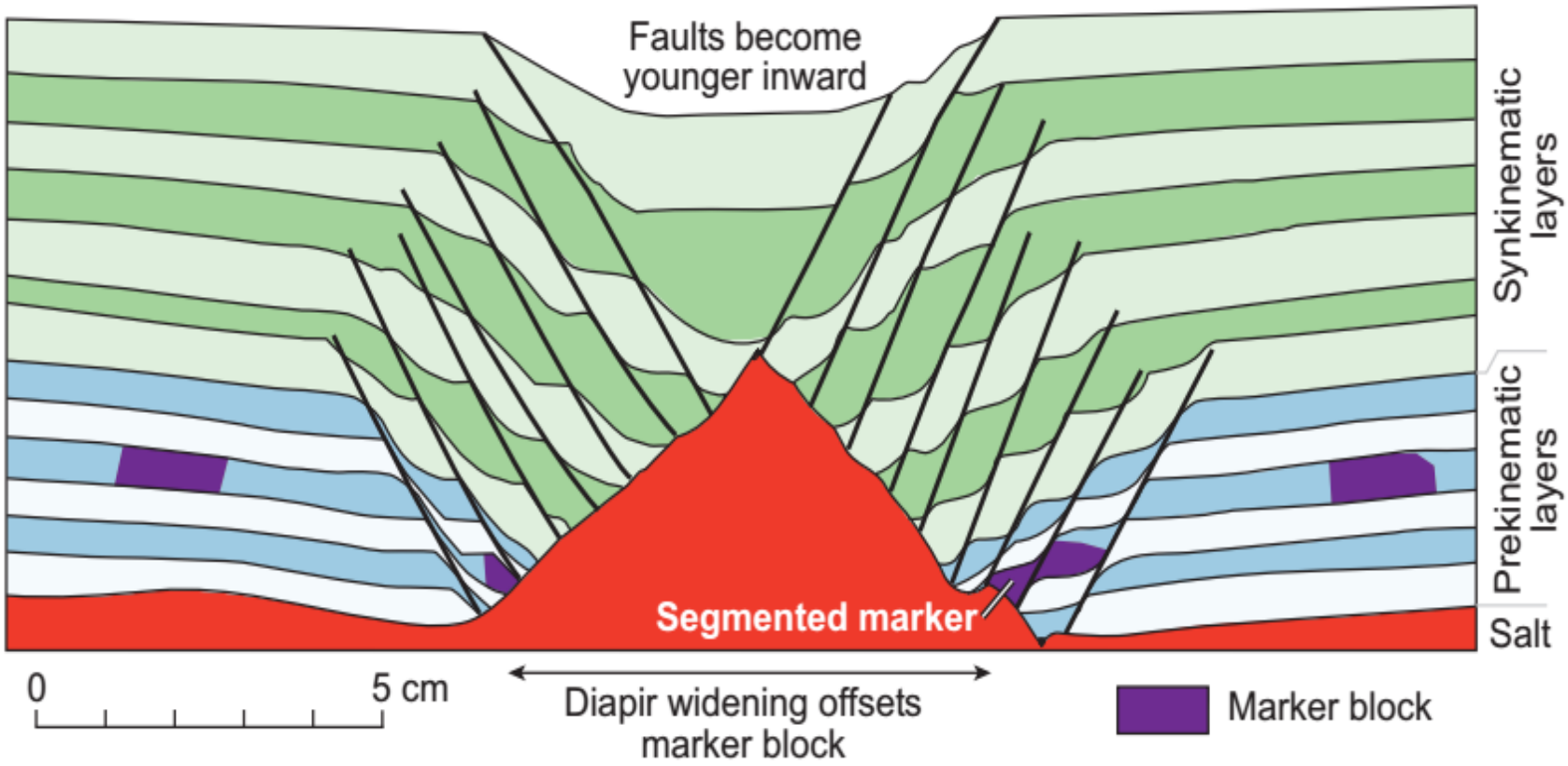

Fig. 1.21. Diagram illustrating a reactive salt diapir with prekinematic and synkinematic layers cross-cut by growth faults in a profile section. Extension is accommodated entirely by faulting above the diapir, but is accommodated entirely by salt flow at the base. Midway up the diapir, extension is accommodated partly by flow of salt and partly by faulting. Extension is equal at these three levels, despite taking different forms. Figure from Jackson and Hudec (2017) who adapted it from Vendeville and Jackson (1992).

1.4.3.2 Active diapirism

Active diapir rise occurs when a salt structure arches, uplifts, or shoulders aside its overburden. If the roof of a salt structure is pierced during active salt rise, it is termed active diapirism. This can be driven either by halokinetic processes or by shortening (e.g. Schultzela et al., 1993; Jackson et al., 1994; Hudec and Jackson, 2007; Jackson and Hudec, 2017). Halokinetic (active) diapirism is driven by overburden load on adjoining source layers, creating an upwards pressure of diapiric salt on its roof. Both buoyancy and surface topography can produce the load to drive salt rise, but the weight and strength of the overburden, and the viscosity of the salt, are forces resisting the rise of salt (e.g. Hudec and Jackson, 2007; Jackson and Hudec, 2017) (Fig. 1.22). Thus, active salt rise is influenced most strongly by sediment density, roof strength and anisotropy, as well as salt geometry (Schultzela et al., 1993). Regional shortening can lead to contractional rise of salt in two ways. First, shortening helps to convert displacement load into gravitational load, resulting in diapiric salt moving upwards, where it may arch the roof faster and higher than it would rise by halokinesis alone (Schultzela et al., 1993) (Fig. 1.23). Second, shortening can buckle the overburden above the salt, causing it to rise up into anticlines even if not pushed by pressurised salt. Similarly to active halokinetic rise, the strength and weight of the roof and the viscosity of the salt are also forces resisting the active rise of a diapir.

Arched roofs and upturned collars are two typical types of structures caused by active rise (Jackson and Hudec, 2017). Arched roofs occur where the salt has not pierced to the surface, whereas upturned collars are evidence for formerly active diapir breaking through to the surface. A roof that has been uplifted and arched above a regional datum is the most diagnostic feature of active rise. The arched roof is a drape fold formed by bending. The roof is typically stretched owing to bending, which may result in thinning below seismic resolution (Davison et al., 2000a) or in the formation of crestal normal faults. Erosion or slumping may also thin the arched roofs, causing difficulties in interpretation (Jackson and Hudec, 2017).

Upturned collars are known as shale sheaths, which has long been interpreted from wells on the flanks of salt diapirs, as many of these are too small to be seismically resolved (Atwater and Forman, 1959). Commonly, these upturned collar units are made up of brecciated and sheared deep-marine shales, contributing to drag-induced shear against a diapir rising with respect to the surrounding sediments. Three types of upturns can be formed during active diapirism in different settings, including megaflaps, perched flaps, and injection folds, which are regarded as the diagnostic of active diapirism (Jackson and Hudec, 2017) (Fig. 1.24).

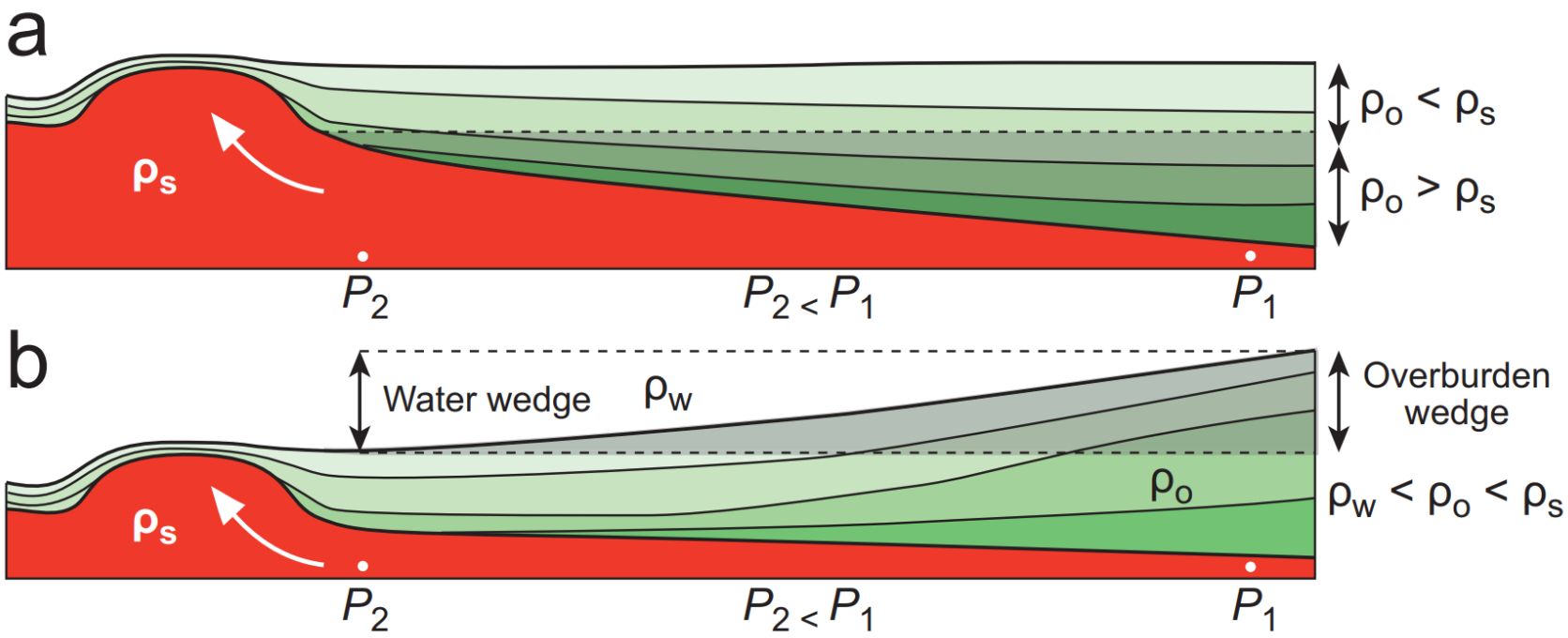

Fig. 1.22. Schematic illustration for halokinetic active diapirism, which can be driven by two types of gravitational loading depending on the density of water (ρ_w), the overburden (ρ_o) and salt (ρ_s). P=Lithostatic pressure exerted by the overburden. Figure from Jackson and Hudec (2017).

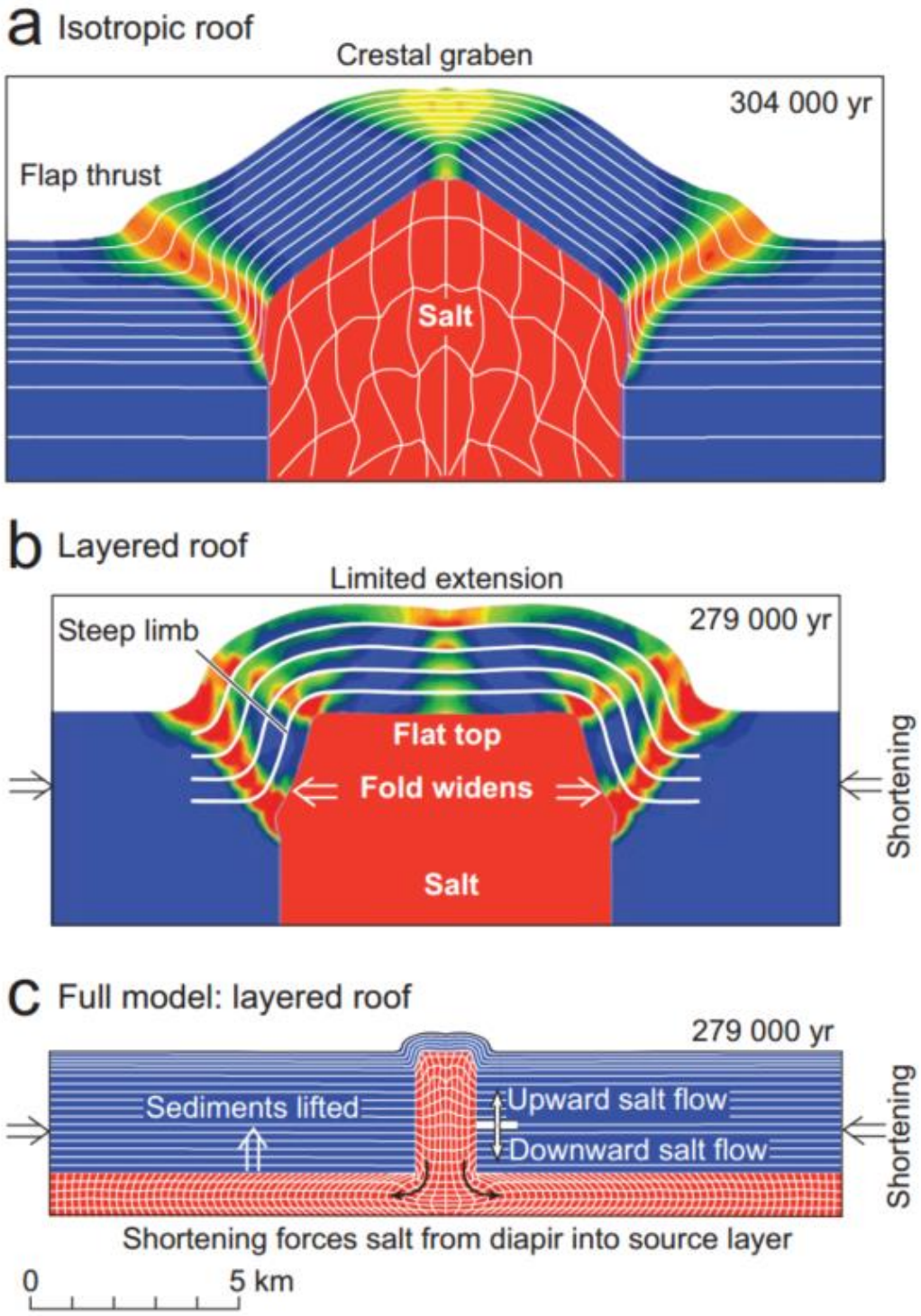

Fig. 1.23. Numerical modelling illustrating how regional shortening promotes the active rise of salt in ways depending on the diapir's roof properties. Contours show intensity of plastic strain, with white being the highest strain; the colour range for plastic strain is different in each example in order to highlight particular features. Sediment–salt density ratio was 1.09; shortening rate was 1 mm/yr. Figure from Jackson and Hudec (2017) who adapted it from Dan Schultz-Ela (1993).

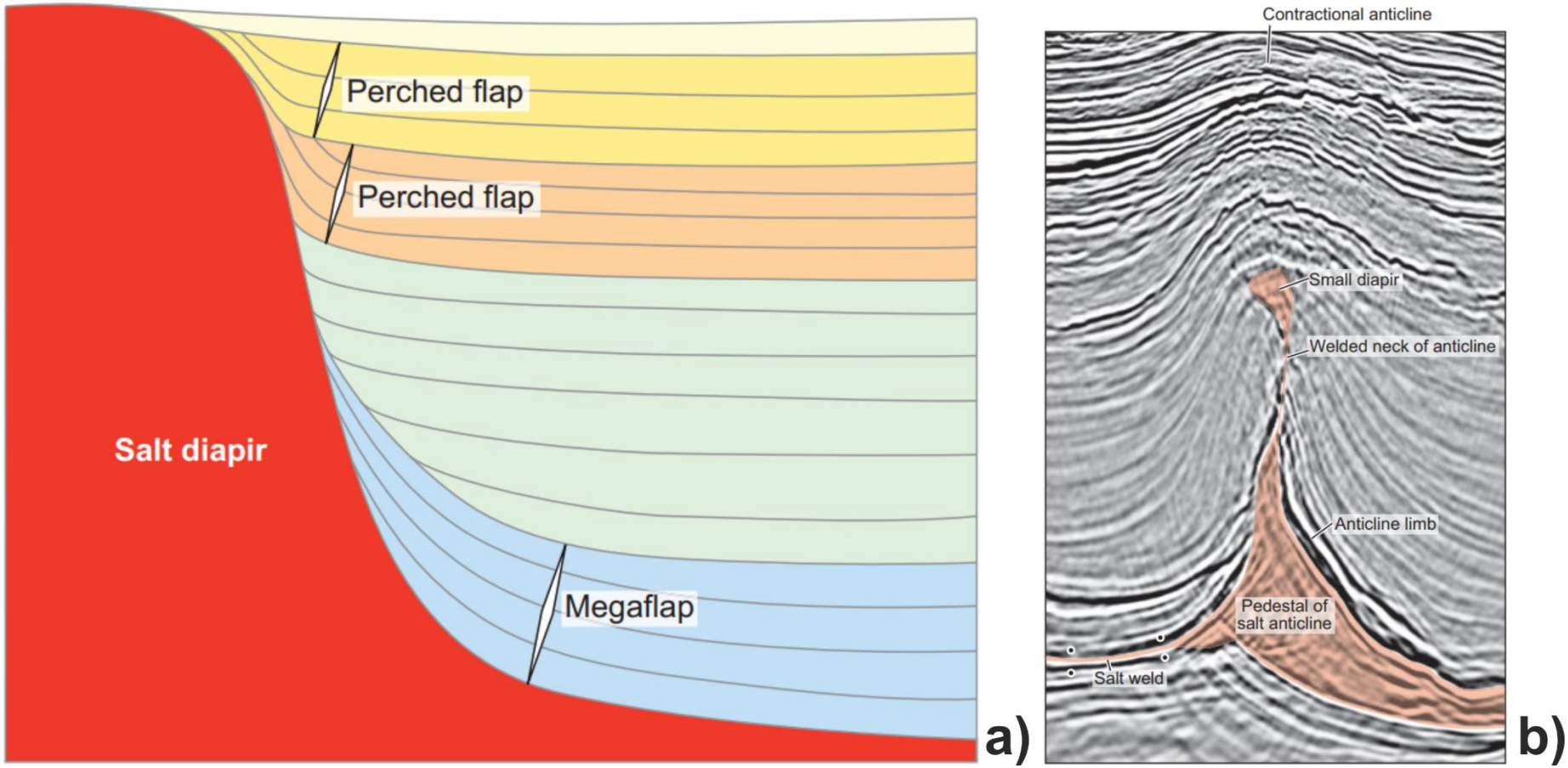

Fig. 1.24. a) Wedges of sediment that originally onlapped an emergent salt diapir become deformed into flaps as the diapir continues to grow. These flaps form on two scales: (1) megaflaps are kilometre-wide and rest directly on the salt; (2) perched flaps are hundreds of meters wide and rest on older overburden strata. b) The core of this salt anticline was pinched shut by regional shortening, during which the salt core broke out as an injection fold, forming a small diapir at its crest. Figure from Jackson and Hudec (2017).

1.4.3.3 Passive diapirism

Passive diapirism can occur in any tectonic setting. However, for passive diapirism to begin, salt must be at the surface. Passive diapirism occurs because a passive (downbuilding) diapir grows in height by maintaining its crest at or near a depositional surface while its base sinks along with the surrounding sediments (e.g. Stewart, 2006; Hudec and Jackson, 2007; Alsop et al., 2016; Jackson and Hudec, 2017) (Fig. 1.25). Passive diapirism can initiate immediately after salt deposition, keeping the salt exposed but with surrounding areas being slowly buried. However, salt must break through its overburden to reach surface and emerge as a passive diapir. Active diapirism is the most common way for salt to reach the surface, but regional shortening or sedimentary topography may also trigger salt to the surface. Deep erosion of an anticline crest is also one important way to initiate a passive diapir, as it may expose much of its salt core (Jackson and Hudec, 2017). In addition, in order for passive diapir to grow, salt must be pressured enough to flow upwards at the sediment surface. The pressure may be generated in three ways. First, the density of overburden is greater than the salt, and salt is then forced to the surface. Second, displacement loading cause salt to rise at the surface. Third, salt may be loaded by depositional topography, resulting in the rise of salt onto the surface (Jackson and Hudec, 2017). However, most passive diapirs can only grow above the surrounding surfaces less than 200 m, which can be calculated by assuming the densities and thickness of salt and overburden (Talbot, 2005). Because there are no room issues in these diapirs, passive or downbuilding diapirs are noted for the mild deformation they impose on country rocks. The diapir resembles a cut-out stamped out of encasing layered strata, whether in vertical section or in horizontal view (Jackson and Hudec, 2017) (Fig. 1.26). Deformation in the overburden is typically limited to subtle thickness changes associated with flow of underlying salt and upturned or sheared strata near the diapir contact (Jackson and Hudec, 2017).

1.4.4 Diapir-related faults

With the formation and growth of salt diapir, the surrounding rocks are subjected to deformation. The deformation of surrounding rock can either be brittle, resulting in the development of fractures and faults, or ductile recording the formation of folds due to the arching and buckling of the roof. Diapir-related faults include radial faults and concentric faults formed around salt diapirs (e.g. Hudec and Jackson, 2007; Jackson and Hudec, 2017).

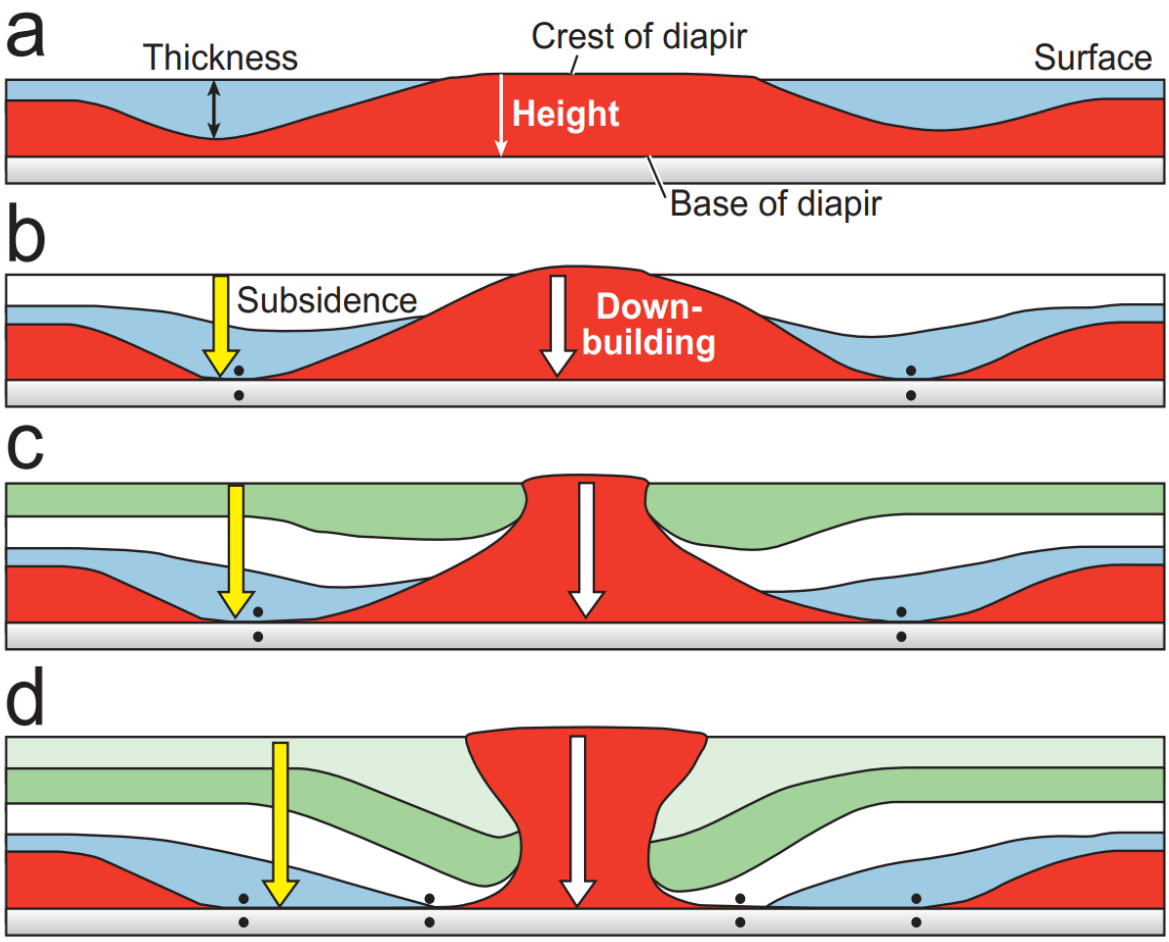

Fig. 1.25. Schematic illustration for the growth of a downbuilding (passive) diapir. It grows in height by maintaining its crest at or near the sedimentary surface, whereas its base sinks together with the surrounding sediments. Figure from Jackson and Hudec (2017) who adapted it from Hudec and Jackson (2011).

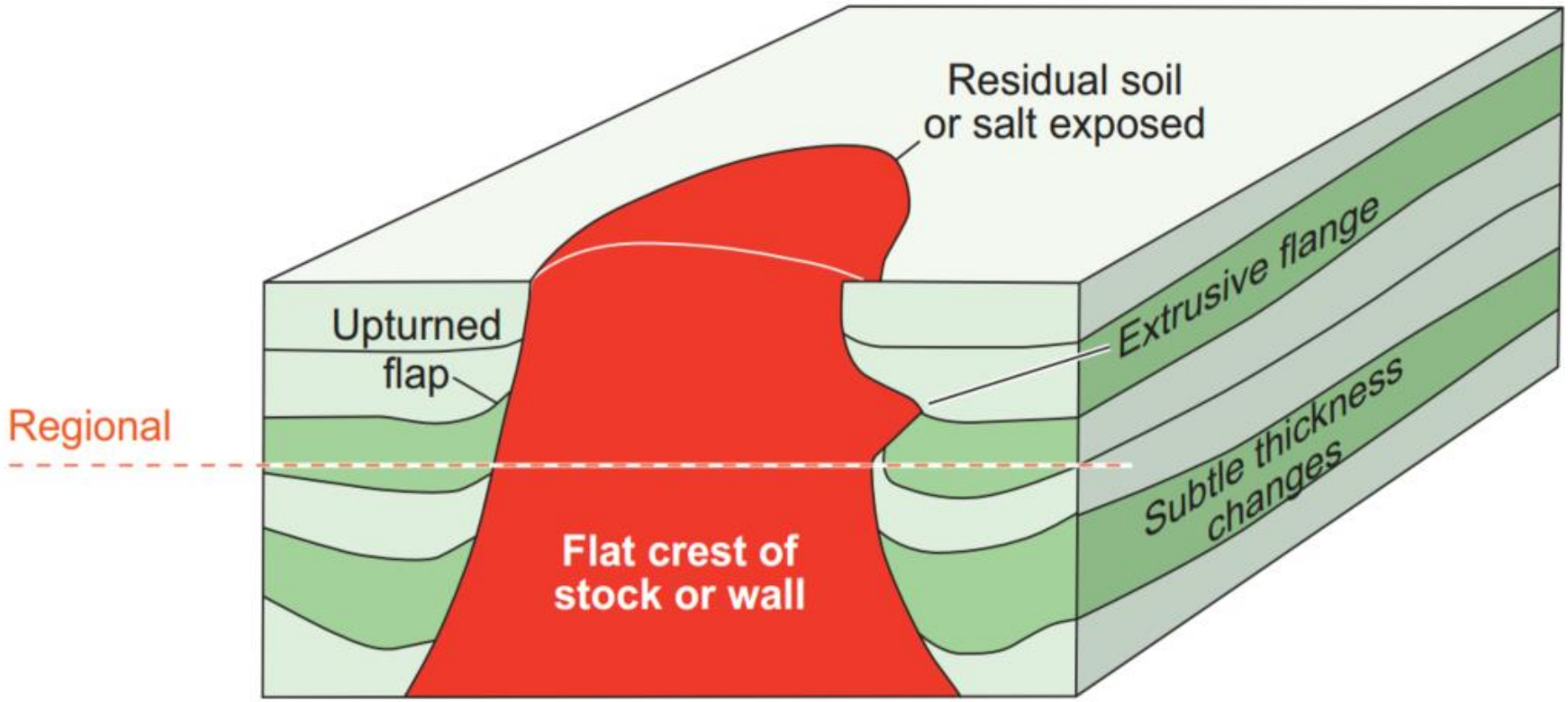

Fig. 1.26. Schematic diagram showing that stratal cutoffs and paucity of deformation in the country rock that are the most important diagnostic features of a passive diapir. Figure from Jackson and Hudec (2017) who adapted it from Jackson et al. (1994).

1.4.4.1 Radial faults

Radial faults are the most common deformation around salt diapirs and are documented in nearly all salt-bearing basins (e.g. Childs et al., 1993; Davison et al., 1993; Stewart et al., 1996; Davison et al., 2000a; Larsen et al., 2002; Hudec and Jackson, 2007; Yin and Groshong, 2007; Carruthers et al., 2013; Jackson and Hudec, 2017; Coleman et al., 2018). These faults abut the diapir contact or curve inwards to intersect it tangentially (Fig. 1.27). There are four different processes forming radial faults. First, some radial faults are formed in domed roofs that have subsequently been pierced, and the outermost parts of these roofs may be preserved even if they have been destroyed during breakthrough. Second, some radial faults may be formed by hoop strain around an expanding diapir. The expansion may result from a flap rotating under active diapirism, or may simply occur as outward forces in salt push the country rock (Nikolinakou et al., 2014). These faults usually have a largest displacement next to the diapir and become smaller outwards as the hoop extension is proportional to the strike curvature of the salt contact (Stewart, 2006). Third, contracting diapirs may also develop radial thrust faults. Fourth, faults initiate at diapirs and propagate outwards, as pre-existing salt structures are the first to deform in regional extension or shortening as they are mechanically weak (Jackson and Hudec, 2017).

1.4.4.2 Concentric faults

Concentric faults can be classified into concentric normal faults and reverse faults. Concentric normal faults can be formed by inward collapse around the constricting stem of a diapir, which will generate circumferentially trending ring faults (e.g. Malthe‐Sørenssen et al., 1999; Stewart, 2006). Other concentric normal faults can be formed by the bending of strata into the salt withdrawal basin rather than by diapiric contraction (Jackson and Hudec, 2017). These faults are located on the outer edges of large salt withdrawal basins, many kilometres away from a diapir contact. As for concentric reverse faults, they are developed due to radial compression of overburden strata resulting from a rapid increase in diapir volume and radius (Davison et al., 1993). These faults are formed to accommodate local shortening and to align it tangentially to the diapir. Pre-existing concentric normal faults can be rotated and reactivated as reverse faults as the strata around a diapir are overturned (Davison et al., 1993).

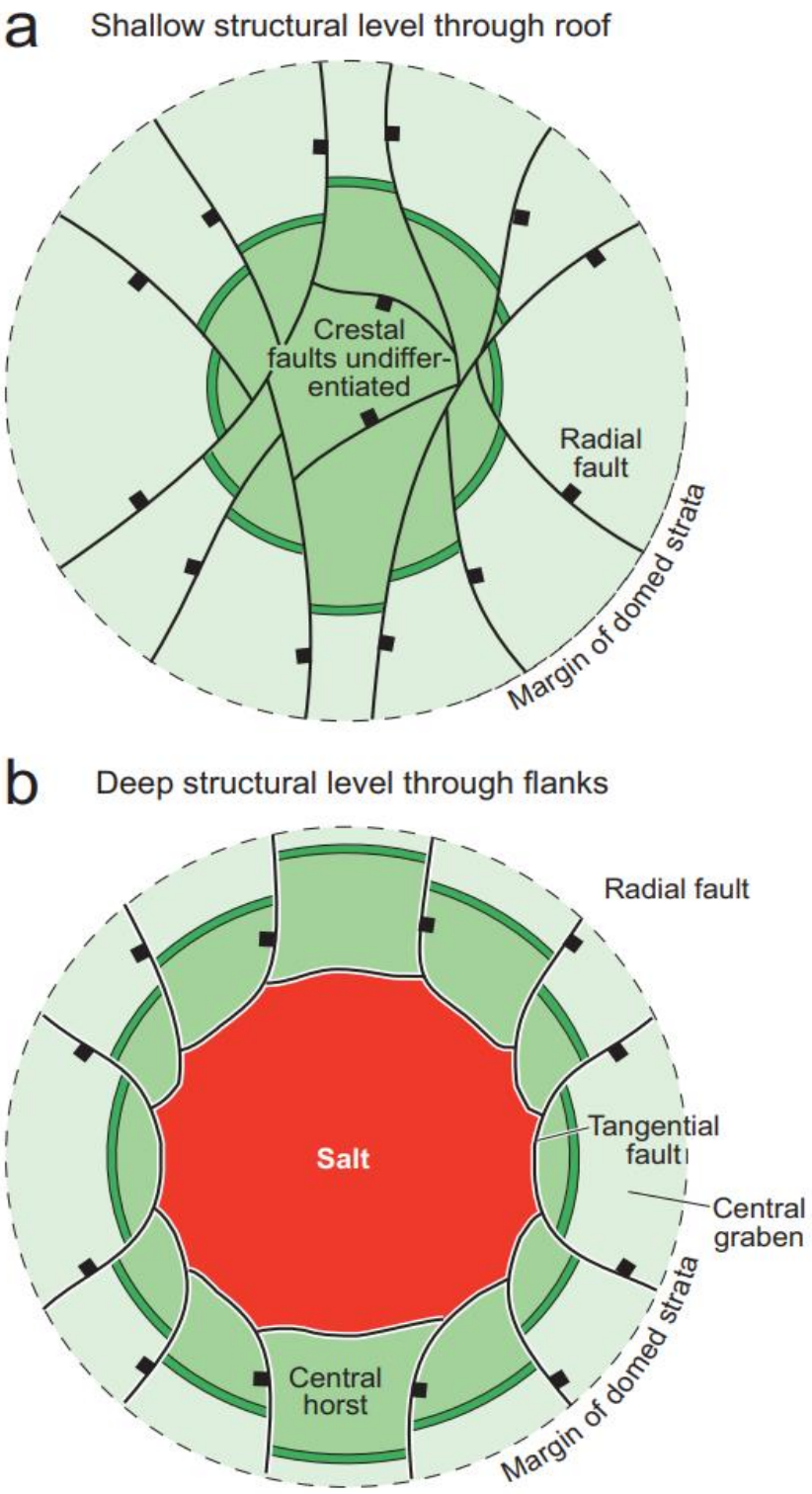

Fig. 1.27. Schematic illustration for radial faults around salt diapirs in shallow and deep structural levels. (a) Shallow radial faults caused by hoop extension of a domed roof. (b) Deep tangential faults indicating a change in the balance between radial and hoop stresses. Figure from Jackson and Hudec (2017).

1.4.5 Diapir fall

Diapir fall is common during salt deformation and its evolution, indicating that a salt diapir crest subsides under some certain conditions. There are at least three situations in which a diapir can fall (Jackson and Hudec, 2017). First, a relative shortage of salt supply to diapirs during extension can result in their fall, as when caused by the depletion of salt in a source layer or too fast a stretching during extension (Vendeville and Jackson, 1992a) (Fig. 1.28). Second, part of a diapir can fall as salt flows from it to another part of the same diapir. Finally, dissolution collapse can also cause a diapir to fall, a phenomenon that is usually impressive at the surface but small on the largest scale of the whole diapir. Large-scale dissolution features are usually limited to the surface, in the zone where a large volume of undersaturated water can circulate against a salt face (Jackson and Hudec, 2017).

1.5 Fluid flow features

Fluid flow features are local anomalies produced by the subsurface flow of fluids, including oil, gas, brine, groundwater and magmatic fluids (e.g. Bruce, 1984; Hovland and Judd, 1988; Cox et al., 2001b; Berndt, 2005; Cartwright, 2007; Davison, 2009; Cathles et al., 2010; Løseth et al., 2011; Andresen, 2012; Collignon et al., 2018). Fluid flow starts from a given source to the surface or atmosphere, or into subsurface sedimentary units, a phenomenon that results in the presence of stratigraphic overpressures. Fluid flow can be instantaneous and catastrophic, but fluid flow caused by sediment mobilisation can last millions of years (Huuse et al., 2010; Andresen, 2012). Fluid flow is widespread in sedimentary basins and is geologically and economically important; it is closely associated with groundwater flow systems, petroleum migration, potential geothermal reservoirs, ore-forming and seabed ecosystems (e.g. Dando et al., 2000; Hovland et al., 2002; Rogers et al., 2012; Wynn et al., 2014).

Fluid flow features on seismic data are typically represented by amplitude anomalies, which occur together with a wide range of geological structures such as pockmarks, mud volcanoes, gas hydrates, chimneys, pipes, sand injection features, carbonate mounds, seeps and related diagenetic phenomena (e.g. Hovland and Judd, 1988; Cox et al., 2001b; Berndt, 2005; Cartwright, 2007; Davison, 2009; Cathles et al., 2010; Løseth et al., 2011; Andresen, 2012; Worden et al., 2016; Collignon et al., 2018; Cartwright et al., 2021). Fluid flow features can be classified based on their geometry, lithology, the type of impact on the surrounding sediment,

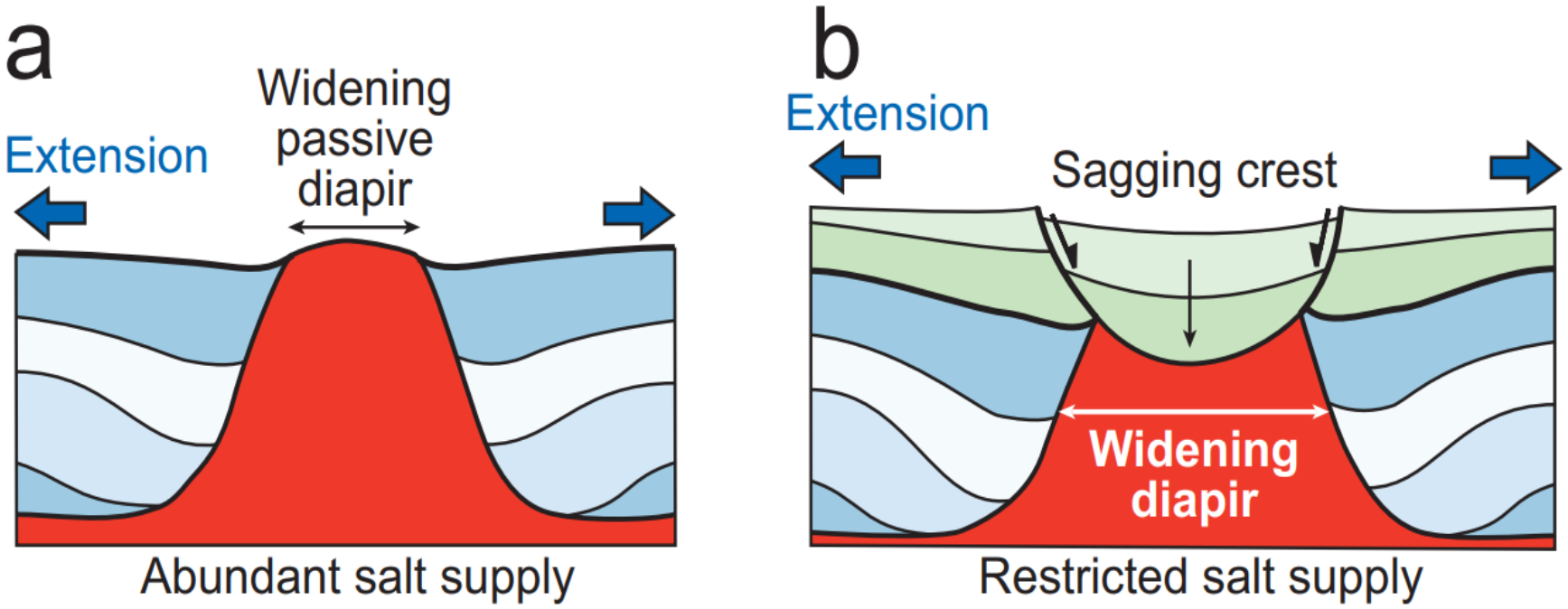

Fig. 1.28. The influence of extension on diapirism depends on diapir geometry and relative salt supply. (a) Regional extension widens a passive diapir and the salt keeps rising with abundant salt supply. (b) Continued extension widens the diapir and leads to diapir fall due to restrictions in salt supply. Figure from Jackson and Hudec (2017).

and causes for their formation (Cartwright, 2007; Andresen, 2012; Collignon et al., 2018). Three major groups of seismic fluid features were summarised by Andresen (2012) according to their formation mechanisms: a) subsurface sediment remobilisation, b) vertically focused fluid flow, and c) laterally extensive fluid flow (Fig. 1.29). Some fluid flow features are associated with two groups; i) mud volcanoes formed due to subsurface sediment remobilisation and ii) vertically focused fluid flow (Andresen, 2012). In addition, there is also a range of direct hydrocarbon indicators on seismic data, which indicate the presence of fluid or fluid contacts (e.g. Cox et al., 2020).

1.5.1 Subsurface sediment remobilisation

Subsurface sediment remobilisation usually relates to fluid flow resulting from overpressure build up, resulting in subsurface sediment remobilisation (e.g. Cartwright, 2007; Andresen, 2012). Sand intrusion complexes and mud volcano systems are typical fluid flow features of clastic sediment remobilisation (Van Rensbergen et al., 2003; Hurst and Cartwright, 2007; Huuse et al., 2007; Cartwright et al., 2008; Huuse et al., 2010; Andresen and Clausen, 2014; Waghorn et al., 2018; Hurst et al., 2021). The remobilisation of clastic sediment is associated with fluidisation of either an overpressured sand or mud source unit upon seal failure and overpressure build-up (e.g. Milkov, 2000; Jolly and Lonergan, 2002; Deville et al., 2010) (Fig. 1.29). Similarly to clastic mud volcano systems, mud-grade carbonate volcano systems are typical fluid flow features of subsurface chalk remobilisation (Andresen, 2012).

1.5.1.1 Sand injection complexes

Sand injections have been observed in different scales, varying from the features observed in cores from the Balder Field (e.g. Jenssen et al., 1993; Newton and Flanagan, 1993) to kilometre-scale seismic features in the North Sea (e.g. Duranti et al., 2002; Hurst et al., 2003a; Hurst et al., 2003b; Huuse et al., 2005). In seismic data, sand intrusions are shown as high-amplitude reflections cross-cutting the surrounding strata, forming a wide range of geometries such as dykes, sills, conical, saucer-shaped and winged intrusions (Molyneux et al., 2002; Huuse et al., 2005; Huuse et al., 2007; Jackson et al., 2011; Andresen, 2012; Andresen and Clausen, 2014; Hurst et al., 2021) (Fig. 1.29).

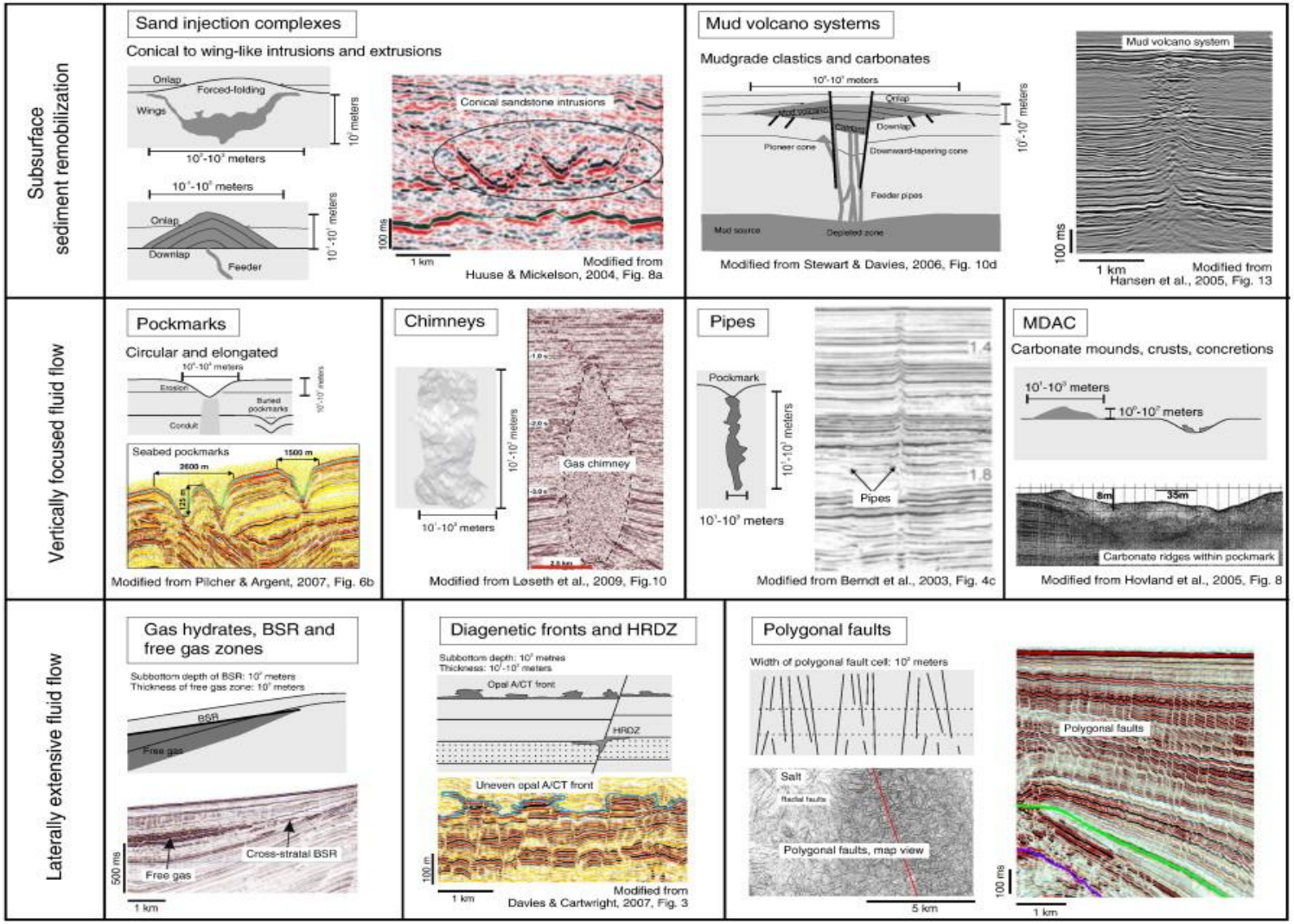

Fig. 1.29. Schematic illustrations and seismic examples of fluid flow features. MDAC= methane derived authigenic carbonates, HRDZ = hydro-carbon related diagenetic zones, BSR = bottom simulating reflection. Figure from Andresen (2012).

1.5.1.2 Mud volcano systems

Mud volcano systems are positive, often conical and crater-shaped fluid escape features on the seafloor, observed in various geological settings around the world, that chiefly comprise mud and other sediments (Milkov, 2000; Dimitrov, 2002; Kopf, 2002; Planke et al., 2003; Mazzini et al., 2007; Mellors et al., 2007; Bonini, 2012; Istadi et al., 2012). They periodically or continuously vent liquid mud, water and hydrocarbon products, forming in thick sedimentary basins where significant overpressures are built at depth – often due to rapid sedimentary loading and hydrocarbon generation (Mazzini et al., 2009; Andresen, 2012) (Fig. 1.30). These phenomena result in density inversion and the upward mobilisation of deep mudstones and accompanying fluids (e.g. Brown, 1990; Milkov, 2000). Therefore, mud volcanoes are important indicators of deep plumbing systems in a sedimentary basin (Fowler et al., 2000; Dimitrov, 2002; Mazzini et al., 2007; Bonini, 2012).

1.5.2 Vertically focused fluid flow

1.5.2.1 Pockmarks

Pockmarks are commonly located in areas where gas is present in near-surface sediments, especially above the acoustically transparent gas chimneys that breach the seafloor (e.g. Hovland and Judd, 1988; Hovland et al., 2002; Cathles et al., 2010). They are usually formed due to expulsive fluid venting, and are recognised as circular to elliptical depressions at the present-day and paleo-seafloor (King and Maclean, 1970; Hovland and Judd, 1988; Hovland et al., 2002; Judd et al., 2007; Cathles et al., 2010; Marcon et al., 2014) (Fig. 1.31). The typical diameters of pockmarks ranges from a few meters to up to >300 m, and from 1 to 80 m in depth but usually <10 m (Hovland and Judd, 1988; Hovland et al., 2002; Gay et al., 2006; Cathles et al., 2010).

1.5.2.2 Chimneys and pipes

Chimneys and pipes form during vertically focused fluid flow and are recognised as vertical extensive either low- or high-amplitude anomalies on seismic data (Heggland, 2005; Løseth et al., 2009; Hustoft et al., 2010; Løseth et al., 2011; Ebrahimi et al., 2013; Heggland, 2013; Cartwright and Santamarina, 2015; Karstens and Berndt, 2015; Räss et al., 2018; Wangen, 2020; Robinson et al., 2021) (Fig. 1.31). Gas chimneys are usually related to dimmed

and distorted amplitudes, whereas pipes may include vertically stacked either high- or low amplitude anomalies (e. g. Andresen, 2012). Several mechanisms related to fluid flow have been proposed to explain the formation of chimneys and pipes, such as free gas migration and fracturing (e.g. Cartwright et al., 2007; Løseth et al., 2009; Cartwright and Santamarina, 2015; Räss et al., 2018).

1.5.2.3 Methane-derived authigenic carbonates

Methane-derived authigenic carbonates (MDAC) are associated with the seepage of methane-rich fluids to the seafloor where anaerobic methane oxidation coupled with bacterial sulphate reduction results in the precipitation of varying carbonates (e.g. Boetius et al., 2000; Hovland, 2007; Judd et al., 2007; Magalhães et al., 2012) (Fig. 1.29). Several observations of MDAC are described in provinces with other focused fluid flow features such as pockmarks (e.g. Hovland et al., 2005; Judd et al., 2007; Andresen et al., 2008; Andresen, 2012).

1.5.3 Laterally extensive fluid flow features

1.5.3.1 Gas hydrates

Gas hydrates (ice-like crystals) are composed of water and gas, where gas molecules are trapped within a framework of hydrogen-bonded water molecules (e.g. Kvenvolden, 1993; Sloan Jr, 2003; Makogon, 2010; Koh et al., 2011; Andresen, 2012) (Fig. 1.29). Gas hydrates and associated free gas zones and bottom simulating reflections (BSRs) are generated in specific temperature and pressure conditions (Kvenvolden, 1988). When the pressure and temperature conditions are changed and the hydrates dissociate and/or dissolve, gas hydrates are likely to start the massive gas release to the ocean and atmosphere (Kvenvolden, 1988; Kvenvolden, 1993). In seismic data, a reduction in p-wave velocity at the transition from gas hydrates in sediments to shallow gas or water in the pore spaces below result in a ‘soft’ seismic reflection - a BSR, or Bottom Simulating Reflector - which mimics the seafloor horizon (Popescu et al., 2007; Andresen, 2012). Gas hydrates represent potential drilling hazards and are avoided in well planning (Andresen, 2012).

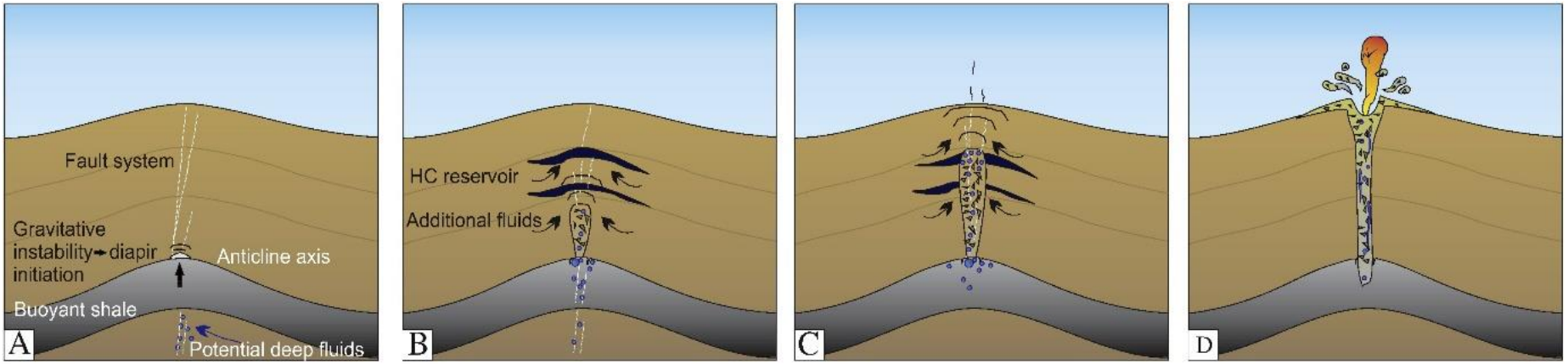

Fig. 1.30. Cartoon diagram showing the growth of a mud volcano in four different stages. Figure from Mazzini (2017).

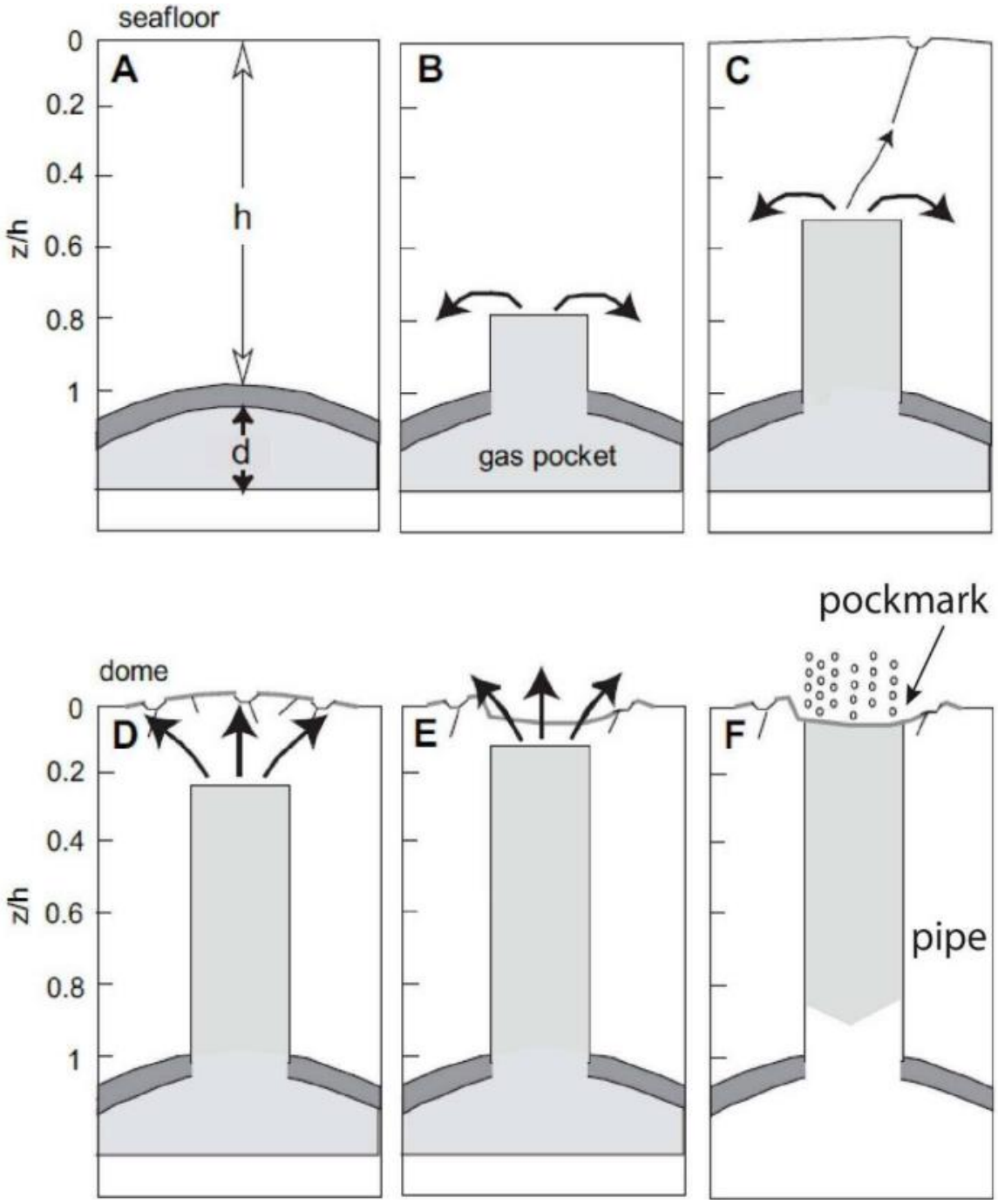

Fig. 1.31. Schematic illustration for the formation of gas chimneys and pockmarks. (A) Gas is trapped below an anticline of a fine-grained sediment (dark grey) forming a capillary seal. (B) Gas is released from a chimney due the seal fails when the gas accumulation accumulates to a certain thickness. (C) The first pockmark forms when the chimney extends about halfway to the seafloor. (D) More pockmarks are formed with more severe sediment deformation above the chimney. (E) Many pockmarks merging into a large pockmark with dimensions like the chimney. (F) When the chimney reaches the surface the gas pocket quickly drains. Figure from Roelofse (2020) who modified it from Cathles et al. (2010).

1.5.3.2 Diagenetic fronts

Diagenetic fronts such as the opal A-CT transition generally occurs during diagenesis (Berndt et al., 2004; Davies, 2005; Cartwright, 2007) (Fig. 1.29). The front arises when opal-A is dissolved and re-precipitated as opal-CT during burial, with this process being often associated with the local production of fluid (Davies and Cartwright, 2007). Opal-CT has a higher impedance contrast when compared to opal-A, resulting in the formation of a high-amplitude reflection that is semi-parallel to the seafloor and often cross-cuts host seismic reflections (Neagu et al., 2010). Focused fluid flow from deeper successions along faults has been suggested as a mechanism possibly forming seed areas for the opal A/CT reaction and/or locally enhancing the reaction rates (Davies and Cartwright, 2007).

1.5.3.3 Hydrocarbon-related diagenetic zones

Hydrocarbon-related diagenetic zones (HRDZs) are associated with hydrocarbon leakage where upward migrating hydrocarbons enter the shallower reservoir and become biodegraded (Andresen, 2012) (Fig. 1.29). HRDZs represent high-amplitude anomalies in relation to velocity pull-up and attenuation in the section below, as biological oxidation of the hydrocarbons generates a strong cementation with high acoustic impedance during the biodegradation (e.g. Cowley and O'brien, 2000).

1.5.3.4 Polygonal fault systems

Polygonal faults systems are networks of non-tectonic normal faults, often tier-bound, that are formed by the volumetric contraction of very fine-grained sediments that compact and dewater during their initial burial (Cartwright and Lonergan, 1996; Cartwright, 1996; Cartwright et al., 2003) (Fig. 1.29). Polygonal fault systems have typical polygonal planforms in plan view and may act as fluid migration pathways, as proven by pockmarks located above the triple-junction of polygonal faults (Gay et al., 2004). Polygonal fault systems have also been observed in areas with diagenetic boundaries such as Opal A-CT boundaries (Cartwright, 2007).

1.5.4 Direct hydrocarbon indicators

Direct hydrocarbon indicators (DHIs) in seismic data may be observed to indicate the existence of fluid or fluid contacts, including bright, dim and flat spots, polarity reversal and velocity push-down (Cox et al., 2020) (Fig. 1.32). These direct hydrocarbon indicators are acoustic manifestations of hydrocarbons within the sedimentary succession, and often appear as local amplitude anomalies. However, amplitude anomalies may also be caused by, for example, cemented zones, overpressured sands, local lithological changes, or sedimentary disruption by previous episodes of fluid flow, so they should be interpreted with caution (Andresen et al., 2011).

Bright spots indicate local increases in seismic amplitude. They commonly relate to the existence of gas in clastic reservoirs, resulting in a decrease in velocity when seismic waves propagate from the overlying seal unit. This increases the negative impedance contrast and brighten the sand reflections in this same reservoir (Cox et al., 2020) (Fig. 1.32a).

Dim spots are generally observed in low-porosity sandstones or carbonates that often have large impedance contrasts from the overlying shale. Due to the presence of hydrocarbon in the sands, it causes the reduction of velocity and density, but it may not decrease enough to reverse the reflection coefficient polarity. Hence, the reduced acoustic impedance contrast between reservoir and seal will reduce the seismic amplitude, creating a ‘dim spot’ (Cox et al., 2020) (Fig. 1.32b).

Flat spots represent fluid contacts between the different fluids, or fluid phases. In subsurface reservoirs, gas is found above oil and oil is found above water/brine due to differences in fluid densities. In a dipping reservoir, the contact between the different fluids will form crosscutting hard reflections due to relative downward increases in velocity and density of pore fluids. The reflection amplitude is greater in highly porous reservoirs due to their low matrix stiffness and high pore fluid content (Cox et al., 2020) (Fig. 1.32c).

Polarity reversal occurs in the presence of hydrocarbon fluids in intermediate porosity reservoirs, with increases in hydrocarbon saturation resulting in local polarity reversals along a single seismic reflector. All in all, the presence of hydrocarbon can decrease the acoustic impedance of a top reservoir reflector, for instance, for acoustic impedance to become less than the overlying seal. This usually results in an abrupt change in reflection polarity at this same top reservoir horizon (Cox et al., 2020) (Fig. 1.32d).

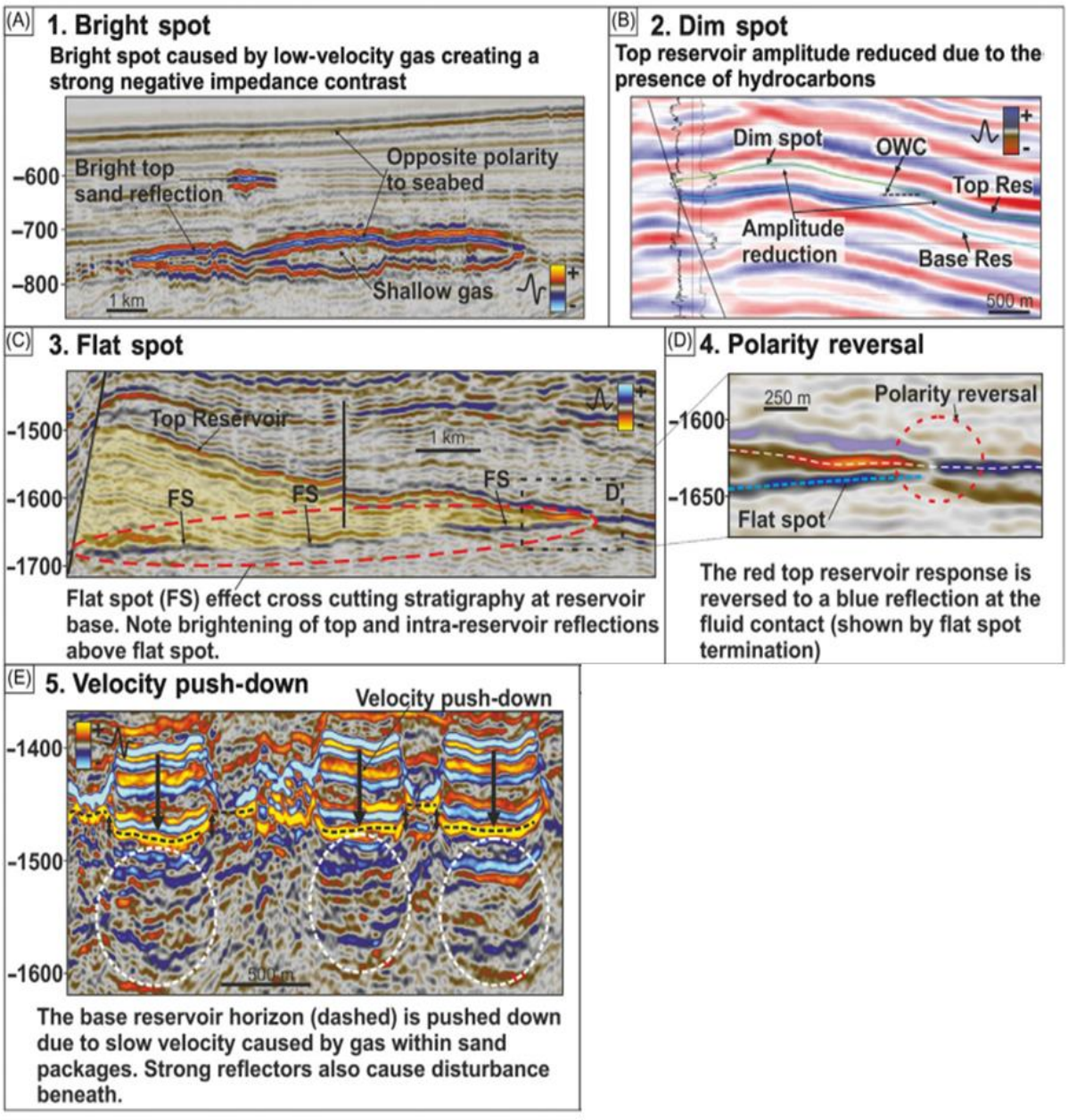

Fig. 1.32. Seismic examples of direct hydrocarbon indicators (DHIs). (A) Bright spot. (B) Dim spot. (C) Flat spot. (D) Polarity reversal. (E) Velocity push-down. Figure from Cox et al., (2020).

Velocity push-down (velocity shadow) relates to hydrocarbon fluids that cause a reduction in velocity, increasing p-wave travel times through a reservoir. This causes seismic reflections to be 'pushed-down' and appear deeper than they are in reality (Cox et al., 2020) (Fig. 1.32e).

1.6 Thesis layout

This thesis is divided into eight chapters. The present chapter introduces the thesis, its rationale and research aims. Chapter 1 also summarises the relevant background literature of main themes covered in this thesis, including fault growth and propagation, mechanical stratigraphy, salt tectonics, and fluid flow features. The geological settings of two study areas are summarised in Chapter 2. The data and main methods used in the thesis are described in Chapter 3, followed by the results of three cases studies in Chapters 4, 5 and 6. The distribution, evolution history and significance of tectonic faulting in a salt minibasin offshore Espírito Santo, SE Brazil are investigated in Chapter 4. Chapter 5 concerns a study of palaeostress states around a rising salt diapir on the Cleaver Bank High, Southern North Sea. The influence of salt structures and faults on the geothermal potential of the Cleaver Bank High, Southern North Sea is investigated in Chapter 6. All results are discussed in Chapter 7, where fault families in two different tectonic settings are compared and contrasted, and the importance of fault families to fluid flow, storage and production in salt-rich basins is demonstrated. Final conclusions are presented in Chapter 8.

Chapter 2

Geological settings of the studied areas

2 Geological setting of the studied areas

2.1 Introduction

This chapter reviews the geological settings of the two study areas considered in this thesis, the Espírito Santo Basin, SE Brazil and the Cleaver Bank High, Southern North Sea. Each section also summarises the structural and stratigraphic evolutions, and known petroleum systems, in each study area.

2.2 Espírito Santo Basin, SE Brazil

The Espírito Santo Basin is located on the southeast continental margin of Brazil and covers an area of ~125,000 km^2, of which 107,000 km^2 are located offshore (Fiduk et al., 2004; Gamboa et al., 2010) (Fig. 2.1). The basin is bounded to the north by the Abrolhos Plateau, a volcanic ridge separating the Espírito Santo Basin from the Cumuruxatiba Basin. To the south, it is separated from the Campos Basin by a largely political boundary, as there is a continuum of rift, sub-salt and supra-salt units from the Santos to the Espírito Santo basins (Fiduk et al., 2004; Gamboa et al., 2010; Mattos and Alves, 2018). Despite being less known than the Campos and Santos Basins to the south, the Espírito Santo Basin still has important hydrocarbon reserves (e.g. Fiduk et al., 2004). This is partly due to its basin structure and tectonic evolution, which are analogous to its counterparts to the south - the Campos and Santos Basins – both recording great exploration success (Estrella et al., 1984; Bruhn and Walker, 1997; Katz and Mello, 2000; Shenyan et al., 2011; Bruhn et al., 2017; Mello et al., 2021).

2.2.1 Tectonic evolution

The Espírito Santo Basin includes a series of rift basins, trending N–S to NNE-SSW, that were formed during Late Jurassic-Early Cretaceous continental rifting and subsequent breakup of the supercontinent Gondwana (Ojeda, 1982; Chang et al., 1992; Fiduk et al., 2004; Mohriak et al., 2008; Alves, 2012; Piedade and Alves, 2017). The tectonic evolution of the Espírito Santo Basin is similar to most rift basins in the South Atlantic Ocean and can be divided into four separate stages: rift onset, syn-rift, transitional, and drift (Chang et al., 1992; Bruhn and Walker, 1997; Fiduk et al., 2004; Gamboa et al., 2012) (Fig. 2.2).

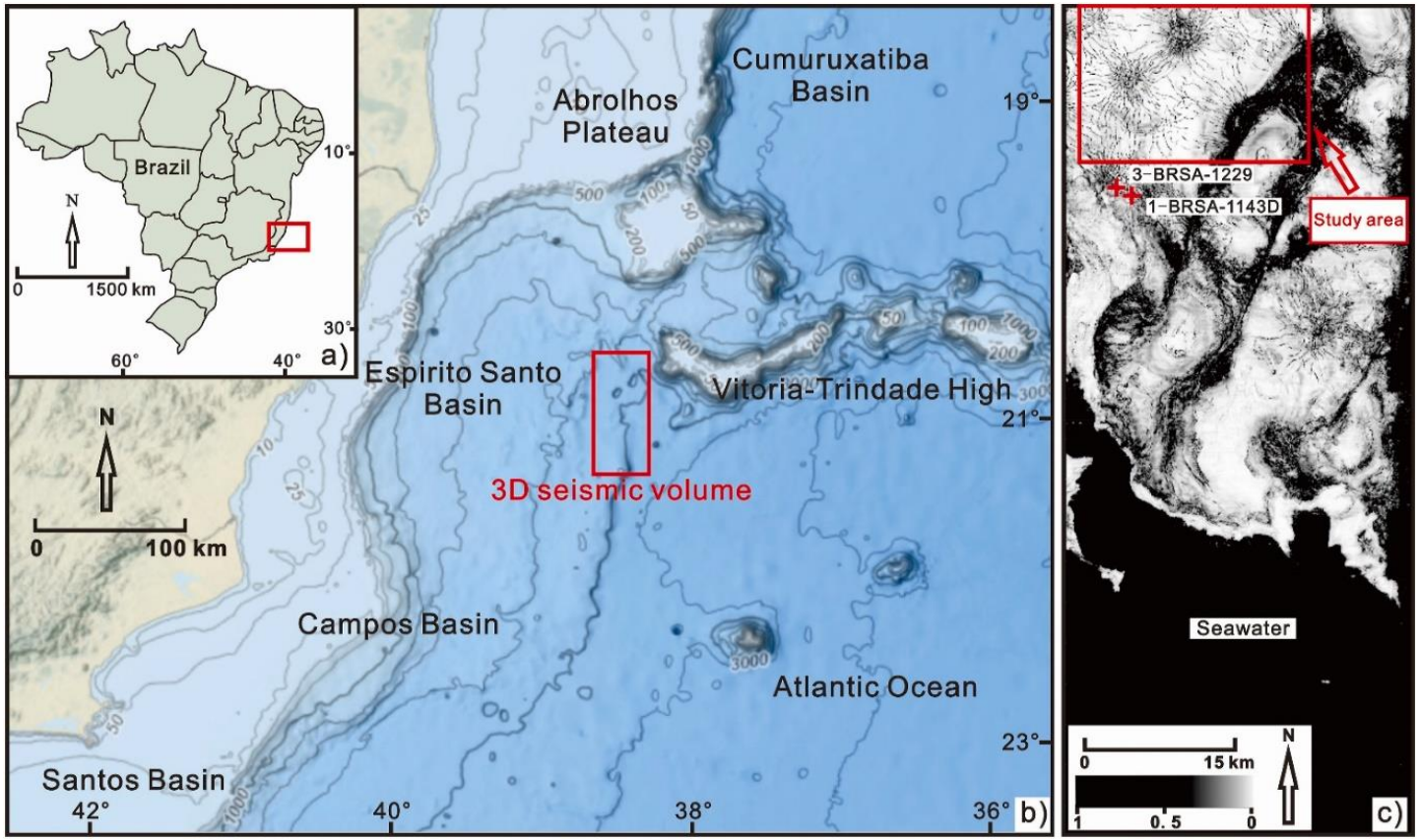

Fig. 2.1. a) Location of Fig. 1b) in relation to Brazil and its continental margin. b) Bathymetric map highlighting the location of the Espírito Santo Basin and its adjacent structural units. Note that the Espírito Santo Basin is bounded by the volcanic Abrolhos Plateau to the north and is separated from the Campos Basin to the south by a political boundary. The red polygon indicates the location of the 3D seismic volume. Topographic map is taken from the National Center for Environmental Information. c) Entire 3D seismic volume image showing the location of study area in Chapter 4 as marked by a red polygon and two wells (3-BRSA-1229 and 1-BRSA-1143D) in a seismic variance time-slice (Z = −3000 ms two-way time).

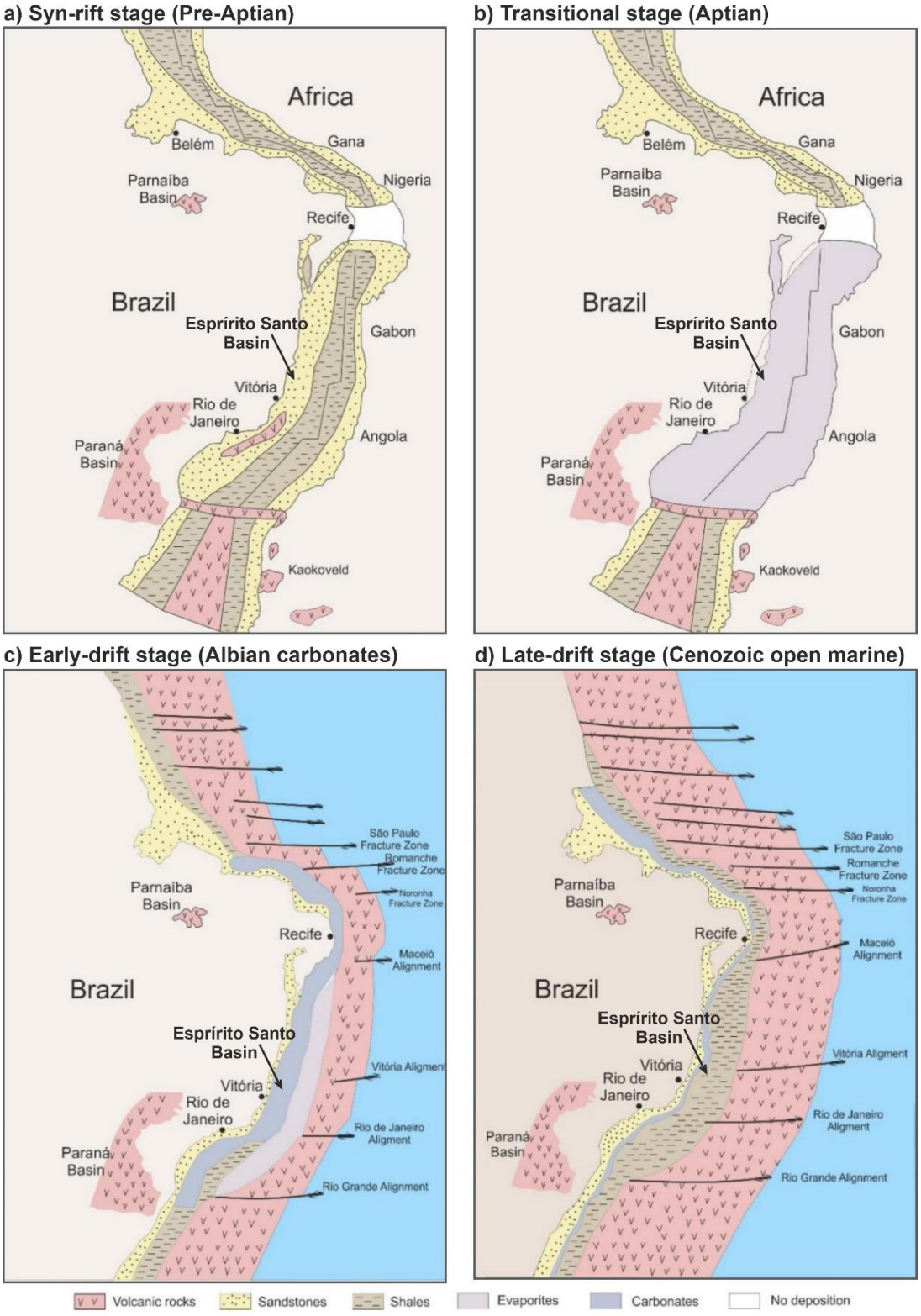

Fig. 2.2. Schematic illustration of four tectonic evolution stages of SE Brazil. a) Syn-rift stage dominated by continental deposition; b) Transitional stage characterised by the deposition of evaporites; c) Early drift stage marked by the development of carbonate platforms and d) Late drift stage showing the open marine deposition. Figure from Mattos (2017) who modified it from Ojeda (1982).

2.2.1.1 Rift-related evolution of the Espírito Santo Basin

The rift onset stage of the Espírito Santo Basin occurred in the Late Jurassic-Early Cretaceous and was characterised by the onset of lithospheric extension at a regional scale (Ojeda, 1982; Cainelli and Mohriak, 1999; Fiduk et al., 2004; Mohriak et al., 2008). Moderate tectonism and intense volcanism occurred at this stage throughout SE Brazil, with the Espírito Santo Basin becoming rapidly filled with coarse-grained fluvial strata, alluvial fan deposits and localised evaporites (Ojeda, 1982; Chang et al., 1992; Cainelli and Mohriak, 1999; Mohriak and Rosendahl, 2003) (Fig. 2.2a).

The syn-rift stage lasted from late Berriasian/Valanginian to the early Aptian (Ojeda, 1982; Fiduk et al., 2004; Gamboa, 2011; Qin et al., 2016). It was marked by intense tectonism due to enhanced lithospheric extension and asthenospheric uplift accompanying the formation of the Eastern Brazilian Rift (Cainelli and Mohriak, 1999; Mohriak and Rosendahl, 2003). Syn-rift units comprise lacustrine sediments in elongated and faulted sub-basins formed between the Santos and the Sergipe/Alagoas Basins. Three main facies associations were deposited at this stage: 1) alluvial fan/fan deltas and transitional deposits, 2) lacustrine marls and shales, and 3) lacustrine pelecypod limestones, usually termed *coquinas* in the Brazilian geological literature (Ojeda, 1982; Demercian et al., 1993; Cainelli and Mohriak, 1999) (Fig. 2.2a).

2.2.1.2 Halokinesis and Cenozoic evolution

The transitional stage occurred from early Aptian to late Aptian/early Albian, a period of time associated with continental breakup occurring to the east (i.e. outboard) of the Espírito Santo Basin (Ojeda, 1982; Fiduk et al., 2004; Alves et al., 2020). At this stage, the activity of large faults became concentrated at the locus of continental breakup to the east. Lithospheric extension significantly enhanced regional subsidence as recorded by the deposition of shallow water microbial carbonates, itself followed by the precipitation and accumulation of >3000 m of evaporites on the SE Brazil-West Africa conjugate margin (Davison et al., 2012). Such a transitional unit reflects a continental-breakup sequence with a typical regressive-transgressive cycle (Alves and Cunha, 2018; Alves et al., 2020) (Fig. 2.2b).

The drift stage spanned from the Albian to present-day and marks the main phase of ocean spreading between South America and Africa (Ojeda, 1982; Fiduk et al., 2004; Gamboa, 2011). At this stage, tectonic activity was chiefly associated with thermal subsidence and marine deposition predominated in the Espírito Santo Basin (Chang et al., 1992; Cainelli and

Mohriak, 1999). The drift stage comprises two distinct megasequences: an early drift transgressive megasequence and a late drift regressive megasequence (Chang et al., 1992; Cainelli and Mohriak, 1999). The early drift transgressive megasequence records the deposition of carbonate intervals below muddy and sandy turbidites, representing shallow water environments that deepened upwards until the end of the Cretaceous (Ojeda, 1982; Chang et al., 1992; Mohriak et al., 2008; Qin et al., 2016) (Fig. 2.2c). The late drift regressive megasequence was marked by open marine deposition, reflecting the progressive filling of the Espírito Santo Basin's continental shelf and slope (Ojeda, 1982; Chang et al., 1992; Mohriak et al., 2008) (Fig. 2.2d). Additionally, intrusive magmas have been recorded by multiple studies in the northern part of the Espírito Santo Basin, and their origin is associated with mantle plumes or hot spots migrating from the Brazilian craton, across the rift basins, to oceanic crust (Meisling et al., 2001; Cobbold et al., 2001; Fiduk et al., 2004). The Abrolhos Plateau, separating the Espírito Santo Basin from the Cumuruxatiba Basin, was formed between 55 and 40 Ma due to the movement of the Trindade Hot Spot across the northern Espírito Santo Basin (Fiduk et al., 2004).

Due to regional extension and continuous subsidence, halokinesis occurred in the study area in response to differential loading by overburden strata, gravity spreading and downslope gravity gliding on top of evaporite successions (Demercian et al., 1993; Fiduk et al., 2004). Significant uplift and tilting of the continental slope have also occurred during the emplacement of the Abrolhos Plateau, which would have accelerated downslope gravity gliding and thus explain the large number of deforming structures in the Early Cenozoic (Fiduk et al., 2004). Halokinesis started straight after the deposition of salt during the Albian and peaked during the Late Cenozoic (Fiduk et al., 2004; Alves, 2012). It divided the basin into three tectonic domains with different structural styles: proximal extensional, transitional and distal compressional (Rouby et al., 2003; Vendeville, 2005; Gamboa et al., 2010; Mohriak et al., 2012; Qin et al., 2016) (Fig. 2.3). The proximal extensional domain includes salt rollers, salt walls along conjugate normal faults, turtle anticlines and rafts (Mohriak et al., 2008). The transitional domain is characterised by salt diapirs, while the distal compressional domain is dominated by allochthonous salt such as salt canopies and overhangs (Demercian et al., 1993; Davison, 2007). The location of study area in Chapter 4 is between the transitional and the distal compressional domains (Fig. 2.3).

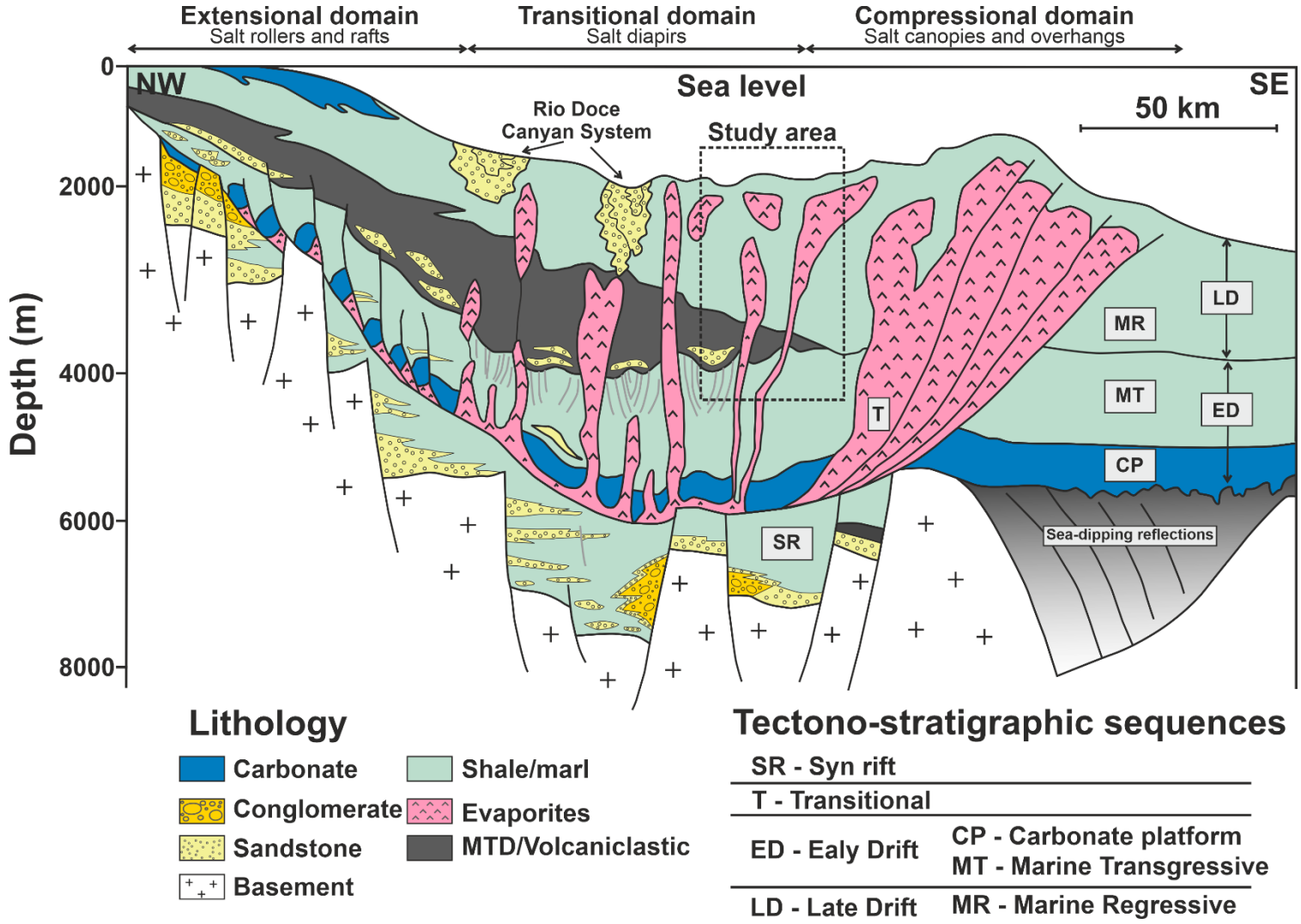

Fig. 2.3. Schematic illustration of three structural domains in the Espírito Santo Basin and related strata representing main tectonic stages. The location of study area in Chapter 4 is shown by a black dashed rectangle. Figure modified from Gamboa (2011) and Fiduk et al. (2004).

2.2.2 Stratigraphy

The stratigraphy of the Espírito Santo Basin can be divided into three groups: the Nativo Group, Barra Nova Group and Espírito Santo Group in their chronostratigraphic order (França et al., 2007) (Fig. 2.4).

2.2.2.1 The Nativo Group

The Nativo Group is bounded by a regional unconformity to the bottom, separating this unit from the Pre-Cambrian basement, and is limited to the top by the Barra Nova Group. The Nativo Group consists of the Cricaré and Mariricu Formations, which were deposited from the Valanginian to the Aptian (Fig. 2.4). The Cricaré Formation can be subdivided into the Jaguaré and Sernambi Members, while the Mariricu Formation can be subdivided into Mucurí and Itaúnas Members. The Nativo Group comprises continental siliciclastic rocks interbedded with volcaniclastic deposits at its bottom, and thick evaporitic deposits that are mainly composed of halite and anhydrite at the top of the group (Asmus et al., 1971; Ojeda, 1982; Chang et al., 1992; Mohriak and Rosendahl, 2003; França et al., 2007).

2.2.2.2 The Barra Nova Group

The Barra Nova Group is bounded by Pre-Urucutuca unconformities to its top and consists of Albian to Cenomanian strata deposited over the Itaúnas Member evaporites (Fig. 2.4). The Barra Nova Group comprises the São Mateus and Regência Formations, which were deposited in a proximal marine setting (São Mateus Formation) and distal marine environment in the case of the Regência Formation (França et al., 2007). The São Mateus Formation includes sandstones deposited over a succession of shales, siltstones and carbonates, while the Regência Formation comprises relatively thick limestones, carbonate mudstones and wackestones with ostracods (Asmus et al., 1971; França et al., 2007).

2.2.2.3 The Espírito Santo Group

The Espírito Santo Group comprises Cenomanian to Holocene strata deposited over the Barra Nova Group, and is subdivided into five distinct formations: the Urucutuca, Abrolhos, Caravelas, Rio Doce and Barreiras Formations. The Urucutuca Formation is composed of

shales interbedded with conglomerates, limestones and sandstones, later deformed by salt tectonics between the Cenomanian to the Coniacian in the proximal parts of the study area. On the distal margin, dark shales and sands were deposited during this time (Cainelli and Mohriak, 1999; França et al., 2007). The Coniacian-Maastrichtian Urucutuca Formation includes sandy turbidites at the bottom and significantly shales and sandstones on the proximal margin, whilst marls were deposited in more distal parts. The volcaniclastic Abrolhos Formation was deposited from the Selandian (Paleocene) to the Bartonian (Eocene), together with thick turbidite successions in channelised bodies whose geometry and distribution were controlled by halokinesis (Figueiredo and Mohriak, 1984; Cainelli and Mohriak, 1999; França et al., 2007).

The Caravelas Formation was deposited from the Bartonian (Eocene) to the Holocene and comprises turbidites, calcarenites and calcareous mudstones, all deposited over the sediments of the Abrolhos Formation and interfingering with the upper part of the Urucutuca and Rio Doce formations (Alves and Cartwright, 2009). The Rio Doce Formation was also deposited from the Bartonian to the present day, and is formed of sandstones interbedded with shales and siltstones that interfinger with the Caravelas Formation on the distal margin (França et al., 2007). The Barreiras Formation comprises strata deposited in fluvial and alluvial environments interfingering with the Rio Doce Formation on the proximal margin (Vieira et al., 1994).

2.2.3 Petroleum systems

The Espírito Santo Basin, as one of the typical salt-bearing basins in SE Brazil, reveals a vibrant hydrocarbon potential. The first petroleum exploration success in the Espírito Santo Basin was recorded onshore in 1969, and offshore exploration began in 1974 together with the adjacent Santos and Campos Basins (Fiduk et al., 2004). For the last two decades, large petroleum fields have been discovered in deep water areas of the Espírito Santo Basin, particularly around salt structures.

2.2.3.1 Source rocks

In the Espírito Santo Basin there are two source rock intervals within syn-rift strata deposited in different environments. During late Berriasian to middle Barremian, lacustrine shales containing Type I kerogen were deposited in deep, narrow and asymmetric fresh-water rift basins. Here, the source potential is higher in the basin axes where several thin high-TOC

layers are recorded (Fiduk et al., 2004). During middle to late Barremian, widespread thick-bedded calcareous shales containing Type II kerogen were deposited in broad, shallow, saline lacustrine basins, giving rise to the dominant source rock in the basin (Fiduk et al., 2004).

Inside transitional stage strata there are thin black, organic-rich shales associated with evaporite successions that contain Type II kerogen. These were deposited in high-salinity, oxygen-poor lagoonal conditions (Estrella et al., 1984; Fiduk et al., 2004). As for the drift strata, organic-rich shales have been encountered when drilling Cenomanian to Turonian transgressive marine intervals (Fiduk et al., 2004). These sequences contain Type III kerogen and have reached thermal maturity in the Espírito Santo Basin (Cobbold et al., 2001; Gibbs et al., 2003).

2.2.3.2 Reservoir rocks

The main reservoir intervals in the Espírito Santo Basin include Albian carbonates in the Regência Formation, Campanian and Maastrichtian sandstones in the Urucutuca Formation, and Cenozoic regressive sandstones in the Urucutuca, Rio Doce and Barreiras Formations (Fiduk et al., 2004). The Albian carbonates were deposited over underlying salt and later formed rafts and large turtle-back structures (Figueiredo and Mohriak, 1984; Cainelli and Mohriak, 1999). Campanian and Maastrichtian sandstones are mainly turbidite deposits accumulated in channels, canyons and fan complexes, thought to show the greatest reservoir potential in deep water areas of the basin (França et al., 2007). Cenozoic regressive sandstones were mainly deposited in slope and deep basin environments, with channelized deposits within submarine canyons, turbidites and basin floor fan deposits comprising the best reservoirs in distal parts of the Espírito Santo Basin (Vieira et al., 1994; França et al., 2007).

2.2.3.3 Seal rocks

As source rocks can be also considered to be useful seal intervals for hydrocarbons, late Berriasian to Barremian lacustrine shales, Aptian evaporites, and Cenomanian to Turonian marine shales are the main sealing units in the Espírito Santo Basin. Late Berriasian to Barremian lacustrine shales are mainly considered as local cap rocks inside the basin axes (França et al., 2007). However, the Aptian evaporites are a regional cap rock due to its low permeability, significant thickness and wide distribution in basin (Chang et al., 1992; Fiduk et al., 2004). Cenomanian to Turonian transgressive marine shales can also form competent cap rocks above the Aptian salt, sealing channel fill and basin floor sandstones (Mohriak and Rosendahl, 2003).

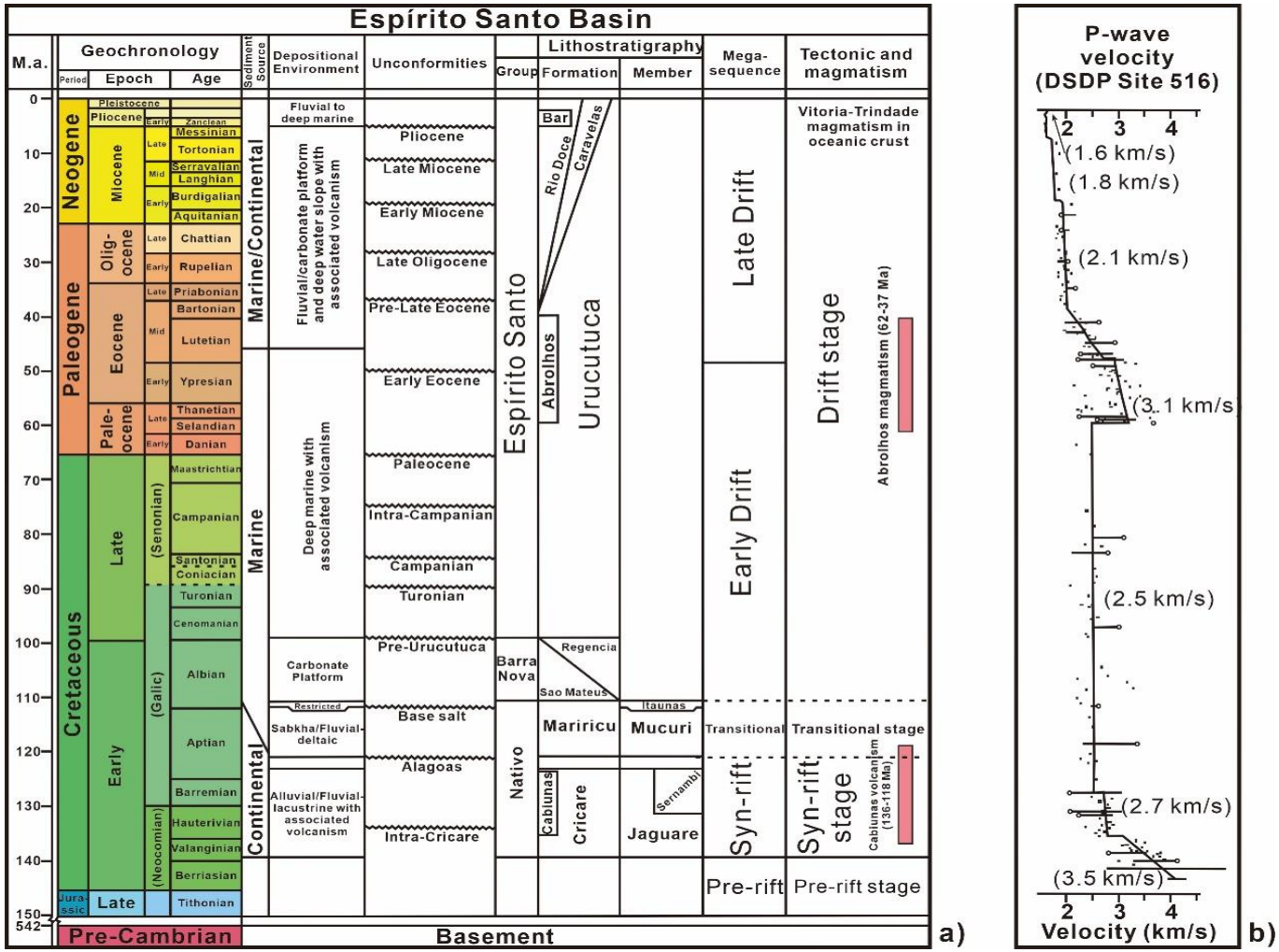

Fig. 2.4. a) Tectono-stratigraphic chart of the Espírito Santo Basin showing main depositional units and their depositional environments. Four tectonic evolutionary stages, episodes of magmatism and five megasequences are highlighted in the figure. Figure modified from Mattos and Alves (2018). B) Velocity data profile for well DSDP 516 for the Rio Grande Rise (Barker et al., 1983).

2.3 Cleaver Bank High, Southern North Sea

The Cleaver Bank High is an important gas producing area of the Southern North Sea. It spans ~8000 km^2 and bounds the Broad Fourteens Basin to the north (Quirk, 1993) (Figs. 2.5 and 2.7). The Cleaver Bank High was first part of a foreland basin during the Variscan orogeny and was later affected by multiple tectonic episodes (Ziegler, 1990; De Jager, 2007) (Fig. 2.6). The Zechstein Group decouples the Permian Rotliegend Group below from Triassic-Holocene strata above (Fig. 2.7; Stewart and Coward, 1995; Ten Veen et al., 2012; Alves and Elliott, 2014). Previous work identified multiple basement fault trends beneath the Zechstein Group, the main evaporitic unit in the Southern North Sea (Schroot and Haan, 2003; Ligtenberg et al., 2011).

2.3.1 Tectonic-stratigraphic evolution

2.3.1.1 Upper Palaeozoic

During the Carboniferous, the Cleaver Bank High was located in a foreland position relative to the Variscan orogen and became the locus of important sedimentation (Limburg Group; Ziegler, 1990; De Jager, 2007). The Variscan orogeny, as the tectonic event responsible for the closure of the Proto-Tethys Ocean, imposed a general N-S compressional regime along northern Europe at the end of the Paleozoic (Devonian and Early Carboniferous; Schroot and Haan, 2003; Van Ojik et al., 2020). At this time, three different fault trends (E-W, NW-SE and NE-SW) inherited from older basement weakness zones became active on the Cleaver Bank High (Schroot and Haan, 2003). At the end of the Carboniferous, tectonic subsidence on the edges of the Variscan orogen was followed by regional thermal uplift and igneous underplating, a phenomenon resulting in the erosion of Upper Carboniferous strata (Fattah et al., 2012b). In some areas, more than 1000 m of the Carboniferous Coal Measures were eroded below a regional Base Permian Unconformity (Quirk, 1993). Older faults were also reactivated in the latest Carboniferous-Early Permian, forming large-scale NE-SW and NW-SE conjugate systems (Ziegler, 1990).

Thermal relaxation and regional subsidence predominated on the Cleaver Bank High after latest Carboniferous-Early Permian tectonics. A succession of aeolian, fluvial sediments and desert-lake deposits was thus deposited in the Late Permian as part of the Rotliegend Group (Van Wees et al., 2000; Doornenbal and Stevenson, 2010) and this was subsequently covered

by evaporites, carbonates and clays in the Zechstein Group, reflecting a period of late crustal extension and subsidence (Fattah et al., 2012b). On the Cleaver Bank High, tectonic extension followed a E–W direction during the Permian (Van Ojik et al., 2020).

2.3.1.2 Mesozoic

The Triassic was also marked by E-W extension (Ziegler, 1990) and, consequently, the Cleaver Bank High recorded at this time the accumulation of silty claystone, minor evaporites, carbonates and sandstones, all part of the Upper and Lower Germanic Trias Group (Fig. 2.6). During the Early Jurassic (Early Kimmerian tectonic phase), extension near the study area still occurred along an E-W direction, and thus controlled the deposition of the Altena Group within the Broad Fourteens Basin. Halokinesis started at this time, imposing an important structural decoupling between sub- and supra-salt strata (James, 2003).

Thermal doming and uplift of the Cleaver Bank High occurred in the Middle and Late Jurassic (Ziegler, 1990; De Jager, 2007). This tectonic phase was associated with continental rifting and resulting sea-level fall, which caused widespread erosion over structural highs in the Southern North Sea; the so-called Mid and Late Kimmerian phases (Ziegler, 1990; De Jager, 2007; Ten Veen et al., 2012). On the Cleaver Bank High, Upper Triassic and Lower Jurassic strata are completely absent (Quirk, 1993). Sea level rose once again during the Early Cretaceous and the study area was gradually flooded; therefore, siliciclastic intervals in the Rijnland Group accumulated over Triassic strata and, locally, the Zechstein Group (Schroot and Haan, 2003). The main direction of extension was reoriented NE-SW from the Late Kimmeridgian to the Early Cretaceous (Deckers and van der Voet, 2018).

Regional thermal subsidence prevailed in the Late Cretaceous and a thick succession of limestones, the Chalk Group, was subsequently deposited (Fattah et al., 2012b). The Alpine orogeny was initiated in Central Europe at this same time due to convergence of the African and Arabian plates with Eurasia (De Jager, 2007; Fattah et al., 2012b). This resulted in the onset of NW-SE tectonic compression on the Cleaver Bank High. Moderate halokinesis occurred due to this same compression, as suggested by the local thinning of the Chalk Group strata towards salt structures.

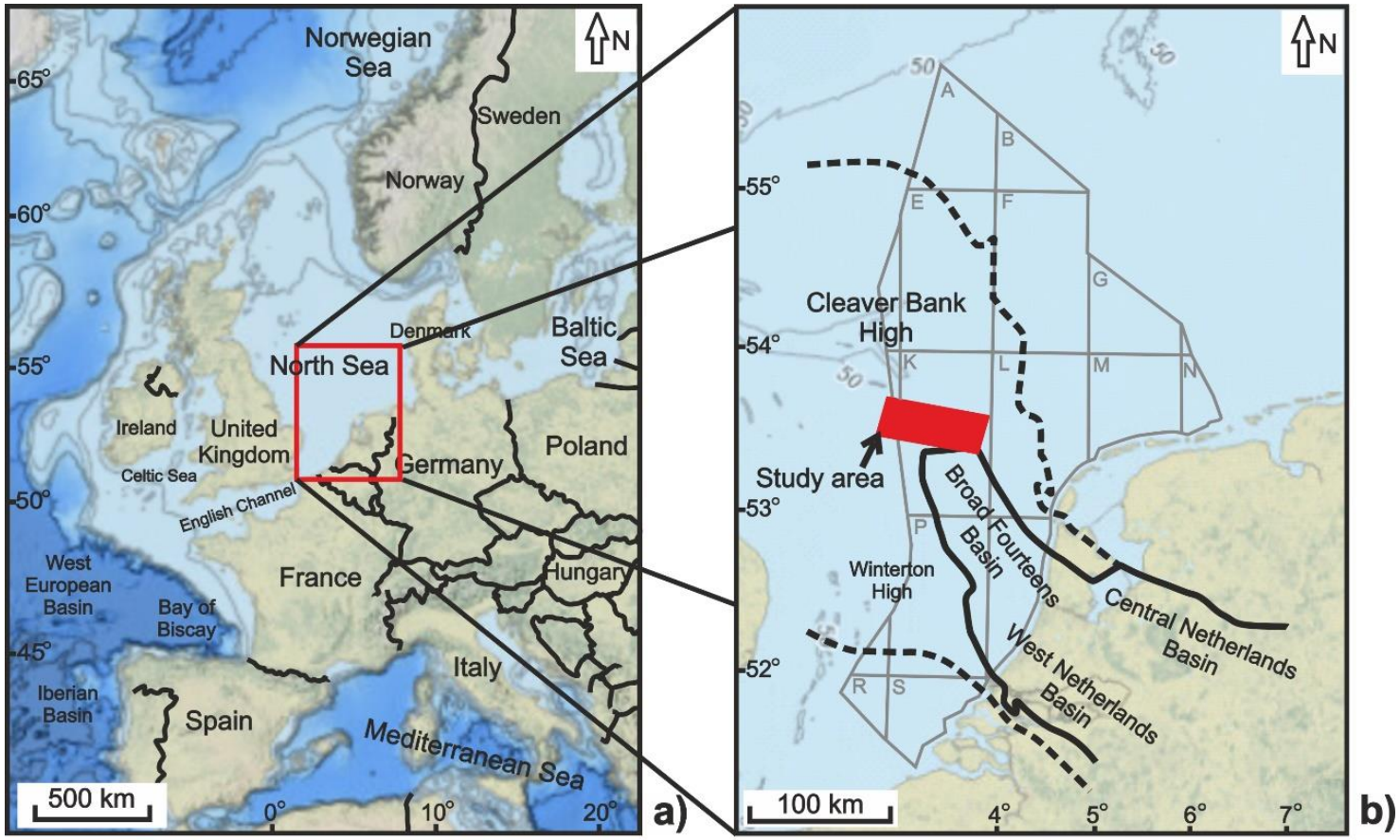

Fig. 2.5. a) Bathymetric map of NW Europe and its continental margin. The red polygon shows the location of Fig. 1b. b) Bathymetric map showing the position of the Dutch sector of the Southern North Sea, which is bounded by the grey polygon. The Broad Fourteens Basin, Central Netherlands Basin and West Netherlands Basin are highlighted by a black solid line, whereas the Cleaver Bank and Winterton highs are highlighted by a black dash line. The red rectangle shows the location of the 3D seismic volume. Bathymetric map is taken from the National Centre for Environmental Information.

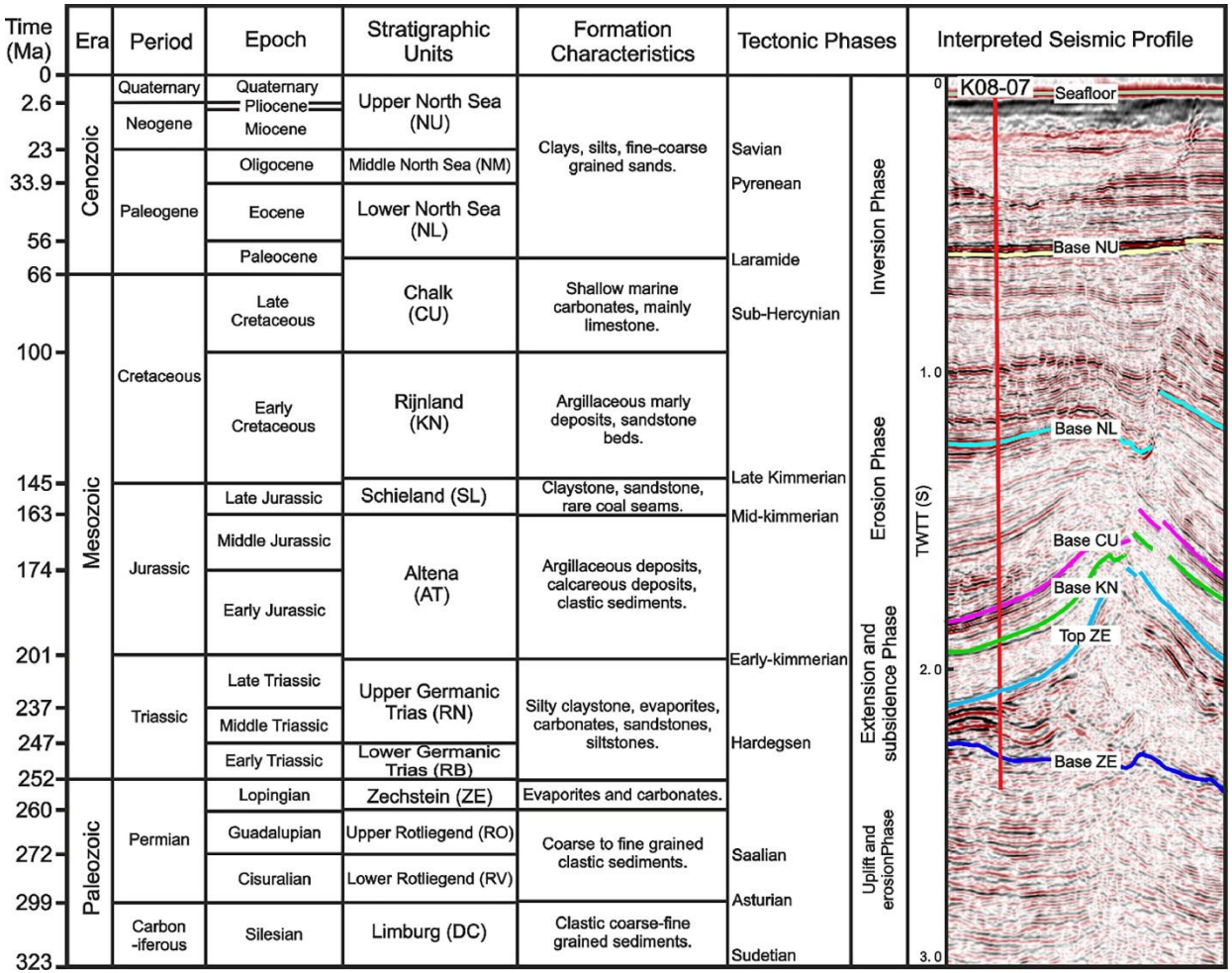

Fig. 2.6. Tectono-stratigraphic chart for the Cleaver Bank High showing main stratigraphic units and formation characteristics (modified from Harding and Huuse, 2015). Multiple tectonic events and four tectonic evolutionary phases are highlighted in the figure. Main seismic-stratigraphic horizons, correlated with data from well K08-07, are shown in the seismic profile.

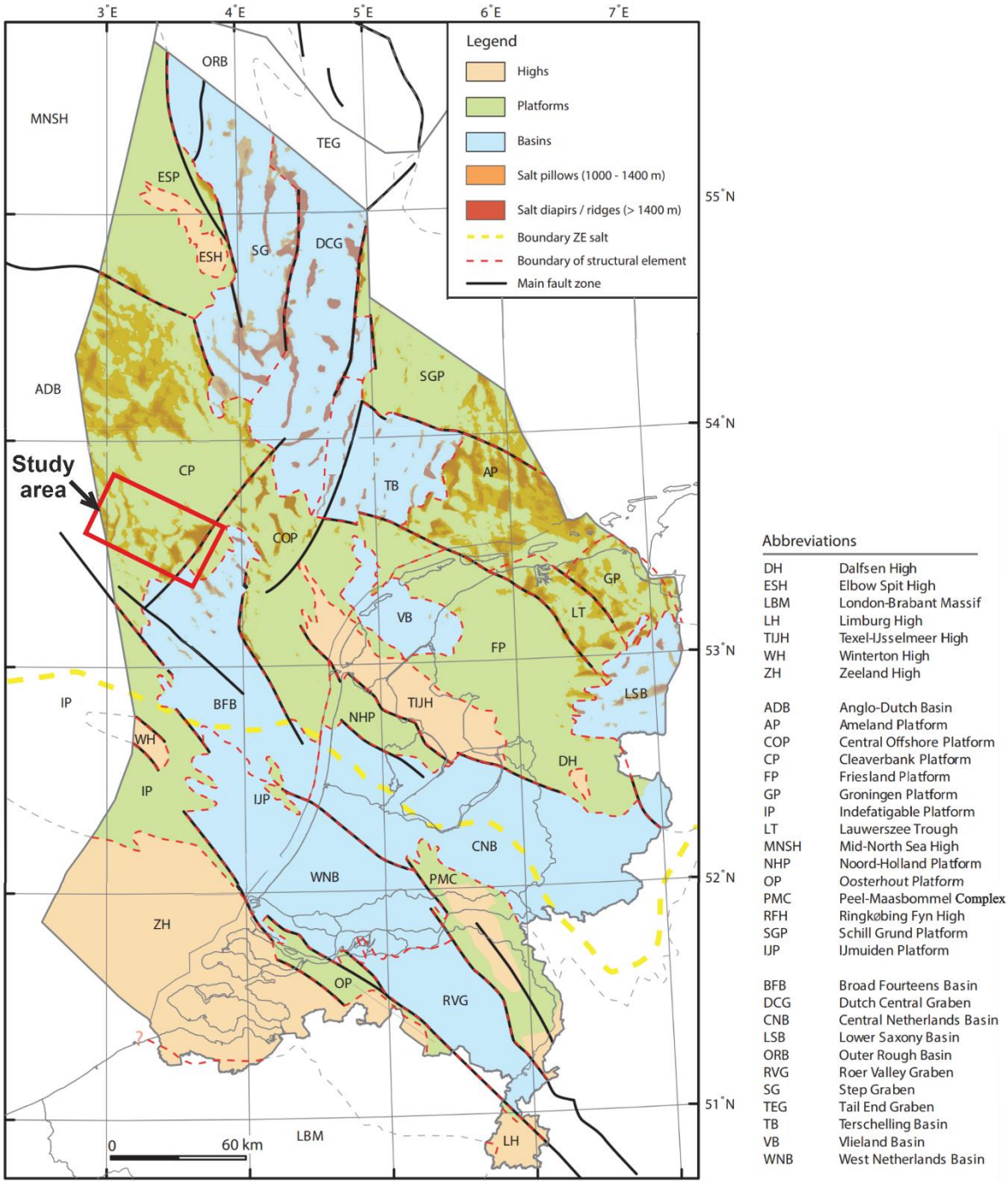

Fig. 2.7. Main structural elements and salt structures in the Dutch sector of the North Sea Basin. The red polygon shows the location of the 3D seismic volume in Chapters 5 and 6. Note that Cleaver Bank High documented in this thesis is named as Cleaver Platform on this map produced by the Geological Survey of the Netherlands. Figure modified from Ten Veen et al. (2012).

2.3.1.3 Cenozoic

On the Cleaver Bank High, Cenozoic sediments are unconformable over the Chalk Group. They consist of clays, silts and fine to coarse sands. Two important inversion episodes affected the study area during the Paleogene, Mid-Paleogene Pyrenean and Late Paleogene Savian tectonics. Apatite fission-track data show that the Cleaver Bank High was locally uplifted during the Pyrenean inversion (Alberts et al., 1991). In contrast, Savian tectonic inversion is marked by a broad, regional unconformity separating Paleogene from Neogene strata (Chen, 2016). During the Cenozoic, the main direction of compression remained oriented NW-SE and reverse faults, thrusts and pop-up structures were locally formed (Van Ojik et al., 2020). In addition, salt movement occurred in the Eocene-Oligocene, accompanying tectonic inversion (Glennie, 1997; Harding and Huuse, 2015; Deckers et al., 2022). Major fold structures cored by salt pillows were initiated or amplified during the multiple Cenozoic tectonic phases occurring during the Cenozoic (Stewart and Coward, 1995; Stewart, 2007; Ten Veen et al., 2012; Hernandez et al., 2018).

2.3.2 Petroleum systems

Multiple gas plays have been found on the Cleaver Bank High, indicating the existence of petroleum systems. Produced gas on the Cleaver Bank High constitutes a mixture of wet and dry gas, which were generated from Westphalian Coal Measures and possibly also from pre-Westphalian source rocks (Gerling et al., 1999; De Jager, 2007; Fattah et al., 2012a; Fattah et al., 2012b).

2.3.2.1 Source rock

The Coal Measures of the Carboniferous Limburg Group is regarded as an important source rock on the Cleaver Bank High. The Westphalian Coal Measures records the deposition of fluvial-deltaic sediments consisting of clastic rocks interstratified with coal beds (Powell et al., 2000). Type III kerogen is recorded in coal bearing source rocks of the Westphalian Maurits and Klaverbank formations (Gerling et al., 1999). It started generating gas during the Upper Triassic, with the increase of gas generation during the Paleogene and the gas generation continuing in present-day (Fattah et al., 2012a; Fattah et al., 2012b).

Besides the Westphalian Coal Measures, pre-Westphalian marine deposits (Namurian and Dinantian) are thought to have contributed to gas accumulations. The Dinantian source rock in the study area comprises deltaic and coal bearing sediments, with Type III kerogen and a total organic carbon (TOC) ranging from 0.9% to 1.9% (Gerling et al., 1999). Similarly to the depositional settings in the Dinantian, the Namurian source rocks consist of marine and deltaic sediments, and include source rocks with Type II kerogen (Gerling et al., 1999). The pre-Westphalian source rocks entered the hydrocarbon generation window in the Late Carboniferous, which started producing gas in the Permian (Fattah et al., 2012a; Fattah et al., 2012b).

2.3.2.2 Reservoir rocks

The sand units of the Upper Rotliegend Group and Limburg Group are the main reservoir rocks on the Cleaver Bank High (Fattah et al., 2012a). The Slochteren Formation is an important reservoir formation in the Rotliegend Group, consisting of sandstone-dominated succession locally containing a considerable proportion of interbedded conglomerates. It was deposited in aeolian and fluvial setting, acting as an important reservoir in the southern sector of the Cleaver Bank High (Fattah et al., 2012a). Comparatively, the Westphalian Hospital Ground Formation is the main reservoir in Carboniferous strata, consisting of sandstones deposited by fluvial systems draining sediment from northern sources (De Jager, 2007).

2.3.2.3 Seal rocks

As salt rock is one of the best seal rocks in petroleum geology, the Zechstein evaporite units covering large parts of the Cleaver Bank High are regarded as a key seal unit (Fattah et al., 2012a; Fattah et al., 2012b). It includes sediments in repetitive cycles (Z1-Z5 in the Netherlands), which were controlled by the interplay of transgressions from the Arctic and evaporation of seawater in the arid Southern Permian Basin (Taylor, 1998; Peryt et al., 2010). In addition, clays and evaporites of the Silverpit Formation, inter-Westphalian shales and faults have also provided important local seals (De Jager and Geluk, 2007).

Chapter 3

Data and methods

3 Data and methods

3.1 Introduction

This thesis uses three-dimensional (3D) seismic reflection data correlated with wells to interpret subsurface geological structures, especially fault families around salt structures. The interpreted seismic volumes and multiple wells were initially acquired and drilled for hydrocarbon exploration. These data are now used for research at the 3D Seismic Laboratory, Cardiff University. This chapter provides the detailed information about the seismic datasets used in this thesis. Well data used in this thesis are also briefly introduced, helping to establish a robust chronostratigraphic framework for the interpreted seismic units. Additionally, the general methodology behind seismic interpretation, volume attributes mapping, structural and stress analysis is presented here. Specific methods used for different dataset are introduced in Chapters 4, 5 and 6.

3.2 3D Seismic and well data used in this thesis

This thesis focuses on two study areas that are the Espírito Santo Basin, SE Brazil and the Cleaver Bank High, Southern North Sea. The details of 3D seismic and well data used herein are summarised below.

3.2.1 Salt minibasin in the Espírito Santo Basin

The interpreted 3D seismic reflection data provided by CGG covers an area of 360 km^2 across the Espírito Santo Basin, SE Brazil, at a water depth ranging from 1630 to 2050 m (Fig. 2.1). The seismic volume was acquired with a 6 × 5700 m array of streamers in 2004, and it was pre-stacked time migrated with a 12.5 × 12.5 m grid line spacing. Seismic data processing included resampling, spherical divergence corrections and zero-phase conversions, all undertaken prior to data stacking (Fiduk et al., 2004; Alves, 2012; Ze and Alves, 2016; Piedade and Alves, 2017). Data are displayed using the European SEG standard for polarity in which a change in acoustic impedance from low to high is shown as a red seismic reflection, and from high to low is shown in blue. The seismic volume was processed in the time domain following a sampling rate of 2 ms, re-sampled at 4 ms, with a dominant frequency of 40 Hz. This resulted

in a minimum vertical resolution (1/4 of the wavelet frequency, or λ/4) ranging from 11 to 19 m at the depth of strata investigated in this work.

Two wells (3-BRSA-1229 and 1-BRSA-1143D) are located in vicinity of the study area provide gamma-ray, lithology and V_p (p-wave velocity) data (Biancardi et al., 2020). Wells 3-BRSA-1229 and 1-BRSA-1143D have respectively a total depth of 4644 and 6493 m, and both penetrate strata ranging from the Early Cretaceous to the Pliocene-Pleistocene. Well correlations were also completed to identify lithological variations in the seismic-stratigraphic units interpreted in this study, and a chronostratigraphic framework was established based on Ze and Alves (2021) (Fig. 3.1).

3.2.2 Southern margin of the Cleaver Bank High

The seismic data used in this work includes a 3D seismic reflection volume and is located at the southern margin of the Cleaver Bank High, Southern North Sea between 53.35°-53.76°N and 3.81°-3.95°E. It was provided by Rock Rose NL CS5 BV, covering an area of ~2120 km^2 with an average water depth of 35 m (Fig. 2.5). Inline and crossline spacings of the seismic data are 25 m, as they have been processed with a 25×25 m bin size. Stratigraphic and P-wave velocity (V_p) data, obtained from boreholes tied to discrete seismic reflections, reveal a minimum vertical resolution (λ/4) ~40 m below the main salt unit in the study area, and ~12 m in the shallowest Cenozoic strata. The seismic data are zero-phased and displayed using the European SEG polarity convention, in which an increase in acoustic impedance is shown as a red seismic reflection, while a decrease in acoustic impedance coincides with black seismic reflections.

Forty-eight (48) wells are located in the study area, providing Gamma Ray (GR), Lithology, Density (RHOB), Sonic (DT) and Bottom-hole temperature (BHT) data. Most wells penetrate strata ranging from the Carboniferous (Limburg Group) to the Quaternary (North Sea Group). Well correlations are completed in this study area to identify lithological variations and establish a chronostratigraphic framework for the interpreted seismic-stratigraphic units (Fig. 3.2).

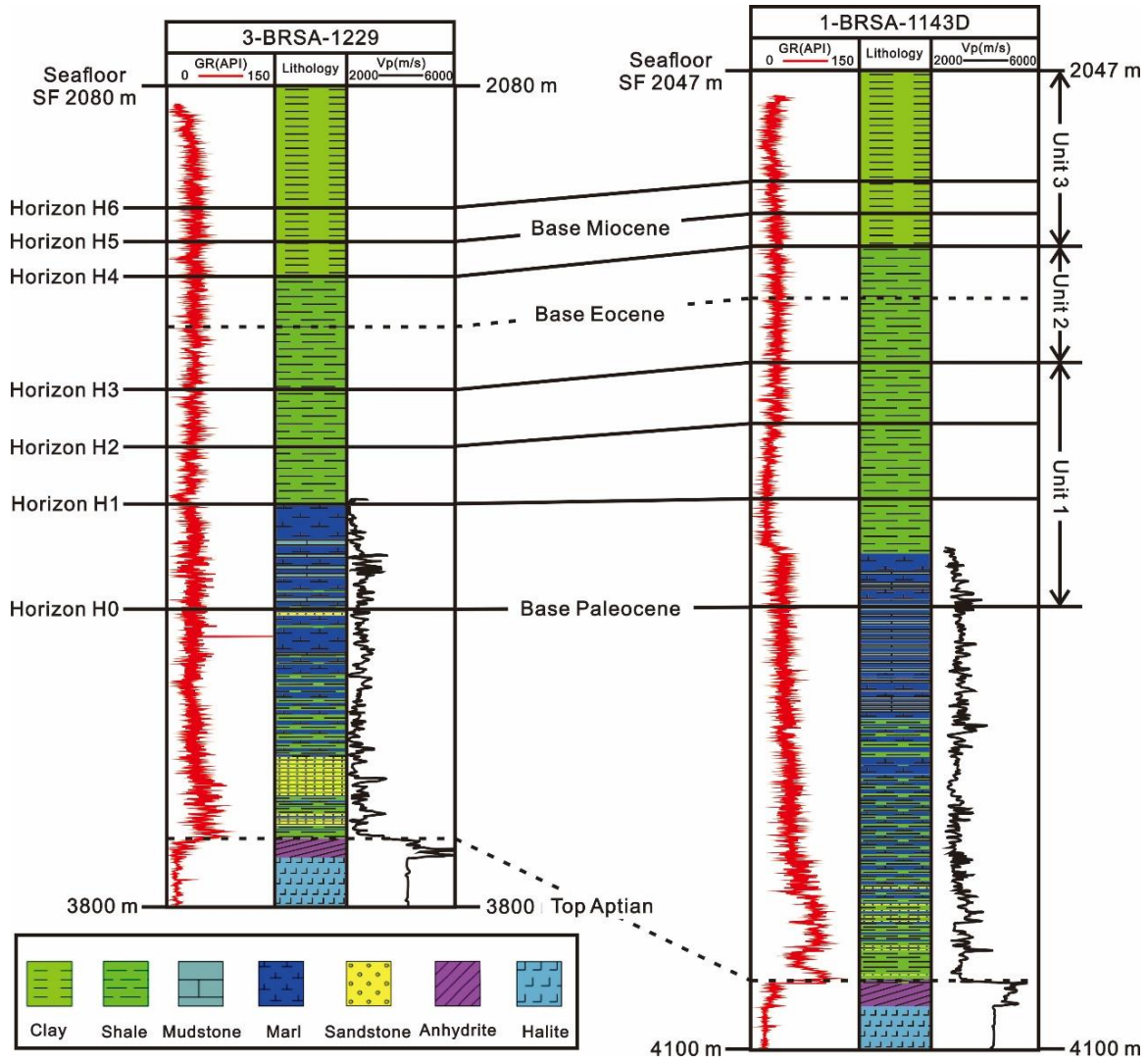

Fig. 3.1. Well profile correlation for Wells 3-BRSA-1229 and 1-BRSA-1143D located near the study area. Chronostratigraphic framework, lithology, gamma-ray (GR) and V_p (p-wave velocity) wireline curves are shown. Note this figure is a part of research result in Chapter 4.

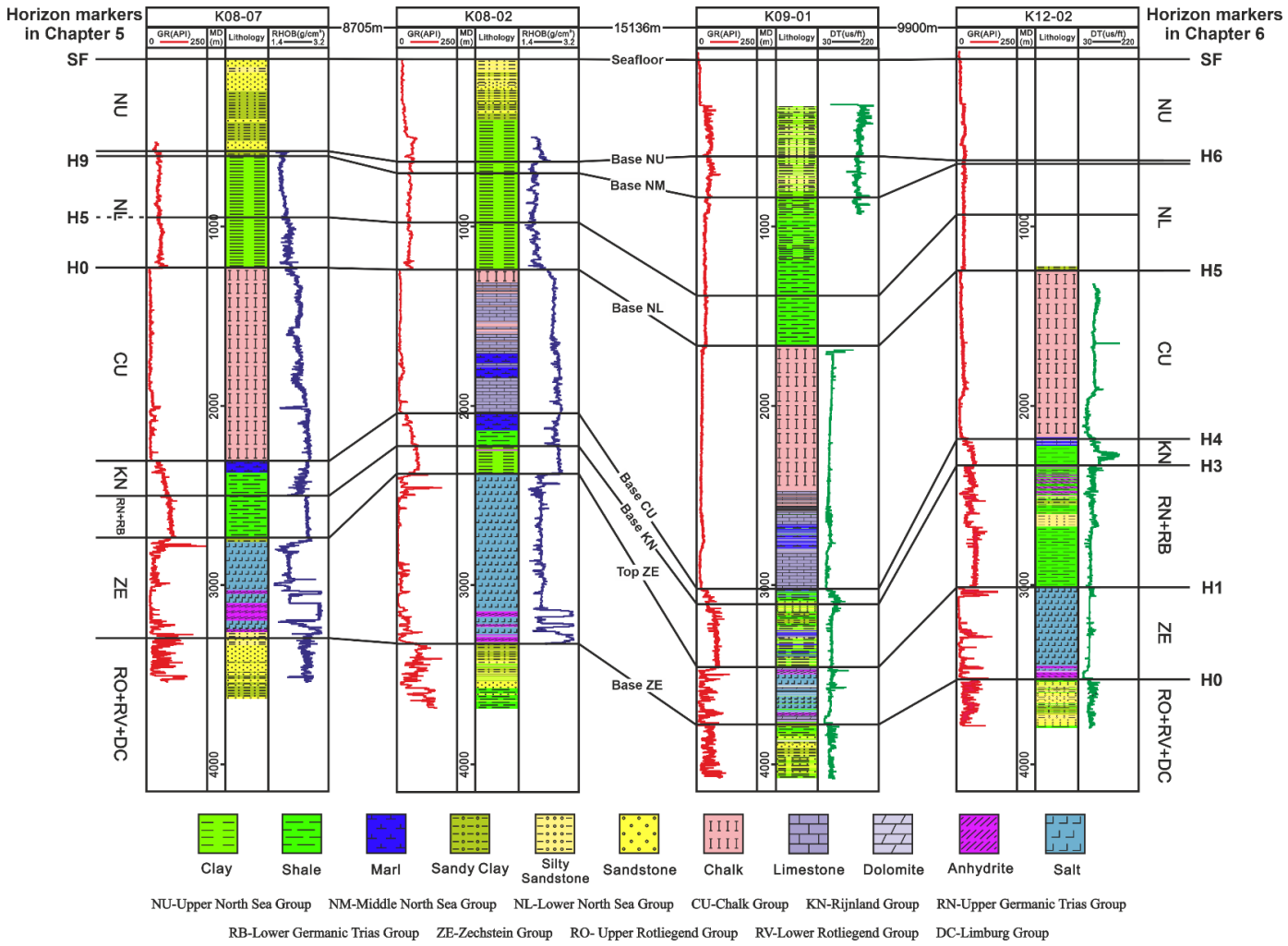

Fig. 3.2. Stratigraphic correlation for wells K08-07, K08-02, K09-01 and K12-02 located in the study area. Stratigraphic framework, lithology, gamma-ray (GR), density (RHOB) and sonic log (DT) wireline curves are shown, and horizon markers in Chapters 5 and 6 are indicated. Note this figure is a part of the research results provided in Chapters 5 and 6.

3.3 Seismic data interpretation

Seismic data interpretation in this thesis is entirely completed on Schlumberger Petrel 2019. The methods used to interpret faults and horizons in the study area are described below, and main seismic attributes used to reveal key geological features are also introduced.

3.3.1 Horizon and fault interpretation

A number of seismic reflections were mapped as horizons representing stratigraphic boundaries in the two study areas. Horizons interpreted in Chapters 4, 5 and 6 were correlated with industry wells drilled in/around the study areas, and the process that is known as well tie to seismic has been finished by using check-shot data recorded on wells. Key horizons were first manually interpreted along the inline and crossline directions, and the spacing chosen to interpret each horizon varied according to the complexity of specific areas. In the areas with laterally continuous reflections, the horizons were mapped using a 20- to 10-line spacing. In the areas of high structural complexity such as those affected by halokinesis, the horizons were mapped using spacing that ranges from 2 to 5 lines.

Automatic horizon tracking was used to interpret horizons, considering the manually picked seismic reflections as seed points. The auto-tracking (or auto-picking) option on Petrel 2019 involves the algorithm operation that tracks reflections with similar features in terms of phase and amplitude in surrounding seismic traces. The 3D auto-tracking is occasionally interrupted by changes in seismic attributes, which could be associated with faults, fluid low and stratigraphic unconformities. Hence, manual checking and constant edits of the auto tracked horizons are thus necessary to establish a locally continuous and reliable stratigraphic framework (Hart, 1999).

Faults were interpreted along inlines, crosslines and arbitrary lines, and they were interpreted using different line spacing depending on the nature and complexity of the investigated structures. The line spacing most frequently adopted were 2, 4 and 10, and a tight spacing is used to provide reliable displacement analyses for selected faults. The number of fault sticks for each fault varied according to its length, but there are at least three fault sticks for each interpreted fault.

3.3.2 Seismic attribute analyses

Volume and surface seismic attributes are used to visualise and constrain interpretations in three dimensions on structural and stratigraphic studies. A wide variety of seismic attributes are available in Petrel®, and in this thesis several seismic attributes, especially variance attribute, were used and were described below.

Variance (or coherence): Variance is a measure of the waveform similarity, recording how similar a given trace is to its neighbouring trace. Similar traces are mapped as low variance values, while discontinuities have high variance values (Brown, 2011). The variance attribute highlights irregularities such as faults, depressions, chaotic pipe interiors and salt walls.

Isochron maps: They are also known as thickness maps, recording the time difference between two given horizons or surfaces. They are key in this thesis for showing the thickness variation of seismic units in the study areas.

Ant tracking: It is developed based on the concept of ant colony systems to determine discontinuities such as faults in 3D seismic data. This attribute uses the principles of swarm intelligence, which explains the collective behaviour of social insects in finding the shortest path between the nest and a food by communicating via a chemical substance known as Pheromone (Ngeri et al., 2015).

3.4 Well data: Interpretation and data provided

Well data analysis in this thesis mainly includes the well correlation and bottom-hole temperatures correction, which are described in detail below.

3.4.1 Well correlation profiles

Well correlation is an important process that involves establishing the relationship between different subsurface rock layers or formation encountered in wells. Two well correlation profiles are mapped in two study areas (Figs. 3.1 and 3.2), helping to identify the vertical and lateral extent of various stratigraphic formations. In more detail, well correlation profile in Chapter 4 was plotted by using two wells, and their complete well profiles were provided by the Brazil oil company - Petrobras, including lithology and its corresponding Gamma-Ray

curves. P-wave curve was calculated and plotted by the colleague Cerys Biancardi on Rok-Doc®, providing the information about rock properties. Later, the stratigraphic boundaries were identified on wells based on lithology variations, and two wells correlation was finished on CorelDRAW®. Similarly, the well correlation profile in Chapters 5 and 6 was mapped by using four wells, and well data and profiles were available on the websites of Dutch Oil and Gas portal (DLOG). Finally, the well correlation profile was also finished on CorelDRAW®, helping to establish the chronostratigraphic framework.

3.4.2 Bottom-hole temperatures (BHTs) correction

Bottom-hole temperature recorded on log-headers can be unreliable, but they are often used to constrain the subsurface thermal regime due to the absence of better-quality data. Hence, BHTs must be corrected to suggest the real subsurface temperature regime. In this thesis, three correction methods provided by ZetaWare, Inc (Corrigan, 2003) were applied, depending on the type of information available. The Horner correction can be used when three of more self-consistent BHTs from a given depth are available, with this correction involving the plotting of BTHs in a given well vs. time (Chapman et al., 1984). Based on a study of 983 BHT and associated equilibrium temperature estimates (T_{eq}), the T_{eq} uncertainty (1 sigma) using the Horner correction is ± 8°C (Corrigan, 1997). Time-Since-Circulation corrections are suggested when time-since-circulation information is available but deemed unsuitable for the Horner correction (Corrigan, 2003). With the Time-Since-Circulation correction, uncertainty in T_{eq} estimates (1 sigma) is in the order of ± 6-12 °C with a post-circulation time of 10 hours, decreasing to ± 3-6°C with a post-circulation time of 30 hours (Corrigan, 2003). When only BHTs are available with no time-since-circulation information, a Last-Resort correction is recommended by simply adding 18°C to the original temperatures (Corrigan, 2003). For the Last-Resort correction, the expected T_{eq} uncertainty is ± 9°C (Corrigan, 2003). Based on the T_{eq} uncertainty caused due to three correction methods, the Horner correction for BHTs performs better than the Time-Since-Circulation correction. The Time-Since-Circulation correction for BHTs has a lower uncertainty in T_{eq} than the Last-Resort correction. Thus, the Horner correction for BHTs is chosen over the Time-Since-Circulation correction, and the latter is chosen over the Last-Resort correction.

3.5 Structural analyses

After the interpretation of faults on the seismic profiles on Petrel®, faults were imported into Move® as fault 3D surfaces that consist of fault-point data. These fault-point data were received by discretising faults interpreted into facets, and time-depth conversions were implemented for these data on Move® (See 3D depth conversion on Move® tutorial). Key fault attributes, including dip, strike and azimuth were calculated on Move® for each fault vertex using the Attribute Analyser Toolbar. Later, fault surfaces were imported into stress analysis module for stress modelling. In addition, fault displacement -length, fault displacement-depth and stress analyses were completed in this thesis.

3.5.1 Fault displacement vs. length and depth analyses

The relationship between maximum displacement (D_{max}) and length (L) of a fault trace provides key insights into the mechanisms of fault initiation, growth and evolution through time (Watterson, 1986; Walsh and Watterson, 1988; Peacock and Sanderson, 1991; Cowie and Scholz, 1992a; Kim and Sanderson, 2005). In parallel, the relationship between fault displacement (D) and depth (Z) provides insights into fault reactivation and a fault's nucleation position (Mansfield and Cartwright, 1996; Cartwright and Mansfield, 1998; Baudon and Cartwright, 2008a, b). In this thesis, fault displacement was calculated using trigonometry rules to discern the throw and heave for a fault (Fig. 3.3), considering the fault as a pure dip-slip fault. Throw and heave were measured at cut-off horizons for selected faults on Petrel®, and the measurement complies with the minimum sampling interval defined in Tao and Alves (2019). The latter authors proposed that minimum throw/displacement sampling intervals are related to the length of a fault; sampling intervals should be less than 5% of the fault length when the latter is < 3500 m, or 3% of the fault length when this is > 3500 m (Ze and Alves, 2019). After the measurement, displacement data originally gathered in two-way travel time were converted to meters by using time-depth data. Plots of maximum displacement (D_{max}) against length (L) and depth (Z) for the selected faults in each study case were then compared to previous published data for normal, strike-slip and reverse faults (e.g. Kim et al., 2005).

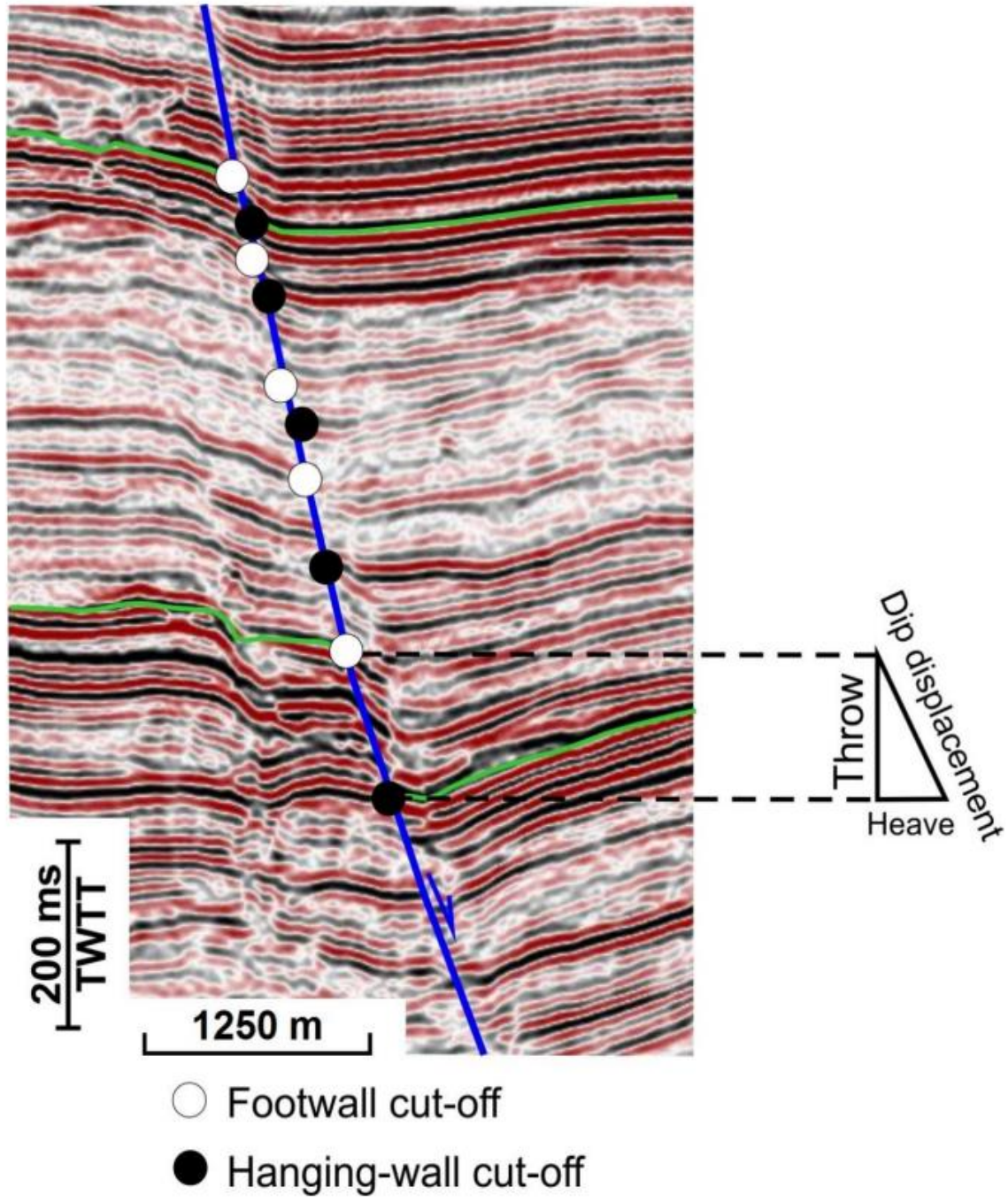

Fig. 3.3. Seismic example illustrating the technique used to measure the throw and heave by the difference between footwall (represented by the white dots) and hanging-wall (represented by black dots) cut-offs. Dip displacement is calculated using trigonometry rules that take into account the throw and heave of a fault. Figure from Mattos (2017).

3.5.2 Stress analysis

Stress inversions were applied in Chapters 4 and 5 to estimate palaeostress tensors from faults interpreted in each study area. Such a method relies on the basic assumption that slip on each fault plane occurs in the direction of maximum resolved regional shear stress (Pollard et al., 1993), and was completed using the Stress Analysis Module on Move®. This module is based on the direct inversion method of Angelier (1990), and uses dip-slip data of the interpreted faults, including dip and dip azimuth. It is important to note that stress inversions for the faults interpreted in this thesis were applied by assuming all interpreted faults as dip-slip faults, indicating that stress inversion results may not be the true palaeostress state.

Slip tendency and leakage factors computed in Chapter 4 on Move's® Stress Analysis Module also used the palaeostress azimuths obtained from stress inversions. Normalised leakage factors values were calculated, estimating favourable fluid pathways. As the palaeostress tensors obtained from stress inversion are not those representing the present-day stress regime, the slip tendency and leakage factor results in Chapter 4 have certain limitations, and do not fully indicate the most favourable fluid pathways at present. However, they represent the stresses that generated the interpreted faults, and highlight any changes in the azimuth of such stresses in time and space.

Slip tendency (T_s) indicates the likelihood of a fault to slip, and is defined as the ratio of resolved shear (τ) to normal stress (σ_n) (Equation 3.3; Morris et al., 1996; Lisle and Srivastava, 2004). It has no units and ranges from 0 to 1, where higher values indicate a higher likelihood of a fault to slip. It is dependent on the differential stress ratio and on the orientation of the fault surface in relation to the orientation of a given stress field. Therefore, the slip tendency can be expressed as:

$$T_s = \tau / \sigma_n \qquad \text{Equation 3.1}$$

Leakage factor (L) is a measure of the fluid transmissivity of faults and is defined as the ratio of pore pressure (Pp) to the difference between normal (σ_n) and shear stresses (τ) on a particular fault surface (Equation 3.4; see stress analysis on Move® tutorial). Normalised leakage factor represents the ratio of leakage factor to the maximum value of leakage factor from a set of faults. Pore pressure used in this study is the normal hydrostatic pressure calculated

based on the depth at which the fault have first nucleated. Leakage factor determines the likelihood of fault-seal failure; the higher the value, the greater the likelihood of a fault to act as a pathway for fluid. Therefore, the leakage factor can be written as:

$$L=P_p/(\sigma_n - \tau) \qquad \text{Equation 3.2}$$

Chapter 4

Fault analysis of a salt minibasin offshore Espírito Santo, SE Brazil

4 Fault analysis of a salt minibasin offshore Espírito Santo, SE Brazil

4.1 Abstract

High-quality 3D seismic reflection and well data are used to investigate the distribution, evolution history and significance of tectonic faulting in a salt minibasin offshore Espírito Santo, SE Brazil. Displacement-length (D_{max}-L) plots, displacement-depth (D-Z) plots and structural maps are compiled to understand the growth history of distinct fault families. Interpreted structures include crestal, corridor, listric and keystone faults. Their geometry, orientation and relative distribution reveal important differences. In detail, listric faults were formed following a NW to WNW strike, and show multiple bright spots and pockmarks around them. The strata into which listric faults sole out have similar seismic, lithological and petrophysical characters to known Cenomanian to Turonian source rocks, which comprise shales and marls with high gamma-ray values. Low-amplitude to transparent seismic facies further indicate the presence of ductile, highly likely organic-rich shales and marls. As a result, three evolutionary stages can be identified: a) Stage 1 is characterised by the formation of NW- or WNW-striking listric faults, keystone faults and the onset of reactive diapirism; b) Stages 2 and 3 record active diapirism due to a relative increase in sediment loading, documenting the formation of many crestal, corridor and keystone faults. Normalised leakage factor analyses reveal keystone faults to be the most favourable pathways to fluid migrating in the investigated salt minibasin. Conversely, listric faults are likely to form barriers and baffles to fluid in their lower parts.

4.2 Introduction

Salt minibasins are small basins, or depressions, surrounded by upwelling salt whose movement is dependent on the loading of synkinematic strata onto relatively thick evaporite successions (Jackson and Talbot, 1986; Jackson and Hudec, 2017). This forms a feedback loop between continuous sedimentation in salt minibasins and halokinesis. Primary and secondary minibasins are two fundamental types of basins identified in such settings, resting either on autochthonous or allochthonous salt, or on an equivalent salt weld. Consequently, secondary

minibasins do not contain the oldest supra-salt stratigraphy that marks the early stages of halokinesis (Pilcher et al., 2011; Jackson and Hudec, 2017).

An important aspect is that distinct fault families may occur around salt minibasins, with their geometry, orientation and distribution being closely related to the growth of a minibasin *per se* (Lopez, 1990; Rowan et al., 1999). For example, crestal faults are commonly developed above salt structures that surround minibasins, and they usually form planar growth faults rooting into the crests of diapirs, generating symmetric grabens above the latter (Rowan et al., 1999; van den Berg et al., 2004). In parallel, corridor faults pertain to faults generated above buried salt pillows, observed to connect discrete, but distant, salt structures. Corridor faults are often planar and comprise structural corridors that are preferential pathways for fluid (Mattos and Alves, 2018). Listric faults are another type commonly observed in salt minibasins (Lopez, 1990; Diegel et al., 1995; Rowan et al., 1999). Their dip becomes gentler with depth, resulting in their characteristic concave-upwards shape (e.g. Bally et al., 1981; Shelton, 1984; Imber et al., 2003). The generation of listric faults in salt minibasins is commonly associated with viscous or ductile layers at depth (Shelton, 1984; Dula Jr, 1991; Imber et al., 2003; Brun and Mauduit, 2008; Bose and Mitra, 2009) or, instead, local overpressure build-up due to abnormal pore pressure gradients in faulted stratigraphic intervals (McNeill et al., 1997; Mandl, 1999; Hillis, 2003; Suppe, 2014; Yuan et al., 2020). Sediment compaction also plays an important role in forming listric faults, as these must flatten after they are buried by continued sedimentation, due to sediment compaction (Davison, 1987; Xiao and Suppe, 1989; Cartwright and Lonergan, 1996; Cartwright and Mansfield, 1998). The development of all these fault families in salt minibasins, especially listric faults, is significant for hydrocarbon exploration, fluid-flow characterisation and carbon and energy storage, as they can act as effective fluid pathways or, instead, can form favourable traps for fluid (Rowan et al., 1999; Cox et al., 2001a; Gartrell et al., 2004).

As a typical salt-bearing basin in SE Brazil, the Espírito Santo Basin comprises multiple fault families developed in the vicinity of growing salt structures (Fiduk et al., 2004; Mattos and Alves, 2018). In this same basin, Demercian et al. (1993) and Fiduk et al. (2004) have related the largest listric faults to tectonic extension accommodated on the proximal parts of the margin due to gravitational spreading and gliding of overburden rocks over Aptian salt. Ze and Alves (2016) have shown that relatively small listric faults accommodate strain and stress on the crests of the salt structures. Ze and Alves (2021) have also revealed the existence of fluid flow through strata-bound domino faults in vicinity of the study area, whereas Mattos

(2018) has studied the fault families around salt diapirs to show that fault corridors linking adjacent salt structures are favourable fluid migration pathways. Nevertheless, little is known about the distribution and evolution history of different fault families in large areas of SE Brazil, and the South Atlantic region as a whole.

The aim of this work is to investigate the distribution, evolution history and significance of distinct fault families in a salt minibasin formed in deep-water sectors of the Espírito Santo Basin (Fig. 2.1). This work will also implement stress analyses to the interpreted fault families and indicate the potential fluid flow pathways in salt minibasins. In summary, this work addresses the following research questions:

a) What is the importance of listric faults and their soling out intervals as structures signing the presence of rheologically weak, muddy successions in salt minibasins?

b) What is the chronology of faulting around salt structures when comparing them to other fault families in the Espírito Santo Basin?

c) Which of the interpreted fault families is more favourable to form fluid-flow pathways in salt minibasins?

4.3 Database and chapter-specific methods

The main data for this chapter is a 3D seismic volume from the offshore Espírito Santo Basin, SE Brazil, and two wells (3-BRSA-1229 and 1-BRSA-1143D) located near the seismic volume are also used. For a full description of the seismic and well data, see Section 3.3.1. The seismic interpretation, well correlation and stress analyses applied in this chapter are described in Sections 3.4, 3.5 and 3.6 (Fig. 3.1). It is important to note that the vertical extent is delimited by its bottom boundary at the depth of ~4600 ms. This imposes a limitation on studying salt-related faults, as a greater depth range would have provided a better opportunity to map salt structures and sub-salt stratigraphic units, study the spatial and temporal evolution of salt structures, and analyse the development of sub-salt faults.

The study area comprises a 20 km long, 6 km wide, NE-striking salt minibasin bounded to the west by two salt diapirs (A and B), and by a salt wall to the east (Fig. 4.1). Eight (8) key seismic-stratigraphic reflections, including the seafloor, were interpreted every ten lines (125 m) in seismic volume (Fig. 4.2-4.5). Three principal stratigraphic units were defined based on their internal seismic reflection characters, bounding reflection terminations, and their

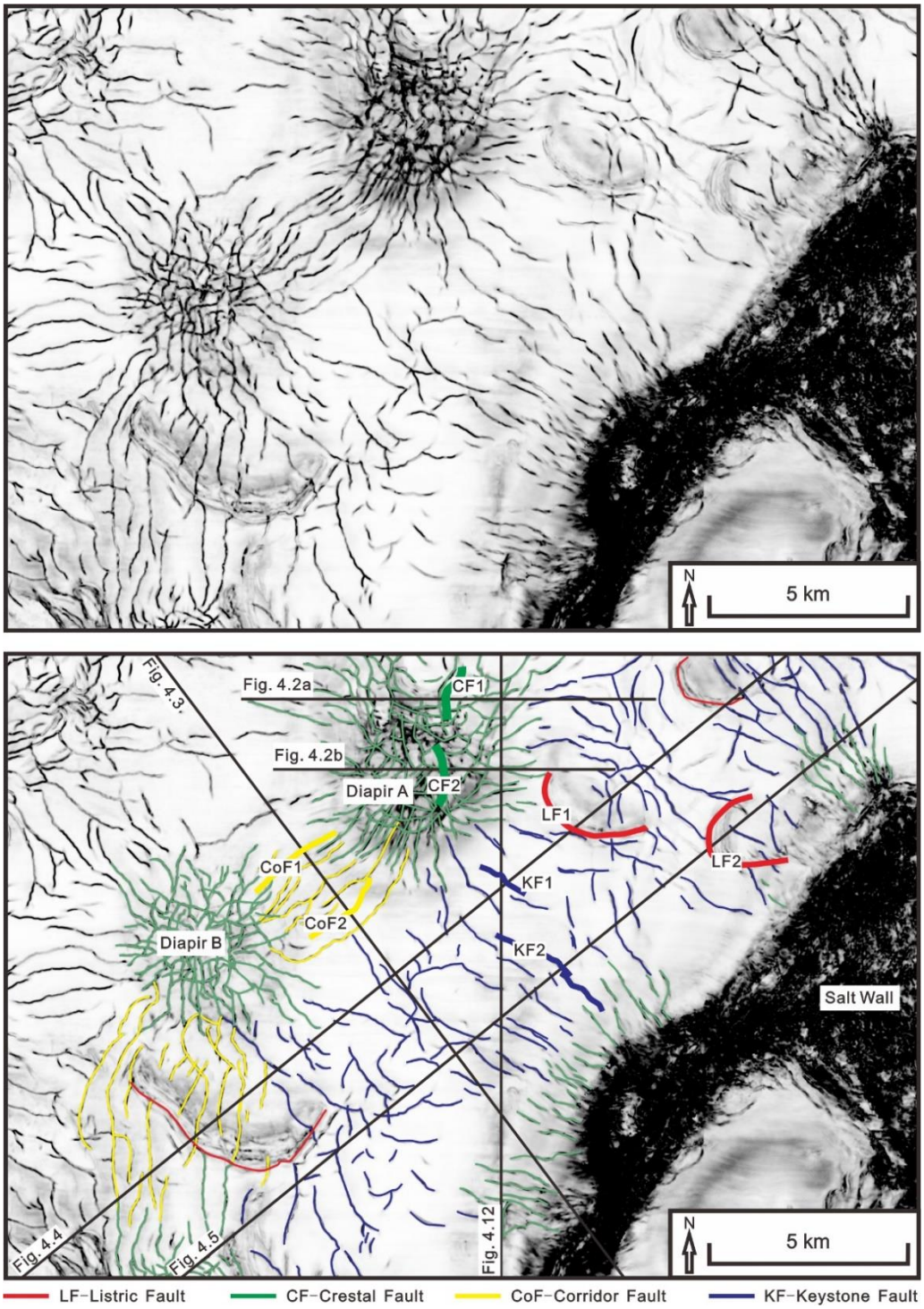

Fig. 4.1. Variance time-slice (Z=-3000 ms two-way time) of the study area highlighting the four fault families and salt structures interpreted in this Chapter. Red, green, yellow, and blue lines indicate listric faults (LFs), crestal faults (CFs), corridor faults (CoFs), and keystone faults (KFs). The seismic profiles shown in Figs. 4.2-4.5 and 4.12 are shown by thin black lines. Eight representative faults from four fault families, shown with bold lines, were selected to carry out displacement-depth (D-Z) and displacement-length (D_{max}-L) analyses (see Figs. 4.8-4.11).

relationship with main structural features. Variance time-slices were used to identify relevant fault families around salt structures (Fig. 4.1).

Eight representative faults from the four interpreted fault families were selected to compile displacement-length along fault (D_{max}-L) and displacement-depth (D-Z) plots, which were used to evaluate fault growth history in the investigated minibasin. In addition, stress inversions were completed to estimate the orientation and distribution of palaeostress tensors responsible for the formation of each fault family observed in the study area, with the exception of listric faults. Listric and keystone faults were formed under the same stress field in the minibasin, suggesting that the palaeostress tensors obtained from keystone faults can be applied to listric faults. Furthermore, slip tendency and leakage factors were also computed to indicate the likelihood of slip and estimate favourable fluid pathways amongst the four fault families.

4.4 Seismic stratigraphy

4.4.1 Unit 1 (horizons H0 to H3)

Unit 1 is the primary seismic interval of interest, comprising a package of low amplitude to transparent seismic reflections somewhat similar to its underlying supra-salt strata (Figs. 4.2-4.5). The base of Unit 1 is marked by horizon H0, a low-to moderate-amplitude negative reflection tied to the base of Paleocene strata, whereas the top of Unit 1 is bounded by a high-amplitude negative reflection defined as horizon H3. Between horizons H0 and H3, two other horizons (H1 and H2) are mapped with moderate-amplitude positive reflections. These two horizons (H1 and H2) divide Unit 1 into three different sub-units, respectively named Unit 1a, 1b and 1c. The seismic amplitude of internal reflections in Unit 1a is slightly higher than in Unit 1b and 1c. Faulting is common inside Unit 1, but most faults do not propagate below its lower boundary (horizon H0). This is likely due to the relatively higher ductility of strata in Unit 1 when compared to the intervals above and below, a character resulting in faults terminating at this level. Unit 1 is up to 600 ms thick in the salt minibasin of interest, but this value decreases slightly towards the flanks of adjacent salt structures (Fig. 4.6).

Unit 1 is composed of shale in its upper part (Unit 1b and 1c) and marl in its lower part (Unit 1a), with varying thickness and relative proportions of shale vs. marl at various locations (Fig. 3.1). Thin mudstone layers occur as intercalations in the essentially marly Unit 1a. Due to lithological changes, gamma-ray values reveal significant variations at depth. Unit 1b and

1c record high gamma-ray values, especially Unit 1c, but they gradually decrease towards the base of Unit 1b. There is an increase in gamma-ray values from Unit 1a to 1b, and this increase correlates with the boundary between shale to marl in well data (e.g., well 1-BRSA-1143D; Fig. 3.1). Unit 1a presents higher gamma-ray values than Units 1b and 1c above, indicating Unit 1a contains a higher volume of shale than these former. In addition, gamma-ray values continue to increase below horizon H0 towards the top of the Aptian salt, although values in Unit 1 are similar to the underlying supra-salt strata (Fig. 3.1).

4.4.2 Unit 2 (horizons H3 to H4)

Unit 2 is bounded at its base by horizon H3, and at the top by horizon H4, a moderate- to high-amplitude positive reflection (Figs. 4.2-4.5). At the middle of Unit 2 there is one high-amplitude negative reflection that correlates with the base of Eocene strata. This unit comprises a 200–500 ms thick package, which is the thickest (~500 ms) in the studied salt minibasin (Fig. 4.6). Unit 2 is the thinnest (~200 ms) above the salt diapirs. The unit shows low-amplitude to transparent seismic reflections in its lower part, but its upper part is marked by moderate-to high-amplitude seismic reflections. Faulting is common, with most faults propagating upwards and downwards into Unit 2.

The lithology of Unit 2 is very similar to the interval between horizon H1 and H3 (Unit 1b and 1c), as both are composed of shale. However, Unit 2 does not show marked changes in lithology and gamma-ray curves remain high and relatively constant (Fig. 3.1).

4.4.3 Unit 3 (horizon H4 to the seafloor)

Unit 3 is bounded at its base by horizon H4, whereas its top coincides with the seafloor. Its thickness ranges from 400 to 800 ms, and shows low-amplitude to transparent internal reflections incised by submarine channels in some areas (Figs. 4.2-4.5). Two other horizons H5 and H6 were interpreted in this unit. Horizon H5 is a high-amplitude positive seismic reflection tied to the base of the Miocene, which is located two reflections above horizon H4. Horizon H6 is a high-amplitude positive reflection under another prominent high-amplitude negative reflection (Figs. 4.2-4.5). Most faults in the study area offset horizons H4 to H6, and many are truncated on their upper tips by mass-transport deposits (MTDs), which mark the remobilisation of seafloor strata due to the influence of gravity forces.

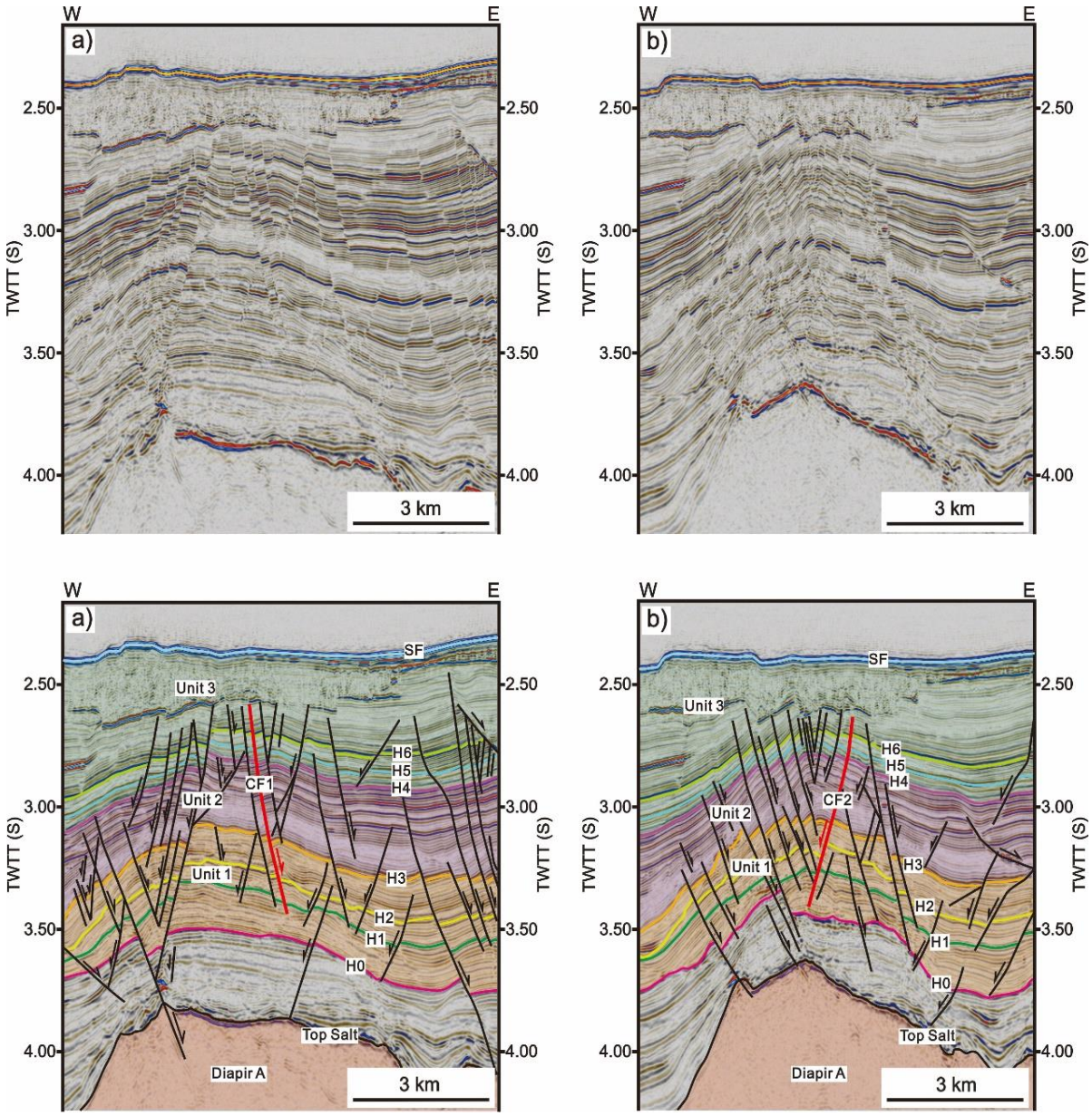

Fig. 4.2. Seismic profiles showing representative crestal faults 1 (CF1) and 2 (CF2) in the study area. Red bold and black lines represent faults, while other coloured lines mark the different seismic-stratigraphic horizons interpreted in the study area. The location of the seismic profile is shown in Fig. 4.1. SF=Seafloor.

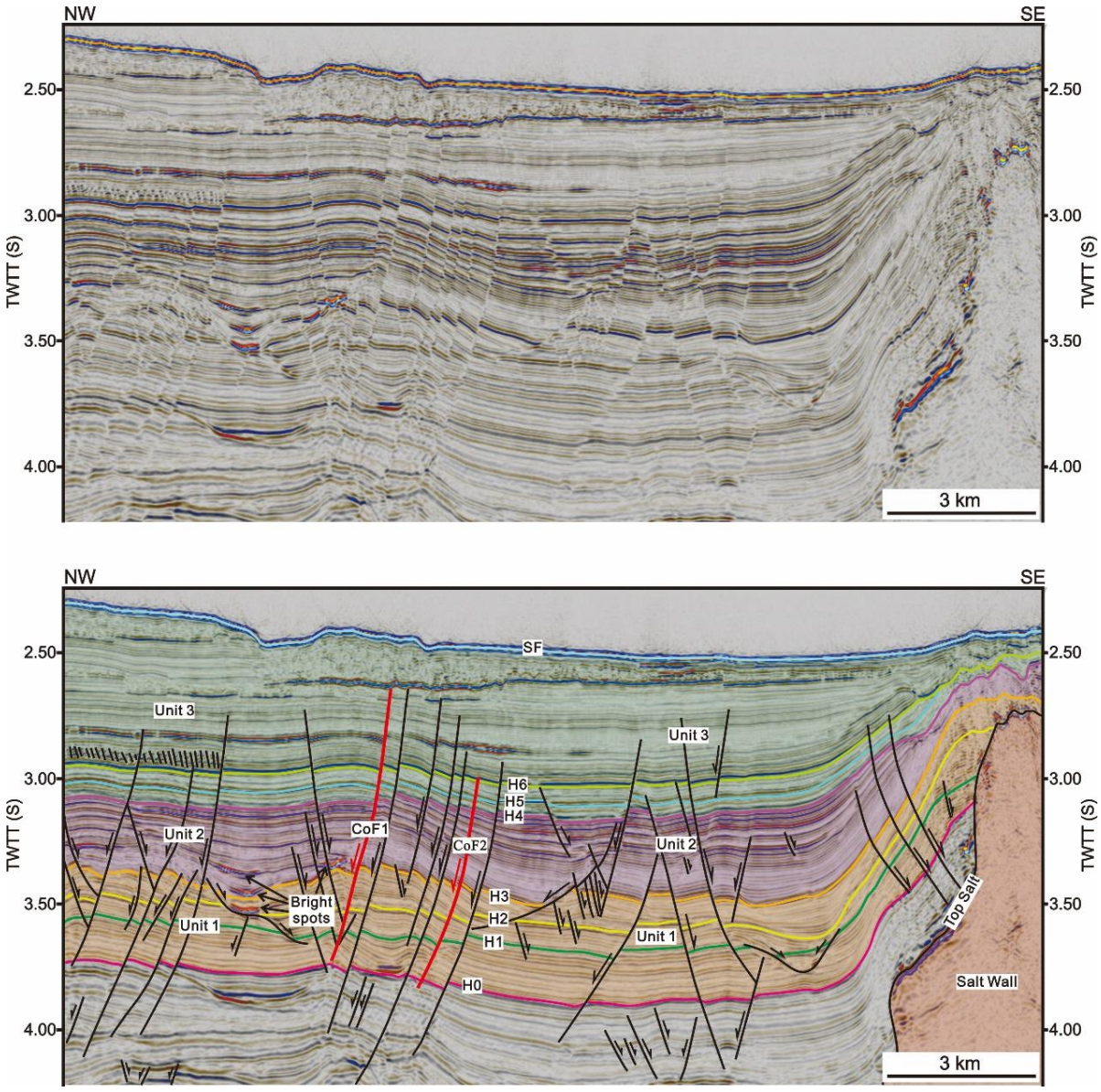

Fig. 4.3. Seismic profiles showing representative corridor faults 1 (CoF1) and 2 (CoF2) in the study area. Red bold and black lines represent faults, while the other coloured lines mark the seismic-stratigraphic horizons interpreted in the study area. Bright spots are indicated in the figure. The location of the seismic profile is shown in Fig. 4.1. SF=Seafloor.

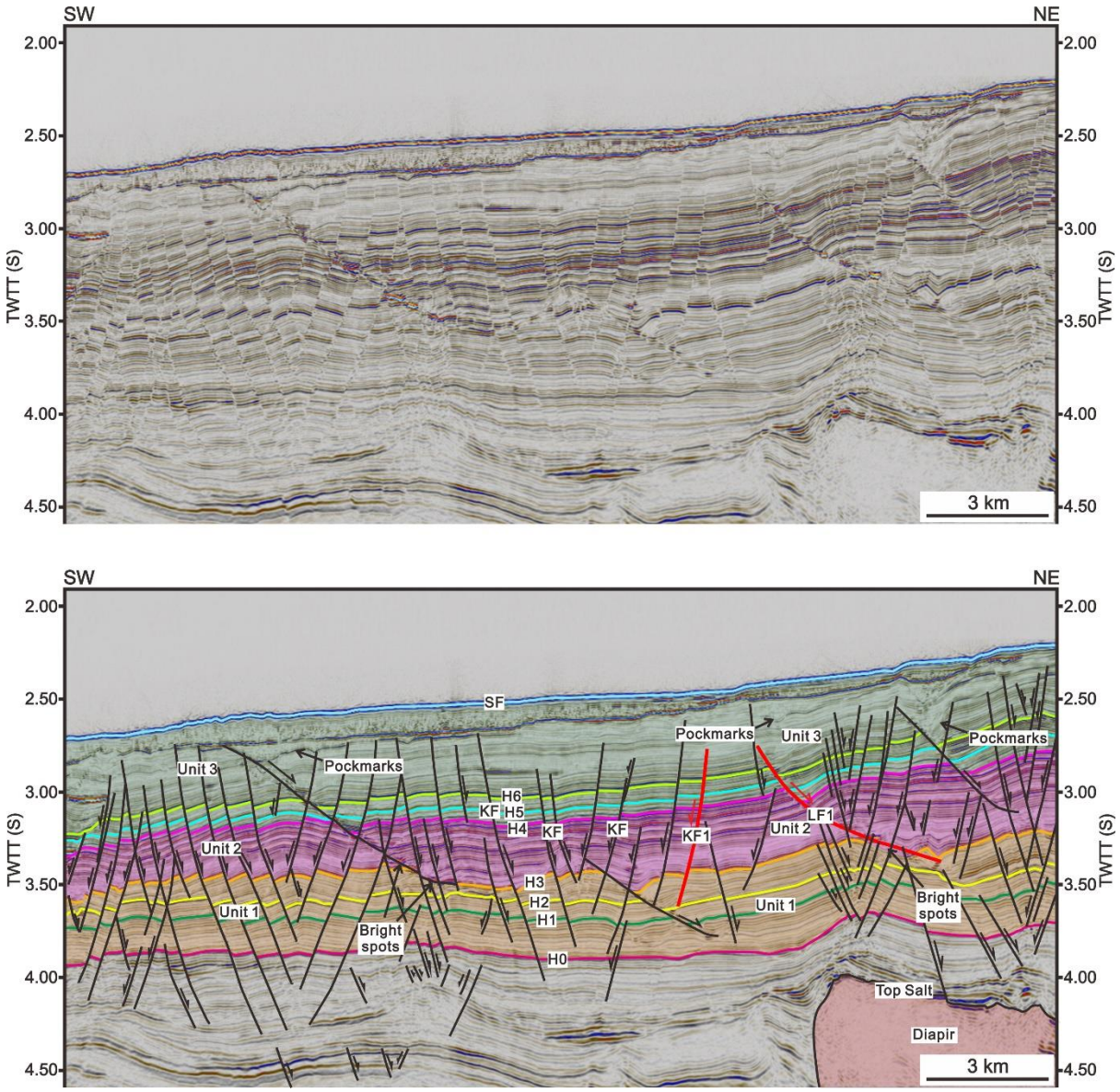

Fig. 4.4. Seismic profiles showing representative listric fault 1 (LF1) and keystone fault 1 (KF1). Red bold and black lines represent faults, while other coloured lines mark the different seismic-stratigraphic horizons interpreted in the study area. Bright spots and pockmarks are indicated in the figure. The location of the seismic profile is shown in Fig. 4.1. SF=Seafloor; KF=Keystone fault.

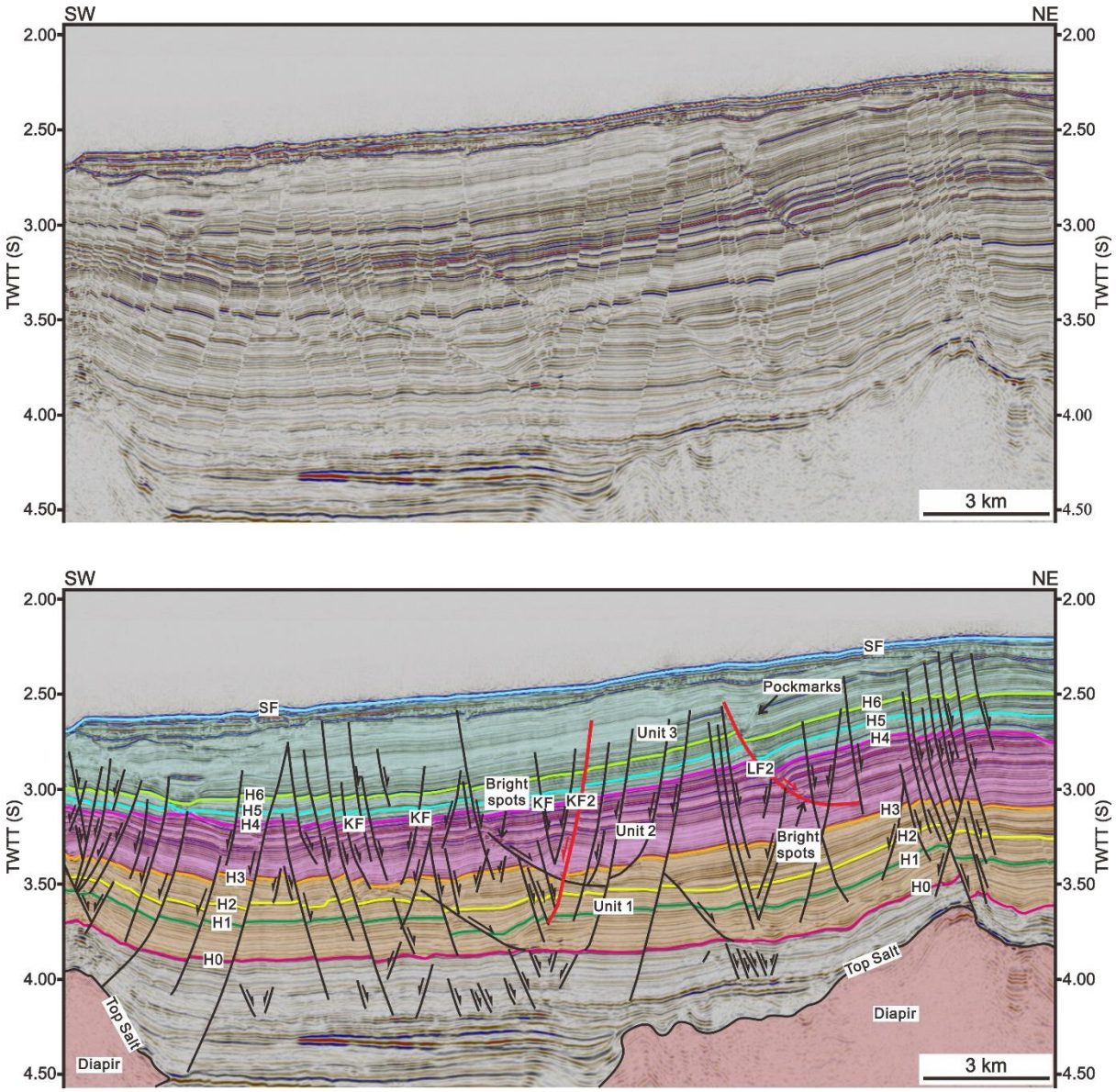

Fig. 4.5. Seismic profiles showing representative listric fault 2 (LF2) and keystone fault 2 (KF2). Red bold and black lines represent faults, while other coloured lines mark the different seismic-stratigraphic horizons interpreted in the study area. Bright spots and pockmarks are also indicated in the figure. The location of the seismic profile is shown in Fig. 4.1. SF=Sea-floor; KF=Keystone fault.

Unit 3 is mainly composed of clay and shows high, relative constant gamma-ray values in its lower part, especially between horizons H4 and H6 (Fig. 3.1). Its top part comprises a large volume of turbidites, which present relative low gamma-ray values.

4.5 Fault families around salt structures

Faults developed in the study area comprise four (4) fault families based on their geometry, orientation, distribution and relationship with main salt structures: a) crestal faults, b) corridor faults, c) listric faults, and d) keystone faults (Figs. 4.1 and 4.7). Crestal faults include radial and concentric faults developed above salt structures. Corridor faults pertain to faults connecting different salt structures, forming structural corridors that are preferential pathways for fluid (Mattos and Alves, 2018). Keystone faults were formed in the syncline of the salt minibasin in the form of antithetic arrays, forming symmetric extensional grabens between them (Figs. 4.4 and 4.5). Listric faults were also developed in salt minibasins, but their geometries and periods of activity showed significant differences with keystone faults. In this section, eight (8) representative faults were selected from the four fault families to compile displacement-length (D_{max}-L) and displacement-depth (D-Z) plots (Figs. 4.8-4.11). These data are used to evaluate the growth history of faults.

4.5.1 Crestal faults

A total of 239 crestal faults were manually mapped over salt diapir A, which is located in the northern part of the study area (Fig. 4.1). Crestal faults are well developed above this diapir, offsetting horizons H4 to H6 upwards to a depth just below a near-seafloor MTD (Figs. 4.1 and 4.2). Downwards, they terminate in Unit 1 to form graben structures above diapir A (Fig. 4.2). Crestal faults strike towards the NNE and have dips over 42° (Figs. 4.6 and 4.7).

Crestal faults 1 (CF1) and 2 (CF2) are respectively 1.5 km and 1.8 km long, N-striking, but show opposite dips; CF1 dips to the east, while CF2 dips to the west (Fig. 4.2). Their maximum displacement reaches 135 m and 153 m, respectively (Fig. 4.8). Crestal fault CF1 grew by the lateral linkage of distinct segments, as shown by the rugged profile of its D_{max}-L plot. A prominent linkage point is located around the position of Profile e (Fig. 4.8). It is also clear from D-Z data that the maximum displacement of CF1 occurs around horizon H3, with a

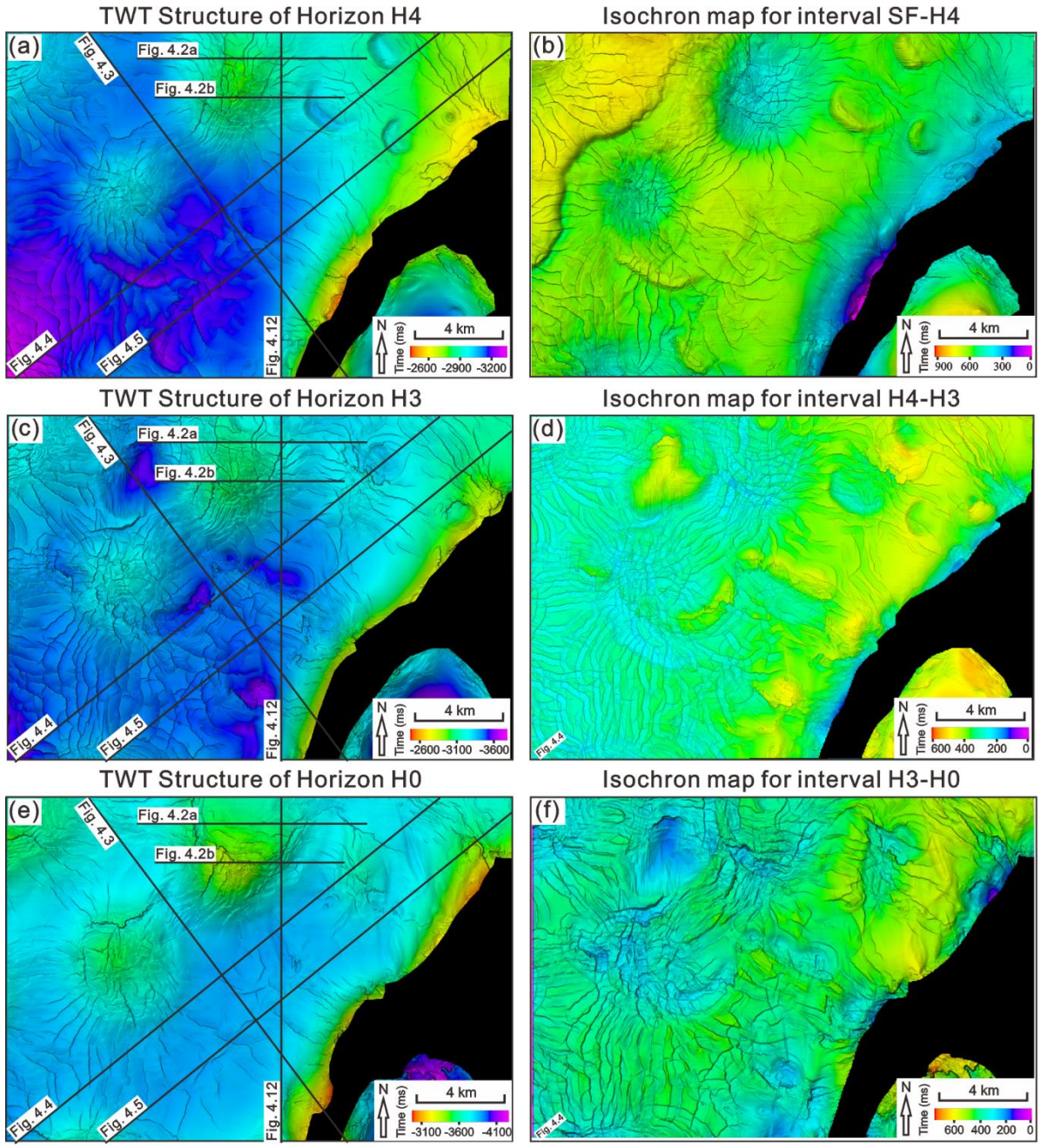

Fig. 4.6. TWT structural and isochron maps for representative horizons and intervals in the study area. a), c), and e) TWT structure of horizons H4, H3, and H0, respectively. b), d), and f) Isochron maps for intervals between the SF (seafloor) and horizon H4, between horizons H4 and H3, and between horizons H3 and H0.

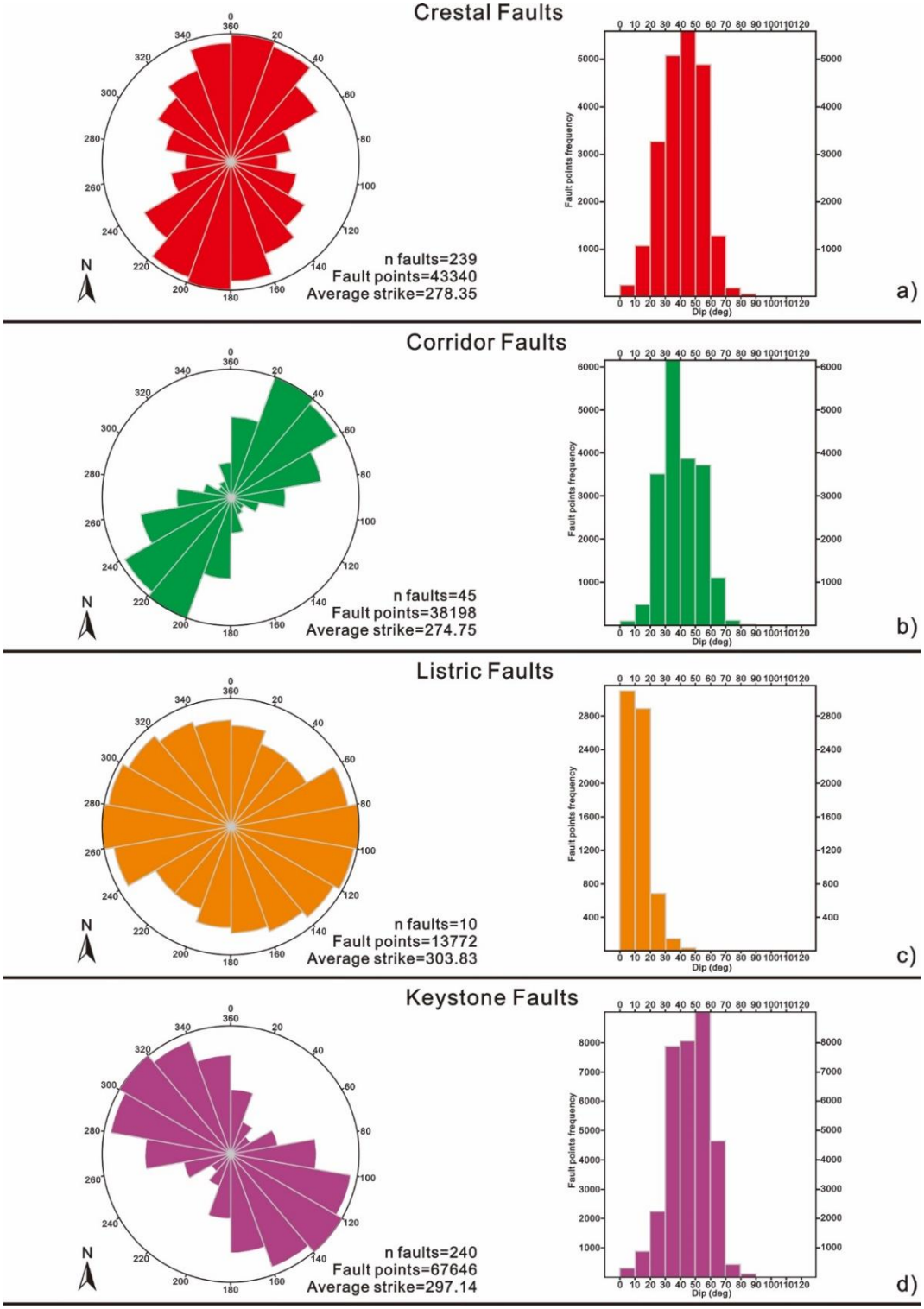

Fig. 4.7. Rose diagrams and histograms of strike and dip for each fault family in the study area plotted by using fault-point data. Crestal faults are predominantly NNE-striking and their dips range from 22.6º to 58.7º. Corridor faults are NE-striking and their dips vary from 23.8º to 58.2º. Listric faults are mainly NW-striking, but their dips range from 2.3º to 22.9º. Keystone faults are NW-striking with dips varying from 29.7º to 64.0º. Note the radius value of the rose diagram is plotted as a ratio of equal area.

decrease in displacement occurring between horizons H3 and H4 (Fig. 4.8). This suggests fault reactivation during the deposition of Unit 2.

Crestal fault CF2 is an isolated fault revealing a rugged 'C' type in D_{max}-L data (Fig. 4.8b). However, similarly to CF1, it shows multiple displacement minima values in its T-Z plots, implying that it was likely to be formed by dip linkage. The maximum displacement of CF2 occurs below horizon H3, showing that it first nucleated at this depth (Fig. 4.8). Interestingly, there are marked drops in displacement from 110 m to 32 m around horizon H3 at the position of profile g (Fig. 4.8g), suggesting that fault reactivation occurred at this level.

4.5.2 Corridor faults

Forty-five (45) corridor faults were recognised in the region between salt diapirs A and B, in the northwest part of the study area (Fig. 4.1). Corridor faults are NE-striking, with dips over 39°, and offset strata between horizons H1 to H6 (Figs. 4.3 and 4.7). Some of the largest corridor faults also offset strata at horizon H0 and below (Fig. 4.3). They strike in a similar direction to the radial faults formed between diapirs A and B (Fig. 4.1).

Corridor faults 1 (CoF1) and 2 (CoF2) were chosen as representative corridor faults in the study area (Fig. 4.1). They are 2.5 km and 2.2 km long and dip to the northwest, with displacement maxima of 97 m and 99 m, respectively (Fig. 4.9). CoF1 offsets strata at horizon H1 and terminates below the near-seafloor MTDs, while CoF2 offsets strata between H0 and H6. Both faults are single, isolated faults, as they have typical 'C-type' profiles in D_{max}-L plots (Fig. 4.9). Their displacement maxima mainly occur around horizon H3, indicating they are likely to nucleate around horizon H3. In addition, both faults record a decrease in displacement between horizons H3 and H4 (Fig. 4.9). This suggests that fault reactivation occurred at the level of Unit 2.

4.5.3 Listric faults

Ten (10) listric faults were mapped as NW- to WNW-striking structures dipping to the northeast (Figs. 4.1, 4.4, 4.5 and 4.6). In plan-view, listric faults are curved, show variable lengths, and are cross-cut by adjacent faults (Fig. 4.6). On vertical seismic profiles, they are steep in their upper part but gradually sole out into Unit 1 (Figs. 4.4 and 4.5). Their dip ranges from 2° to 23° (Fig. 4.7), as they are gentler than the other fault families. Most listric faults are

growth faults, i.e. they show thickening in strata adjacent to hanging-wall depocenters, a character that can be used to indicate their relative ages (Childs et al., 2003; Childs et al., 2017). Listric faults also reveal larger displacements when compared to the other fault families; they can be interpreted as structures accommodating extension along a NE-SW direction (Figs. 4.6 and 4.10).

Representative listric faults 1 (LF1) and 2 (LF2) are 2.4 km and 3.2 km long, with displacement maxima of 1254 m and 717 m, respectively (Fig. 4.10). They offset strata between horizons H4 and H6, soling out in the uppermost part of Unit 1 (Figs. 4.4, 4.5 and 4.10). Both listric faults are offset by other faults, especially LF1, indicating they were formed earlier than the faults that offset them. Because of these offsetting faults, LF1 and LF2 show rugged shapes in their D_{max}-L plots (Fig. 4.10). For instance, the marked displacement minima recorded between horizons H3 and H4 in D-Z profiles were likely to be caused by younger faults offsetting them (Fig. 4.10). Displacement maxima in both LF1 and LF2 are recorded below horizon H4, implying that the two faults nucleated below the latter horizon (Fig. 4.10). Interestingly, the positions of displacement maxima are recorded close to the listric faults' lower tips (Fig. 4.10), indicating they were not formed by the linkage between a steeply dipping fault and a gently dipping detachment. They nucleated around their lower tips, and propagated upwards (with minor downward propagation) to generate their present-day curvature.

4.5.4 Keystone faults

Two-hundred and forty (240) keystone faults were mapped in the salt minibasin of interest, and they offset variable strata spanning horizons H0 to H6 (Figs. 4.4 and 4.5). Keystone faults are mainly NW-striking, relatively steep (>46.8°), with a few NE-striking faults occurring in the southern part of the minibasin (Fig. 4.5).

Keystone faults 1 (KF1) and 2 (KF2) were chosen as representative faults in this work. They are 1.4 km and 3.1 km long, with displacement maxima of 114 m and 110 m, respectively (Fig. 4.11). Both faults strike to the NW and dip to the southwest; they are also relatively steep and offset strata between horizons H1 to H6 (Figs. 4.4 and 4.5). KF1 records a displacement maximum around horizon H3 (Fig. 4.11), indicating that it first nucleated at this level. There are also significant displacement minima below horizon H4 (Fig. 4.11f), suggesting KF1 might have experienced some degree of reactivation at this level. KF2 is formed by lateral segment

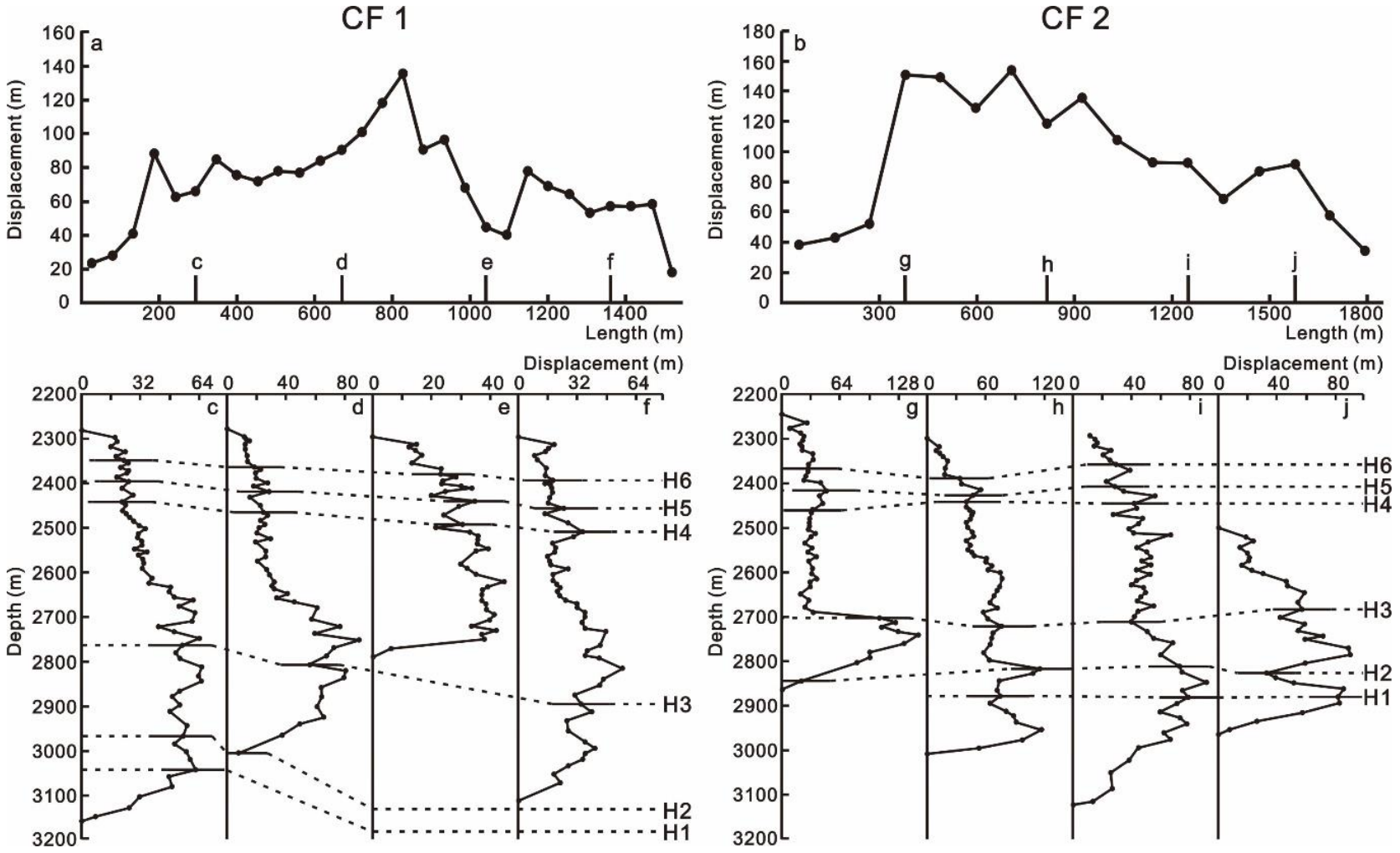

Fig. 4.8. Displacement-length along fault (D_{max}-L) and displacement-depth (D-Z) plots of crestal faults 1 (CF 1) and 2 (CF 2) highlighted in Figs. 4.1 and 4.2. The vertical lines c-j in the D-L plots above indicate the location of the D-Z plots shown below. The dashed lines mark the seismic-stratigraphic horizons interpreted in this study.

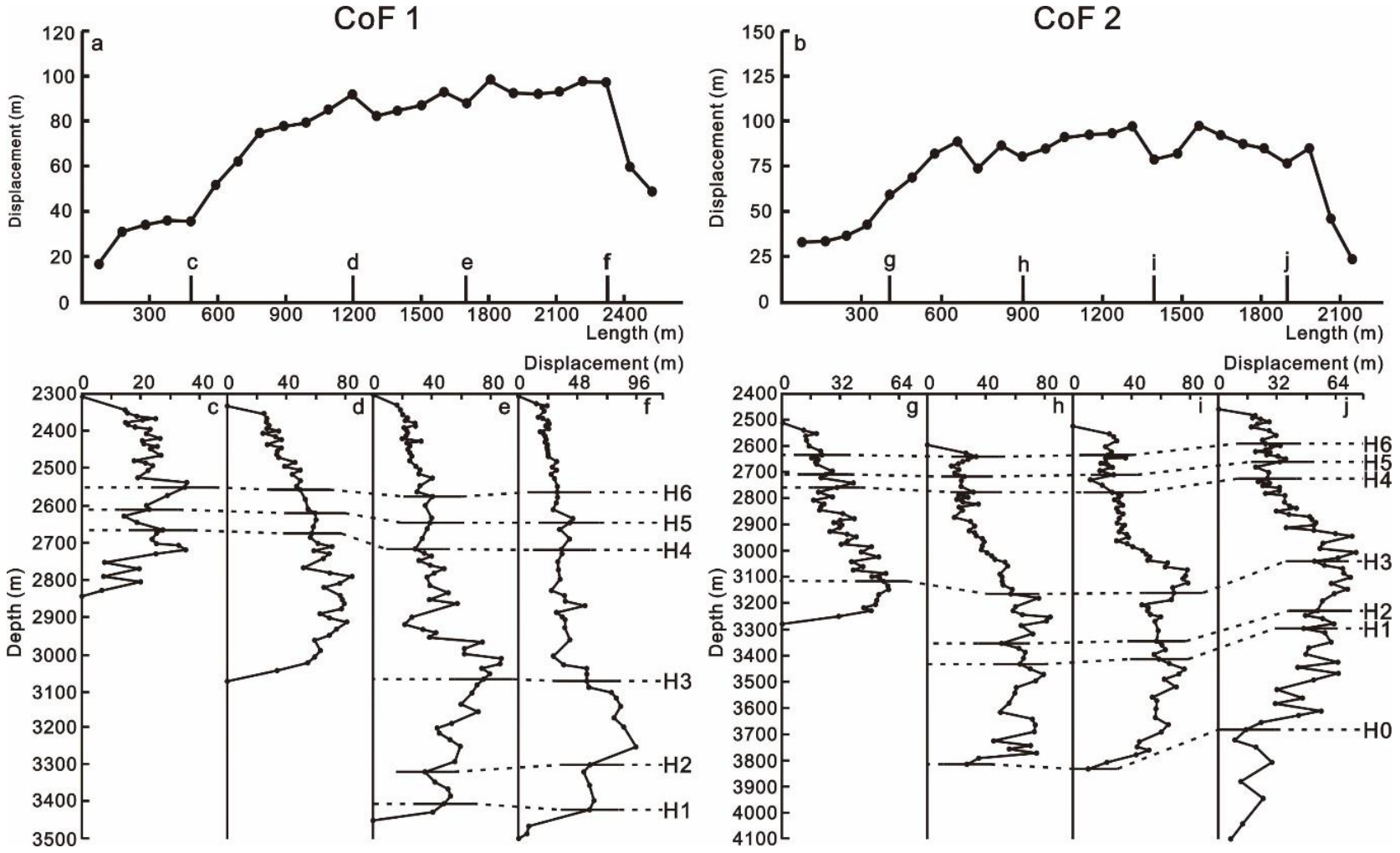

Fig. 4.9. Displacement-length along fault (D_{max}-L) and displacement-depth (D-Z) plots of corridor faults 1 (CoF 1) and 2 (CoF 2) imaged in Figs. 4.1 and 4.3. The vertical lines c-j in the D-L plots above indicate the location of the D-Z plots shown below. The dashed lines mark the seismic-stratigraphic horizons interpreted in this study.

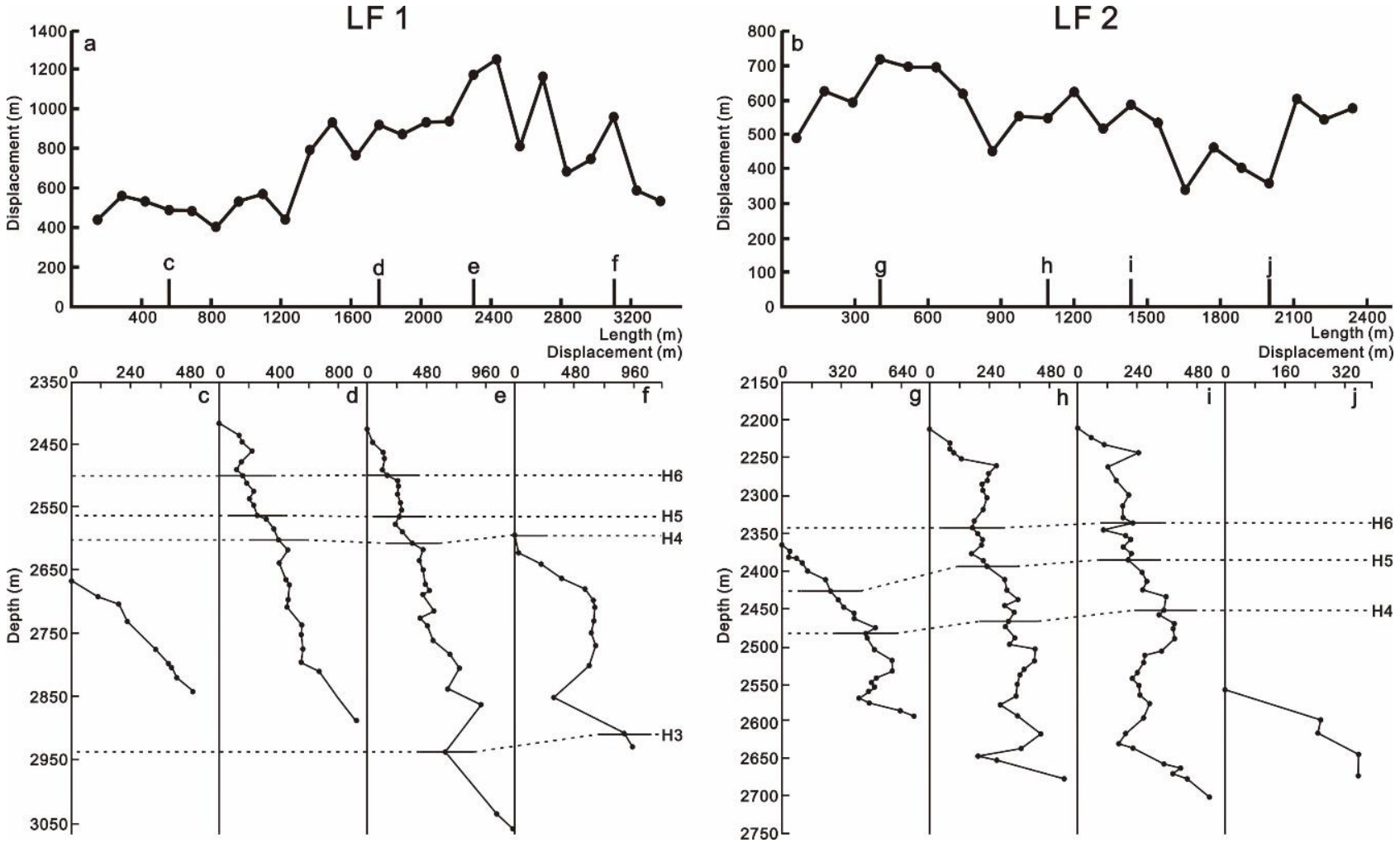

Fig. 4.10. Displacement-length along fault (D_{max}-L) and displacement-depth (D-Z) plots of listric faults 1 (LF 1) and 2 (LF 2) imaged in Figs. 4.1, 4.4 and 4.5. The vertical lines c-j in the D-L plots above indicate the location of the D-Z plots shown below. The dashed lines mark the seismic-stratigraphic horizons interpreted in this study.

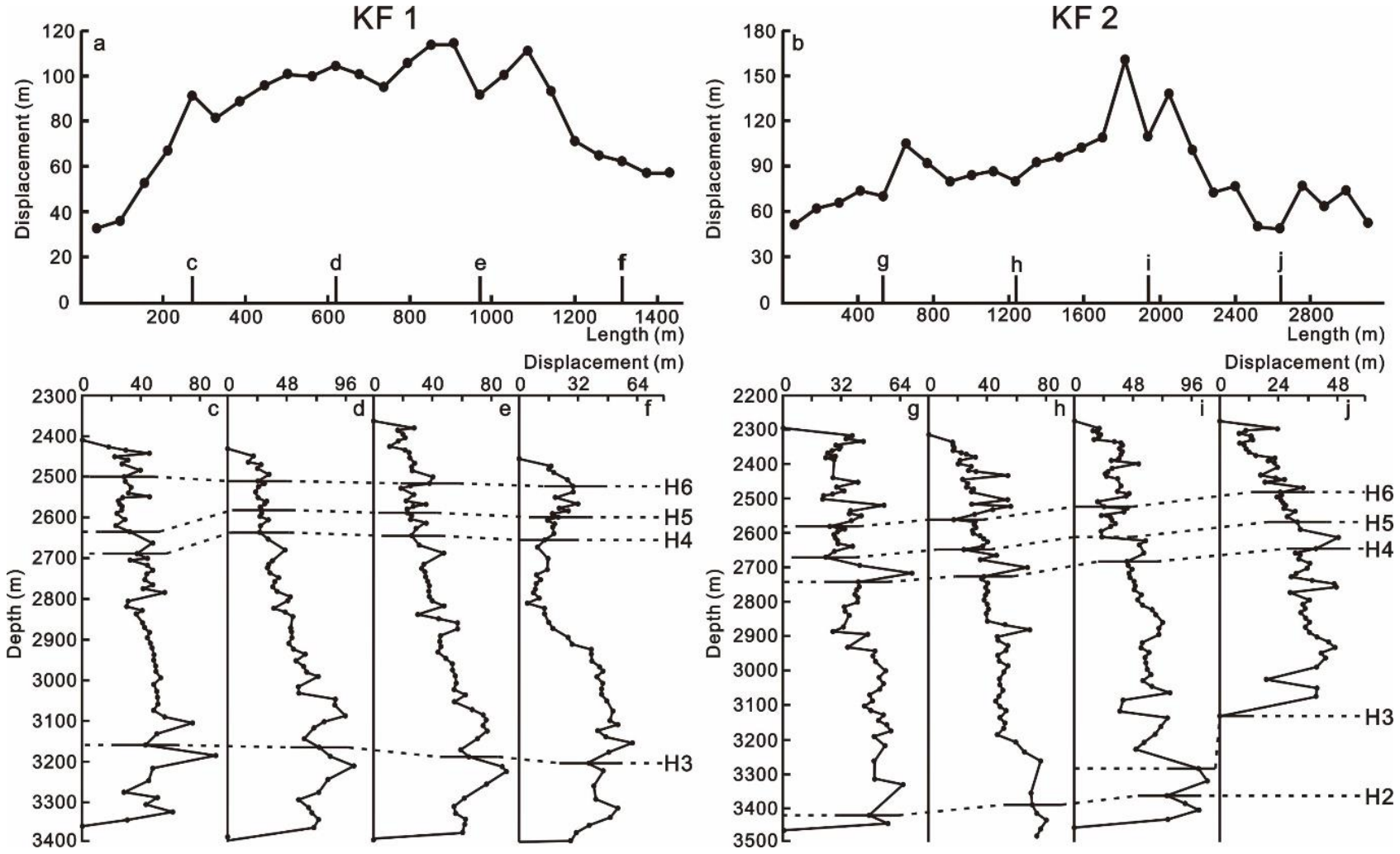

Fig. 4.11. Displacement-length along fault (D_{max}-L) and displacement-depth (D-Z) plots of keystone faults 1 (KF 1) and 2 (KF 2) imaged in Figs. 4.1, 4.4, and 4.5. The vertical lines c-j in the D-L plots above indicate the location of the D-Z plots shown below. The dashed lines mark the seismic-stratigraphic horizons interpreted in this study

linkage as there is significant displacement minima along its striking direction, and this minima correlate with the linkage points observed in variance time-slices (Fig. 4.1). The maximum displacement value for KF2 occurs near horizon H2 (Fig. 4.11), implying that it first nucleated at this level.

4.6 3D visualisation of listric faults and investigated relationship with specific shale units

Listric faults are well developed in the investigated salt minibasin and their lengths vary from 1.0 to 7.2 km. They are also observed at different depths in the study area (Figs. 4.4-4.6 and 4.12). It is clear that listric faults developed in the south of the minibasin are deeper when compared to similar faults to the north (Figs. 4.1-4.3 and 4.12). In addition, growth strata reveal that listric faults in the south were formed earlier than those in the north. Two listric faults in the south of the minibasin were developed in Unit 1, with strata thickening in their hanging-wall depocenters (Fig. 4.12). In contrast, in the north of the minibasin, LF1 and LF2 sole out at the top interval of Unit 1 (Figs. 4.4 and 4.5), and growth strata indicate they were formed after the deposition of Unit 1.

A key characteristic is that all listric faults analysed in this work sole out at the level of Unit 1, a package of low amplitude to transparent seismic reflections (Figs. 4.4, 4.5 and 4.12). Furthermore, borehole data show that Unit 1 is composed of shale and marl with high gamma-ray values. Overpressure in Unit 1 is suggested by the existence of large pockmarks close to the upper tips of listric faults rooting at depth in this unit (Figs. 4.4 and 4.5). In fact, large-scale pockmarks have been previously considered to indicate the episodic loss of fluid due to over-pressure build-up in underlying strata (Müller et al., 2018). Additionally, listric faults in the study area sole out into Unit 1, but they have not offset its lower boundary.

This work interprets the formation of listric faults as related to local overpressure based on the mechanism proposed by Yuan et al. (2020). This may also explain the fact that listric faults in the south of minibasin formed earlier and deeper than those in the north, since Unit 1 is deepening to the south and local overpressures were putatively reached earlier in this part of the investigated salt minibasin when compared to its northern part.

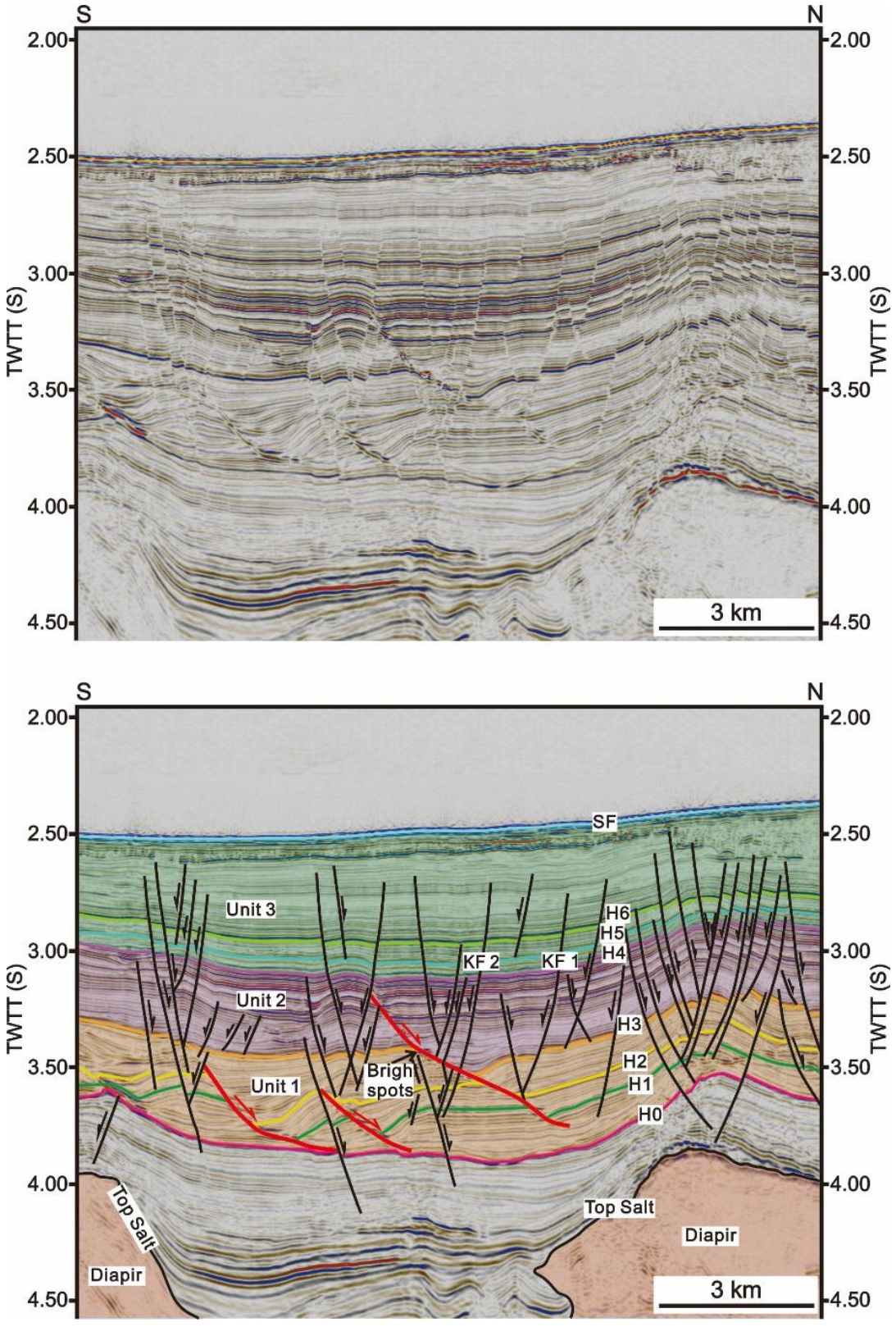

Fig. 4.12. Seismic profiles highlighting the distribution of listric faults in the study area. Red bold and black lines represent faults, while other coloured lines mark the different seismic-stratigraphic horizons interpreted in the study area. Bright spots are indicated in this figure. The location of the seismic profile is shown in Fig. 4.1. SF=Seafloor.

4.7 Fluid-flow potential in distinct fault families

To understand the orientation and distribution of the principal palaeostress tensors in the study area, stress inversions were completed for all interpreted fault families. Stress inversion results for the 534 faults interpreted in the study area show a stress tensor with a sub-vertical σ_1 plunging 86.8° along the azimuth of 39.2°. A sub-horizontal σ_2 plunges −2.1° along the azimuth of 349.3°, accompanied by σ_3 plunging −2.5° along the azimuth of 79.4°. However, as there are more than two preferential strike directions for faults in the study area due to halokinesis, stress inversions were completed separately for each fault family to obtain their own principal palaeostress tensors except listric faults (Table 4.1). Listric faults and keystone faults were formed under the same stress field in minibasin, and most listric faults were offset by keystone faults, suggesting that the palaeostress tensors obtained from keystone faults can be applied to listric faults. Stress inversions results were thus used to complement slip tendency and leakage factor analyses for each fault family (Figs. 4.13 and 4.14).

Slip tendency models reveal marked differences among the four interpreted fault families (Fig. 4.13). Keystone faults record the largest average slip tendency (0.65), with values varying from 0.38 to 0.95 (Fig. 4.13e). In addition, NW-striking keystone faults record significantly higher slip tendency values than NE-striking keystone faults, meaning that the former (keystone) faults have the highest probability to slip. Corridor faults show the second largest average slip tendency (0.63), with ranges in slip tendency similar to keystone faults, from 0.38 to 0.9 (Fig. 4.13c). Crestal faults have lower average slip tendency than corridor faults (0.55), and values range from 0.3 to 0.83 (Fig. 4.13b). Listric faults become the lowest average slip tendency (0.15), with values ranging from 0.06 to 0.25 (Fig. 4.13d). These observations suggest that listric faults have the lowest tendency to slip.

Normalised leakage factors were also calculated based on the stress tensor considered for each fault family, and they show similar trends to slip tendency (Fig. 4.14). The normalised leakage factor values for keystone faults mainly range from 0.45 to 0.95 with an average value of 0.72 (Fig. 4.14e), showing that these faults have the highest probability of conducting fluid among the four fault families. Corridor and crestal faults record similar average normalised leakage factor (0.71 and 0.66), with values ranging from 0.45 to 0.94 and 0.33 to 0.91, respectively (Figs. 4.14b and c). Listric faults show the lowest average normalised leakage factor (0.3), with values ranging from 0.11 to 0.56.

Faults	Number of faults	σ_1		σ_2		σ_3	
		Plunge	Azimuth	Plunge	Azimuth	Plunge	Azimuth
Total faults (Including listric faults)	534	86.8	39.2	-2.1	349.3	-2.5	79.4
Crestal faults	239	88.8	56.0	-0.8	11.5	-0.8	101.5
Corridor faults	45	88.9	78.4	-0.9	43.0	-0.7	133.0
Keystone faults	240	-89.4	88.6	0.4	133.6	0.4	43.6

Table 4.1. Stress inversion values obtained considering the total number of faults and each fault family separately. Results from palaeostress inversions suggest a sub-vertical σ_1 and sub-horizontal σ_3. Note that a negative value of plunge indicates that the plunge is measured below the reference plane.

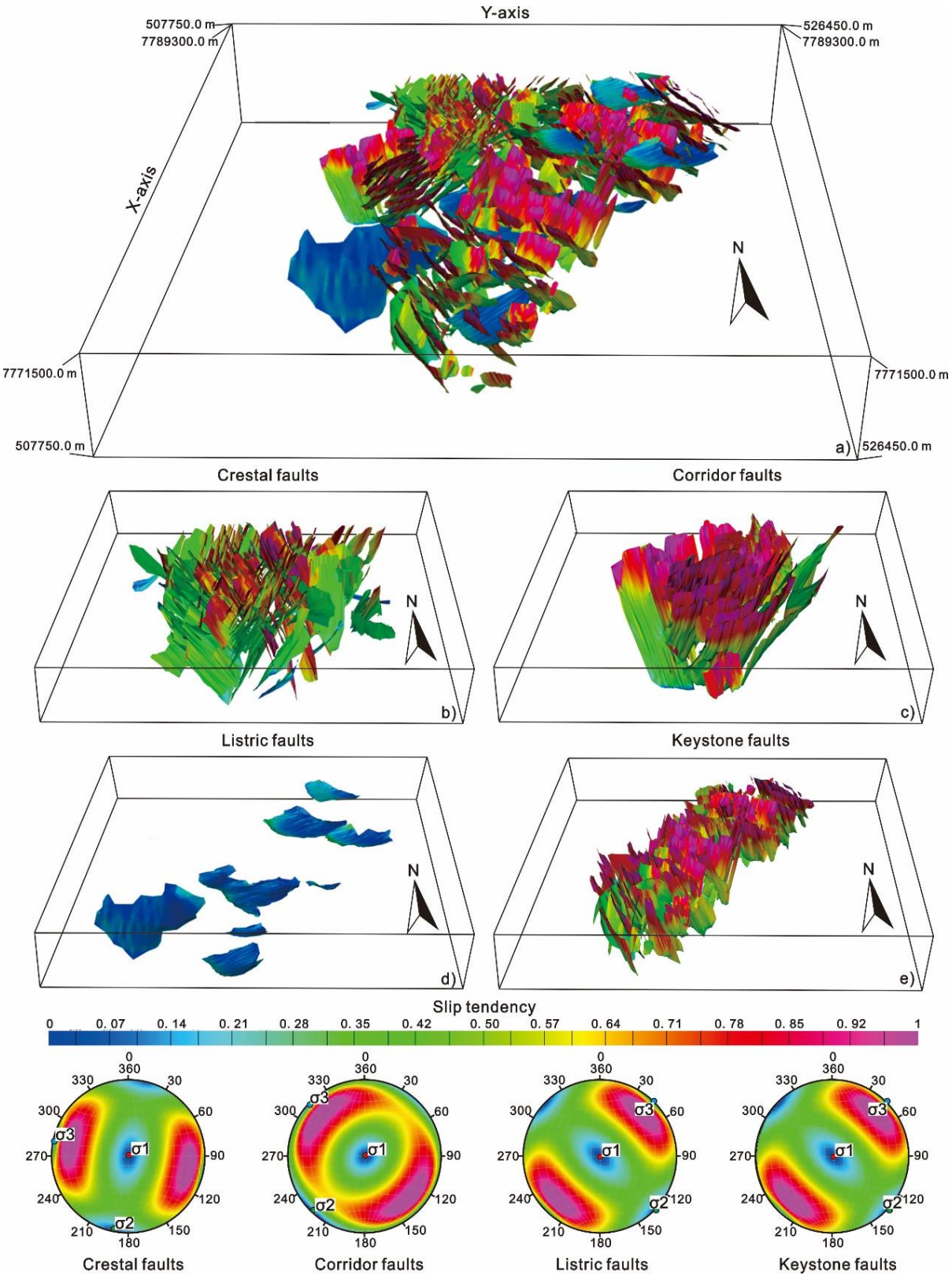

Fig. 4.13. a) Slip tendency analysis for the four fault families in this article considering the palaeostress tensor obtained separately from each family. b)-e) Slip tendency analysis for crestal, corridor, listric, and keystone faults.

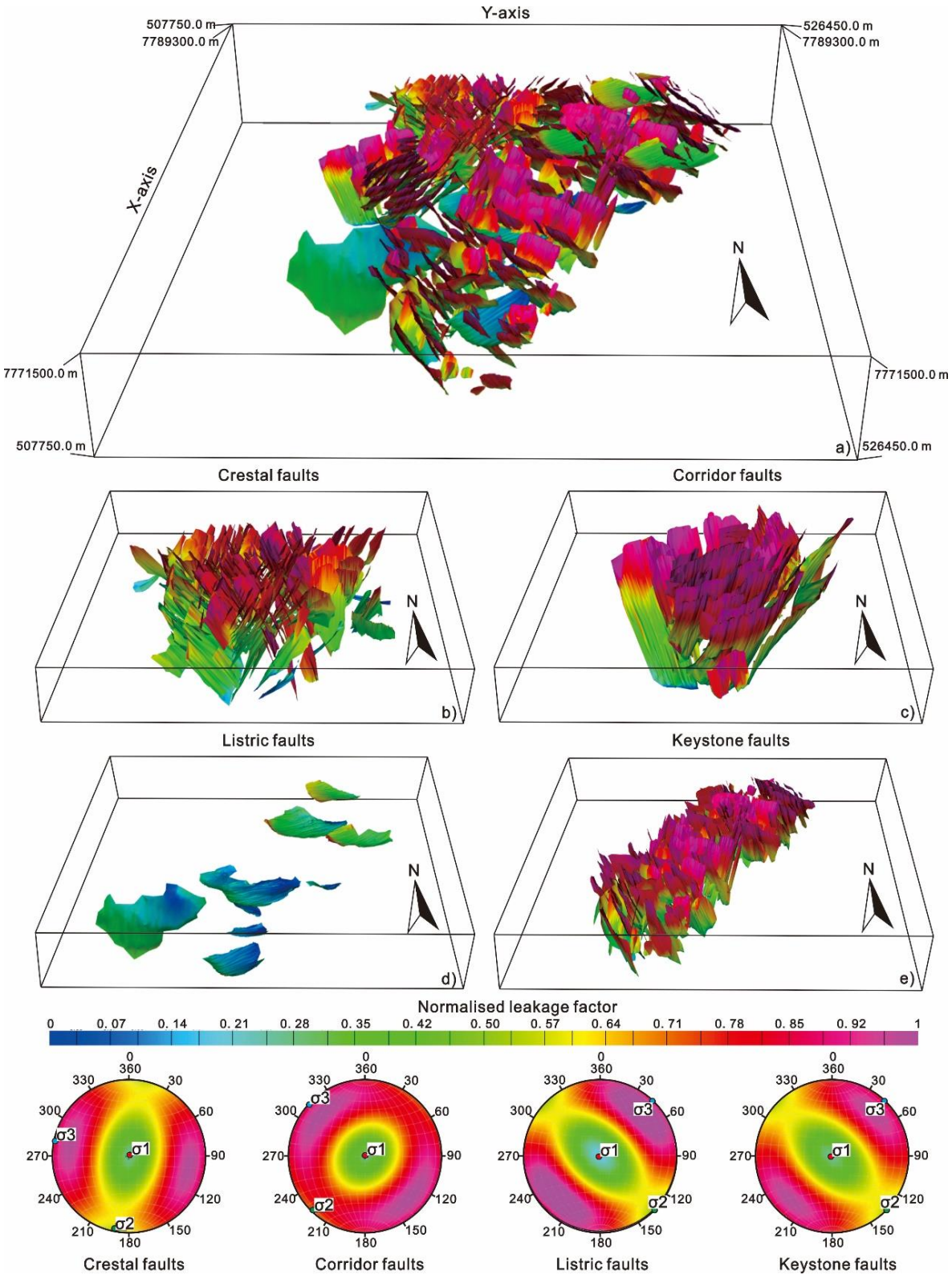

Fig. 4.14. a) Normalised leakage factor analysis for the four fault families in this article considering the palaeostress tensor obtained separately from each family. b)-e) Normalised leakage factor analysis for crestal, corridor, listric, and keystone faults.

According to the data described above, keystone faults record the highest values for slip tendency and normalised leakage factors, and NW-striking keystone faults show larger values than other directions of keystone faults. Corridor and crestal faults have similar values for slip tendency and leakage factor. Conversely, listric faults show the lowest values in both slip tendency and leakage factors. Moreover, the dip and depth of faults significantly influences the calculated slip tendency and leakage factor values, as high angle and shallow faults record higher values for both parameters than low angle and deep faults.

4.8 Discussion

4.8.1 Significance of listric faults and their soling out intervals

One of the key questions arising from this study concerns the significance of listric faults in salt minibasins. As previously mentioned, listric faults sole out in Unit 1, which is composed of shale and marl with high gamma-ray values in borehole data (Fig. 3.1). In addition, multiple bright spots, one known indicator of hydrocarbons, are observed in the lower part of listric faults (Figs. 4.4, 4.5 and 4.12), a character showing that the lower part of listric faults acts as a barrier or seal to hydrocarbons and other fluids. Large pockmarks are also observed close to the upper tip of listric faults, indicating the existence of local strata overpressures.

The strata in which listric faults sole out overlies thick salt, indicating that potential overpressure occurs in supra-salt strata. These overpressures may be caused by dehydration at smectite-illite transition depths, or by the generation of hydrocarbons from source rocks, both occurring after specific threshold temperatures are reached (Bruce, 1984). The supra-salt strata below Unit 1 were deposited in the early-drift stage, and correlate with upper Cretaceous intervals in the Lower Urucutuca Formation. They comprise Cenomanian to Turonian transgressive marine deposits with Type III kerogen, capable of producing high-API oil and gas (Mello and Maxwell, 1990; Fiduk et al., 2004). This kerogen should have reached thermal maturity - though buried at a relative shallow depth of around 1300–2000m - because a major thermal pulse in the early to middle Eocene has been recognised on multiple well data from the continental shelf. This thermal pulse is associated with the emplacement of the Abrolhos volcanic Plateau (Cobbold et al., 2001; Meisling et al., 2001; Gibbs et al., 2003; Fiduk et al., 2004). Due

to the presence of bright spots in the lower part of listric faults, this work suggests that overpressure in the study area was caused by the cracking of hydrocarbons in Cenomanian to Turonian strata, which was locally heated due to the high thermal conductivity of underlying salt.

The Lower Urucutuca formation is composed of shale and marl, documenting the highest gamma-ray values in the study area (Fig. 3.1). At the same time, it comprises low amplitude to transparent seismic reflections in seismic data (Figs. 4.2-4.5 and 4.12). The interval into which listric faults sole out has similar seismic, lithological and petrophysical characters to Lower Urucutuca strata (Figs. 4.2-4.5 and 4.12). In parallel, the interval in question was deposited in an evolving salt minibasin, in which strata is potentially rich in organic carbon due to its restricted ocean circulation (Dow, 1984; Lopez, 1990). Thus, it is highly likely that listric fault sole out in ductile, potentially organic-rich shales and marls, though drilled wells crossing such horizon did not provide total organic carbon (TOC) data. The soling out intervals directly overlie Lower Urucutuca source rocks deposited in the Cenomanian-Turonian (Cobbold et al., 2001; Gibbs et al., 2003; Fiduk et al., 2004), suggesting they add to the known source-rock potential of the Espírito Santo Basin.

4.8.2 Faults as markers of distinct stages of halokinesis

Tectonic faults are one of the most common brittle structures in sedimentary basins. As part of a typical salt-bearing basin, the formation and evolution of faults in the study area have been strongly influenced by halokinesis. Three evolutionary stages were identified between horizon H0 and the seafloor, i.e. within the drift stage of the Espírito Santo Basin (Fig. 4.15).

Stage 1 (Paleocene), between seismic horizons H0 and H3, is characterised by the formation of a few NW- or WNW-striking listric faults, keystone faults (Fig. 4.6e), and marks the onset of diapirism in the study area. Several WNW-striking listric faults revealing significant strata thickening in their hanging walls were formed during this stage (Figs. 4.6f and 4.12), and accommodated displacement along a NE-SW direction. At this same time, NW- to WNW-striking keystone faults were also developed, responding to the establishment of a NE-SW direction of extension (Fig. 4.6e). However, the activity of salt diapirs and walls was minor during Stage 1 as only few crestal faults and corridor faults were formed around these same structures. Corroborating this interpretation, the thickness of strata between horizons H0 and H3 is relatively constant in the study area (Fig. 4.6f), and no significant erosion occurred on top of salt structures (Fig. 4.15a). This relatively weak halokinesis can be explained by the

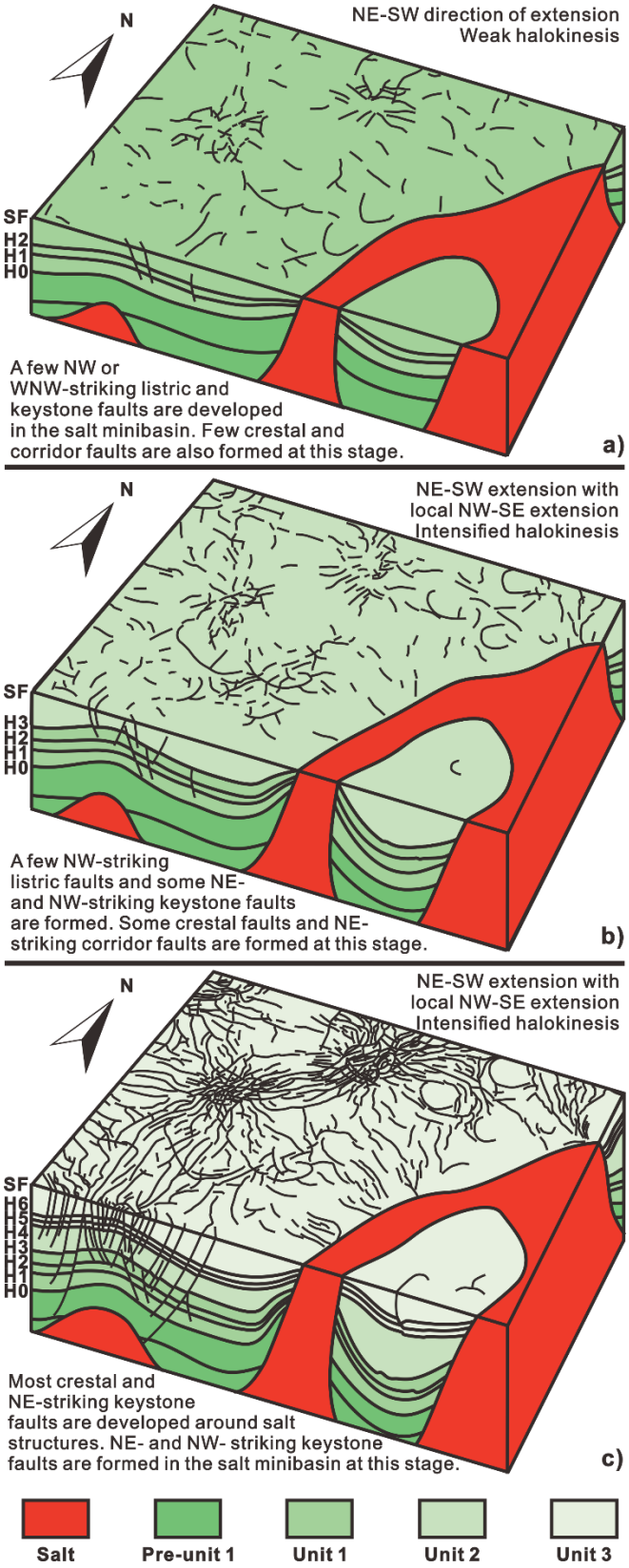

Fig. 4.15. Schematic block diagram model of the three evolution stages interpreted in the study area. a) Stage 1 (Paleocene); b) Stage 2 (Late Paleocene-Early Oligocene); c) Stage 3 (Late Oligocene-Recent).

absence of significant sediment loading and, as a result, NE-SW extension predominated in the study area during Stage 1.

Stage 2 (Late Paleocene-Early Oligocene), marked by strata deposited between horizons H3 and H4, records active diapirism as a consequence of enhanced sediment loading over the salt, and lead to the development of crestal and NE-striking corridor faults (Figs. 4.6c and 4.15b). A few NE- and NW-striking keystone faults, plus NW-striking listric faults, were also developed during this stage (Fig. 4.6c). Halokinesis was intensified with increasing sediment loads, with salt diapirs and walls developing by active diapirism. NE-striking corridor faults started to form at this stage, synchronously with crestal faults (Fig. 4.6c). In contrast to Stage 1, strata are thicker in salt minibasins (up to 450 m) compared to the units accumulated on top of salt structures (less than 200 m), proving that significant erosion, or non-deposition, occurred above the latter (Fig. 4.6d). The development of several NW-striking listric faults and multiple NW-striking keystone faults still denote a predominant NE-SW direction of extension in the investigated salt minibasin (Fig. 4.6c).

With continuing halokinesis, the salt underlying the studied minibasins was withdrawn to feed the surrounding salt diapirs and walls, promoting moderate extension along a NW-SE direction (Fig. 4.15b). This eventually formed NE-striking faults, which intersected the NW-striking keystone and listric faults (Fig. 4.6c). Such a cross-cutting relationship is obvious in the southern part of the main salt minibasin in the study area, as large volumes of salt were withdrawn in this region. Conversely, in the northern half of the minibasin there is only one small salt diapir below horizon H3, leading to the generation of crestal faults with different strikes (Fig. 4.15b).

Stage 3 (Late Oligocene-Recent), spanning strata between horizon H4 and the seafloor, is characterised by more intense (active) diapirism due to increased sediment loading, a process resulting in the formation of multiple crestal faults around salt structures, NE-striking corridor faults, NW- and NE-striking keystone faults (Fig. 4.6a). These faults present variable geometries, although the main salt minibasin was still controlled by a NE-SW direction of extension, as NW-striking keystone faults were developed during this stage (Fig. 4.6a). There was also NW-SE extension in the southern part of the salt minibasin, which led to the generation of the NE-striking faults that intersect NW-striking keystone faults (Fig. 4.15c). In addition, these same keystone faults were formed after the listric faults considered in this work, and they offset the latter in the study area. Later in the evolution of the salt minibasin, a large mass-transport deposit (MTD) was accumulated near the seafloor due to widespread gravity spreading and

downslope sediment movement (Figs. 4.2-4.4). MTDs exhibit a high variability in size and internal character in the study area (Biancardi et al., 2020), and truncate the upper tip of several faults, especially crestal faults developed above salt diapirs (Fig. 4.2).

4.8.3 Implications for the establishment of favourable fluid pathways

Faults can act as effective conduits for fluid in sedimentary basins but, conversely, they can also locally act as barriers to fluid along fault zones (Cox et al., 2001a; Gartrell et al., 2004). In practice, it is commonly difficult to determine whether a fault acts as conduit or barrier to fluid flow, as its sealing competence is influenced by multiple factors such as the lithology of the strata crossed by the fault, its displacement, fault-gouge geometry, fault geometry in relation to local stress fields, post-deformation cementation, interactions between fluids and host rock, and other processes (Caine et al., 1996; Fisher and Knipe, 2001; Koledoye et al., 2003; Manzocchi et al., 2010). In the study area, four (4) fault families are developed around salt structures, and it is of great importance to identify and model the favourable pathways for fluid migrating from deeper strata (e.g. Gartrell et al., 2004; Hovland, 2007; Davison, 2009; Andresen et al., 2011). Fault and fluid flow mapping can also be helpful to predict geohazards associated with fluid flow and seafloor leakage such as submarine slope instability, or the sudden formation of pockmarks and near-seafloor fluid pipes (Elger et al., 2018; Cartwright et al., 2021). In this study, a normalised leakage factor was estimated for each of the four fault families to provide information about which is the most favourable fluid pathways.

Normalised leakage factors are the highest for keystone faults, ranging from 0.45 to 0.95 for an average value of 0.73 (Fig. 4.14e). Keystone faults are thus highly likely to act as conduits for fluid. In addition, keystone faults were active during all three evolution stages considered in this work, propagating into Unit 1 – regarded as a potential source interval. This means keystone faults are more likely to contribute to the migration of fluid from deeply-buried source rocks to shallow reservoirs. Corridor and crestal faults show leakage factor values varying from 0.45 to 0.94 and 0.37 to 0.91, respectively, with average values of 0.71 and 0.66 (Fig. 4.14). The leakage factor values for corridor and crestal faults are similar to those of keystone faults, suggesting they are also likely to act as pathways for fluid. Most of these faults were formed during Stages 2 and 3 under the effect of active diapirism and have propagated at different depths, including into Unit 1. They were also developed on top of salt diapirs where

hydrocarbon tends to accumulate, so the reservoirs close to the upper part of crestal faults and corridor faults are possible exploration targets.

Listric faults have the lowest normalised leakage factor value ranging from 0.11 to 0.56, with an average of 0.4, indicating that they are more likely to act as barriers and baffles to fluid. This character explains the multiple bright spots encountered in the lower part of listric faults. However, listric faults are usually growth faults in the study area, and were mainly formed during Stages 1 and 2. They continued to be active for a long period, promoting the leakage of fluid in their upper parts, and generating large pockmarks above their upper tips. Therefore, based on the leakage factor data, keystone faults constitute the most favourable fluid pathways in the study area. Corridor and crestal faults also show potential to form pathways for fluid flow, but listric faults are likely barriers to fluid, particularly in their lower parts.

4.9 Chapter-specific conclusions

Chapter 4 aimed at understanding the distribution, evolution history and significance of different fault families in a salt minibasin, and any favourable fluid pathways offshore Espírito Santo Basin (SE Brazil). The main conclusions of this work can be summarised as follows:

a) Four fault families are identified based on their geometry, orientation, distribution and relationship with main salt structures. Crestal faults were formed around salt structures together with radial and concentric faults. Corridor faults were developed among discrete salt diapirs, linking them through long corridors of oriented, conjugate fault families. Listric and keystone faults were formed in salt minibasins and were related to important extensional stresses.

b) The development of listric faults can indicate the existence of subsurface overpressure in strata. Moreover, the intervals into which listric faults sole out comprise soft and ductile strata, which is highly likely associated with source rocks. These intervals may be added to the known source-rock potential of a given basin, identifying their depth and relative thickness.

c) Three fault evolution stages are identified in the study area. Stage 1 records the formation of a few NW- and WNW-striking listric and keystone faults in response to the onset of reactive diapirism. Stages 2 and 3 mark a shift to active diapirism in the study area promoted by increasing sediment loading, and lead to the formation of crestal, corridor and keystone faults.

d) Normalised leakage factors show that keystone faults are the most favourable fluid pathways in the study area. Corridor and crestal faults also show potential as pathways for fluid. Conversely, listric faults are likely barriers and baffles to fluid, particularly in their lower parts.

Chapter 5

Palaeostress state around a rising salt diapir inferred from seismic reflection data

5 Palaeostress state around a rising salt diapir inferred from seismic reflection data

5.1 Abstract

A 3D seismic volume and borehole data from the Dutch North Sea are used to investigate the palaeostress state around a rising salt diapir. The results show radial, polygonal and keystone faults around the diapir of interest, which are separated into eight zones based on their geometry, strike and overall distribution. Principal fault families include: a) 400–3500 m long radial faults developed in flanking and corner areas of the salt diapir, and known to have accommodated the stretching resulting from its rise, b) 200–1500 m long polygonal faults providing a record of the stress conditions farther from radial faults, and c) 1000–1800 m long keystone faults controlled by the rise of a buried salt pillow during Paleogene tectonic inversion. Stress inversions for 10,401 interpreted faults reveal that the maximum principal palaeostress (σ_1) is close to vertical, whereas intermediate and minimum principal palaeostresses (σ_2 and σ_3) are sub-horizontal, though variable in their magnitudes and orientations. Palaeostresses in flanking zones of the salt diapir show marked differences when compared with corner zones, but the combination of minimum principal palaeostresses from all flanking and corner zones formed a triangular stress ring around the salt diapir. The width of this stress ring was not only associated with the rise of the salt diapir, but also largely influenced by adjacent salt structures. Minimum principal palaeostresses estimated from polygonal fault systems are nearly normal to the boundary between polygonal and radial faults, implying that the rise of the salt diapir influenced the stress field in the outer part of its flanks. Stress inversion is shown here as a key method to understand the palaeostress state around the salt diapirs with triangular geometry and multiple growth stages, providing insights into their evolving stress states. This work also has implications to the analysis of salt diapirs, and their adjacent strata, in areas posed for carbon sequestration, gas storage, and the production of oil and gas.

5.2 Introduction

Salt diapirs are common structures of sedimentary basins in which evaporites are thick, mobile, and pierce their overburden strata (Jackson and Talbot, 1986; Jackson and Hudec,

2017). The strata above and flanking salt diapirs are usually deformed, forming arched roofs crossed by multiple salt-related fault families (Alsop, 1996; Davison et al., 1996; Rowan et al., 1999; Davison et al., 2000a). The formation and growth of these salt-related faults are controlled by the stress conditions associated with the salt diapirism per se (Vendeville and Jackson, 1992b; Carruthers et al., 2013; Wenau and Alves, 2020; Zhang et al., 2022). For instance, radial faults extend outwards from salt diapirs to accommodate the circumferential stretching of their arched roofs (Jackson et al., 1994; Mandl, 1999; Stewart, 2006; Yin and Groshong, 2007), whereas keystone faults develop in the hinge zone of salt diapirs and form symmetric extensional grabens above them (Harding and Lowell, 1979; Rowan et al., 1999; Alves, 2012).

A significant aspect is that salt-related faults may become favourable fluid flow paths, or seals, for fluid accumulated in subsurface reservoirs (Davison et al., 2000b; Cox et al., 2001a; Gartrell et al., 2004). However, boreholes drilled near these reservoirs often record technical problems, leading to unforeseen costs or even their complete abandonment (Bradley, 1978; Langer and Heusermann, 2001; Dusseault et al., 2004). Most issues occur because rising salt diapirs impose significant stress perturbations on adjacent strata (Seymour et al., 1993; Dusseault et al., 2004; Sanz and Dasari, 2010a; van-der-Zee et al., 2011; Nikolinakou et al., 2014). In recent years, numerical and geomechanical models have been increasingly used to figure out the stress conditions around salt diapirs, the main motivation for this work being conventional oil and gas exploration (Luo et al., 2012; Nikolinakou et al., 2012; Nikolinakou et al., 2014; Teófilo et al., 2018; Hooghvorst et al., 2020), the need to find new options regarding CO_2 and H_2 storage (Chiaramonte et al., 2008; Chang et al., 2011; Ouellet et al., 2011; Ozarslan, 2012; Maia da Costa et al., 2019), and analyses of seal competence above and within salt structures regarded as potential and feasible storage sites for compressed air (Warren, 2017; Gasanzade et al., 2021). Also known from the literature are structural analyses of mining prospects within, or near, halokinetic structures (Davison et al., 1996; Behlau and Mingerzahn, 2001; Van Gent et al., 2011). As key examples of recent work, Hooghvorst et al. (2020) used 3D static geomechanical models to predict stresses around salt diapirs in the Tarfaya Salt Basin, Morocco. In addition, Lagrangian finite element forward models were used to discern the effect of deposition and salt movement in local stresses around a hypothetical salt diapir (Nikolinakou et al., 2014). Finally, 3D geomechanical models of salt structures were deemed useful to map out 3D stress fields around diapirs with multiple shapes (van-der-Zee et al., 2011). However, despite all this published work, fault or fracture analyses based on seismic-reflection or outcrop

data have been sparsely used to reveal the palaeostress state around salt diapirs, though these approaches may provide more objective results (Quintà et al., 2012; Carruthers et al., 2013). Only limited seismic interpretative work has so far been focused on understanding the stress state around circular or sub-circular salt diapirs (e.g. Carruthers et al., 2013). Their study was focused on two small adjoining salt stocks, each one 2 to 3 km in diameter. In nature, many salt diapirs are larger than those in Caruthers et al. (2013) and show irregular shapes, so little is known about the palaeostress state surrounding the great majority of salt diapirs that are not small or concentric in their shape.

Salt diapirs formed in the Dutch North Sea are often surrounded by laterally extensive polygonal fault systems in Cenozoic claystone and shale (Cartwright, 2011; Carruthers et al., 2013). Polygonal faults are regarded as non-tectonic faults, formed by the volumetric contraction of very fine-grained sediments that compact and dewater during their initial burial (Cartwright and Lonergan, 1996; Cartwright et al., 2003). Yet, abrupt changes from a typical polygonal fault pattern to arrays of radial faults are observed around the flanks of diapirs (Davison et al., 2000b; Stewart, 2006; Stewart, 2007; Carruthers et al., 2013). These radial faults are formed by the circumferential stretching of strata when the salt diapirs grow (Jackson et al., 1994; Stewart, 2006; Yin and Groshong, 2007) or via stock widening (‘stem push’), a mechanism that is capable to reactivate pre-existing radial faults, or form new ones under changing stress conditions (Coleman et al., 2018). Faults developed around salt diapirs are therefore capable of providing a relatively accurate record of the stress states associated with halokinesis (Quintà et al., 2012; Carruthers et al., 2013; Coleman et al., 2018).

Carruthers et al. (2013) applied the geometry of polygonal fault patterns to reconstruct the evolving stress state of two salt diapirs in the UK Central Graben. Their work was based on the conclusion that polygonal faults are sensitive to local perturbations in horizontal stresses. Two possible mechanisms are proposed to explain the position of radial-polygonal fault boundaries: (1) the cessation of stretching caused by arching during diapir rise (Davison et al., 2000b; Carruthers et al., 2013), or (2) the limit of hoop stresses produced by radial loading of the overburden from a pressurised salt stock (Carruthers et al., 2013).

This work investigates the palaeostress state around a large triangular salt diapir in plan view on the Cleaver Bank High, around 12.5 km wide, surrounded by polygonal faults. All seismically resolved faults (10,401 in total) were manually mapped around this salt diapir using high-quality 3D seismic data. Stress inversions were then applied to reveal the palaeostress state around the diapir of interest. This work provides insights into the evolving stress state

around a large rising triangular salt diapir, an approach with implications to the analysis of salt structures and their adjacent strata in areas posed for carbon, hydrogen and natural gas storage, as well as the production of subsurface oil and gas. In summary, this work addresses the following research questions:

a) What is the structural evolution history of irregularly shaped salt structures?

b) How does halokinesis control the formation and development of the fault families surrounding the salt diapir of interest?

c) What are the differences in stress state amongst the different zones surrounding irregularly shaped salt diapirs?

5.3 Database and chapter-specific methods

The main data for this chapter is a 3D seismic volume from the southern margin of the Cleaver Bank High, Southern North Sea, and seven (7) wells drilled in the study area are also used (Fig. 5.1). For a full description of the seismic and well data, see section 3.3.2. The seismic interpretation, well correlation and stress analyses applied in this chapter are described in sections 3.4, 3.5 and 3.6.

In this work, eight key seismic-stratigraphic horizons are interpreted and correlated with borehole data, showing the main chronostratigraphic framework (Fig. 3.2). Seven other seismic horizons are interpreted within the Lower North Sea Group (Figs. 5.2-5.5). In addition, graphs recording the number of faults offsetting the interpreted seismic horizons are compiled to identify tier boundaries in polygonal fault systems (Figs. 5.2-5.5). This is because polygonal fault tiers are generally identified by comparing the polygonal planforms of faults at different horizons and by analysing the clustering of basal and upper fault tips at specific horizons (Cartwright and Lonergan, 1996; Carruthers et al., 2013). Thus, plots of the number of faults intersecting each seismic horizon are useful to identify the positions of each tier and their respective boundaries (Carruthers et al., 2013). In this work, three principal seismic-stratigraphic units are defined in Cenozoic strata based on the tier boundaries of polygonal fault systems (horizon H5) and regional stratigraphic unconformities (horizon H9) (Fig. 3.2). Isochron maps for these three seismic-stratigraphic units, and the Late Cretaceous Chalk Group, are plotted to understand the growth history of the salt diapir of interest to this study.

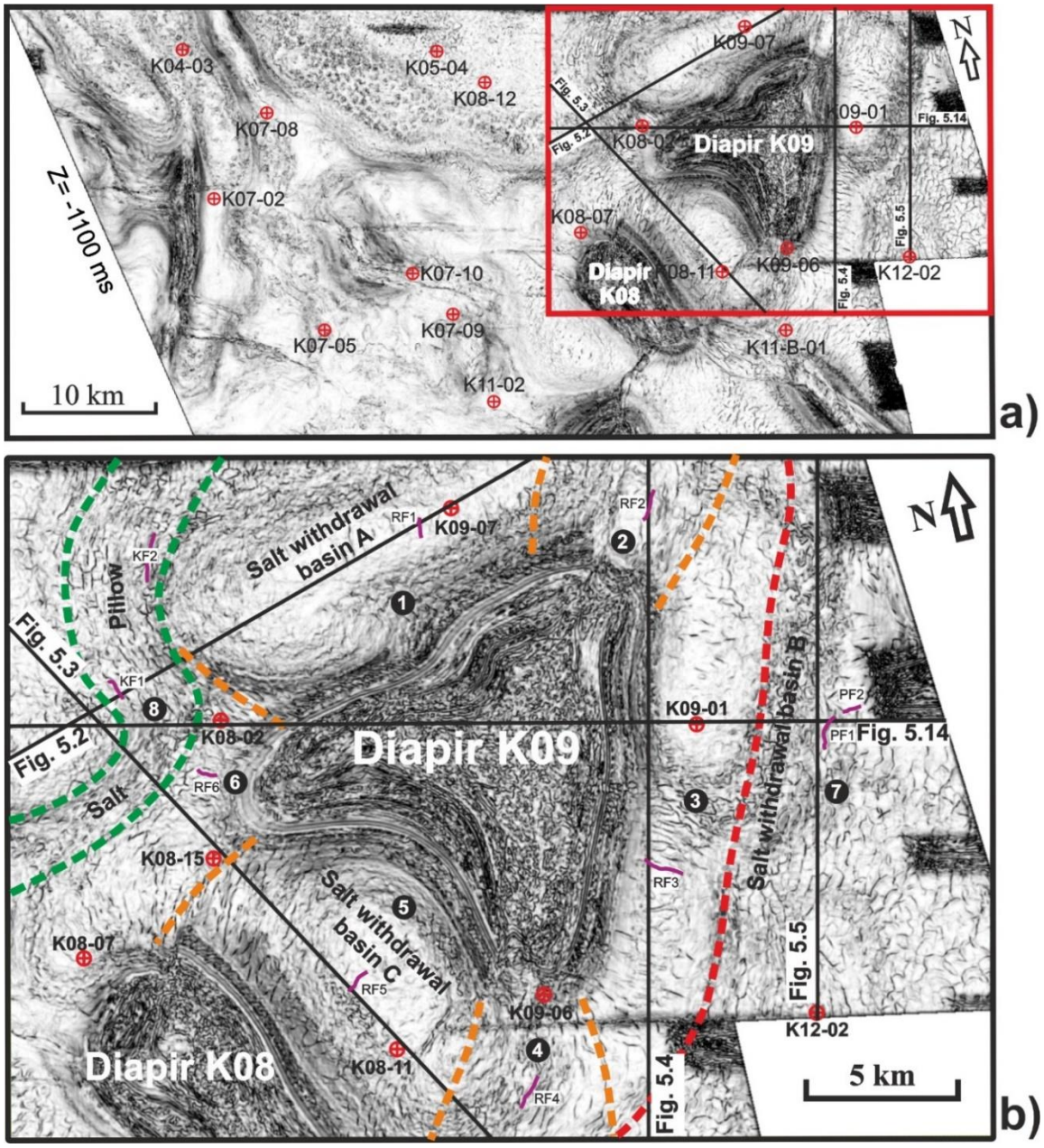

Fig. 5.1. a) Variance map (Z = -1100 ms two-way time) highlighting the location of b), which is bounded by red polygon. b) Variance time-slice (Z= -1100 ms two-way time) of the study area, highlighting eight zones and salt structures interpreted in this work. Six flanking or corner zones are separated by orange dash lines and labelled 1 to 6. Zones where polygonal and key-stone faults were developed are bounded by red or green lines, which are labelled 7 and 8, respectively. Boreholes are separately shown by a red cross and circle. The seismic profiles shown in Figs. 5.2-5.5 and 5.14 are shown by black lines. Ten faults in total from eight zones, shown with purple lines, were selected for throw-length (T_{max}-L) and throw-depth (T-Z) analyses (see Figs. 5.9-5.11).

The study area comprises a large triangular salt diapir that bounds gas field K09-ab-B to the west. To this diapir is given the name diapir K09 based on the quadrant of the Southern North Sea in which it mostly occurs (Fig. 5.1). Diapir K09 is surrounded by three salt withdrawal basins along its three distinct flanks (Figs. 5.1-5.5). Radial faults are well developed near diapir K09, with polygonal and keystone faults developed further away from this structure (Fig. 5.1). Variance time-slices were used to identify the fault families developed around diapir K09 (Fig. 5.1).

A total of 10,401 faults were manually interpreted every two crosslines/inline (50 m) around this same diapir (See Appendix A). Fault-point data were obtained by discretising the faults interpreted on Petrel® into facets, and time-depth conversions were applied to these data on Move®. Rose diagrams representing the distribution of fault strikes for each zone were plotted using fault-point data on Move®; the radius value of the rose diagrams is plotted as a ratio of equal area. The mapped faults were used to identify eight zones based on their geometry, strike and overall distribution (Fig. 5.1; Table 5.1). Additionally, ten faults in total from the eight zones were selected to compile throw-length (T_{max}-L) and throw-depth (T-Z) plots, which were later used to study the faults' growth history (Watterson, 1986; Walsh and Watterson, 1988; Cowie and Scholz, 1992a; Kim and Sanderson, 2005; Omosanya et al., 2015; Omosanya, 2020). The criteria of Tao and Alves (2019) was used to record throw data for distinct fault segments. Tao and Alves (2019) proposed that minimum throw/displacement sampling intervals are related to the length of a fault; sampling intervals should be less than 5% of the fault length when the latter is < 3500 m, or 3% of the fault length when this length is > 3500 m.

Stress inversions are applied in this work to estimate palaeostress tensors from faults interpreted in each zone. Ant tracking maps were compiled to highlight changes in the width of flanking and corner zones around salt diapir K09. Additionally, dip maps for four key horizons were plotted to compare flanking with corner zones.

5.4 Seismic stratigraphy

5.4.1 Unit 1 (horizons H0 to H5)

Unit 1 consists of a package with low- to moderate-amplitude internal seismic reflections (Figs. 5.2-5.5). It is bounded at its base by horizon H0 (or Base NL, Lower North Sea Group), a high-amplitude reflector that correlates with the base of Paleogene strata. Its top is

bounded by a moderate- to high-amplitude reflector named horizon H5 (Figs. 5.2-5.5). The thickness of Unit 1 varies between 20 and 470 ms, with strata in the eastern part of the study area being thicker than in the west (Fig. 5.7). In addition, four seismic reflections were interpreted between horizons H0 and H5, dividing Unit 1 into five different sub-units.

Unit 1 is composed of clay and shale with moderate gamma-ray values (~50 API), but low-density values (~1.9 g/cm^3) (Fig. 3.2). Faults are common inside Unit 1 but rarely propagate below its base (Figs. 5.2-5.5). This is because the underlying Chalk Group is composed of chalk and other carbonate rocks that are relatively hard (Rafavich et al., 1984; Ferrill and Morris, 2008; Ferrill et al., 2017). Conversely, there are multiple faults propagating upwards into Unit 2 (Figs. 5.2-5.5).

5.4.2 Unit 2 (horizons H5 to H9)

Unit 2 is bounded at its base by horizon H5 and at its top by horizon H9 (or Base NM, Middle North Sea Group), a low- to moderate-amplitude reflector that correlates with the base of the Middle North Sea Group (Figs. 5.2-5.5). Three seismic reflections are interpreted between horizons H5 and H9, dividing Unit 2 into sub-units, 2a to 2d. Sub-units 2a, 2c and 2d consist of distinct low amplitude or transparent seismic reflections, whereas sub-unit 2b includes a package of moderate- to high-amplitude seismic reflections (Figs. 5.2-5.5). The thickness of the entire Unit 2 varies from 87 to 540 ms, decreasing towards the flanks of diapir K09 (Fig. 5.7). Unit 2 is also composed of clay and shale with moderate gamma-ray (~50 API) and low density values (~2.0 g/cm^3) (Fig. 3.2). Faulting is ubiquitous in this interval; although a few faults propagate upwards into Unit 3, most faults terminate near horizon H9 (Figs. 5.2-5.5).

5.4.3 Unit 3 (horizon H9 to the Seafloor)

The base of Unit 3 coincides with horizon H9, whereas its top is delimited by the seafloor (Figs. 5.2-5.5). Its thickness ranges from 470 to 860 ms, comprising an interval with moderate- to high-amplitude seismic reflections. Unit 3 includes the Middle and Upper North Sea groups, which are separated by horizon Base NU, Upper North Sea group (Figs. 5.2-5.5). Unit 3 is composed of clay, sandy clay, silty sandstone and sandstone, recording gamma-ray values of ~60 API in its lower part and low gamma-ray values (~25 API) in its upper part

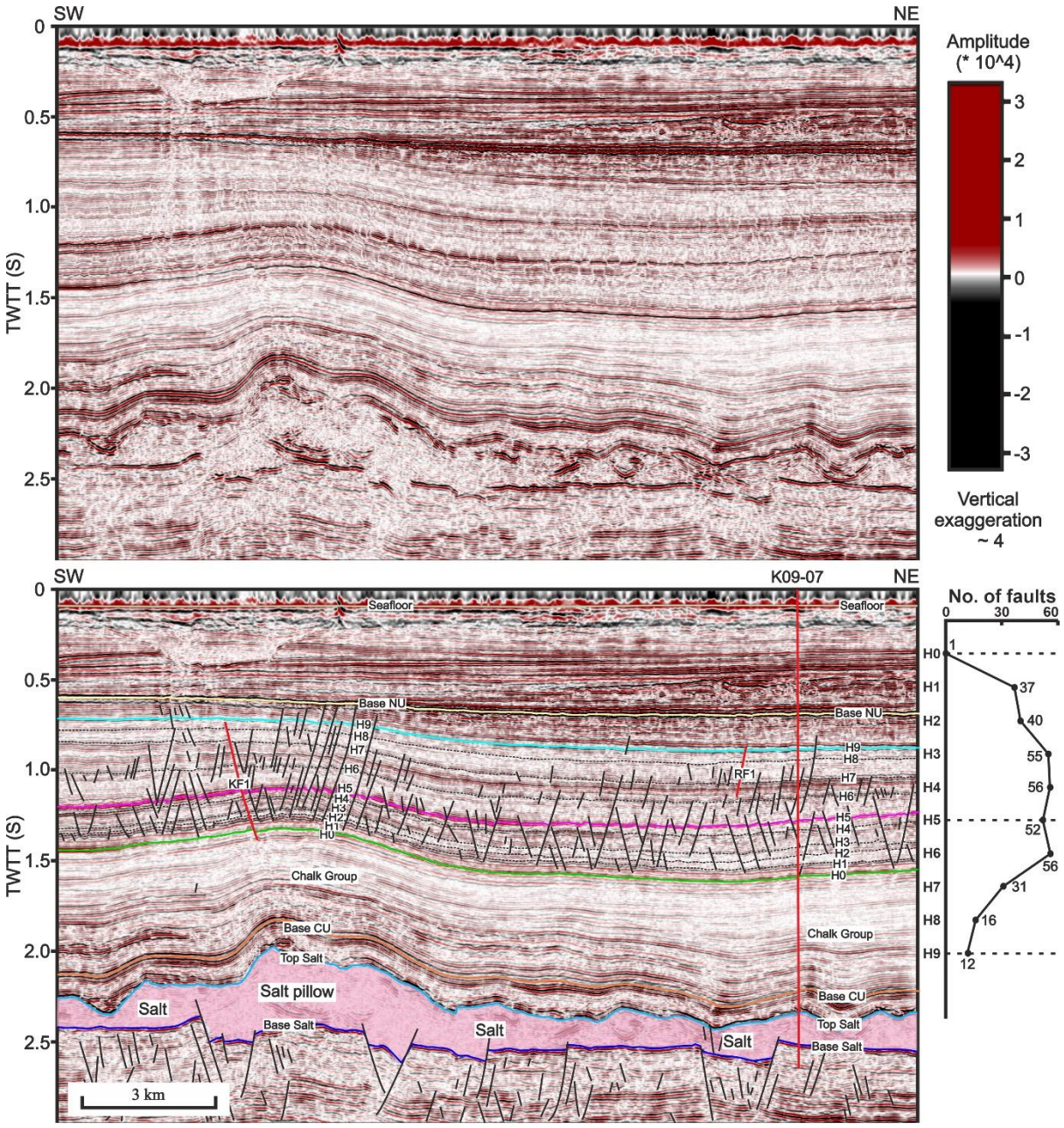

Fig. 5.2. Seismic profile across the salt pillow and salt withdrawal basin A highlighting the presence of keystone faults and radial faults. Eight seismic horizons correlated with well K09-07 are shown by different colour lines and labels, whereas seven other horizons are shown by black dash lines and labels. Faults are represented by black or red lines, including keystone fault 1 (KF1) and radial fault 1 (RF1). Well (K09-07) is shown by a red bold line. Plot on the right of seismic section highlights the number of faults intersecting different horizons on the seismic profile. The location of the seismic profile is shown in Fig. 5.1. CU-Chalk Group

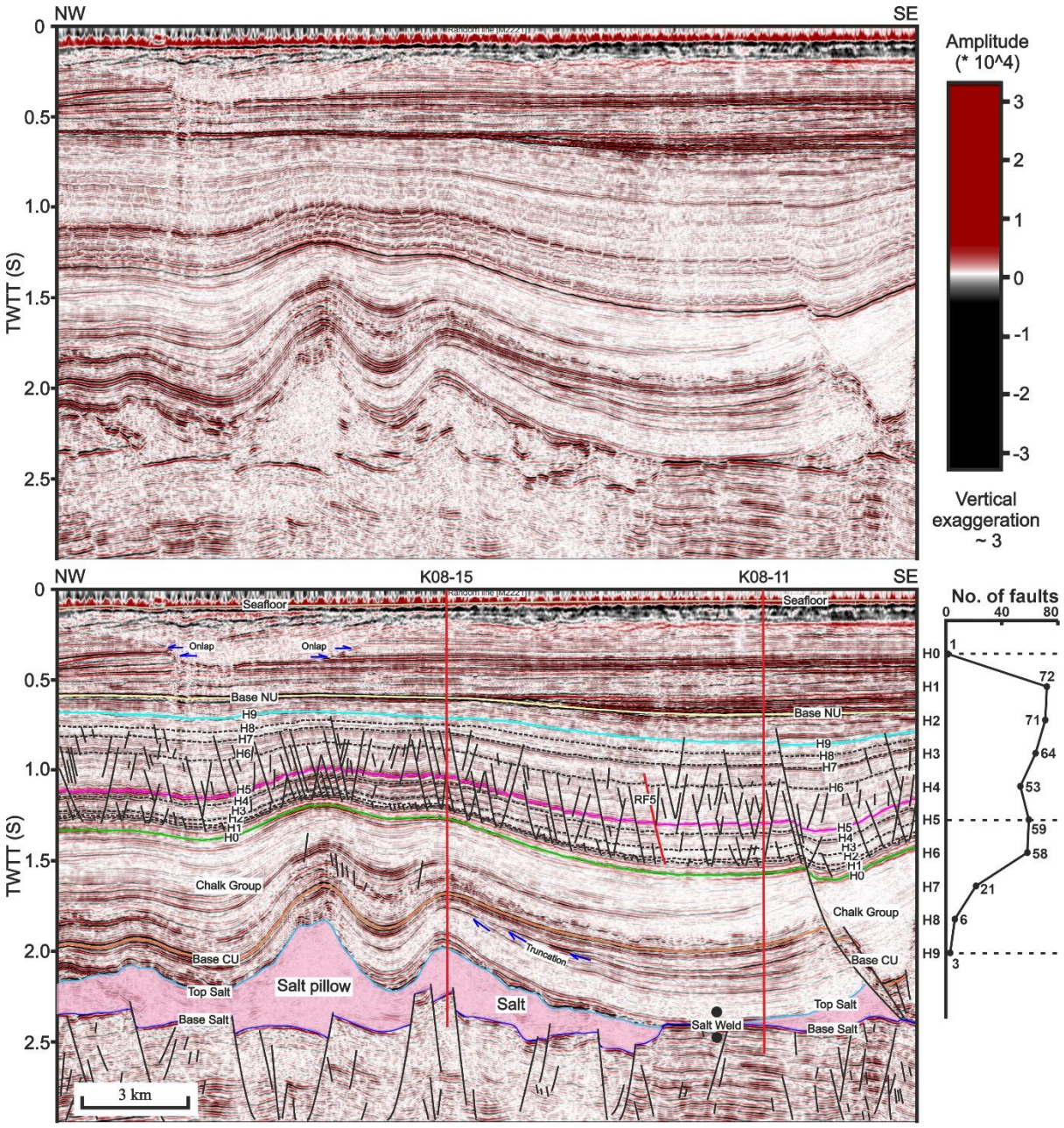

Fig. 5.3. Seismic profile across the salt pillow and salt withdrawal basin C highlighting the presence of keystone and radial faults. Eight seismic horizons correlated with wells K08-15 and K08-11 are shown by different colour lines and labels, whereas seven other horizons are shown by black dash lines and labels. Faults are represented by black or red lines, including radial fault 5 (RF5). Wells K08-15 and K08-11 are shown by red bold lines. A salt weld is highlighted by two black circles. Plot on the right of seismic section shows the number of faults intersecting different horizons on the seismic profile. The location of the seismic profile is shown in Fig. 5.1. CU-Chalk Group

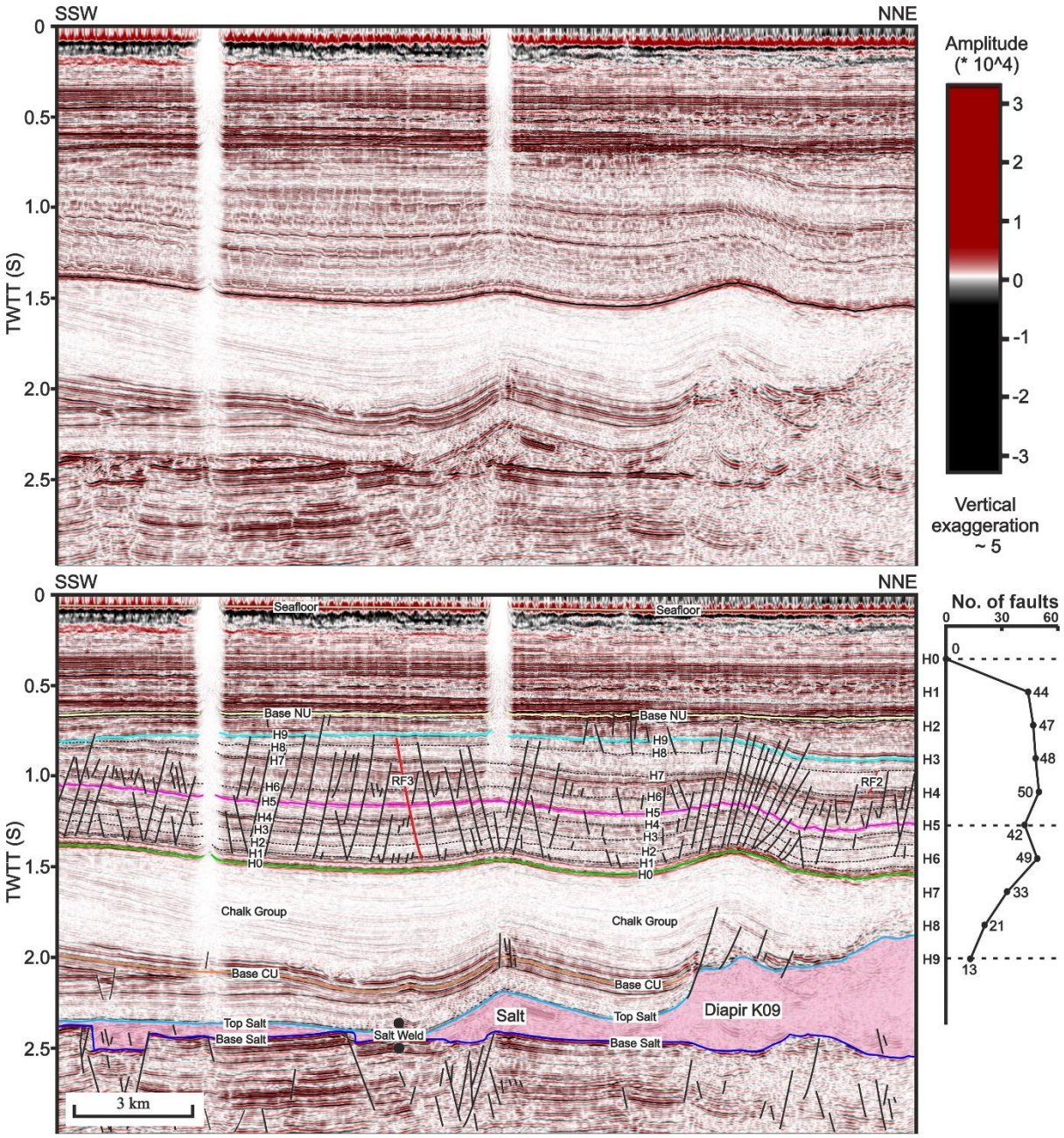

Fig. 5.4. Seismic profile across salt withdrawal basin B highlighting the presence of radial faults. Eight seismic horizons are shown by different colour lines and labels, whereas seven other horizons are shown by black dash lines and labels. Faults are represented by black or red lines, including radial fault 3 (RF3). A salt weld is highlighted by two black circles. Plot on the right of seismic section shows the number of faults intersecting different horizons on the seismic profile. The location of the seismic profile is shown in Fig. 5.1. CU-Chalk Group

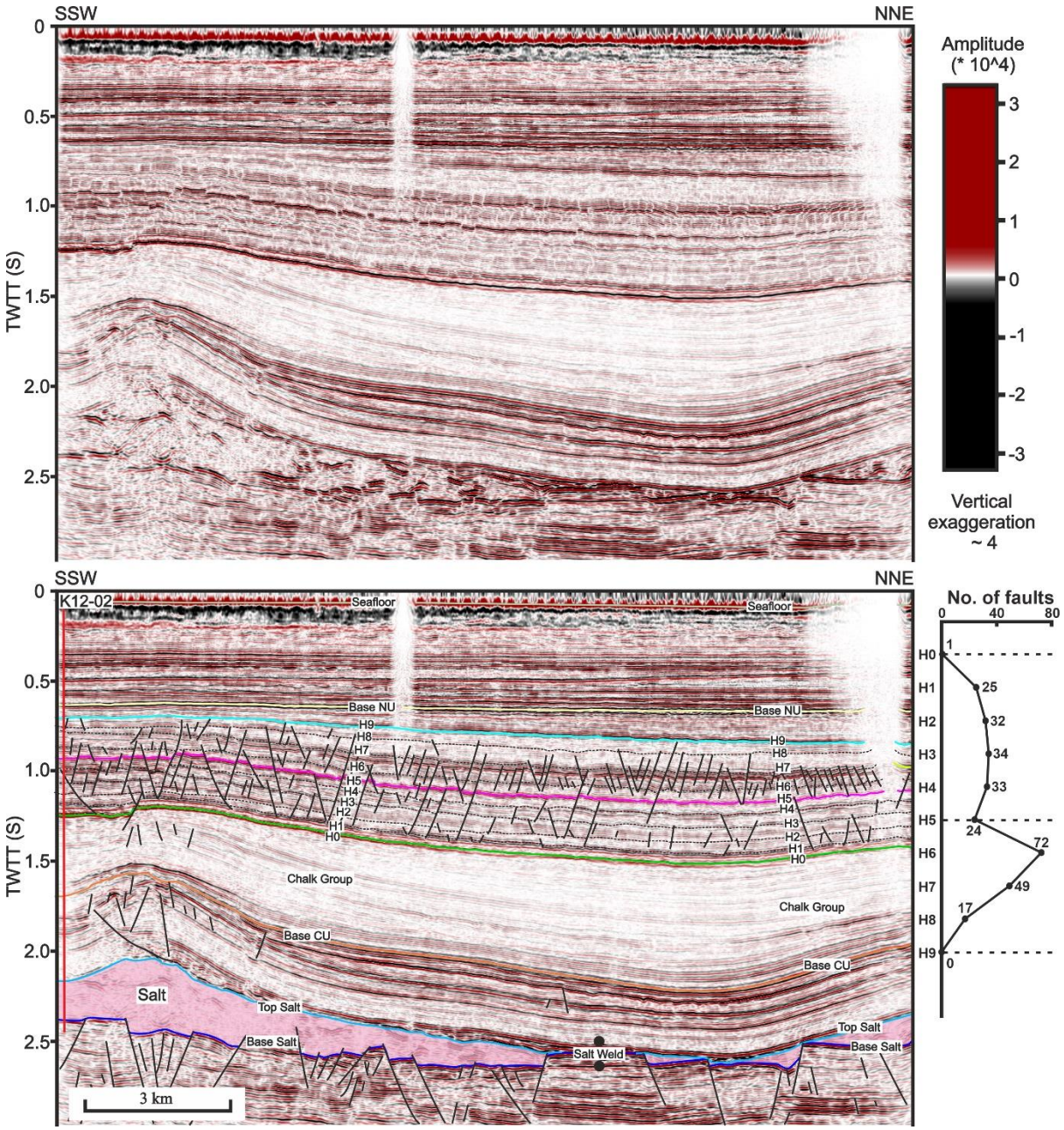

Fig. 5.5. Seismic profile across salt withdrawal basin B showing polygonal faults. Eight seismic horizons correlated with well K12-02 are shown by different colour lines and labels, whereas seven other horizons are shown by black dash lines and labels. Faults are represented by black lines. Well K12-02 is shown by a red bold line. A salt weld is shown by two black circles. Plot on the right of seismic section shows the number of faults intersecting different horizons on the seismic profile. The location of the seismic profile is shown in Fig. 5.1. CU-Chalk Group

(Fig. 3.2). A few faults are developed in the Middle North Sea Group, between horizons H9 and NU, but are rarely observed between horizon NU and the seafloor (Upper North Sea Group) (Figs. 5.2-5.5).

5.5 Salt structures and surrounding fault families

5.5.1 Geometry of salt structures

Diapir K09 is a large triangular diapir in plan view, spanning an area of around 95 km^2 at the depth of -1100 ms two-way time (Fig. 5.1). It penetrates Triassic to Holocene strata overlying large basement faults (Fig. 5.14). Diapir K09 is surrounded by three salt-withdrawal basins along its north, east and southwest flanks; respectively basins A, B and C (Fig. 5.1). In this same area, diapir K09 is separated from basin B by a large NE-striking Mesozoic fault crossing the entire seismic volume (Figs. 2.7 and 5.3), as also shown in Fig. 1 of Ten Veen et al. (2012).

Basins A to C were mainly developed in the Paleogene, as marked thickening occurs in the Lower North Sea Group between horizons H0 and H9 (Fig. 5.7). On seismic profiles, salt welds are observed below these basins (Figs. 5.3-5.5). In addition, basin B is wider than basins A and C, partly because the two latter are limited by other salt structures, not only by diapir K09 (Figs. 5.6 and 5.7). For instance, basin C is also bounded by the relatively large diapir K08 to the west, while a S-shape salt pillow developed near the northwest flank of diapir K09, covering an area of around 38 km^2 at the depth of -1100 ms two-way time (Fig. 5.1).

5.5.2 Fault families developed around diapir K09

Faults developed near diapir K09 include radial, polygonal and keystone faults (Figs. 5.1 and 5.6). Eight (8) distinct zones are recognised based on the geometry, strike and distribution of such faults (Fig. 5.1). Flanking zones concern the areas where radial faults are developed along the flanks of diapir K09, with these faults showing similar strikes, particularly in zones 1, 3 and 5, with average orientations of N182, N107 and N63 (Figs. 5.1 and 5.6). Comparatively, corner zones comprise radial faults developed around the corners of diapir K09 (Figs. 5.1 and 5.6). The strike of these radial faults varies as one travels from one flank to the other, along the diapir corners, as in zones 2, 4 and 6 (Fig. 5.1). In addition, polygonal

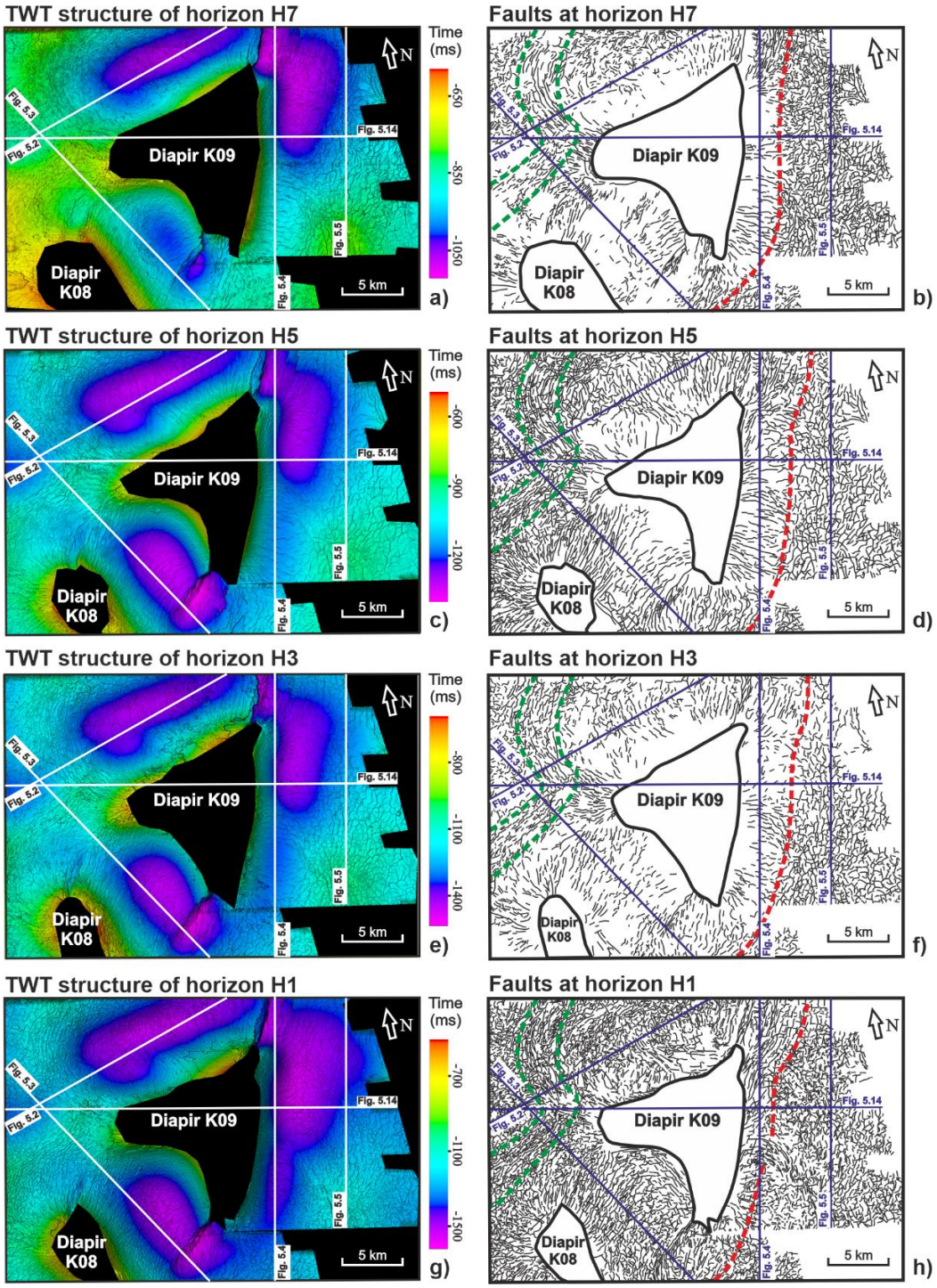

Fig. 5.6. TWT structural and fault maps for four horizons in the study area, highlighting the variation of faults at different horizons. a), c), e) and g) TWT structure of horizons H7, H5, H3 and H1, respectively. b), d), f) and h) Faults at horizons H7, H5, H3 and H1, respectively. Faults are shown by black lines in fault maps. Zone where keystone faults were developed are bounded by green dash lines, and zones where radial and polygonal faults were developed are separated by a red dash line. The seismic profiles shown in Figs. 5.2-5.5 and 5.14 are shown by white or blue lines.

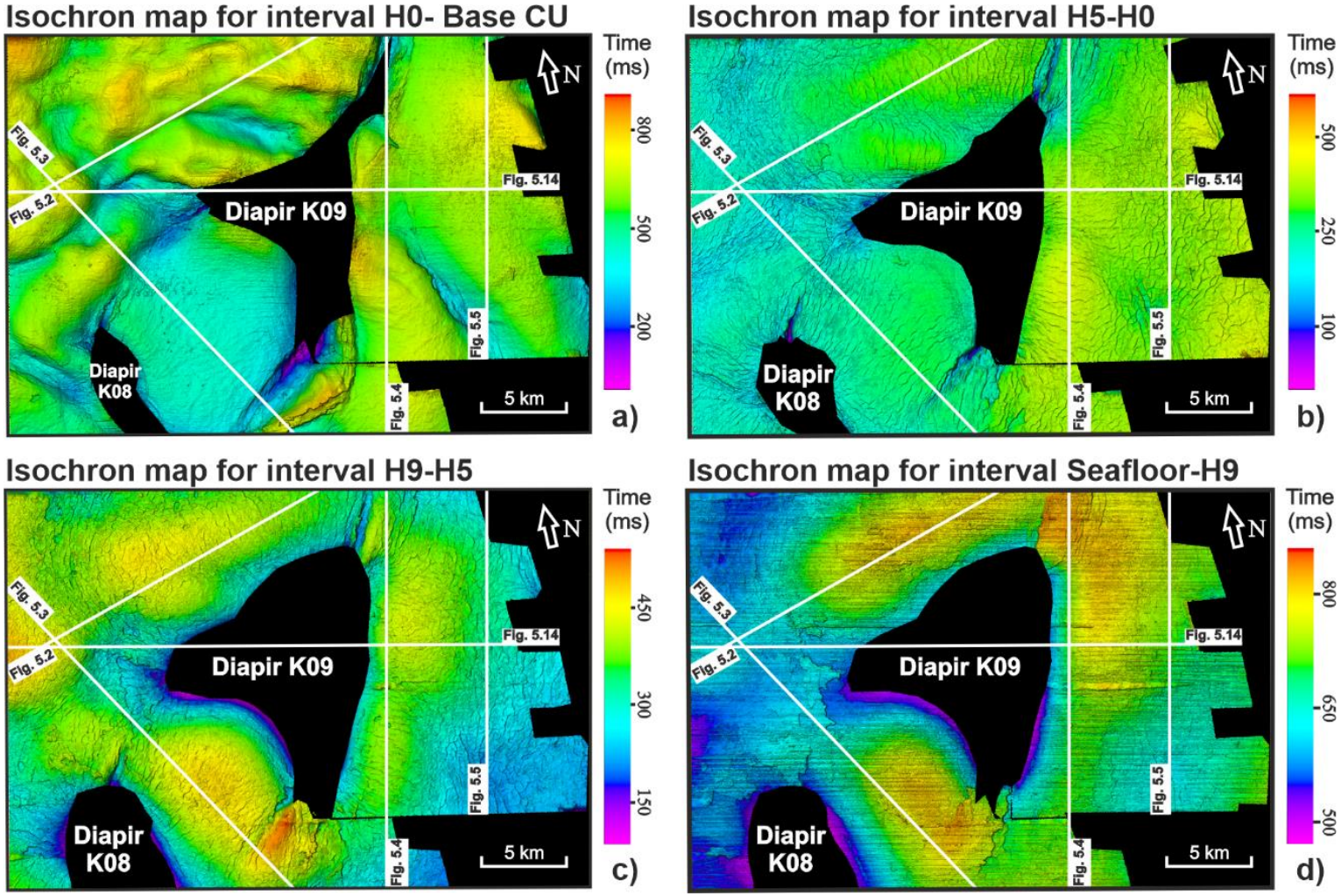

Fig. 5.7. Isochron maps for seismic intervals in the study area. a-d) Isochron maps for seismic intervals between horizon H0 and Base CU, between horizons H5 and H0, between horizons H9 and H5, and between the Seafloor and horizon H9. The seismic profiles shown in Figs. 5.2-5.5 and 5.14 are shown by white lines. CU-Chalk Group

Faults in eight zones	Number of faults	Main Strike	Mean strike	Mean dip	Dip range
Radial faults in flanking zone 1	938	N-S	181.7	56.1	47.4 - 65.4
Radial faults in corner zone 2	201	SW-NE	136.4	55.5	47.6 - 65.2
Radial faults in flanking zone 3	1248	NW-SE	107.0	57.9	51.1 - 66.3
Radial faults in corner zone 4	226	SW-NE	355.1	56.7	46.2 - 66.9
Radial faults in flanking zone 5	445	SW-NE	62.6	52.8	47. 3 - 68.1
Radial faults in corner zone 6	192	NW-SE	165.0	54.7	46.3 - 65.0
Polygonal faults (Tier 1) in zone 7	4788	SW-NE	58.4	56.0	48.4 - 65.2
Polygonal faults (Tier 2) in zone 7	1571	SW-NE	61.4	54.7	47.3 - 64.3
Keystone faults in zone 8	792	SW-NE	152.8	53.3	45.8 - 63.3

Table 5.1. Summary of fault attributes compiled within the eight zones developed around salt diapir K09.

faults were developed in zone 7, next to flanking zone 3 (Figs. 5.1 and 5.6). The timing of formation of radial and polygonal faults is likely to be the same, as they both were constrained to Paleogene strata (Figs. 5.2-5.5). Keystone faults were formed in zone 8 above the salt pillow, with strikes parallel to this latter (Figs. 5.1 and 5.6).

5.5.2.1 Radial faults

Radial faults are well developed in the vicinity of diapir K09 (Figs. 5.1 and 5.6). In plan view, their distribution and number show significant differences with depth, a character associated with the growth history of diapir K09 itself (Fig. 5.6). For example, radial faults occur over a wider area at horizons H3, H5 and H7 when compared to horizon H1 (Fig. 5.6). Their spacing at the level of horizons H3, H5 and H7 is also broader than at horizon H1 (Fig. 5.6). The strike and number of radial faults vary in distinct zones (Fig. 5.6; Table 5.1). The strike of radial faults in flanking zones are clearly oriented when compared with the variably striking of radial faults in corner zones. Radial faults are near-normal to the flank of diapir K09 in flanking zones, whereas they are roughly parallel to the direction of its corner bisector in corner zones (Fig. 5.8). Furthermore, the number of flanking radial faults is usually greater than corner radial faults (Table 5.1).

In seismic data, most radial faults are similar to polygonal faults, i.e., they are restricted to shale or clay intervals in the Lower North Sea Group (Figs. 5.2-5.5). However, plots of the number of radial faults at each seismic horizon show important differences when compared to polygonal faults (Figs. 5.2-5.5). In the study area, radial faults are not tier bounded as polygonal faults are. Radial faults have also different length, throw and spacing values when compared to polygonal faults. The length of radial faults ranges from 400 to 3500 m, and throws vary from 9 to 45 m. The spacing of radial faults varies from 10 to 140 m, values that are larger than those of polygonal faults (Fig. 5.6).

Six radial faults were selected to compile throw-length (T_{max}-L) and throw-depth (T-Z) plots; radial fault 1 (RF1) to radial fault 6 (RF6) (Fig. 5.9). RF1, RF3 and RF5 are 800, 2080 and 1020 m long, respectively dipping to the W, NNE, and SE (Fig. 5.1). RF1 was formed by the lateral propagation and linkage of fault segments, as distinct throw minima are shown in the T_{max}-L plot in Fig. 5.10a. In contrast, RF3 and RF5 are isolated faults as shown by their rugged curve profiles, which reveal the highest throw near their centre but the lowest throw at their lateral tips (Figs. 5.9k and u). The maximum throw of RF1 occurs near horizon H5, while

throw maxima for RF3 and RF5 occur around horizon H6. Multiple throw minima are observed on their T-Z plots, suggesting they were likely to be formed by dip linkage (Fig. 5.9).

Corner radial faults RF2, RF4 and RF6 are 1104, 1700 and 875 m long, dipping respectively to the SE, SE, and NNE (Fig. 5.1). RF2 is an isolated fault, showing a rugged curve profile that shows the highest throw near the center position of RF2 but the lowest throw at both sides in T_{max}-L data (Fig. 5.9b). RF4 and RF6 were formed by the lateral propagation and linkage of fault segments, as distinct throw minima are shown in their T_{max}-L plots (Fig. 5.9l and 5.9v). The maximum throw of RF2 occurs near horizon H3, while throw maxima for RF2 and RF3 occur around horizon H6. Similarly to RF1, RF3 and RF5, multiple throw minima in T-Z plots suggest they were likely to be formed by dip linkage (Fig. 5.9).

5.5.2.2 Polygonal faults

Polygonal fault systems are typically characterised by their geometric planforms, which are often restricted to specific tiers (Cartwright, 1994). In the study area distinct polygonal planforms are observed in basin B within shale or clay intervals of the Lower North Sea Group (Figs. 5.1 and 5.6). The area occupied by the polygonal faults changes with depth (Figs. 5.6 and 5.13), reflecting variations in the span of radial faults during the rise of diapir K09. In addition, plots recording the number of faults intersecting each seismic horizon show minimum values (curve minima) in horizons H0, H5 and H9, whereas maximum values (curve maxima) are recorded in horizons H3 and H6 (Fig. 5.5). This reveals the presence of two distinct polygonal fault tiers in the study area; Tier 1 occurs between horizons H0 and H5, while Tier 2 spans the interval between horizons H5 and H9 (Fig. 5.5). The boundary between Tiers 1 and 2 is located at horizon H5, where most faults tip out, though a few polygonal faults are linked across this same horizon (Fig. 5.5).

A total of 4,788 polygonal faults were interpreted in Tier 1, and 1,571 polygonal faults were interpreted in Tier 2 (Table 5.1). The thickness of Tiers 1 and 2 is around 500 and 450 m, respectively (Fig. 5.7). Polygonal faults in Tier 1 are shorter than those in Tier 2, ranging from 200 to 1200 m (Tier 1) and 350 to 1500 m (Tier 2). Fault throws in Tier 1 are similar to Tier 2, varying from 5 to 35 m. In parallel, polygonal faults in Tier 1 are formed closer than in Tier 2, with their spacing ranging from 140 to 400 m in Tier 1 and from 300 to 500 m in Tier 2. In addition, polygonal faults in Tiers 1 and 2 are aligned, although appearing to be randomly distributed on the structural maps in Fig. 5.6.

Polygonal faults in Tier 1 strike to the NE, mainly from N0 to N60, and their dips range from 48.4° to 65.2° (Fig. 5.8h; Table 5.1). Similarly, polygonal faults in Tier 2 also strike to the NE, mainly from N0 to N60, and their dips range from 47.3° to 64.3° (Fig. 5.8i; Table 5.1). This indicates that polygonal faults were influenced by the stress field surrounding diapir K09, which promoted their preferential alignment. However, this surrounding stress field did not significantly change when polygonal faults were formed as they show similar strikes across horizon H5 in both Tiers 1 and 2 (Figs. 5.8h and i).

Two polygonal faults were selected to compile throw-length (T_{max}-L) and throw-depth (T-Z) plots, polygonal fault 1 (PF1) and 2 (PF2) (Fig. 5.10). PF1 and PF2 are 1260 m and 830 m long, dipping respectively to the SE and NNE (Fig. 5.10). PF1 is an isolated fault, showing a rugged curve profile with its maximum throw value near the centre of PF1. Throw minima occur near its lateral tips, though its eastern half is intersected by another fault (Fig. 5.10a). PF2 grew via the lateral propagation and linkage of fault segments, as distinct throw minima occur in T_{max}-L data between the positions of profiles i and j (Fig. 5.10b). PF1 offsets strata between horizons H1 and H9, while PF2 offsets strata between horizons H1 and H7.

Throw maxima in PF1 occur just below horizon H3, suggesting it probably first nucleated at this depth (Fig. 5.10). Interestingly, multiple throw minima are observed on the T-Z profiles of PF1 (Figs. 5.10c, d and e), suggesting it was formed by dip linkage. The throw maxima of PF2 occurs around horizon H4, indicating it nucleated around this horizon (Fig. 5.10). Multiple throw minima are also observed in T-Z data for PF2 (Figs. 5.10g-j), also suggesting it was formed by dip linkage. Throw minima occur around horizon H5, which separates Tiers 1 and 2 (Figs. 5.10d, e and j). This implies PF1 and PF2 were formed by the linkage of polygonal faults growing separately in both tiers.

5.5.2.3 Keystone faults

Keystone faults were developed above a salt pillow next to flanking zone 1 and corner zone 6 (Fig. 5.1). In plan view, their strikes are parallel to the salt pillow, i.e., NNE to NE with an average N153 strike (Fig. 5.1; Table 5.1). Their length ranges from 1000 to 1800 m, while throws vary from 5 to 40 m. The number of keystone faults is greater at horizons H1 and H5 than near horizons H3 and H7, which are ~500 and ~390 in former and ~260 and ~230 in latter, respectively (Fig. 5.6). Consequently, keystone faults' spacing at horizons H1 and H5 is much smaller than at horizons H3 and H7 (Fig. 5.6). On seismic profiles, keystone faults form small

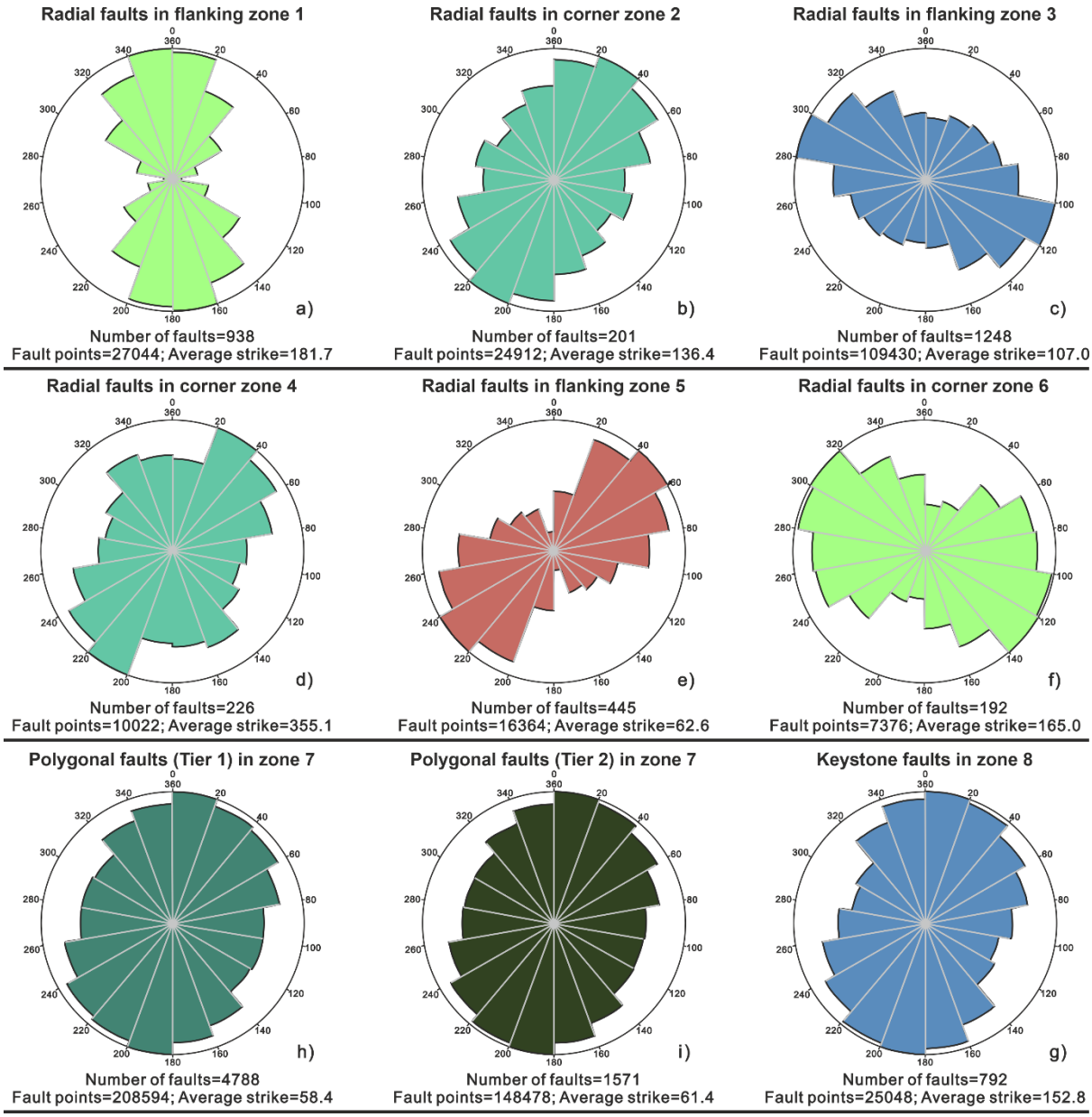

Fig. 5.8. Rose diagrams showing the strike of faults in each interpreted zone, plotted using fault-point data. a) Radial faults in flanking zone 1. b) Radial faults in corner zone 2. c) Radial faults in flanking zone 3. d) Radial faults in corner zone 4. e) Radial faults in flanking zone 5. f) Radial faults in corner zone 6. g) Polygonal faults (Tier 1) in zone 7; h) Polygonal faults (Tier 2) in zone 7; i) Keystone faults in zone 8. Note that the radius value of the rose diagram is plotted as a ratio of equal area.

Fig. 5.9. (Next page) Throw-length along fault (T_{max}-L) and throw-depth (T-Z) plots for radial fault 1 (RF1) to radial fault 6 (RF6), which are shown in Figs. 5.1 and 5.2-5.4. The vertical dashed lines c-j, m-t and w-ad in the T_{max}-L plots above indicate the location of the T-Z plots. Dashed lines mark the seismic-stratigraphic horizons interpreted in this study.

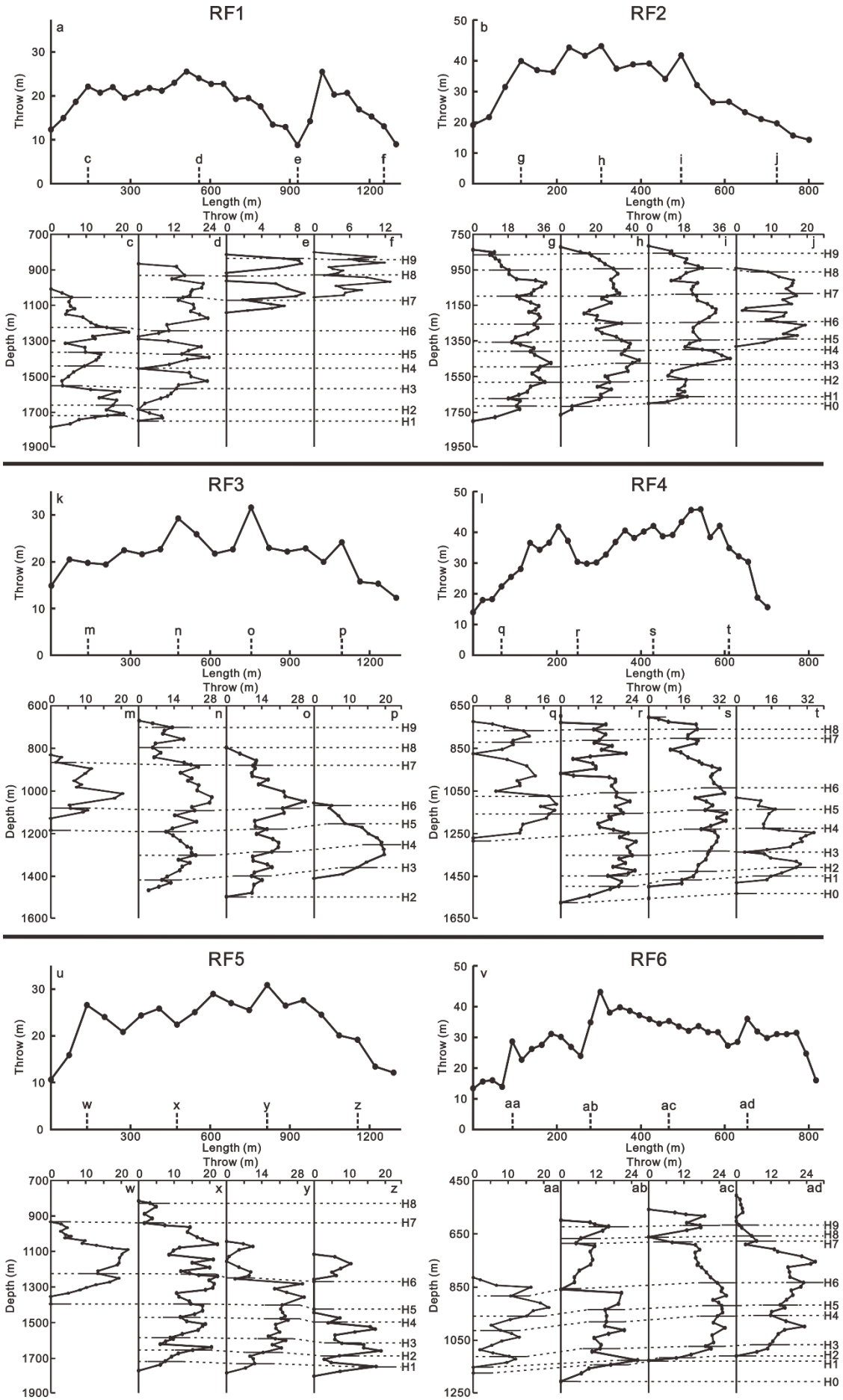
RF1
RF2
RF3
RF4
RF5
RF6
Throw (m)
Length (m)
Depth (m)
H0
H1
H2
H3
H4
H5
H6
H7
H8
H9

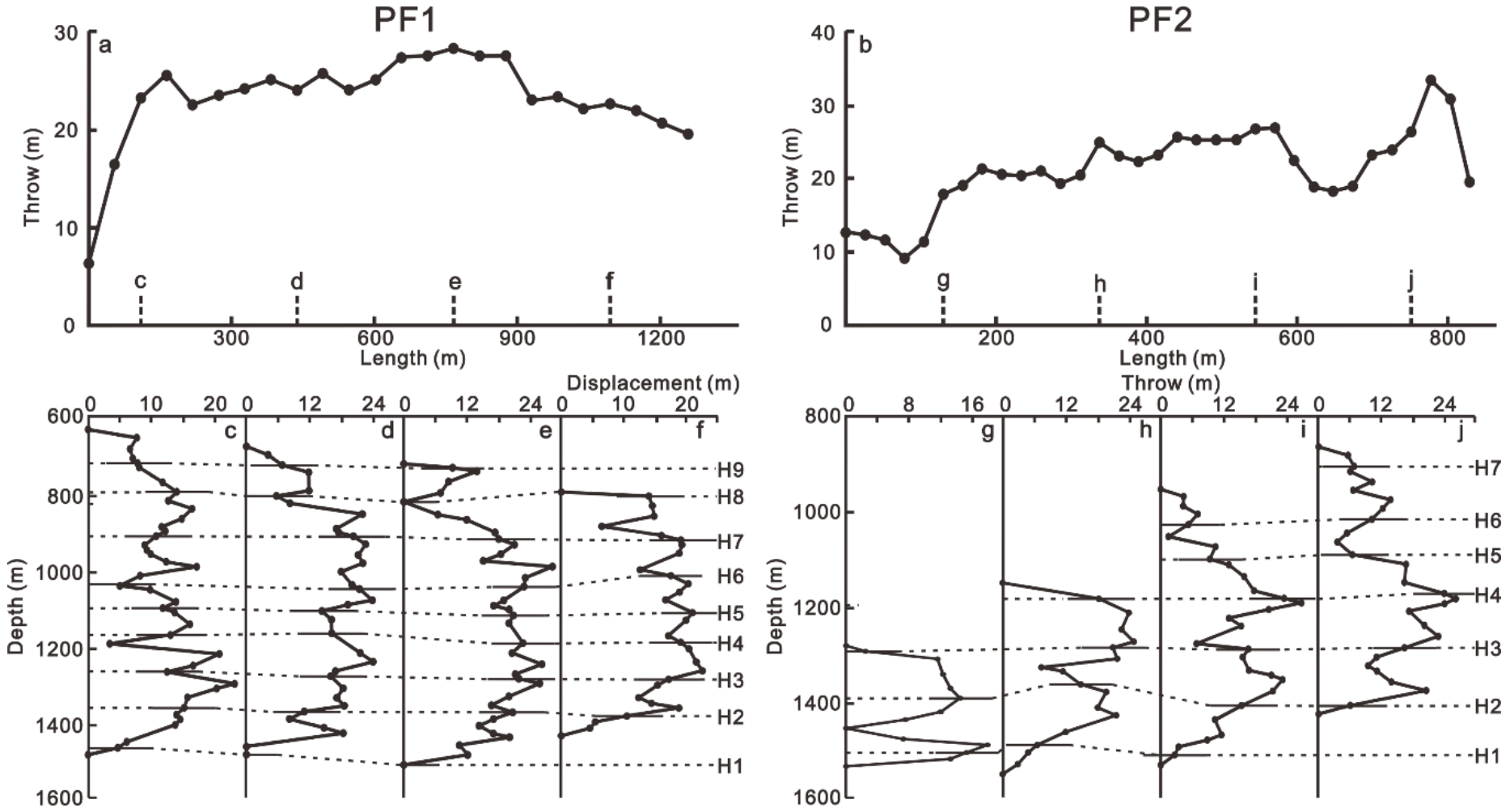

Fig. 5.10. Throw-length along fault (T_{max}-L) and throw-depth (T-Z) plots for polygonal faults 1 (PF1) and 2 (PF1), which are shown in Figs. 5.1 and 5.13. The vertical dashed lines c-j in the T_{max}-L plots above indicate the location of the T-Z plots. Dashed lines mark the seismic-stratigraphic horizons interpreted in this study.

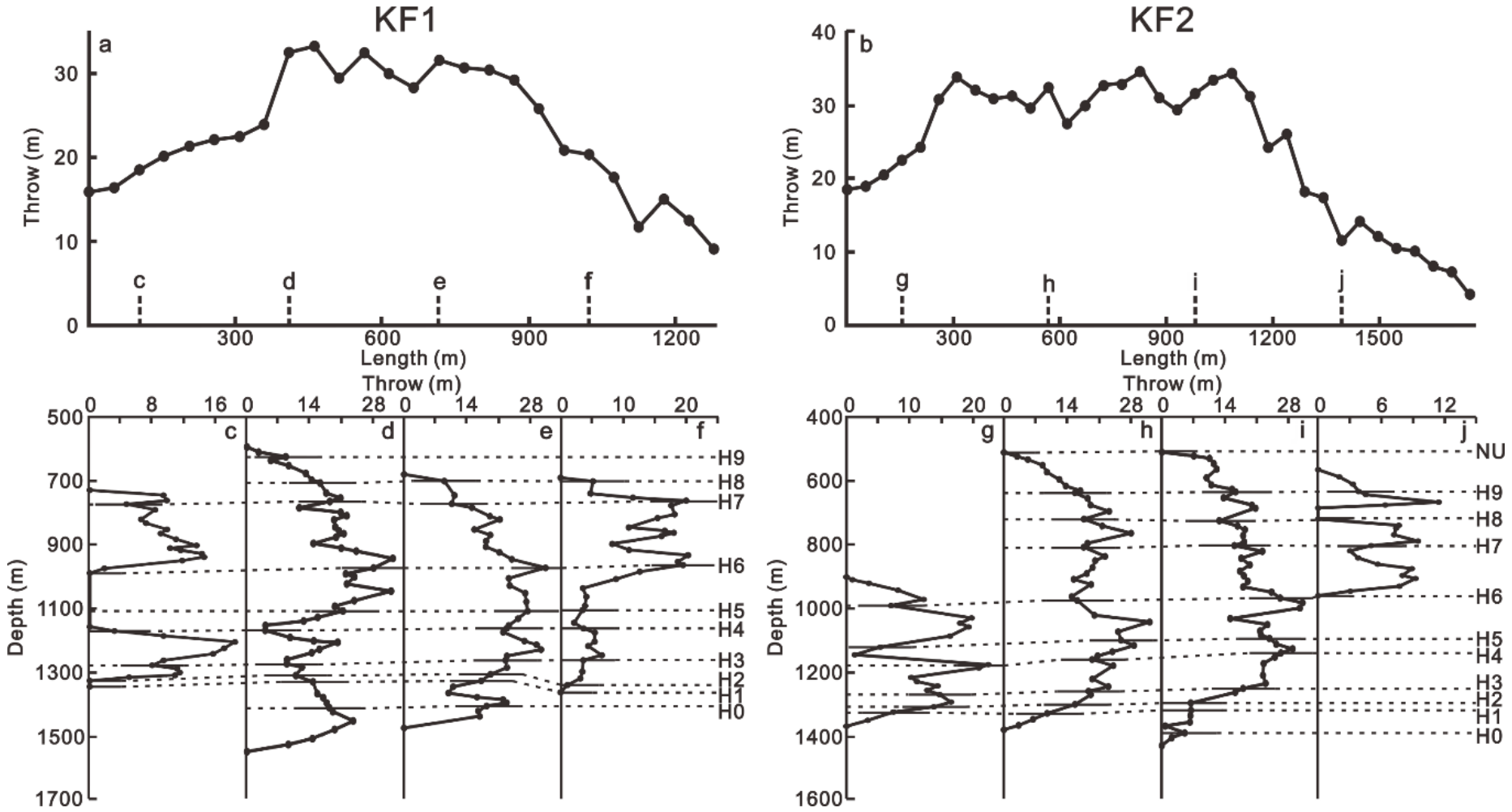

Fig. 5.11. Throw-length along fault (T_{max}-L) and throw-depth (T-Z) plots for keystone faults 1 (KF1) and 2 (KF2), as shown in Figs. 5.1 and 5.2. The vertical dashed lines c-j in the T_{max}-L plots above indicate the location of the T-Z plots. Dashed lines mark the seismic-stratigraphic horizons interpreted in this study.

symmetric grabens above a salt pillow (Figs. 5.2 and 5.3). Fault dips range from 45.8° to 63.3°, for a mean dip of 53.3°. Most keystone faults are restricted to the relatively muddier Lower North Sea Group, though a few propagate into the Middle North Sea Group (Figs. 5.2 and 5.3).

Two NE- and N-striking keystone faults were selected to compile throw-length (T_{max}-L) and throw-depth (T-Z) plots, keystone fault 1 (KF1) and 2 (KF2) (Fig. 5.1). They are 1280 and 1760 m long, and dip respectively to the NEE and NW (Fig. 5.1). Both are isolated faults, as they have rugged curve profiles that show the highest throw near the centre but the lowest throw at the fault tips in T_{max}-L data (Figs. 5.11a and b). Fault KF1 offsets the strata between horizons H0 and H9, while KF2 offsets strata between horizons H0 and NU (Upper North Sea Group). The upper part of KF1 is bounded by horizons H8 or H9, while the upper part of KF2 is limited by horizon NU. Both faults record throw maxima near horizon H6 (Fig. 5.11), indicating they probably first nucleated at this horizon. Multiple throw minima are visible on T-Z plots, implying they were formed by the dip linkage of distinct fault segments (Fig. 5.11).

5.6 Stress inversion for faults developed around diapir K09

Radial faults around salt diapirs can be useful to understand the orientation of principal palaeostress tensors (e.g. Quintà et al., 2012). Radial faults are ubiquitous around diapir K09 and can be divided into six zones based on their geometry, orientation and distribution (Fig. 5.1). In parallel, polygonal faults are aligned (Figs. 5.8h and i), indicating they have been influenced by the superposition of regional and local stresses. As local stresses in the study area were mainly caused by the rise of diapir K09, stress inversions for these polygonal faults provide useful data to understand the stress state around the diapir of interest, though polygonal faults are regarded as non-tectonic faults. Considering polygonal faults occur in two distinct tiers, palaeostress conditions were inverted separately for each tier, i.e. for 4788 faults in Tier 1 and 1571 faults in Tier 2 (Fig. 5.12; Table 5.2). Stress inversions were also applied to the 792 keystone faults mapped close to diapir K09 (Fig. 5.12; Table 5.2).

The results of stress inversion show that maximum principal stress tensors (σ_1) are nearly vertical in all eight zones (Table 5.2). Accordingly, intermediate (σ_2) and minimum (σ_3) principal stress tensors are nearly horizontal (Table 5.2). It is important to note that the minimum principal stresses obtained from all flanking and corner zones form a triangular stress

ring around diapir K09 (Fig. 5.12). The width of this stress ring correlates with the width of flanking or corner zones developed around the diapir, but with marked variations. Also, the width of flanking and corner zones developed around diapir K09 varies with depth (Figs. 5.6 and 5.13). For instance, the width of flanking zone 3 is around 2.2 km near horizon 1 (Fig. 5.6h), but increases to around 4.4 and 3.3 km at horizons H3, H5 and H7, respectively (Figs. 5.6b, d and f). The width of flanking and corner zones is also different among the six zones (Figs. 5.6 and 5.13), a character that is mainly associated with presence of adjacent salt structures. For example, flanking zones 1 and 5 are wider than flanking zone 3 at different depths (Fig. 5.13). In addition, minimum principal stresses obtained from radial faults in zones 1, 3 and 5 are parallel to the flanks of diapir K09 (Fig. 5.12). Conversely, minimum principal stresses obtained from corner zones 2, 4 and 6 are normal to the directions of its corner bisector (Fig. 5.12). Interestingly, the minimum principal stresses obtained from the two tiers of polygonal faults have similar directions, and they are nearly normal to the boundary between the polygonal and radial faults (Fig. 5.12). Finally, the minimum principal stresses estimated from keystone faults are near-normal to the strike of their underlying salt pillow (Fig. 5.12).

5.7 Discussion

5.7.1 Structural evolution of salt structures

As the largest salt structure in the study area, diapir K09 has experienced several phases of growth since the Late Permian. Halokinesis first occurred from Middle Triassic to Early Cretaceous, as indicated by thinning of strata between the top salt and CU horizons towards the flanks of the diapir (Figs. 5.7 and 5.14). The precise time for the onset of halokinesis is not clear due to the large depositional hiatus spanning part of the Triassic and the whole of Jurassic strata on the Cleaver Bank High, a character resulting from Mid and Late Kimmerian erosion (Remmelts, 1995). Halokinesis, nonetheless, also occurred during the Late Cretaceous, as shown by the thinning of the Chalk Group towards the diapir (Figs. 5.14 and 5.15). This halokinesis likely responded to active diapirism driven by Late Cretaceous tectonic inversion (Laramide Inversion; De Jager, 2007; Fattah et al., 2012b; Harding and Huuse, 2015). Overburden loading was probably a secondary process driving halokinesis at this time, and was in great part promoted by the presence of a relatively thick (1300 m) Chalk Group (see well K09-01).

Faults in eight zones	σ_1		σ_2		σ_3	
	Plunge	**Azimuth**	**Plunge**	**Azimuth**	**Plunge**	**Azimuth**
Radial faults in flanking zone 1	-87.4	89.6	0.2	174.4	2.6	84.4
Radial faults in corner zone 2	87.9	51.9	-2.0	33.2	-0.7	123.2
Radial faults in flanking zone 3	-86.0	199.7	-0.8	301.0	-4.0	31.1
Radial faults in corner zone 4	87.8	183.5	2.0	30.6	-1.0	120.5
Radial faults in flanking zone 5	-84.2	136.9	0.6	53.3	5.8	143.3
Radial faults in corner zone 6	-88.6	103.6	1.4	114.6	-0.3	204.6
Polygonal faults (Tier 1) in zone 7	88.3	356.9	-1.4	29.6	0.9	119.6
Polygonal faults (Tier 2) in zone 7	88.5	8.0	-1.4	28.4	0.5	118.3
Keystone faults in zone 8	88.9	358.4	-1.0	20.8	0.4	110.8

Table 5.2. Principal palaeostress tensors obtained from stress inversions in the eight zones developed around salt diapir K09. Results show σ_1 is nearly vertical, whereas σ_2 and σ_2 are sub-horizontal. Note that a negative value of plunge indicates that the plunge is measured below the reference plane.

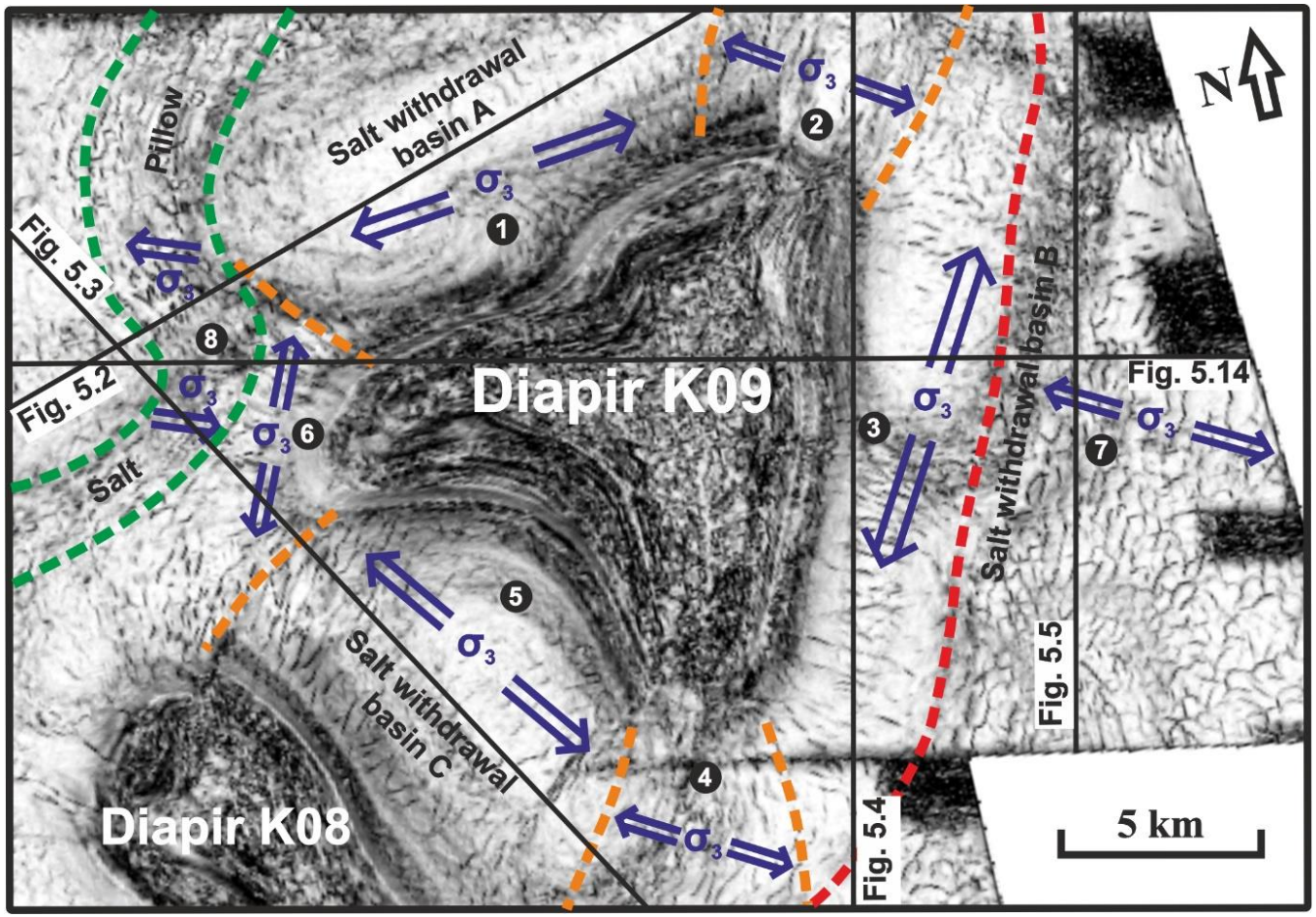

Fig. 5.12. Variance time-slice (Z= -1100 ms two-way time) showing the minimum principal palaeostress tensors (σ_3) obtained from stress inversions for each zone. The direction of minimum principal palaeostress for each zone is highlighted by blue arrows. Six flanking or corner zones are separated by orange dash lines and labelled 1 to 6. Zones where polygonal and keystone faults were developed are bounded by red or green lines, which are labelled 7 and 8, respectively. The seismic profiles shown in Figs. 5.2-5.5 and 5.14 are shown by black lines.

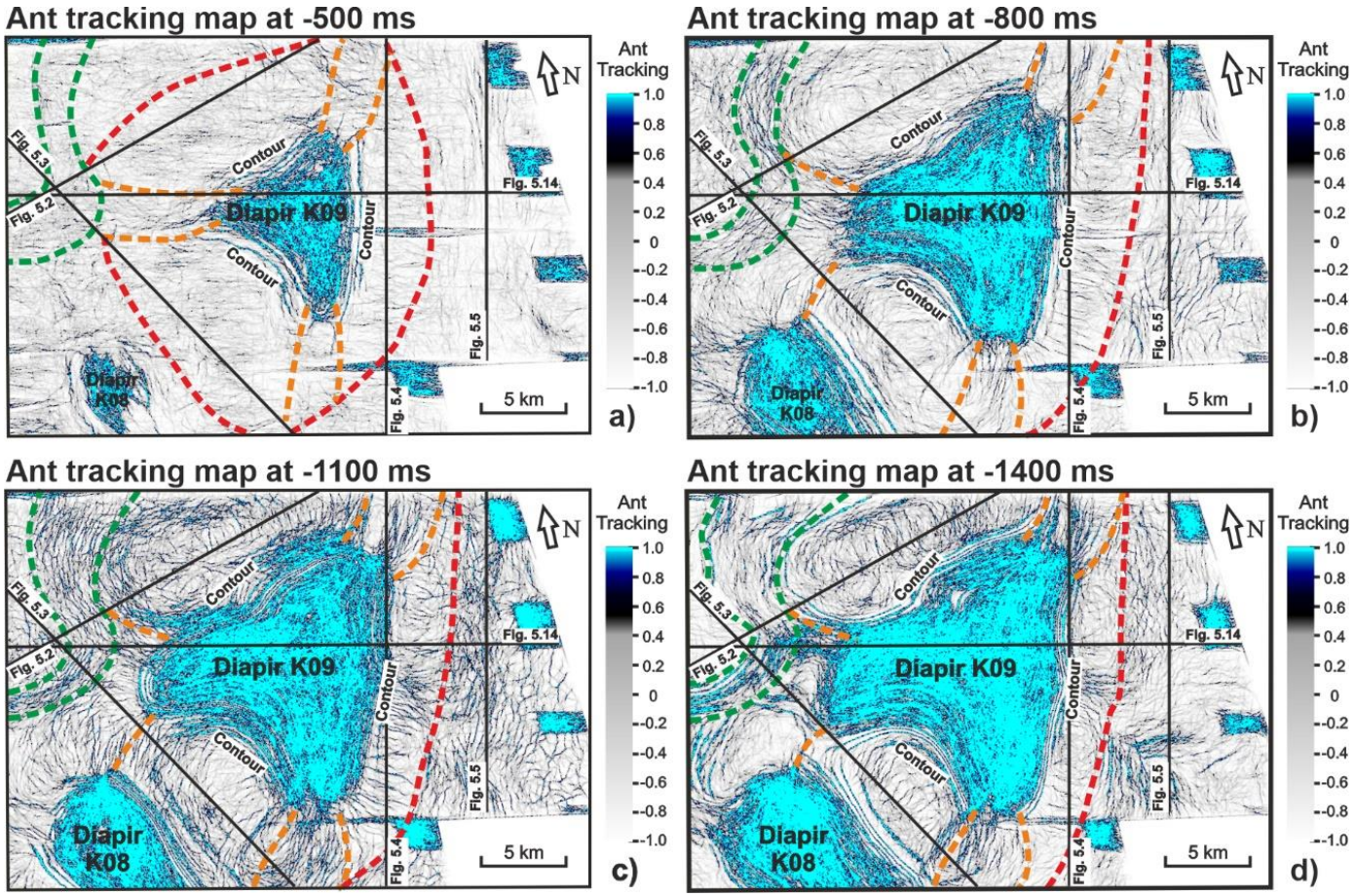

Fig. 5.13. Ant tracking maps at different depths in the study area, showing the width change of flanking and corner zones around salt diapir K09 with depth. Contour lines developed around diapir K09 indicates the areas in which strata are more folded and rarely crossed by faults. Six flanking or corner zones are separated by orange dash lines. The zones where polygonal and keystone faults were developed are bounded by red or green lines. a-d) Ant tracking maps at -500, -800, -1100 and -1400 ms, respectively. The seismic profiles shown in Figs. 5.2-5.5 and 5.14 are shown by black lines.

Diapir K09 continued its growth in the Paleogene, forming three salt-withdrawal basins around its flanks (Figs. 5.14 and 5.15). Significant halokinesis occurred between the Eocene and Oligocene in association with Pyrenean tectonic inversion (Harding and Huuse, 2015), indicating the occurrence of active diapirism. It generated an angular unconformity between the Lower and the Middle North Sea Groups (Horizon H9) (Figs. 5.14 and 5.15). It also caused local stress perturbations around diapir K09 during its rise, resulting in the alignment of adjacent polygonal faults (Fig. 5.8), and suggesting that diapir K09 was at or near the surface at this time (Fig. 5.15c).

Important halokinesis driven by active diapirism also occurred in the Oligocene and Miocene in association with Savian tectonic inversion, as revealed by the angular unconformity separating Paleogene from Neogene strata at the base of the Upper North Sea Group (Fig. 5.14). At this time, the three salt-withdrawal basins in the study area became shallower, denoting the gradual burial of diapir K09 (Figs. 5.2, 5.3, 5.14 and 5.15). With increasing deposition, diapir K09 was gradually covered by Neogene strata. It nevertheless continued to grow due to active diapirism in the Late Neocene and Quaternary, leading to important thinning of the Upper North Sea Group (Figs. 5.14 and 5.15a).

The triangular shape, in plan view, of diapir K09 is attributed to the existence of a large NE-striking Mesozoic fault zone and adjacent salt-withdrawal basins (Fig. 5.14). A large NE-striking fault zone controlled the morphology of the eastern flank of diapir K09 during the Mesozoic. With the later (Cenozoic) rise of diapir K09 and adjacent salt structures, its north and southwest flanks were formed due to the development of salt-withdrawal basins A and C. This also explains why the east flank of diapir K09 is less curved than its north and southwest flanks (Fig. 5.13).

As for the salt pillow in the study area, it was formed during Late Cretaceous tectonic inversion (Figs. 5.14 and 5.15), as suggested by the fact that the Chalk Group is relatively thin above this pillow. The salt pillow continued growing during the Paleogene, resulting in the further thinning of Lower North Sea Group above it (Figs. 5.14 and 5.15).

5.7.2 A model explaining how halokinesis controlled the formation and development of surrounding fault families

Halokinesis exerts an important control on the fault families surrounding diapir K09,

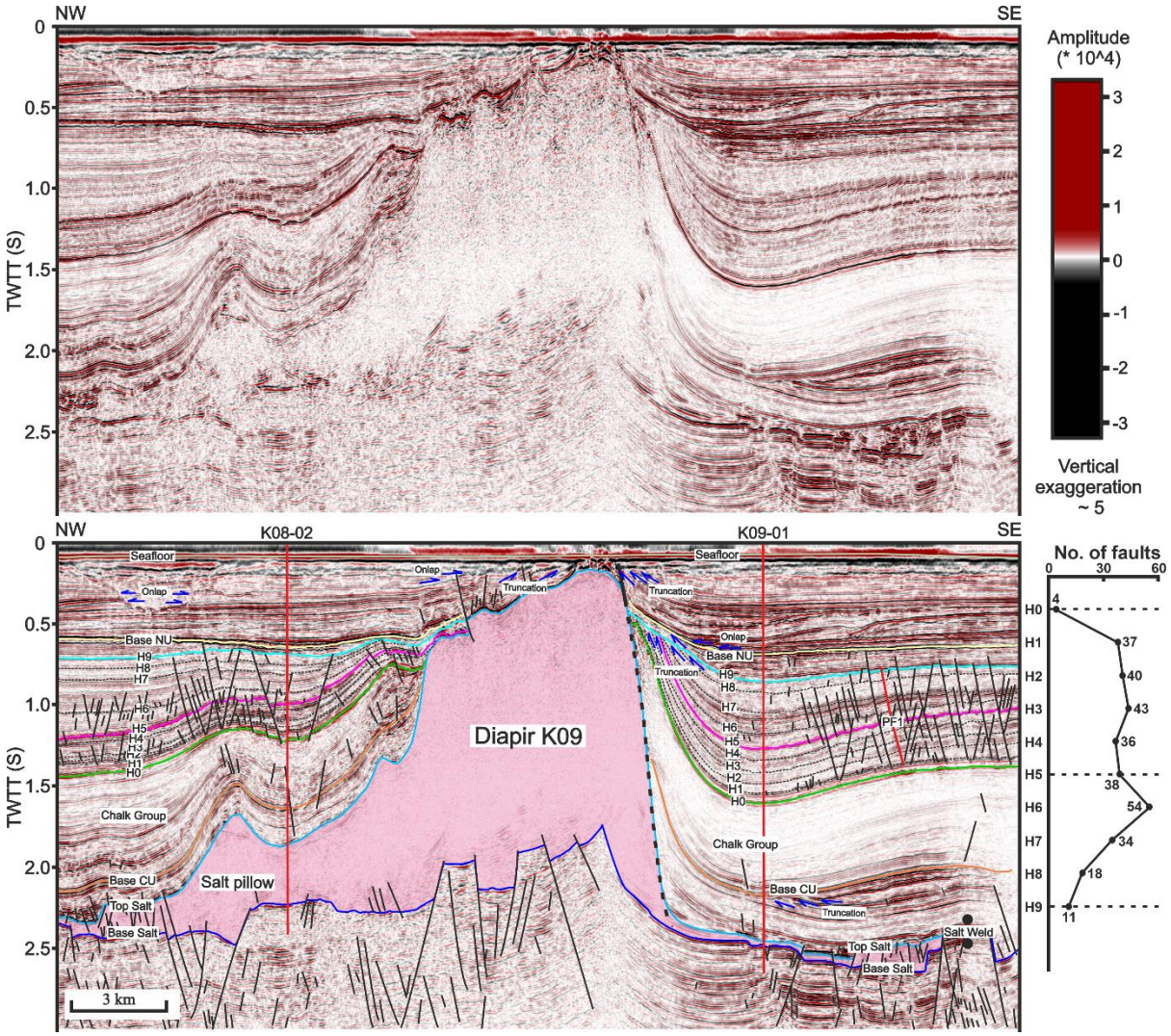

Fig. 5.14. Seismic profile across salt diapir K09 highlighting the thinning of strata towards it. Eight seismic horizons correlated with wells K08-02 and K09-01 are shown by different colour lines and labels, whereas seven other horizons are shown by black dash lines and labels. Faults are represented by black or red lines, including polygonal fault 1 (PF1). Wells K08-02 and K09-01 are shown by red bold lines. A salt weld is shown by two black circles. Plot on the right of seismic section shows the number of faults intersecting different horizons on the seismic profile. The location of the seismic profile is shown in Fig. 5.1. CU-Chalk Group

including on their geometries and strikes. In the study area, faults are well developed in Paleogene clay or shale, but their geometry, orientation and spacing show marked differences with depth (Fig. 5.6). Faults developed around diapir K09 have also experienced multiple evolution stages. This work suggests that halokinesis controlled the formation and growth of the interpreted fault families in three distinct stages (Fig. 5.15).

Stage 1, represented by the interval between horizons H0 and H5, records important halokinesis due to an increase in the thickness of sediment loading the salt-withdrawal basins surrounding diapir K09 (Fig. 5.15c). At the start of Stage 1, between horizons H0 and H2, halokinesis was moderate as limited Paleogene strata were deposited around diapir K09. Polygonal faulting predominated at this time, covering a large area of salt-withdrawal basin B and parts of salt-withdrawal basins A and C (Figs. 5.6g and h). These polygonal faults were randomly distributed in terms of their locations and strikes at this stage, but closely spaced and with small throws. Radial faults were limited to a small area near diapir K09, particularly within salt-withdrawal basin B (Figs. 5.6g and h). This basin was at this time only bounded by diapir K09, a character resulting in limited stretching during the rise of this salt structure (Figs. 5.1 and 5.6). Comparatively, salt–withdrawal basins A and C were also bounded by other salt structures; stretching associated with the rise of diapir K09 and adjacent salt structures affected a relatively large area in the two latter basins (Figs. 5.1 and 5.6).

Halokinesis was intensified between horizons H2 and H5 due to the deposition of increasing volumes of sediment around diapir K09. Thinning of strata is observed towards diapir K09 at a level between the two latter horizons (Fig. 5.14). Radial faults spanned a relatively wide area at this time as stretching produced by the rise of diapir K09 was also intensified (Figs. 5.6c-f). Some of these radial faults started to link with polygonal faults, as suggested by their T-Z plots, proving that radial faults were formed by distinct dip linkage of segments (Fig. 5.9). Comparatively, polygonal faults were limited to the eastern part of basin B (Figs. 5.6e and f). In addition, the length and spacing of polygonal faults were enhanced at the level of horizon H5 (Figs. 5.6e and f), where polygonal planforms are clearly observed (Figs. 5.6c and d). Polygonal faults in Tier 1 were aligned to the NE (Figs. 5.6e, 5.6f and 5.8h), a direction related to NW-SE extension caused by underlying salt withdrawal towards diapir K09.

Stage 2, represented by strata and structures between horizons H5 and H9, records significant halokinesis – likely due to the combined effect of Pyrenean tectonic inversion and sediment loading (Harding and Huuse, 2015) (Fig. 5.15b). Radial faults were developed in a relatively small area, and their number sharply decreased at this stage, likely due to the rapid

rise of diapir K09, which facilitated the folding of clayey and shaley strata adjacent to this structure, but inhibited the development of radial faults (Figs. 5.14 and 5.15) (e.g. Alsop et al., 2000). Moreover, the increase in overburden loading around diapir K09 resulted in a slight decrease in the width of the flanking and corner zones, as overburden loading controls the lateral limit of hoop stresses around salt diapirs (Carruthers et al., 2013). Hence, fewer radial faults were developed during Stage 2 when compared to Stage 1, while radial faults were developed in a smaller area. Radial faults were also linked to other faults in greater numbers, forming linked structures during Stage 2 (Fig. 5.4). These large radial faults offset horizons H0 to H9, with throw minima occurring near horizon H9 (Fig. 5.9). These throw minima suggest their upper tips are truncated by horizon 9, the regional unconformity associated with the Pyrenean inversion episode.

Similarly to Stage 1, polygonal faults were developed in the eastern part of basin B, and their number is higher at horizon H7 compared to horizons H3 and H5 (Fig. 5.6a and b). This is because many polygonal faults in Tier 2 crosscut horizon H7. Additionally, several polygonal faults were dip-linked with other polygonal faults, as shown by their T-Z plots (Fig. 5.10). During Stage 2, Polygonal faults in Tier 2 were also aligned to the NE due to halokinesis. Finally, keystone faults were developed above the salt pillow during this stage, accompanying Pyrenean tectonic inversion, and agreeing with the observation that most keystone faults are bounded by horizon H9. Keystone faults were also linked to other faults during Stage 2, as shown in T-Z data (Fig. 5.11).

Stage 3, comprising strata between horizon H9 and the seafloor, is characterised by a relative quiescence of halokinesis (Fig. 5.15a), as there was no major influence of tectonic inversion on the study area (Harding and Huuse, 2015). Although Savian tectonic inversion occurred at this stage, it had a minor influence when compared to the Pyrenean inversion (De Jager, 2003; De Lugt et al., 2003; De Lugt, 2007). Locally, sedimentation rates exceeded the rate of salt rise, resulting in the blanketing of diapir K09 by strata (Fig. 5.14). As a result, faults were mainly developed below horizon NU, the unconformity separating Paleogene and Neogene strata. Very few radial faults were formed around diapir K09, as halokinesis was minor, while polygonal faults stopped forming as relatively coarse sandy clay, silty sandstone and sandstone were deposited between horizon H9 and the seafloor. A few large keystone faults were developed by dip linkage during Savian tectonic inversion (Fig. 5.11), but their number is markedly lower than in Stage 2. Their upper tips were truncated by horizon NU, accompanying the abrupt throw minima observed in Fig. 5.11.

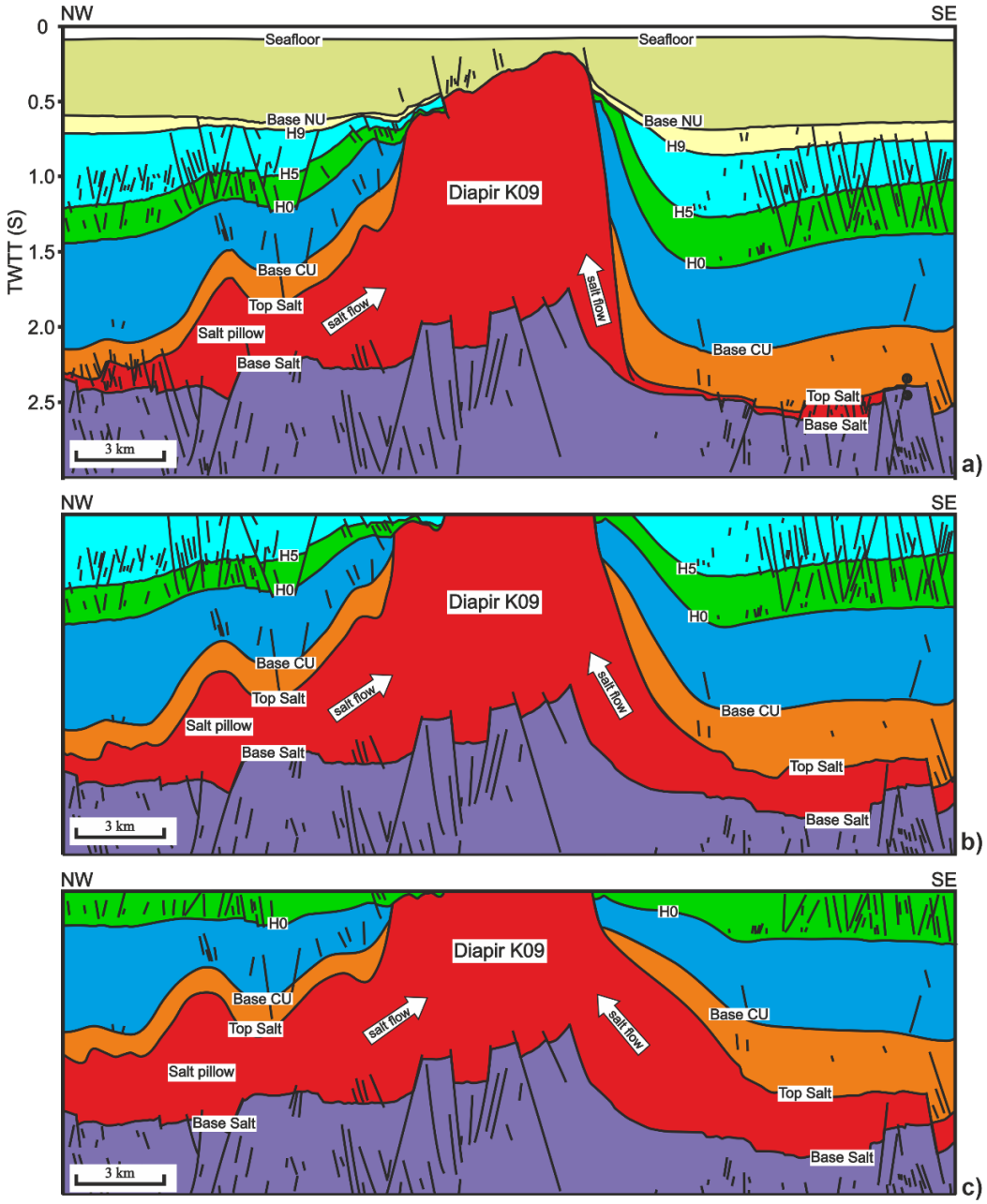

Fig. 5.15. Section showing the Cenozoic evolution of salt diapir K09 and surrounding faults in three structural stages. a) Stage 3 (between horizon H9 and the Seafloor) marks a relative quiescence of halokinesis, forming a few radial faults and keystone faults. b) Stage 2 (between horizons H5 and H9) records significant halokinesis, leading to the formation of a great number of radial faults and keystone faults, whereas polygonal faults are only limited to the southeast part of the section. c) Stage 1 (between horizons H0 and H5) is characterised by important halokinesis, causing the increasing number of radial faults, and polygonal faults start limiting to the southeast part of the section. The location of the section, depicted from Fig. 5.14, is shown in Fig. 5.1. Note this structural evolution only considers vertical movement, without considering lateral salt flow and compression due to structural inversion. CU-Chalk Group

5.7.3 Stress state around triangular salt diapirs

Diapir K09 developed as a rising triangular salt structure and was affected by two Cenozoic episodes of tectonic inversion. This led to the formation and development of multiple faults under a complex stress field. Stress inversions for the interpreted faults show that maximum principal palaeostresses (σ_1) were nearly vertical in all eight zones, whereas intermediate (σ_2) and least principal palaeostresses (σ_3) were sub-horizontal (Fig. 5.12; Table 5.2). This indicates that maximum principal stresses in all eight zones resulted from overburden loading. In addition, the combination of all minimum principal stresses obtained from radial faults show a triangular stress ring around diapir K09 (Fig. 5.12), implying that minimum principal stresses in all flanking and corner zones derived from local triangular stretching related to the rise of this diapir. Against this backdrop, strain in flanking zones shows marked differences when compared with corner zones. Strain in the flanking zones spans a much larger area than in corner zones (Fig. 5.12). The number of radial faults developed in flanking zones is also greater than in corner zones of diapir K09 (Table 5.1), proving that greater stretching occurred in the former (flanking) zones. Minimum principal stresses in flanking zones are naturally parallel to the flank of diapir K09, whereas in corner zones are normal to the direction of the corner bisector (Fig. 5.12). The corner radial faults are thus formed in a transition zone between two contiguous flanking zones. In addition, strata folding is more likely to be observed in flanking zones compared with corner zones, as shown by the distinct contour lines developed around diapir K09 (Fig. 5.13). These contour lines highlight the areas in which strata are more folded and rarely crossed by faults (Figs. 5.13, 5.14 and 5.16). Furthermore, flanking radial faults are usually deeper than corner radial faults (Fig. 5.6), and they are also steeper than the latter (Fig. 5.16). It implies that there are differential loading and compaction between flanking and corner zones, imposing important influences on their stress fields. Hence, the stress field around a triangular salt diapir is complex and significantly different to the relative homogeneous stress field of a circular salt diapir.

The width of the perturbed stress field around diapir K09 varied at different stages, leading to changes in the width of flanking and corner zones (Figs. 5.6 and 5.13). As the salt movement intensified, the width of flanking and corner zones increased (Figs. 5.6 and 5.13), indicating that the triangular-shaped stress rim also increased around the diapir. However, overburden loading can also impose an important influence on the width of the stress field around diapir K09. With the increase loading from overburden strata, a slight decrease in the width of this stress field is observed around this diapir (Figs. 5.6b and d). A character agrees with the

mechanism proposed by Carruthers et al. (2013) in which radial loading of overburden around a circular salt diapir controls the lateral limit of hoop stresses. However, in contrast to Carruthers et al. (2013), salt structures developed adjacent to diapir K09 have also largely influenced the stress field around this latter structure, though their importance was dependent on their position, distance and strike. For example, flanking zones 1 and 5 spanned a much broader area than zone 3 (Fig. 5.6), showing that the overlapping hoop stresses produced by adjacent salt structures and diapir K09, along similar strikes, increased the width of the stretching stress field in flanking radial zones 1 and 5. Comparatively, the stress field above the salt pillow was rarely influenced by diapir K09, as the minimum principal stress was nearly normal to the strike of the pillow (Fig. 5.12). The development of this salt pillow nevertheless limited the width of the extensional stress field produced by diapir K09 (Fig. 5.12).

Polygonal faults are mainly aligned in a NE-SW direction (Figs. 5.6, 5.8h and 5.8i), indicating they were influenced by local stresses. In the Paleogene, regional tectonic stresses in the study area were dominated by NW-SE compression (Ligtenberg et al., 2011; Van Ojik et al., 2020), which had a limited influence on fault strikes. However, minimum principal stresses estimated for the two polygonal fault tiers are also NW-SE striking, a direction normal to the boundary between the polygonal faults and flanking zone 3 (Fig. 5.12). As the forming time of radial faults and polygonal faults is contemporaneous, it shows the existence of stress compartmentalisation around salt structures. The extension direction estimated from polygonal faults corresponds to the movement direction of underlying salt, suggesting that the strike of polygonal faults was controlled by the movement of underlying salt towards diapir K09 (Fig. 5.15). Therefore, the rise of diapir K09 indirectly influenced the stress field in the outer part of flanking zone 3, resulting in the preferred alignment of polygonal faults in a NE-SW direction.

5.8 Chapter-specific conclusions

Chapter 5 aimed at understanding the palaeostress state around a rising triangular salt diapir, information with key implications to the carbon sequestration, gas storage and the production of subsurface oil and gas around salt diapirs. Faults developed around the rising diapir K09, located on the Cleaver Bank High, southern North Sea, were analysed in detail, and stress inversions were completed to reveal the palaeostress state around this salt structure. The main conclusions of this work can be summarised as follows:

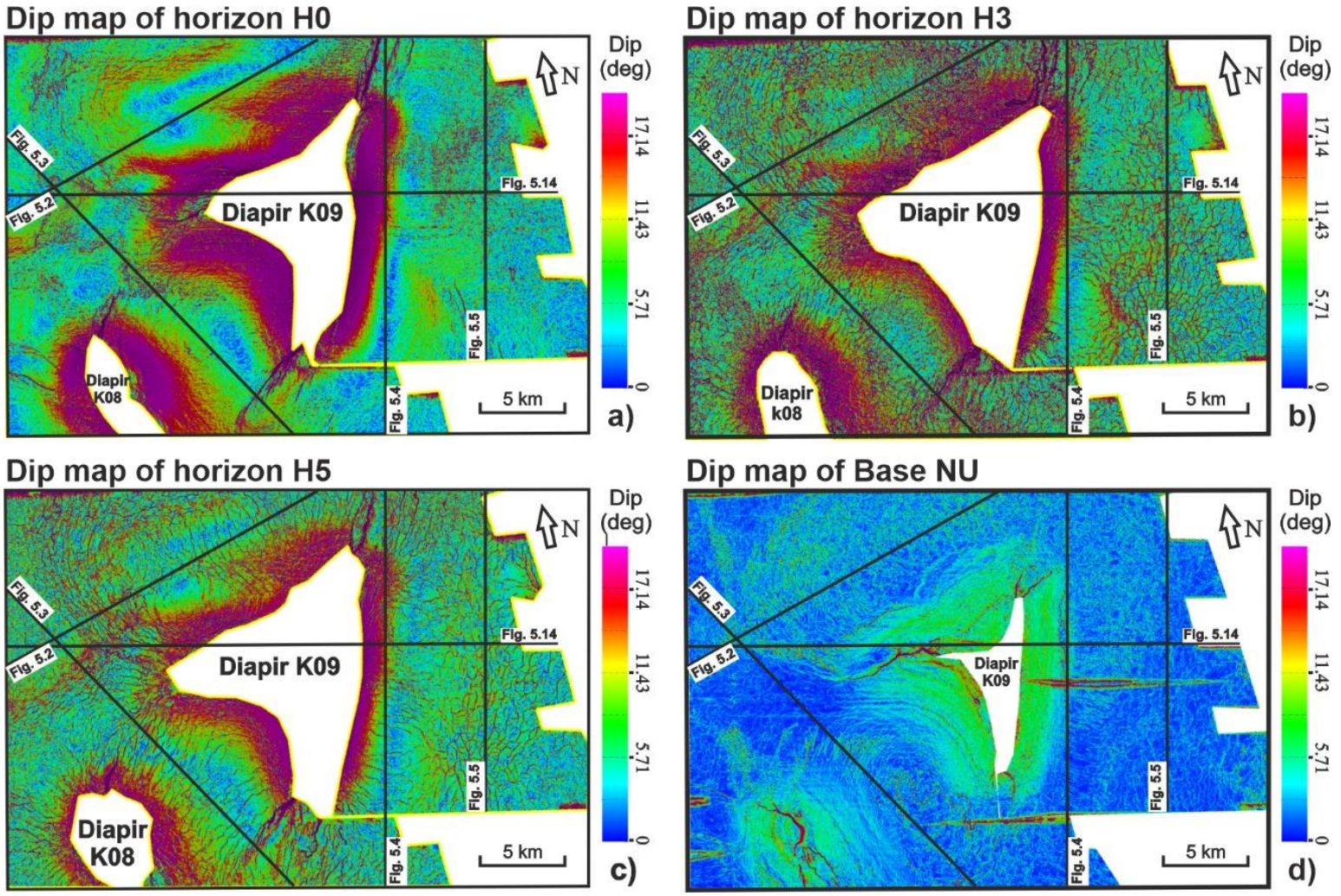

Fig. 5.16. Dip maps of key horizons in the study area, highlighting that dips in flanking zones are much larger than in corner zones at different horizons. a-d) Dip maps of horizons H0, H3, H5 and Base NU, respectively. The seismic profiles shown in Figs. 5.2-5.5 and 5.14 are shown by black lines. NU-Upper North Sea Group

a) Structures around diapir K09 include radial, polygonal and keystone faults, which are separated into eight distinct zones based on their geometry, strike and overall distribution. Radial faults were developed in flanking or corner zones as a way to accommodate stretching during the rise of diapir K09. Polygonal faults were preferentially aligned in the outer part of flanking zones. Keystone faults were mainly controlled by the rise of a salt pillow during Paleogene tectonic inversion.

b) Diapir K09 has experienced multiple phases of growth, with two of these being associated with Cenozoic tectonic inversion. Three salt-withdrawal basins were formed along the flanks of diapir K09. A salt pillow was developed during Late Cretaceous tectonic inversion and was amplified during Pyrenean and Savian tectonic inversion.

c) Halokinesis controlled the generation and growth of fault families in three structural stages. Stage 1 recorded the gradual intensification of halokinesis, resulting in an increase in the number of radial faults, while polygonal faults were limited to a small area. Stage 2 was characterised by significant halokinesis, leading to the formation of a great number of radial faults and keystone faults, whereas polygonal faults remained limited to a small area. Stage 3 marks the moderate halokinesis, forming a few radial faults and keystone faults.

d) Stress inversions for structures interpreted in each zone reveal that the maximum principal palaeostress is nearly vertical, whereas intermediate and minimum principal palaeostress are sub-horizontal. Palaeostresses in flanking zones are different from corner zones. The combination of minimum principal palaeostresses from all flanking and corner zones forms a triangular-shaped hoop stress ring around diapir K09.

e) The width of stress ring was not only associated with the growth of salt diapir, but also strongly influenced by adjacent salt structures. Minimum principal palaeostresses obtained from two tiers of polygonal faults were nearly normal to the boundary between the polygonal and radial faults due to local extension caused by halokinesis. Comparatively, the minimum principal palaeostress in the zone where keystone faults were developed is nearly normal to the strike of the salt pillow below, indicating they were nearly free of any stress perturbations caused by the rise of diapir K09.

Chapter 6

Contrasting influence of salt structures and faults on the geothermal potential of regional structural highs

6 Contrasting influence of salt structures and faults on the geothermal potential of regional structural highs

6.1 Abstract

High-quality 3D seismic reflection data, complemented by 448 bottom-hole temperatures (BHTs) from 48 boreholes, are used to investigate the influence of salt structures and faults on the geothermal potential of the Cleaver Bank High, Southern North Sea. Developed salt structures include multiple salt diapirs, salt pillows and a salt wall, with their presence influencing local geothermal potential; strata deposited above the Zechstein Group record geothermal gradients that are enhanced proportionally to the thickness of this salt unit. Conversely, strata buried below the Zechstein Group reveal a moderate decreasing trend in geothermal gradients as salt thickens. In parallel, large supra-salt faults can act as fluid paths to deep and hot fluid into shallow strata, resulting in the presence of the high geothermal gradients in shallow strata. Geothermal gradients on the footwall of these faults are much higher than that on the corresponding hanging-wall, decreasing as one moves away from them. For example, average geothermal gradients on the footwall of the largest supra-salt fault (Fault A) are, relative to its immediate hanging-wall, 105% higher in the North Sea Group, 26% higher in the Chalk Group, and 41% higher in the Rijnland, Upper and Lower Germanic Trias Groups. Additionally, sub-salt faults influence the geothermal gradient of supra-salt strata in parts of the study area where there is very thin, or even absent, salt (<100 ms; or ~230 m), forming distinct low-amplitude trails of fluid above these same faults. They also indirectly influence geothermal gradient by controlling the position, geometry and distribution pattern of salt structures. As a corollary, three potential geothermal exploration targets are suggested on the Cleaver Bank High, one located on the footwall of a large supra-salt fault, one above thick salt, and a third target above very thin Zechstein strata where low-amplitude fluid chimneys are found. The results in this work can be applied to similar salt-bearing structural highs in Northern Europe and worldwide.

6.2 Introduction

The use of geothermal energy for industrial and domestic purposes has increased for the past 35-40 years, accompanying an ever-rising demand for low-carbon energy (e.g. Gallup, 2009). Geothermal energy is commonly considered as an important and potential resource in many sedimentary basins (Erdlac Jr et al., 2007; Busby, 2014; Daniilidis and Herber, 2017; Alves et al., 2022), but its deployment is still limited when compared to other sources of energy due to its inherent high production and maintenance costs (Younger et al., 2012; Mijnlieff, 2020). Geothermal energy sites are also often affected by some of the drilling hazards occurring in conventional oil and gas fields, at the same time requiring reliable, long lasting hydraulic yields and appropriate water temperatures (ideally beyond 150^{o}C) to produce energy (Glaas et al., 2018; Vidal and Genter, 2018; Reinecker et al., 2019). Local geothermal gradient, reservoir architecture, lithology and industrial-scale water flow rate (or hydraulic yield) are particularly known geological factors controlling thermal energy output in many geothermal projects (Yang et al., 2000; Van Wees et al., 2012; Daniilidis and Herber, 2017; Reinecker et al., 2021).

A positive aspect concerns the fact that local geothermal gradients in sedimentary basins are greatly enhanced by the presence of buried salt intervals. This means that higher-than-normal temperatures occur above thick salt, and lower temperatures below, a phenomenon known as the 'chimney effect' (Jensen, 1983; Jensen, 1990; Wilson and Ruppel, 2007; Canova et al., 2018; Nolan, 2021). Such an effect results from salt having a thermal conductivity that is two to four times greater than in other sedimentary rocks (Zhuo et al., 2016; Jackson and Hudec, 2017; Raymond et al., 2022). In parallel, faults in sedimentary basins, including salt-rich basins, can play an important role in focusing heat and fluid in the upper crust. They may act as favourable migration paths for deep and hot fluid, resulting in local temperature anomalies at shallow depths (Wood et al., 2001; Cloetingh et al., 2010; Hinz et al., 2014; McLean et al., 2018).

Salt structures are well developed on the Cleaver Bank High and include salt diapirs, pillows and walls. Salt diapirs and walls reflect the presence of ductile salt masses piercing their overburden, with salt walls being more elongated than salt diapirs (e.g. Jackson and Hudec, 2017). Salt pillows are upwellings of salt with a concordant overburden that is parallel to the upper salt contact (e.g. Jackson and Hudec, 2017). Salt structures on the Cleaver Bank High experienced multiple phases of growth, and their distribution was controlled by NW-striking sub-salt faults (Oudmayer and De Jager, 1993; Remmelts, 1995). These NW-striking

sub-salt faults were intersected by conjugate NE-striking sub-salt faults, all of which record multiple phases of tectonic reactivation (Schroot and Haan, 2003; Ligtenberg et al., 2011; Van Ojik et al., 2020; Preiss and Adam, 2021; Brennan et al., 2023; Gaitan and Adam, 2023). In addition, a large number of supra-salt faults are observed on the Cleaver Bank High, having accommodated local stresses resulting from prolonged halokinesis (Ten Veen et al., 2012).

The aim of this work is to investigate the influence of salt structures and faults on the geothermal potential of the Cleaver Bank High, as an example of a regional structural high in the Southern North Sea. In summary, this work addresses the following research questions:

a) Is there an influence of salt structures on the geothermal potential of regional structural highs, such as the Cleaver Bank High?

b) How do faults developed on structural highs control the geothermal potential of sub- and supra-salt strata?

c) What potential geothermal exploration targets can be identified on the Cleaver Bank High?

6.3 Database and chapter-specific methods

The main data for this chapter is a 3D seismic volume from the southern margin of the Cleaver Bank High, Southern North Sea, and forty-eight (48) wells drilled in the study area are also used to provide geothermal data (Fig. 6.1). For a full description of the seismic and well data, see section 3.3.2. The seismic interpretation and well correlation applied in this chapter are described in sections 3.4 and 3.5. Five (5) key seismic-stratigraphic units are defined and correlated with borehole data (Figs. 3.2). Thickness maps for four (4) of these units are compiled to show major thickness variations associated with halokinesis and tectonic inversion. In addition, fault maps from four (4) key horizons, superimposed on the areas where the Zechstein Group is >400 ms, highlight the close relationship between faults and salt structures.

A total of 448 BHTs are gathered and analysed in this work based on the log header files and final borehole completion reports from 48 wells. Due to the fact that raw BHTs obtained from the well geophysical logs are usually cooler than true formation temperatures, BHTs are systematically corrected in this work (e.g. Chapman et al., 1984; Deming, 1989). A total of 12 BHTs (out of 448) acquired from sonic cement bond logs (CBLs) effectively represent the true formation temperature - CBLs commonly run from days to years after drilling,

recording the maximum BHT read by a thermometer, or probe (Holgate, 2005). The remaining 436 BHTs (out of 448) are corrected by applying the modelling tools provided by ZetaWare, Inc (Corrigan, 2003). The tools include three correction methods for BHTs, the Horner correction, the Time-Since-Circulation correction and the Last-Resort correction (Corrigan, 2003).

In this work, only three (3) out of 436 BHTs data are suitable for the Horner correction method. A total of 242 BHTs are suitable to be corrected by using the Time-Since-Circulation method, and the remaining 191 BHTs are simply corrected based on the Last-Resort correction method. In addition, measured depths (MDs) of 96 BHT data recorded from inclined boreholes are converted into true vertical depths (TVDs). Finally, corrected BHTs are tied in this work to the five interpreted seismic-stratigraphic units, so as to ensure that each of these units has more than 20 corrected BHTs.

Most wells terminate in the Upper Rotliegend or Limburg Groups, and gather most BHTs below the Zechstein Group, so this work was able to separate the Upper Rotliegend and Limburg Groups in terms of their geothermal potential. Geothermal gradients are calculated considering the seafloor temperature as 7.8^{o}C at a present-day water depth of 35 m (Defant, 1961; Evans and Coleman, 1974). Normal probability plots are compiled to calculate P90, P50 and P10 probabilities for the corrected BHTs and geothermal gradients in each stratigraphic unit (Table 6.1). P90 means that there is, at least, a 90% probability that the values will equal or exceed the low estimate for BHTs or geothermal gradients; P50 indicates at least a 50% probability that the values estimated will equal or exceed the best estimate for BHTs and geothermal gradients; P10 represents a 10% probability of the calculated values to equal or exceed the higher estimate for BHTs and geothermal gradients. In addition, vertical depth is plotted against corrected BHT and geothermal gradient to highlight any depth-dependent changes.

Subsidence and thermal models (1D modelling on PetroMod® 2021) for wells K11-10, K11-02 and K12-12 are used to investigate the burial and thermal histories of the Cleaver Bank High. Stratigraphic units recorded in well completion logs, and their corresponding lithologies, are obtained from the Dutch Oil and Gas portal (NLOG). Main uplift and erosion phases are considered in the study area, especially the Saalian and Mid-Late Kimmerian events. The amount of eroded material is estimated based on the erosion maps published by Fattah et al. (2012b), assuming that the depositional thicknesses of the Step Graben Formation, the Hospital Ground Formation, the Altena Group, the Upper Germanic Trias Group and the Lower Germanic Trias Group are 50, 200, 200, 400 and 500 m, respectively. Palaeo water depth curves are compiled based on the published literature (Fattah et al., 2012b) as well as the lithologies

and depositional environments recognised for specific units. The palaeo temperature at the sediment water interface (SWIT) is calculated with an integrated PetroMod tool, which considers the palaeo water depth and the evolution of ocean surface temperatures through time depending on palaeo-latitude of the study area.

Basal heat flow is obtained from Fattah et al. (2012b) where basal heat flow for well K01-02 is calculated using the 1D tectonic heat flow modelling tool PetroProb (Van Wees et al., 2009). This is because well K01-02 is close to (~45 km in distance) wells K11-10, K11-02 and K12-12 in this work, with very similar geological conditions and burial histories on the Cleaver Bank High. Thermal conductivity values are calculated in this work based on a predefined thermal conductivity model - the Sekiguchi Model on PetroMod® 2021. The radiogenic heat production is calculated for the rock matrices for each of the lithologies. The compaction model is based on the Hydrostatic Athy's law Model where the porosity versus depth curve is a theoretical curve that assumes a hydrostatic pressure and a uniform lithological column. The initial geological model does not include faults and assumes open fluid flow boundaries. Temperature simulations run assuming hydrostatic conditions and only conductive heat flow is assumed in the model. Salt movement and, as a consequence, any related thermal effects are not considered in the models. Nevertheless, modelled present-day temperatures and corrected BHTs are provided, and these are able to highlight the temperature differences between them, and the influence of faults on local temperatures. Vertical thermal conductivities are shown, indicating the influence of lithology variations on geothermal gradients.

Temperature and geothermal gradient maps, which are compiled for specific stratigraphic intervals so to highlight the influence of salt structures on geothermal potential. Temperature maps are calculated using BHTs gathered around the horizon of interest, within an interval 200 m above or below this latter. Average geothermal gradients are used to compile geothermal gradient maps when there is more than one temperature measurement for a particular stratigraphic interval. This work notes that anisotropy effects of deviated wells were not considered when compiling these maps; hence, temperature and geothermal gradient maps compiled in this work are not 100% accurate. Nevertheless, corrected BHTs and geothermal gradients from wells located around faults are recorded in two specific tables, highlighting the influence of faults on the geothermal potential of the study area (Tables 6.2 and 6.3).

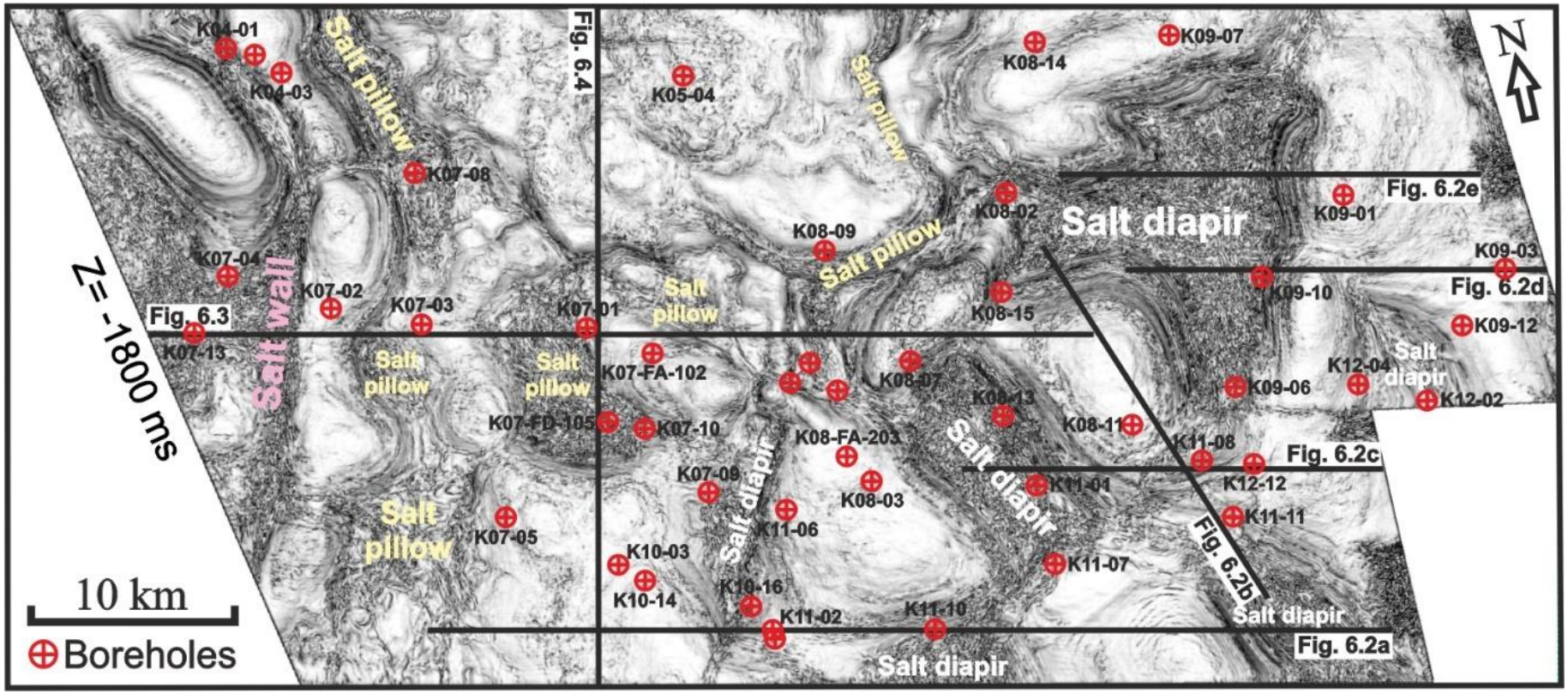

Fig. 6.1. Variance map (Z = -1800 ms two-way time) of the study area, highlighting the position of different salt structures developed in the study area. Boreholes are separately shown by a red cross and circle, and the seismic profiles in Figs. 6.2-6.4 are shown as black lines. The location of this map is indicated in Fig. 2.5.

6.4 Seismic stratigraphy

6.4.1 Unit 1 (Pre-Zechstein Group)

Unit 1 is bounded at its top by horizon H0, a high-amplitude seismic reflection that correlates with the base of the Zechstein Group (Figs. 6.2-6.4). Its base is delimited by the acoustic basement, which occurs at a depth of ~3000 ms two-way travel time (twtt). Unit 1 comprises a ~750 ms thick package with low- to high-amplitude seismic reflections. Sub-salt strata, especially those below thick salt, are usually of low amplitude and show local velocity pull-ups (Figs. 6.2-6.4).

Most wells drilled in the study area terminate within the Upper Rotliegend or Limburg Groups. Dominant lithologies include sandstone, sandy clay and shale. Gamma-ray and density values change dramatically with depth, indicating sharp lithological changes in these two stratigraphic groups (Fig. 3.2). Sub-salt faults are ubiquitous, and most propagate upwards through horizon H0. However, their lower tips are usually hard to observe in seismic data as many sub-salt faults propagate below the acoustic basement (Figs. 6.2-6.4).

6.4.2 Unit 2 (Zechstein Group)

Unit 2 is the primary seismic interval of interest to this study, correlating directly with the Zechstein Group. Its base coincides with horizon H0, whereas its top is horizon H1, a high-amplitude reflection (Figs. 6.2-6.4). Unit 2 consists of chaotic to transparent seismic reflections, though it locally shows distinct high-amplitude reflections. The thickness of Unit 2 varies from 0 ms in salt welds to over 1600 ms in salt diapirs (Figs. 6.2-6.4 and 6.6).

Unit 2 is mainly composed of salt with low gamma-ray and density values (Fig. 3.2). However, its upper boundary includes a thin layer of claystone, which in some areas presents high gamma-ray values and low density values (Fig. 3.2). Dolomite stringers – the high-amplitude features previously mentioned as occurring within salt – are also observed in Unit 2, but are fragmented and gently folded. Faulting is common at its base, but its top is less compartmentalised, except in the northern part (Figs. 6.5 and 6.7). In some areas where thin salt exists, large sub-salt faults propagate into supra-salt strata (Figs. 6.2-6.4).

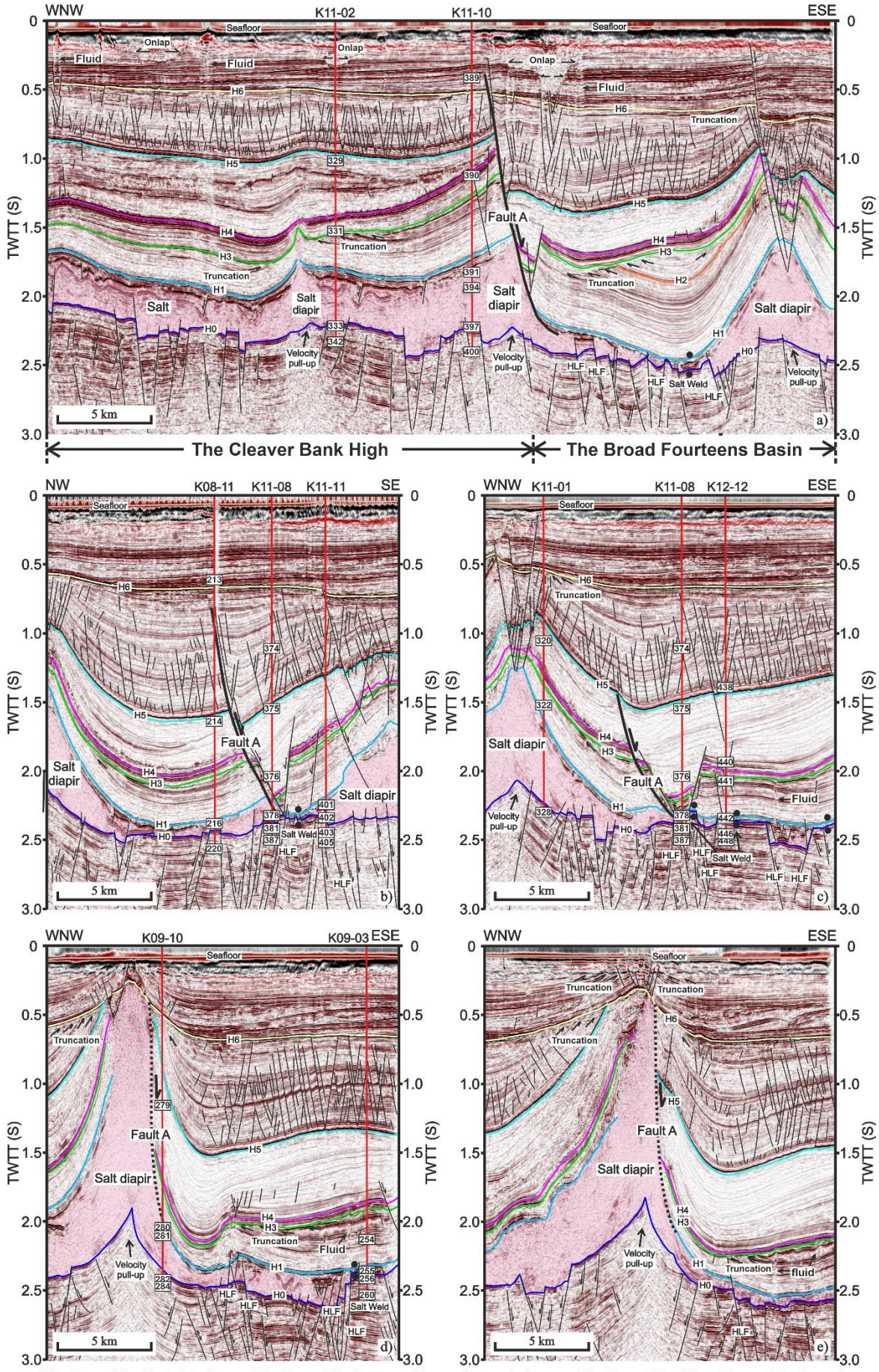

H0 = Base of the Zechstein Group; H1 = Base of the Upper and Lower Germanic Groups; H2 = Base of the Altena Group; H3 = Base of the Rijnland Group; H4 = Base of the Chalk Group; H5 = Base of the Lower North Sea Group; H6 = Base of the Upper North Sea Group

Fig. 6.2. (Previous page) TWTT seismic profiles across the largest NE-striking supra-salt fault (Fault A), showing multiple salt structures, faults and fluid flow paths. Eight seismic horizons correlated with eight wells are shown by different colour lines and labels, and faults are presented with black lines. The figures highlight the two largest salt diapirs in the study area, which are bounded by a large supra-salt fault, Fault A. This fault separates the Cleaver Bank High from the Broad Fourteens Basin. Salt diapirs have irregular geometries, different heights and widths. The location of the seismic profiles is shown in Fig. 6.1. Labels on the borehole trajectories indicate the depth of BHTs numbered in Appendix B. HLF=Hard-linked fault

6.4.3 Unit 3 (Rijnland, Upper and Lower Germanic Trias Groups)

Unit 3 is bounded at its base by horizon H1, whereas its top is delimited by horizon H4, a high-amplitude reflection correlating with the base of the Chalk Group (Figs. 6.2-6.4). On the Cleaver Bank High, Unit 3 includes the Rijnland (KN), Upper (RN) and Lower (RB) Germanic Trias groups, plus the Altena Group (AT) in the small portion of the Broad Fourteens Basin covered by the 3D seismic volume (Fig. 6.2a). The Altena and Rijnland Groups are bounded at their bases by horizons H2, H3, respectively (Figs. 6.2-6.4). Unit 3 consists of low-amplitude to transparent seismic reflections in its lower part, changing to high-amplitude seismic reflections at its top (Figs. 6.2-6.4). Seismic reflections are often truncated beneath the Rijnland Group, marking an angular discontinuity between the Rijnland and the Germanic Trias Groups (Figs. 6.2-6.4). The thickness of Unit 3 ranges from 0 to 900 ms, showing a marked increase towards the south (Fig. 6.6).

Unit 3 consists of shales and marls, but thin anhydrite has also been recorded at borehole (Fig. 3.2). Variable gamma-ray and density values dominate this unit. Faults are not common, except for a few large faults, and crestal faults above salt structures (Figs. 6.2-6.5). Nevertheless, small faults are developed around the base of Unit 3 in the northern part of the study area (Figs. 6.5 and 6.7).

6.4.4 Unit 4 (Chalk Group)

The base of Unit 4 coincides with horizon H4, and its top is horizon H5, a high-amplitude reflection that correlates with the base of the Lower North Sea Group (Figs. 6.2-6.4). Unit 4 comprises low-amplitude to transparent seismic reflections in the eastern part of

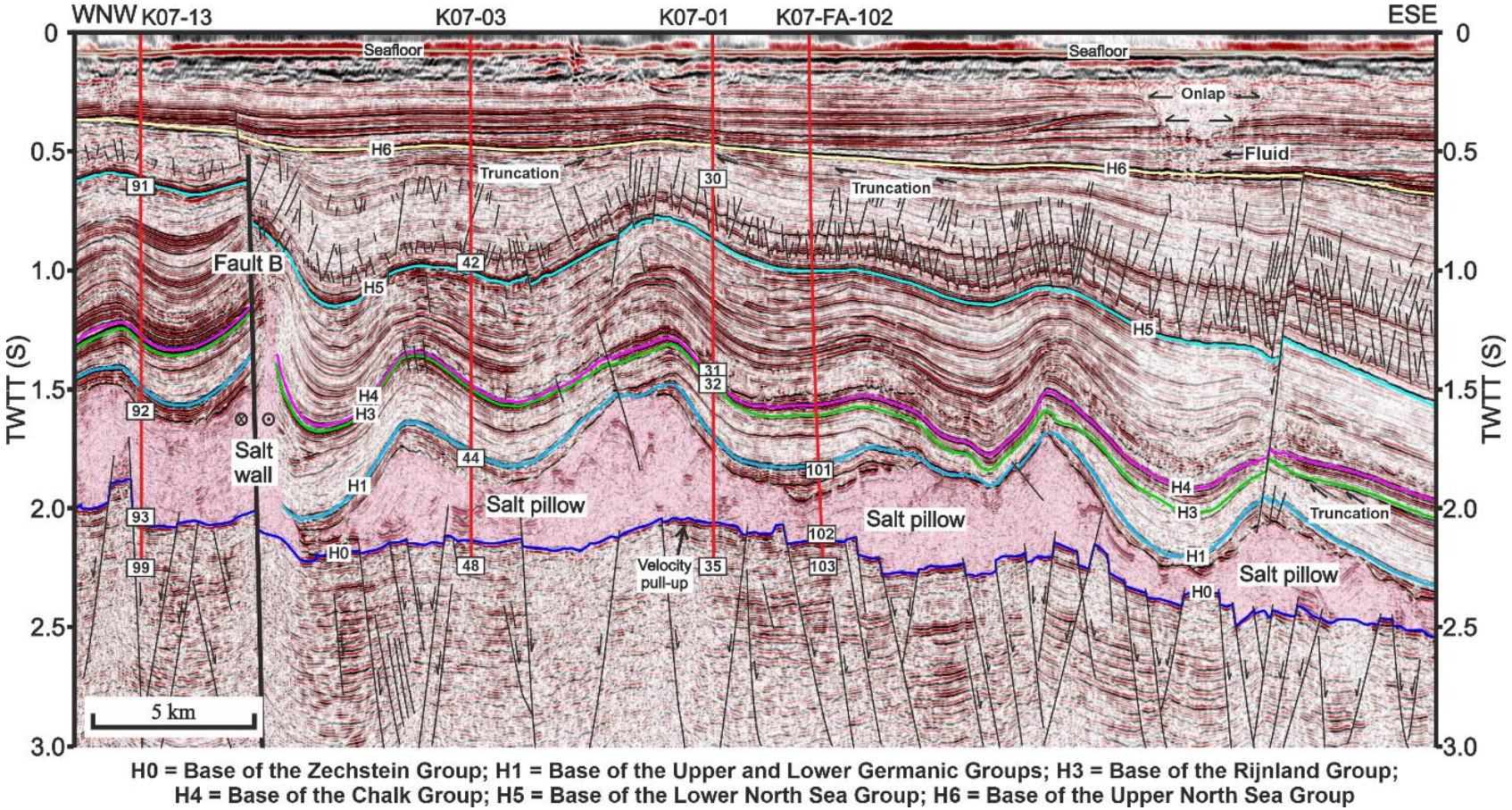

Fig. 6.3. TWTT seismic profile across the largest NE-striking hard-linked fault (Fault B), showing multiple salt structures, faults and fluid flow paths. Seven seismic horizons correlated with four wells are shown by different colour lines and labels, and faults are presented with black lines. Fault B is a large NE-striking dextral strike-slip fault, which is near vertical and propagated from sub-salt units into the North Sea Group. Salt pillows and wall have shown different geometries, heights and widths. The location of the seismic profile is shown in Fig. 6.1. Labels on the borehole trajectories indicate the depth of BHTs numbered in Appendix B.

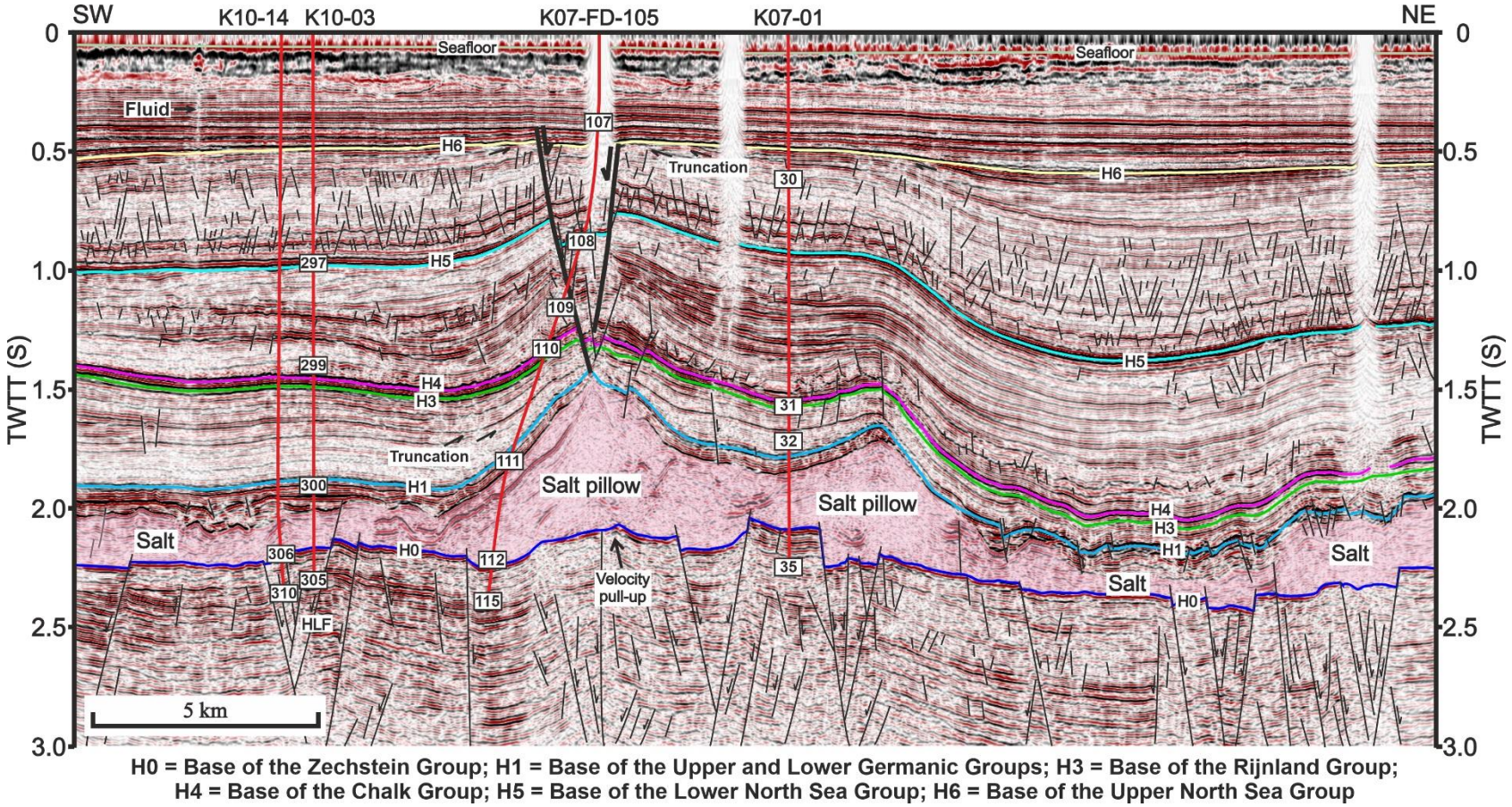

Fig. 6.4. TWTT seismic profile across the large NW-striking crestal faults, showing multiple salt structures and faults. Seven seismic horizons correlated with four wells are shown by different colour lines and labels, and faults are presented with black lines. Two large crestal faults are imaged near Well K07-FD-105, propagating into the Upper North Sea Group. These crestal faults influence the geothermal gradient distribution around the salt pillows in the figure, as Table 6.3 denotes high geothermal gradients next to these faults. The location of the seismic profile is shown in Fig. 6.1. Labels on the borehole trajectories indicate the depth of BHTs numbered in Appendix B. HLF=Hard-linked fault

the study area, changing to moderate- to high-amplitude seismic reflections in the west (Figs. 6.2-6.4). Its thickness is relative uniform, with an average value of 650 ms, though local strata thinning is observed near salt structures (Figs. 6.2-6.4).

Unit 4 is mainly composed of chalk and limestone with low gamma-ray and high density values (Fig. 3.2). Thin marl intervals have also been drilled in this unit. Similarly to Unit 3, faulting is scarce, except for a few large faults, and crestal faults above salt structures (Figs. 6.2-6.5).

6.4.5 Unit 5 (North Sea Group)

Unit 5 is bounded at its base by horizon H5, whereas its top coincides with the seafloor (Figs. 6.2-6.4). This unit includes the Upper (NU), Middle (NM) and Lower (NL) North Sea Groups. The base of the Upper North Sea Group is marked by horizon H6. Its thickness ranges from 100 to over 1600 ms, showing low-amplitude to transparent seismic reflections in its lower part, but moderate- to high-amplitude seismic reflections towards the top (Figs. 6.2-6.4). Strata in Unit 5 thins out on the flanks of salt structures, especially next to the large salt diapirs (Figs. 6.2-6.4 and 6.6).

Unit 5 is composed of siliciclastic sediments, with high gamma-ray and low density values in its lower part, but low gamma-ray in its upper part (Fig. 3.2). The unit comprises claystone and shale in its lower part, but sandy clay and sandstone in its upper part. Faulting is common in its lower part, especially where polygonal faults are present, but most are delimited by horizon H6 (Figs. 6.2-6.4). There are also multiple crestal faults above salt structures, propagating from Unit 4 (Figs. 6.2-6.5).

6.5 Salt structures and fault families on the Cleaver Bank High

6.5.1 Geometry and spatial pattern of salt structures

Salt structures on the Cleaver Bank High have experienced multiple phases of growth, with their geometry and distribution revealing important differences. Salt diapirs are mainly developed in the eastern and south eastern sectors of the study area, showing triangular or sub-

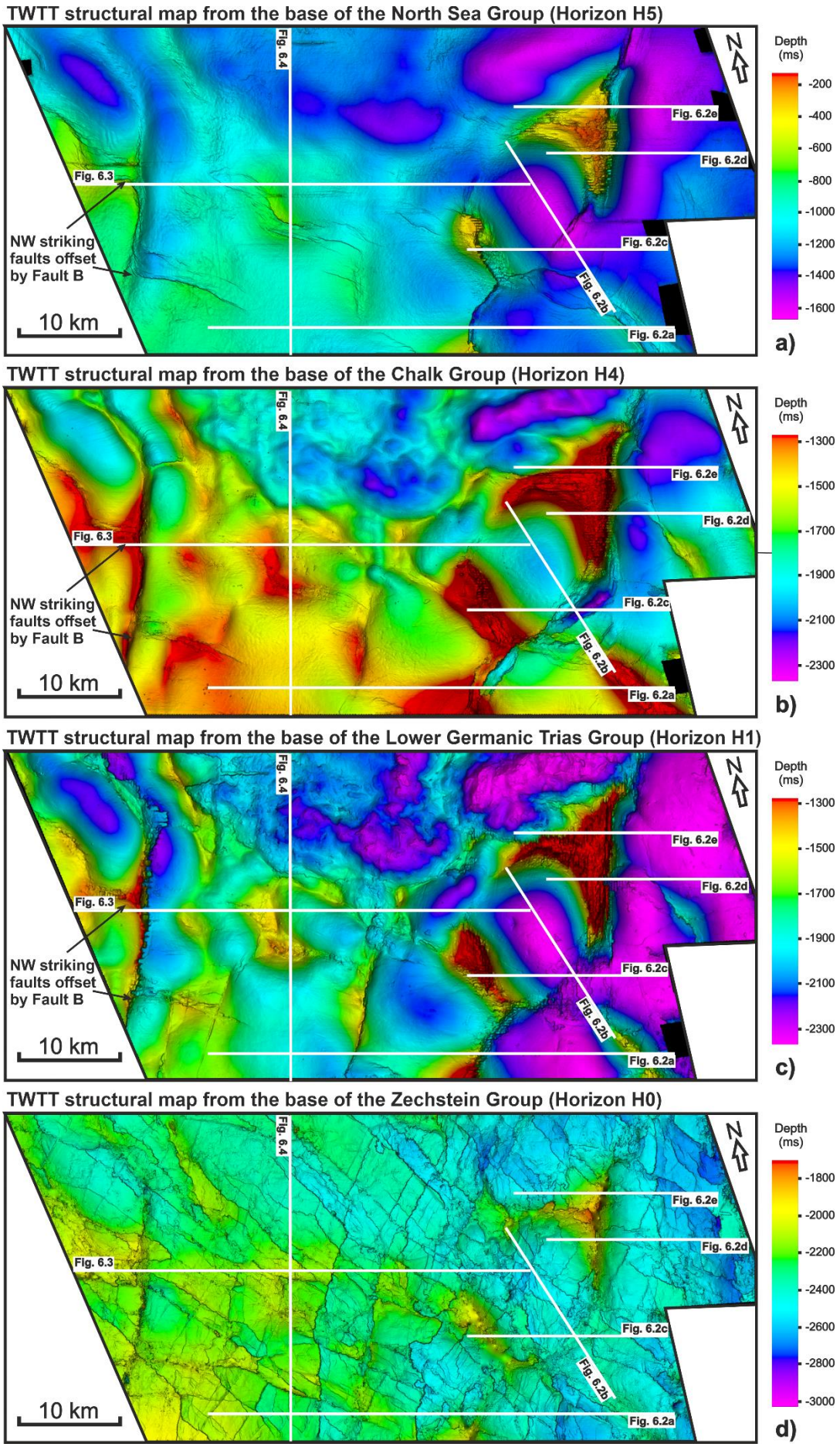
TWTT structural map from the base of the North Sea Group (Horizon H5)
Fig. 6.4
Fig. 6.2e
Fig. 6.2d
Fig. 6.3
NW striking faults offset by Fault B
Fig. 6.2c
Fig. 6.2b
Fig. 6.2a
10 km
N
Depth (ms)
-200
-400
-600
-800
-1000
-1200
-1400
-1600
a)
TWTT structural map from the base of the Chalk Group (Horizon H4)
Fig. 6.4
Fig. 6.2e
Fig. 6.2d
Fig. 6.3
NW striking faults offset by Fault B
Fig. 6.2c
Fig. 6.2b
Fig. 6.2a
10 km
N
Depth (ms)
-1300
-1500
-1700
-1900
-2100
-2300
b)
TWTT structural map from the base of the Lower Germanic Trias Group (Horizon H1)
Fig. 6.4
Fig. 6.2e
Fig. 6.2d
Fig. 6.3
NW striking faults offset by Fault B
Fig. 6.2c
Fig. 6.2b
Fig. 6.2a
10 km
N
Depth (ms)
-1300
-1500
-1700
-1900
-2100
-2300
c)
TWTT structural map from the base of the Zechstein Group (Horizon H0)
Fig. 6.4
Fig. 6.2e
Fig. 6.2d
Fig. 6.3
Fig. 6.2c
Fig. 6.2b
Fig. 6.2a
10 km
N
Depth (ms)
-1800
-2000
-2200
-2400
-2600
-2800
-3000
d)

Fig. 6.5. (Previous page) TWTT structural maps for four key horizons in the study area, including the base of the North Sea Group (Horizon H5), Chalk Group (Horizon H4), Lower Germanic Trias Group (Horizon H1) and Zechstein Group (Horizon H0), respectively. a-c) Maps with the position and spatial distribution of salt structures and supra-salt faults, highlighting the influence of halokinesis on the depth variation of overlying horizons. d) Map showing the spatial distribution of sub-salt faults that mainly consist of NW- and NE-striking faults. The location of the seismic profiles shown in Figs. 6.2-6.4 is shown by the white lines. The position and distribution of salt structures and faults in this figure is indicated in Fig. 6.7.

circular shapes in plan view (Fig. 6.1). The distribution of salt diapirs mainly strikes to the NW and NE, similarly to sub-salt faults (Figs. 6.5-6.7). The two largest salt diapirs in the study area are bounded by a large NE-striking supra-salt fault separating the Cleaver Bank High from the Broad Fourteens Basin (Figs. 6.2, 6.5 and 6.7). This fault is herein named 'Fault A' as it is one of the main structures in the study area (Fig. 6.7). On seismic profiles, salt diapirs have irregular geometries with differing heights and widths (Fig. 6.2). Their height ranges from ~700 to over 1600 ms twtt that is much higher than salt pillows (Fig. 6.6d).

Salt pillows are developed in the western and middle sector of the study area, showing rhomboid to rectangular shapes in plan view (Fig. 6.1). Similarly to the salt diapirs mentioned above, they are also NW- to NE-striking. On seismic profiles, they overlie many NW- and NE-striking sub-salt faults (Figs. 6.2-6.4 and 6.7). Their heights vary from 200 to 850 ms twtt, values that are lower than those of the salt diapirs (Figs. 6.3 and 6.4). In addition, a single salt wall occurs in the western sector of the study area in association with a large NE-SW strike-slip fault (Figs. 6.1 and 6.3). This large strike-slip fault is herein named 'Fault B' as it is one of the main structures in the study area (Fig. 6.7). The salt wall has a width of ~2.5 km, spanning a limited area in the study area. The salt wall shows a taper shape on seismic profiles, and is ~700 ms twtt tall (Figs. 6.2-6.4).

6.5.2 Faults developed on the Cleaver Bank High

Faults are common on the Cleaver Bank High and can be separated into three groups based on their spatial distribution and stratigraphic position relative to the Zechstein Group: a) sub-salt, b) supra-salt and c) hard-linked faults. Supra-salt faults are faults developed above the

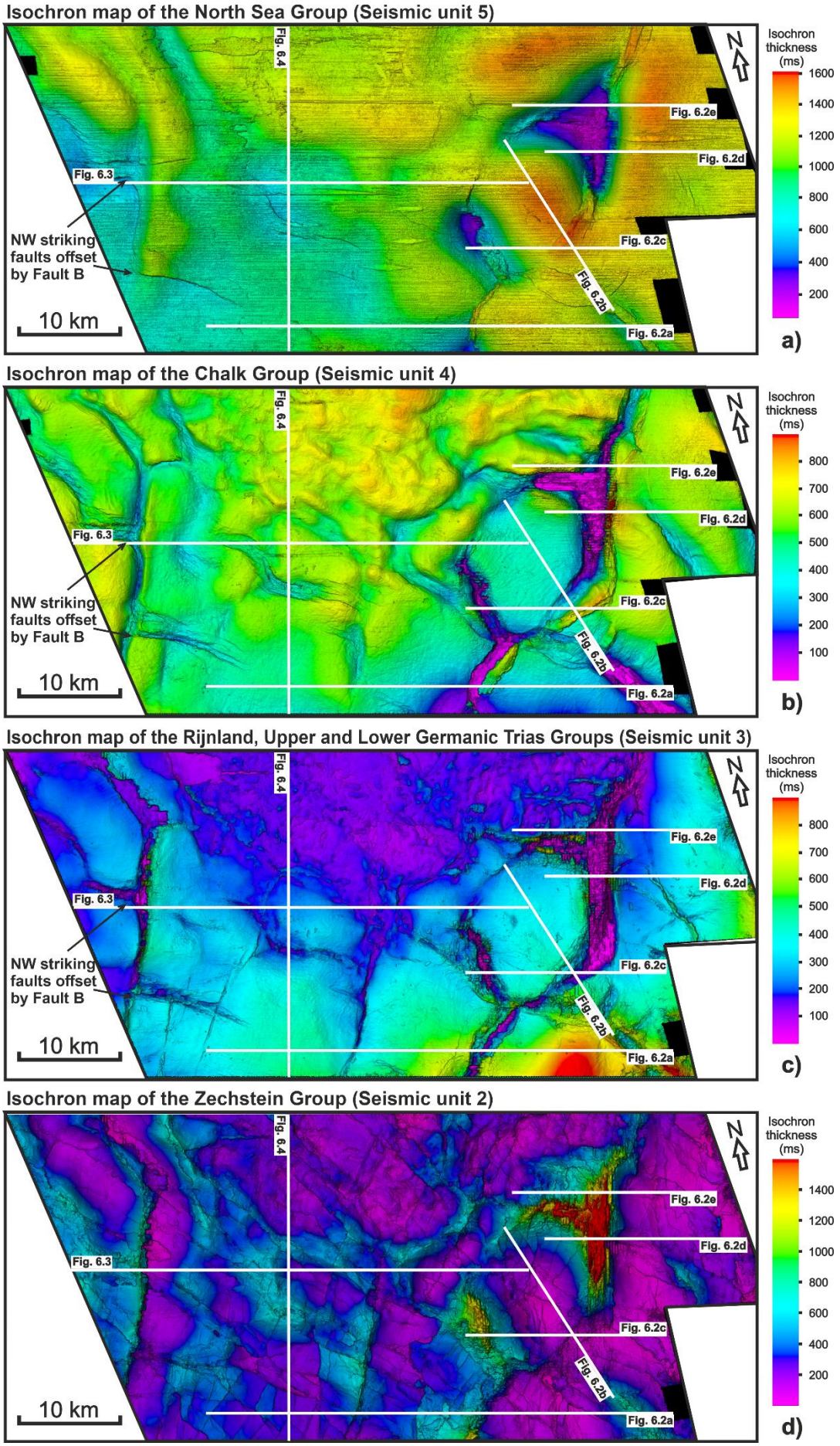
Isochron map of the North Sea Group (Seismic unit 5)
Fig. 6.4
Fig. 6.2e
Fig. 6.2d
Fig. 6.3
Fig. 6.2c
Fig. 6.2b
Fig. 6.2a
NW striking faults offset by Fault B
10 km
N
Isochron thickness (ms)
1600
1400
1200
1000
800
600
400
200
a)
Isochron map of the Chalk Group (Seismic unit 4)
Fig. 6.4
Fig. 6.2e
Fig. 6.2d
Fig. 6.3
Fig. 6.2c
Fig. 6.2b
Fig. 6.2a
NW striking faults offset by Fault B
10 km
N
Isochron thickness (ms)
800
700
600
500
400
300
200
100
b)
Isochron map of the Rijnland, Upper and Lower Germanic Trias Groups (Seismic unit 3)
Fig. 6.4
Fig. 6.2e
Fig. 6.2d
Fig. 6.3
Fig. 6.2c
Fig. 6.2b
Fig. 6.2a
NW striking faults offset by Fault B
10 km
N
Isochron thickness (ms)
800
700
600
500
400
300
200
100
c)
Isochron map of the Zechstein Group (Seismic unit 2)
Fig. 6.4
Fig. 6.2e
Fig. 6.2d
Fig. 6.3
Fig. 6.2c
Fig. 6.2b
Fig. 6.2a
10 km
N
Isochron thickness (ms)
1400
1200
1000
800
600
400
200
d)

Fig. 6.6. (Previous page) Isochron maps for four key seismic-stratigraphic units in the study area, including the North Sea Group (Seismic unit 5), Chalk Group (Seismic unit 4), Rijnland, Upper and Lower Germanic Trias Groups (Seismic unit 3) and Zechstein Group (Seismic unit 2), respectively. a-c) Maps showing the thickness variation in three supra-salt stratigraphic units, marking the thinning of strata towards salt structures. d) Map highlighting the thickness variation in the Zechstein salt, and the distribution of salt structures. The location of the seismic profiles in Figs. 6.2-6.4 is shown by the white lines.

Zechstein Group. Sub-salt faults are faults developed beneath the Zechstein Group, and do not cross its top boundary. Hard-linked faults are faults originating beneath the Zechstein Group that propagate directly, or are linked, to structures in supra-salt strata.

6.5.2.1 Supra-salt faults

A large number of supra-salt faults are developed in the study area, but most are restricted to the North Sea Group, especially the Middle and Lower North Sea Groups (Figs. 6.2-6.5). Faults in the North Sea Group were formed in the Cenozoic, including salt-related and polygonal faults (Figs. 6.2-6.5 and 6.7). Salt-related faults are developed around salt structures, accommodating the stress produced due to the growth of these structures. Conversely, polygonal faults are usually developed away from salt structures, formed by the volumetric contraction of very fine-grained sediments compacting and dewatering during the initial burial phases of strata (Cartwright and Lonergan, 1996; Cartwright et al., 2003). Although faults are abundant in the North Sea Group, they are developed in strata at a depth shallower than ~1670 ms twtt (Figs. 6.2-6.5).

A few large supra-salt faults cross strata above the Zechstein Group (Figs. 6.2-6.5). They detach on the top of the Zechstein Group evaporites and may even propagate into these latter (Figs. 6.2-6.5). These large supra-salt faults are mainly NE- and NW-striking, the largest of which are NE-striking and formed due to NW-SE Mesozoic extension (Figs. 6.7a-c). They have also experienced multiple phases of activity during the Mesozoic and Cenozoic (Figs. 6.2 and 6.3). The larger NE-striking faults are mainly located along the boundary of thick salt intervals (>400 ms) (Figs. 6.2-6.5 and 6.7). Comparatively, NW-striking supra-salt faults are usually developed above salt structures, locally showing en echelon arrangement (Figs. 6.2-

Faults at the base of the North Sea Group (Horizon 5) and Zechstein salt (>400 ms thick)

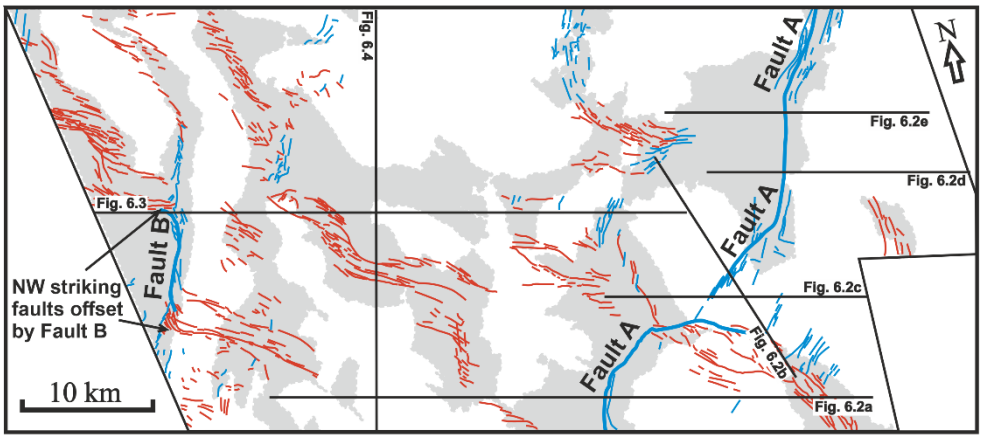

a)

Faults at the base of the Chalk Group (Horizon 4) and Zechstein salt (>400 ms thick)

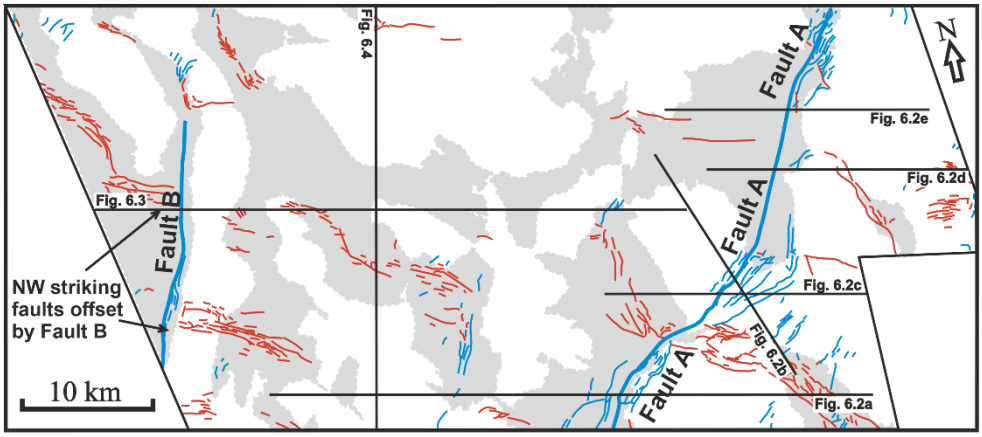

b)

Faults at the base of the Lower Germanic Trias Group (Horizon 1) and Zechstein salt (>400 ms thick)

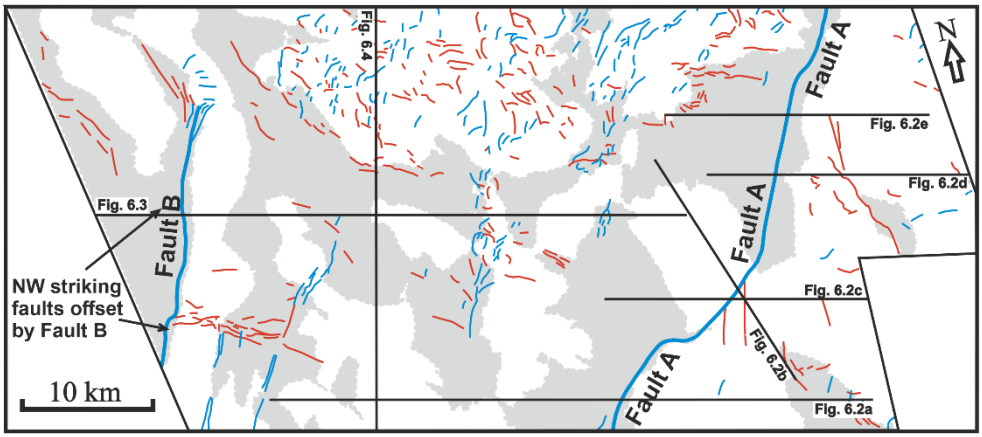

c)

Faults at the base of the Zechstein Group (Horizon 0) and Zechstein salt (>400 ms thick)

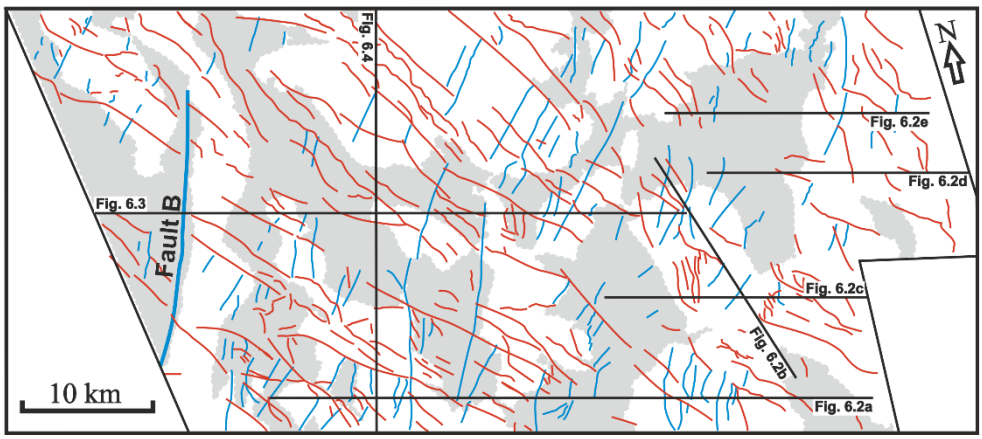

d)

Fig. 6.7. (Previous page) Fault maps at four key horizons superimposed on the areas of the Zechstein salt (>400 ms thick), including the base of the North Sea Group (Horizon H5), Chalk Group (Horizon H4), Lower Germanic Trias Group (Horizon H1) and Zechstein Group (Horizon H0), respectively. a-c) Maps with the distribution of supra-salt faults, highlighting that thick Zechstein salt controls the formation and development of supra-salt faults. Additionally, large supra-salt and hard-linked faults bound the thick Zechstein salt. d) Map with the distribution of sub-salt faults, highlighting the control of sub-salt faults on the position and distribution of overlying salt structures. NW-striking faults are shown by thin red lines. NE-striking faults are shown by thin blue lines, except for Faults A and B marked by thick blue lines. Grey areas represent the regions with Zechstein salt where its thickness is >400 ms. The location of seismic profiles in Figs. 6.2-6.4 is shown by black lines.

6.5 and 6.7). They are crestal faults whose formation is associated with the growth of salt structures. In the northern sector of the study area there is also a cluster of small supra-salt faults developed above thin salt (<400 ms), revealing random strikes (Figs. 6.4, 6.5 and 6.7). These faults were likely formed due to salt movement during the Early Jurassic, as they have small throws and show local thickening of strata at their immediate hanging-wall, at the level of horizon H1 (Fig. 6.4).

6.5.2.2 Sub-salt faults

Sub-salt faults are well developed on the Cleaver Bank High, striking to the NW and NE (Figs. 6.2-6.5 and 6.7). They are longer than supra-salt faults; 0.7 to 15.8 km long (Figs. 6.5 and 6.7). NE-striking faults intersect NW-striking faults, forming rhomboid or rectangular shapes in plan view. Many of these sub-salt faults bound the area where thick (>400 ms) Zechstein salt is observed, and their strikes are similar to those of overlying salt structures (Figs. 6.5-6.7). This implies that sub-salt faults controlled the position and distribution of salt structures in the study area.

In seismic data, sub-salt faults are usually steep and with small throws (Figs. 6.2-6.4). They were mainly formed in the Upper Palaeozoic, and likely inherited from pre-existing weakness zones in the Paleozoic basement (Ziegler, 1990; Schroot and Haan, 2003). These faults have experienced multiple phases of reactivation, resulting in their high length-throw ratios (Ligtenberg et al., 2011; Van Ojik et al., 2020; Alves et al., 2022).

6.5.2.3 Hard-linked faults

There are only a few hard-linked faults in the study area, and most of them show a prevalent NE strike (Figs. 6.3, 6.5 and 6.7). This can be explained by the Mesozoic reactivation of NE-striking sub-salt faults, which caused these to propagate across the Zechstein Group to form hard-linked faults. The largest hard-linked fault (Fault B) is located in the western sector of the study area, and it is a large NE-striking dextral strike-slip fault with a length of 19.4 km (Figs. 6.3, 6.5 and 6.7). Lateral offset in Fault B reaches a maximum of ~9.1 km based on the distance between two equivalent NW-striking faults that were offset by it (Figs. 6.5-6.7). Fault B is nearly vertical and propagated from the sub-salt Rotliegend Group into the relatively shallow North Sea Group (Fig. 6.3).

6.6 Subsurface temperature and geothermal gradients

BHT data reveal corrected temperatures ranging from 26.6^{o}C to 145.7^{o}C, with a near-linear positive correlation with depth (Fig. 6.8a). The temperature trendline in Fig. 6.8a shows a gradient of 38.54^{o}C/km. In contrast, geothermal gradients vary from 26.27^{o}C/km to 121.81^{o}C/km, showing a negative correlation with depth following a power law relationship (Fig. 6.8b). The lowest figure (P90), median (P50) and the highest figure (P10) of corrected BHTs and geothermal gradients are shown to vary in different stratigraphic units (Table 6.1). The P90, P50 and P10 BHTs of supra-salt strata are higher than those in the Zechstein Group and sub-salt strata (Table 1). Conversely, the P90, P50 and P10 of geothermal gradients in supra-salt strata are much lower than those in the Zechstein Group and sub-salt strata (Table 6.1).

The Limburg Group records the highest P90, P50 and P10 BHTs, respectively 114.6^{o}C, 125.3^{o}C and 136.0^{o}C (Table 6.1). The Upper Rotliegend Group has the second highest P90, P50 and P10 BHTs, which are respectively 112.6^{o}C, 121.7^{o}C and 130.9^{o}C. Conversely, the North Sea and Chalk Groups have the lowest P90, P50 and P10 BHTs (Table 1). The P90, P50 and P10 BHTs in the Zechstein Group (Seismic Unit 2) are slightly higher than in the Rijnland, Upper and Lower Germanic Trias Groups (Seismic Unit 3).

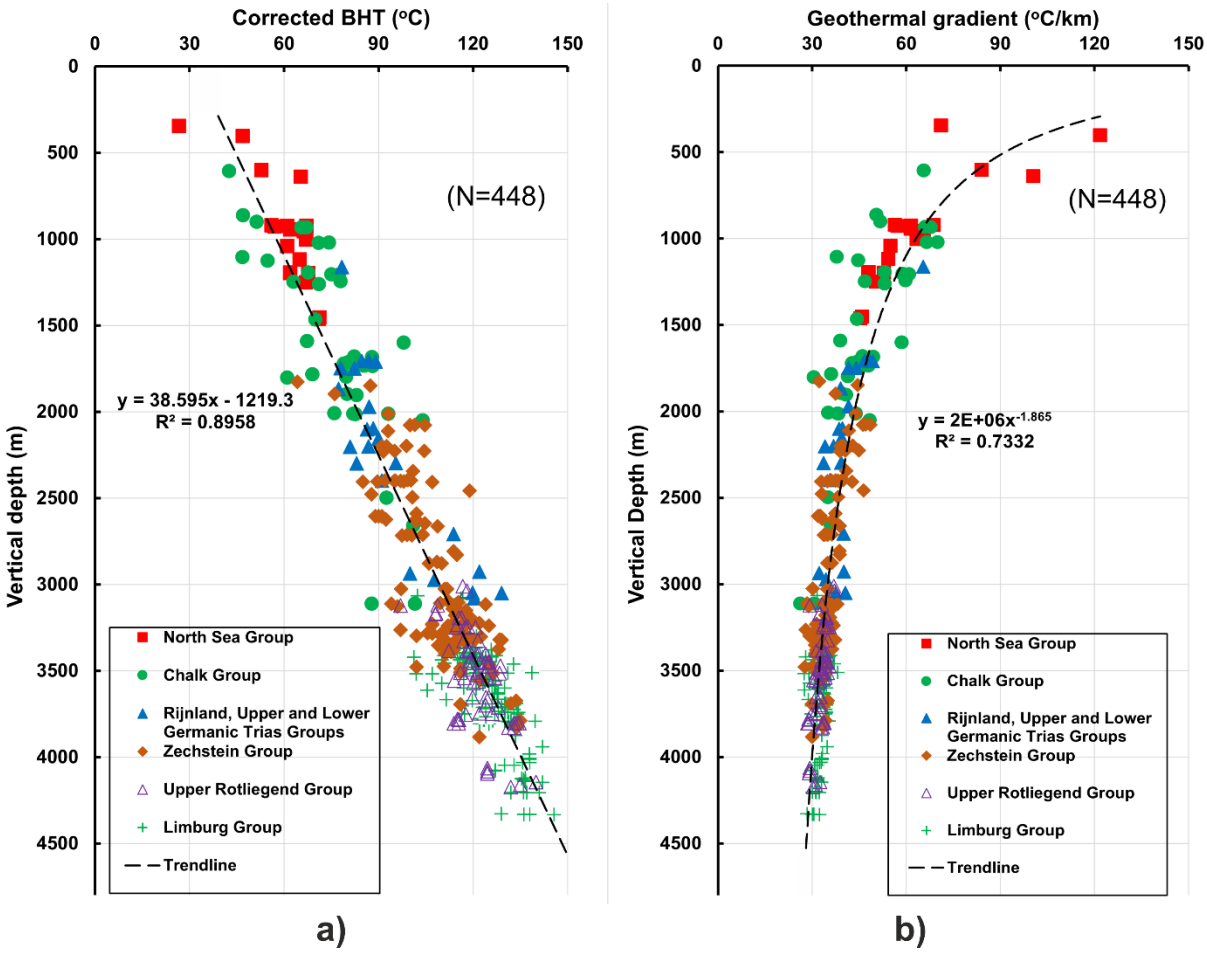

Fig. 6.8. Corrected BHT in five seismic-stratigraphic units recorded from the 48 exploration wells analysed in the study area. The trendline of all (448) corrected BHTs (See Appendix B) shows a near-linear positive correlation with depth, with an average geothermal gradient of 38.54°C/km. b) Geothermal gradient calculated from all (448) corrected BHTs in five seismic-stratigraphic units in the study area. The trendline of all (448) geothermal gradients shows a near-power law decreasing trend in geothermal gradient with depth. Note the trendlines in both figures represent the best fit lines for these data from a mathematical point of view.

	Stratigraphy units	Well Number	Number of BHT data	P90		P50		P10	
				Corrected BHT (°C)	Gradient (°C/km)	Corrected BHT (°C)	Gradient (°C/km)	Corrected BHT (°C)	Gradient (°C/km)
Supra-salt strata	North Sea Group (Seismic Unit 5)	13	22	50.7	42.0	61.4	63.1	72.1	84.1
	Chalk Group (Seismic Unit 4)	23	42	57.8	33.3	76.2	47.0	94.7	60.6
	Rijnland, Upper and Lower Germanic Trias Groups (Seismic Unit 3)	14	24	76.0	32.9	94.5	40.6	113.1	48.4
Zechstein salt	Zechstein Group (Seismic Unit 2)	39	123	92.6	30.1	108.5	35.2	124.4	40.2
Sub-salt strata	Upper Rotliegend Group (Seismic Unit 1)	28	74	112.6	30.3	121.7	32.8	130.9	35.2
	Limburg Group (Seismic Unit 1)	44	163	114.6	30.6	125.3	32.9	136.0	35.2
	Supra-salt strata	35	88	54.4	31.7	77.5	49.3	100.7	66.8
	Sub-salt strata	48	237	113.8	30.5	124.2	32.9	134.6	35.2
	All stratigraphic groups	48	448	84.7	27.2	110.7	36.7	136.7	46.2

Table 6.1. Corrected BHTs and geothermal gradients for different stratigraphic units calculated using normal probability plots.

Temperature at the base of the North Sea Group (Horizon H5)

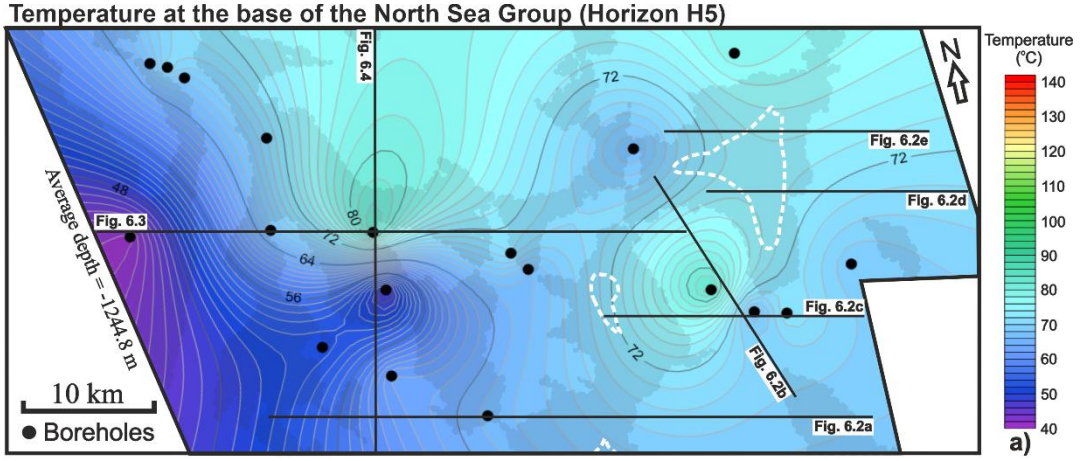

Temperature at the base of the Chalk Group (Horizon H4)

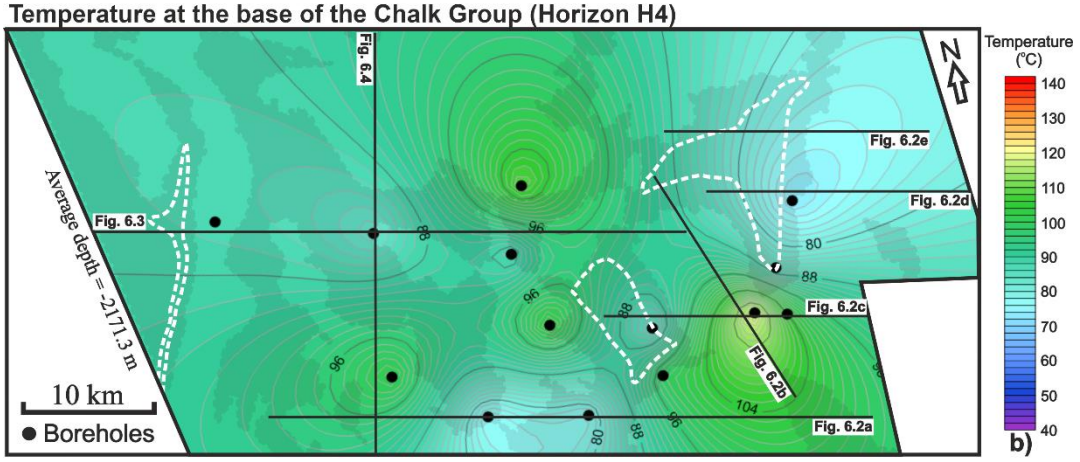

Temperature at the base of the Lower Germanic Trias Group (Horizon H1)

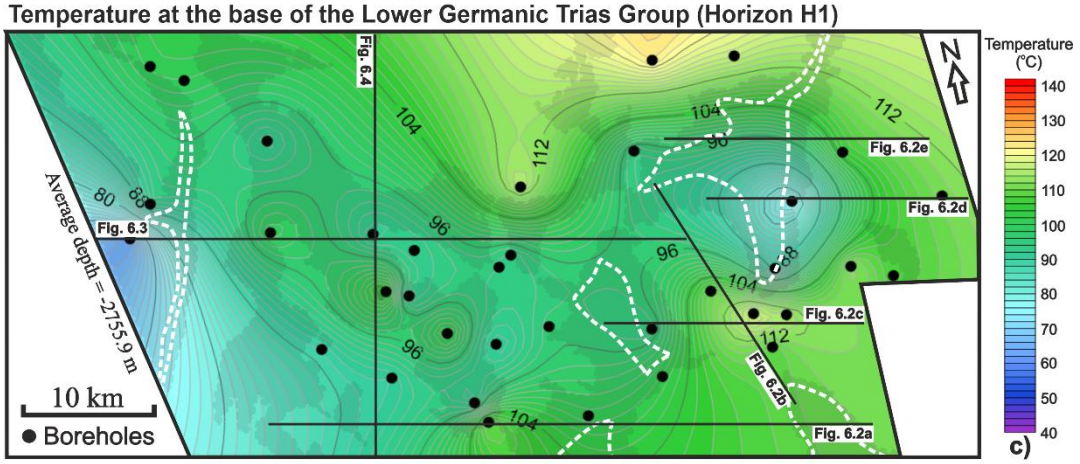

Temperature at the base of the Zechstein Group (Horizon H0)

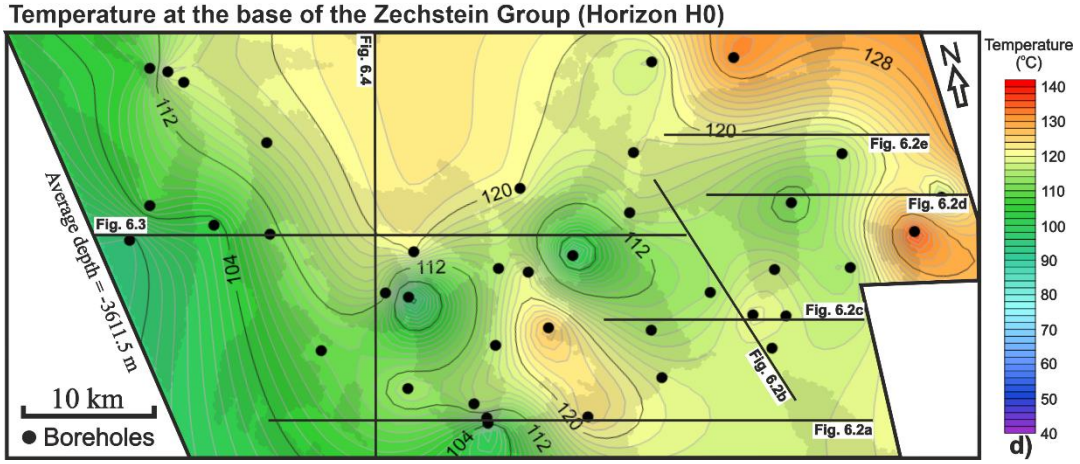

Fig. 6.9. (Previous page) Temperature maps superimposed on the areas of the Zechstein salt (>400 ms thick) at four key horizons, highlighting the subsurface temperature variations in the study area. a-d) Temperature at the base of the North Sea Group (Horizon H5), Chalk Group (Horizon H4), Lower Germanic Trias Group (Horizon H1) and Zechstein Group (Horizon H0), respectively. The Zechstein salt (>400 ms) is shown with the transparent black polygonal filling, and salt piercing boundaries in different horizons are marked by white dashed polygon. The position of borehole data used to compile these maps is marked by black circles, and their names are shown in Fig. 6.1. The location of the seismic profiles in Figs. 6.2-6.4 is shown by black lines.

In terms of geothermal gradients, the North Sea and Chalk Groups record the highest P90, P50 and P10 values for geothermal gradients (Table 6.1). The Upper Rotliegend and Limburg Groups have the lowest P90, P50 and P10 values for geothermal gradient at ~33^{o}C, on average. The P90, P50 and P10 values for geothermal gradient in the Zechstein Group (Seismic Unit 2) and Rijnland, Upper and Lower Trias and Groups (Seismic Unit 3) are very similar to an average of ~38^{o}C/km.

Temperature maps from four (4) key horizons, superimposed on the Zechstein Group, illustrate the recorded variations in subsurface temperatures (Fig. 6.9). They show that the temperature at the base of the North Sea Group (Seismic Unit 5) ranges from 40^{o}C to 82^{o}C, with low-temperature zones mostly located in the western sector of the study area. Zones with relatively high temperatures occur in the northern and eastern sectors (Fig. 6.9a). Temperatures at the base of the Chalk Group vary from 74^{o}C to 117^{o}C, with low-temperature zones in the northeast, northwest and south of the study area (Fig. 6.9b). Similarly to the base of the North Sea Group, high-temperature zones are located to the north, southeast and southwest. The data in Figs. 6.9a and b also show that temperature distribution at the base of the Chalk (Seismic Unit 4) and North Sea (Seismic Unit 5) groups does not correlate with the presence of thick salt (>400 ms) below. Conversely, at the base of the Zechstein Group (Seismic Unit 2) and Rijnland, Upper and Lower Germanic Trias Groups (Seismic Unit 3), temperatures show a good match with the relative distribution of Zechstein salt (Figs. 6.9c and d). Zones with thick Zechstein salt (>400 ms) record lower temperatures when compared to zones with less than 400 ms of salt. BHTs at the base of the Rijnland, Upper and Lower Germanic Trias Groups (Seismic Unit 3) vary from 65^{o}C to 128^{o}C, while BHTs at the base of the Zechstein Group (Seismic Unit 2) range from 95^{o}C to 135^{o}C (Figs. 6.9c and d).

6.7 Burial and thermal histories of the Cleaver Bank High

The burial history of the Cleaver Bank High is similar to other structural highs in the vicinity (e.g. De Jager, 2003; De Jager, 2007; Fattah et al., 2012b). Burial history models for three selected wells highlight two main phases of subsidence and sedimentation during the Early Triassic-Middle Jurassic (~250-175 Ma) and Early Cretaceous-Holocene (~137-0 Ma), which led to the burial maximum recorded in the study area at present (Figs. 6.10a, c and e). In parallel, multiple phases of uplift and erosion occurred during the Late Carboniferous-Early Permian (~307-264 Ma) and Mid-Late Jurassic (~170-150 Ma), the latter of which is associated with the Mid-Late Kimmerian phase (Figs. 6.10a, c and e). Two other phases of uplift are associated with tectonic inversion during the Late Cretaceous (Laramide phase) and Late Oligocene (Savian phase), but recording smaller magnitudes of uplift and erosion when compared to Mid-Late Jurassic uplift.

The thermal history for well K11-10 reveals two major temperature maxima occurring in the Early Cretaceous and Cenozoic (Fig. 6.10a). Pre-Zechstein units reached temperatures of up to 105^{o}C during the Early Cretaceous, increasing to over 110^{o}C during the Cenozoic. In contrast, wells K11-02 and K12-12 show one single temperature maximum during the Cenozoic (Figs. 6.10c and e). The highest modelled temperature for well K11-02 reaches 112^{o}C, and is over 130^{o}C in well K12-12. Modelled present-day temperatures in well K12-12 show a relatively good fit with the corrected BHTs analysed in this work (Fig. 6.10f). Temperature differences between modelled present-day temperatures and corrected BHTs for well K12-12 vary only from 0.6^{o}C to 12.4^{o}C. Due to the thin salt encountered in well K12-12, modelled temperatures above and below the Zechstein Group are not distinctly affected by any salt thermal effect. Comparatively, a marked thermal effect of salt is recorded in wells K11-10 and K11-02, which show obvious variations in geothermal gradients above and below the Zechstein Group – salt is relatively thick near these two wells. Nevertheless, modelled present-day temperatures in wells K11-10 and K11-02 do not fit well with their corresponding corrected BHTs (Figs. 6.10b and d), recording temperature differences of 20.1^{o}C-33.2^{o}C and 14.7^{o}C-26.4^{o}C, respectively. This implies that subsurface temperatures in wells K11-10 and K11-02 are influenced by other factors apart from salt-related thermal effects.

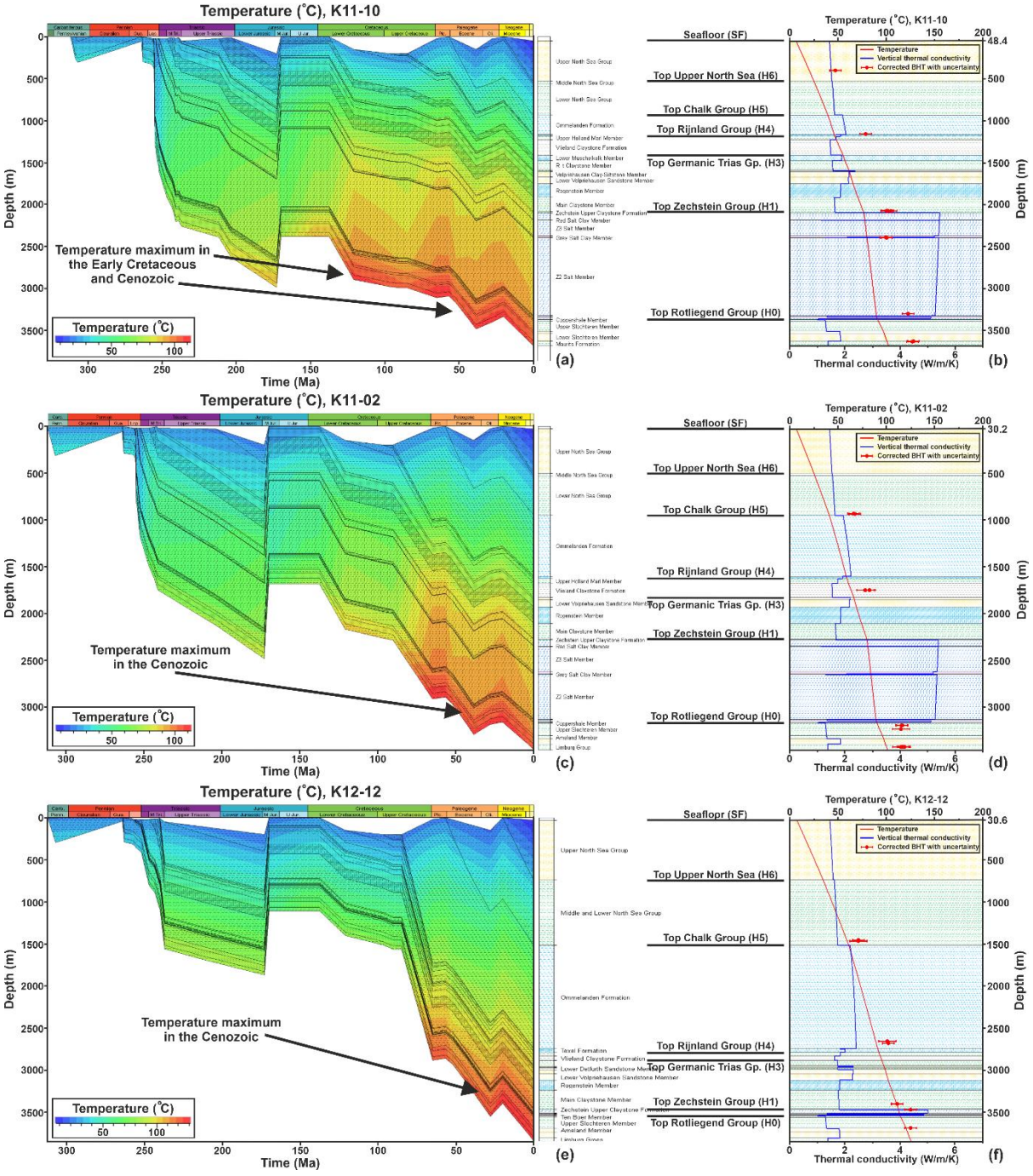

Fig. 6.10. Subsidence and thermal models for wells K11-10, K11-02 and K12-12, highlighting their modelled present-day temperatures, corrected BHTs and vertical thermal conductivities. The subsidence and thermal models provide evidence that temperature maximum occurred in the Early Cretaceous and Cenozoic. Temperature differences between modelled present-day temperatures and corrected BHTs for wells K11-10, K11-02 and K12-12 are respectively 20.1ºC-33.2ºC, 14.7ºC-26.4ºC and 0.6ºC-12.4ºC. This suggests that subsurface temperatures in wells K11-10 and K11-02 are influenced by other factors than the presence of nearby salt structures.

Vertical thermal conductivity for different stratigraphic units was also modelled for wells K11-10, K11-02 and K12-12 (Figs. 6.10b, d and f). Thermal conductivities in different stratigraphic units are mainly controlled by their lithology, although local temperatures can also cause some variability. In the pre-Zechstein units (Seismic Unit 1), thermal conductivity varies between 1.3 and 1.9 W/m/K, values that mainly depend on lithology. Thermal conductivity in the Zechstein Group (Seismic Unit 2) ranges from 1.0 to 5.4 W/m/K. Salt records the highest thermal conductivity which, in subsidence and thermal models, slightly decreases with temperature (burial depth). In contrast, interbedded claystones in the Zechstein Group have the lowest thermal conductivities. As for the Rijnland, Upper and Lower Germanic Trias Groups (Seismic Unit 3), their thermal conductivities vary from 1.6 to 2.5 W/m/k, once again depending on lithology. Thermal conductivities for the Chalk (Seismic Unit 4) and North Sea Groups (Seismic Unit 5) vary between 1.8 and 2.5 W/m/k and 1.5 to 2.5 W/m/k, respectively. They both show a slight increase in thermal conductivity with increasing temperature (burial depth).

6.8 Discussion

6.8.1 Influence of salt structures on geothermal potential

Geothermal gradients in the Zechstein Group and overlying strata show a positive correlation with salt thickness (Fig. 6.11). Conversely, geothermal gradients in sub-salt strata show a slightly negative correlation with the thickness of the Zechstein Group (Fig. 6.11). Negative correlations can be explained by a greater heat flow from sub-salt to supra-salt strata in areas where salt is thicker. In addition, the data in Fig. 6.11 also show multiple outliers, implying that subsurface geothermal gradients are influenced by other factors.

The effect of salt structures on geothermal potential can also be observed on geothermal gradient maps (Fig. 6.12). Areas with thick Zechstein salt (>400 ms) correlate with relatively high geothermal gradients (> 49^{o}C/km) in supra-salt strata (Fig. 6.12a). However, local geothermal gradients are influenced by large supra-salt faults, especially around Fault A. Similarly to supra-salt strata, areas with the thick (>400 ms) Zechstein salt are well matched to areas higher geothermal gradients (>37^{o}C/km) in the Zechstein Group (Fig. 6.12b). Conversely, areas with the thick Zechstein salt (>400 ms) relate to areas of low geothermal gradients (<32^{o}C/km) in sub-salt strata (Fig. 6.12c).

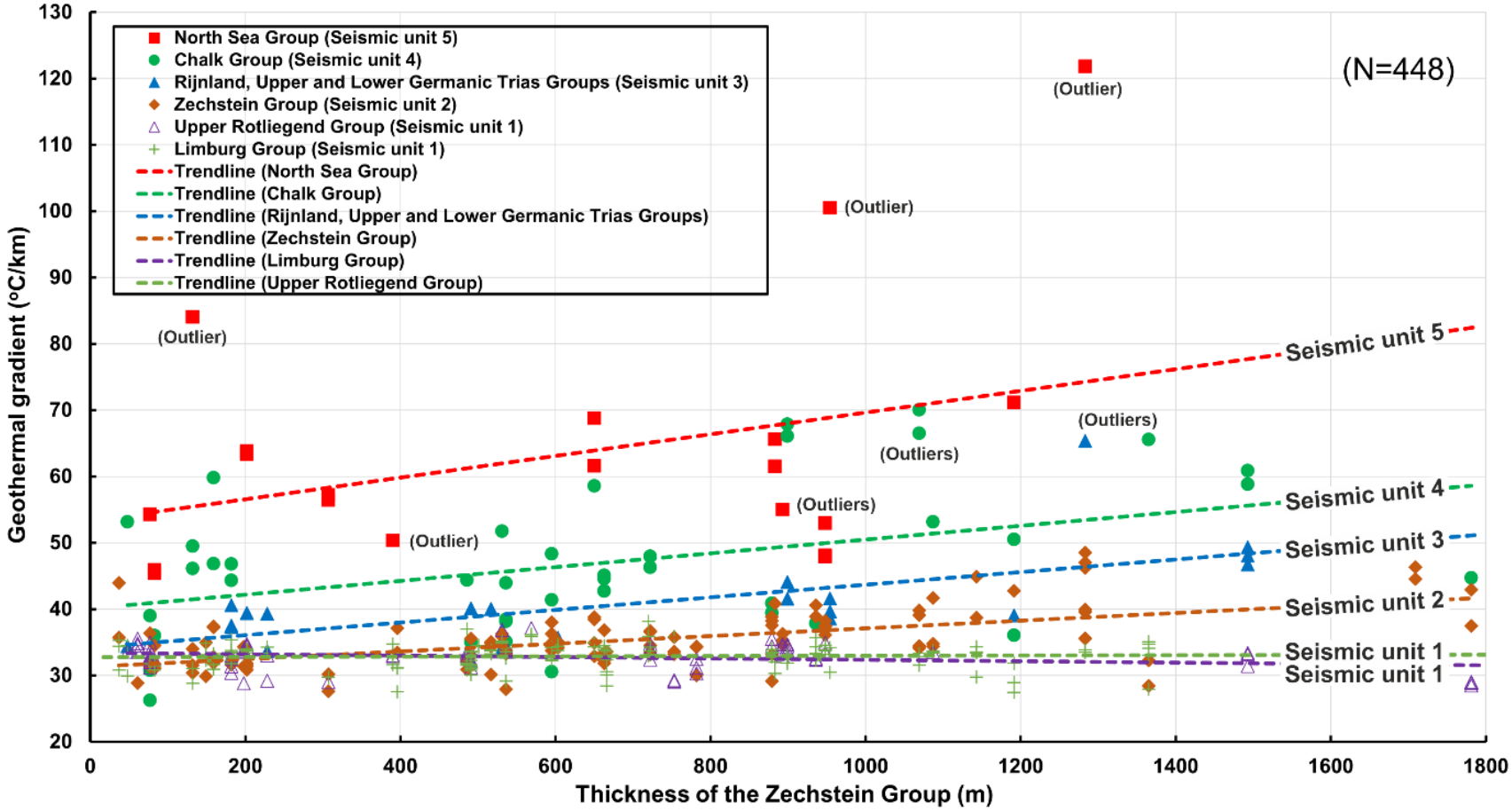

Fig. 6.11. Plot of geothermal gradient for different seismic-stratigraphic units vs. thickness of the Zechstein Group. Geothermal gradients in the North Sea Group (Seismic unit 5), Chalk Group (Seismic unit 4), Rijnland, Upper and Lower Germanic Trias Groups (Seismic unit 3) and Zechstein Group (Seismic unit 2) show a positive correlation with the thickness of the Zechstein Group. In contrast, geothermal gradients in the Upper Rotliegend and Limburg Groups show a negative correlation with the thickness of the Zechstein Group, a character explained by the presence of a greater heat flow from sub-salt to supra-salt strata in areas where salt is thicker.

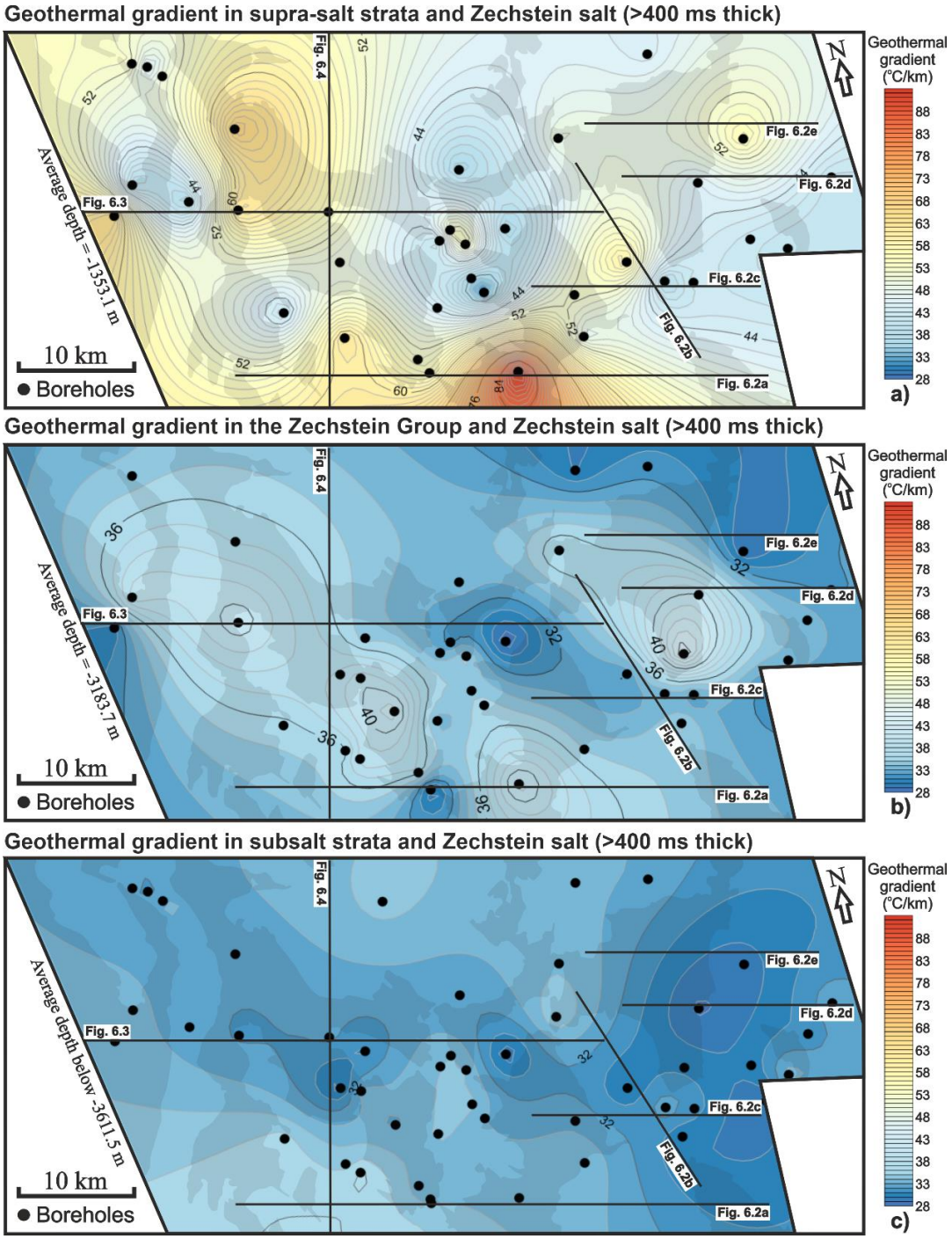

Fig. 6.12. Geothermal gradient maps for supra-salt strata, Zechstein Group and sub-salt strata superimposed on the areas with Zechstein salt (>400 ms thick). a) and b) Maps showing that areas with thick Zechstein salt (>400 ms thick) correlate with relatively high geothermal gradients. c) Map highlighting that areas with the thick Zechstein salt (>400 ms thick) relate to areas of low geothermal gradients. The Zechstein salt (>400 ms thick) is shown with a transparent black polygonal filling. The position of borehole data used to compile these maps is marked by the black circles, and their names are shown in Fig. 6.1. The location of the seismic profiles in Figs. 6.2-6.4 is shown by black lines.

It is also important to stress the influence of the Chalk Group on geothermal gradients (Fig. 6.13). Geothermal gradients in the North Sea and Chalk groups show a negative correlation with the thickness of this latter stratigraphic unit (Fig. 6.13). This can be explained by the low permeability of the Chalk Group, which hinders heat transfer from underlying strata. Moreover, geothermal gradients in the Zechstein Group (Seismic Unit 2) and Rijnland, Upper and Lower Germanic Trias Groups (Seismic Unit 3) also show a negative correlation with the thickness of the Chalk Group (Seismic Unit 4). In addition, geothermal gradients in the Upper Rotliegend and Limburg Groups (Seismic Unit 1) do not show significant changes relative to the thickness of the Chalk Group (Fig. 6.13). Geothermal gradients in the two former units are not influenced by the Chalk Group, as they are buried much below. In parallel, geothermal gradients in shallow strata of the study area are also highly likely to be affected by the palaeoclimate, especially the last glaciation periods (e.g. Fuchs et al., 2015). This impact has been quantified by Fuchs et al. (2015) at the Hannover within the Southern Permian Basin using petrophysical well logs, not far from the study area, at a similar latitude. The authors indicated that geothermal gradient perturbations caused by palaeoclimatic impact can reach 10-12^{o}C/km from the surface down to ~400 m, with such a geothermal gradient perturbation reduced to less than 5^{o}C/km below ~800 m (Fuchs et al., 2015). This implies that the temperature and geothermal gradients measured in shallow strata, in this work, could have been even higher without the palaeoclimatic impact of past glaciations.

6.8.2 The role of faults in influencing geothermal potential

Faults controlled the geometry, position and spatial distribution of salt structures on the Cleaver Bank High (Figs. 6.5 and 6.7). Anomalies in geothermal gradient are recorded close to faults as documented in Tables 6.2 and 6.3.

6.8.2.1 Direct influence of faults on geothermal potential

A direct influence on geothermal potential occurs when focused fluid migration occurs along faults, when these faults act as effective paths to deep and hot fluid (Fig. 6.14). This leads to higher-than-expected geothermal gradients in shallow strata. However, the direct influence of faults on geothermal potential is usually limited to the areas adjacent to these structures. Their influence merely lasts for short periods, if no new hot fluid is transmitted through fault,

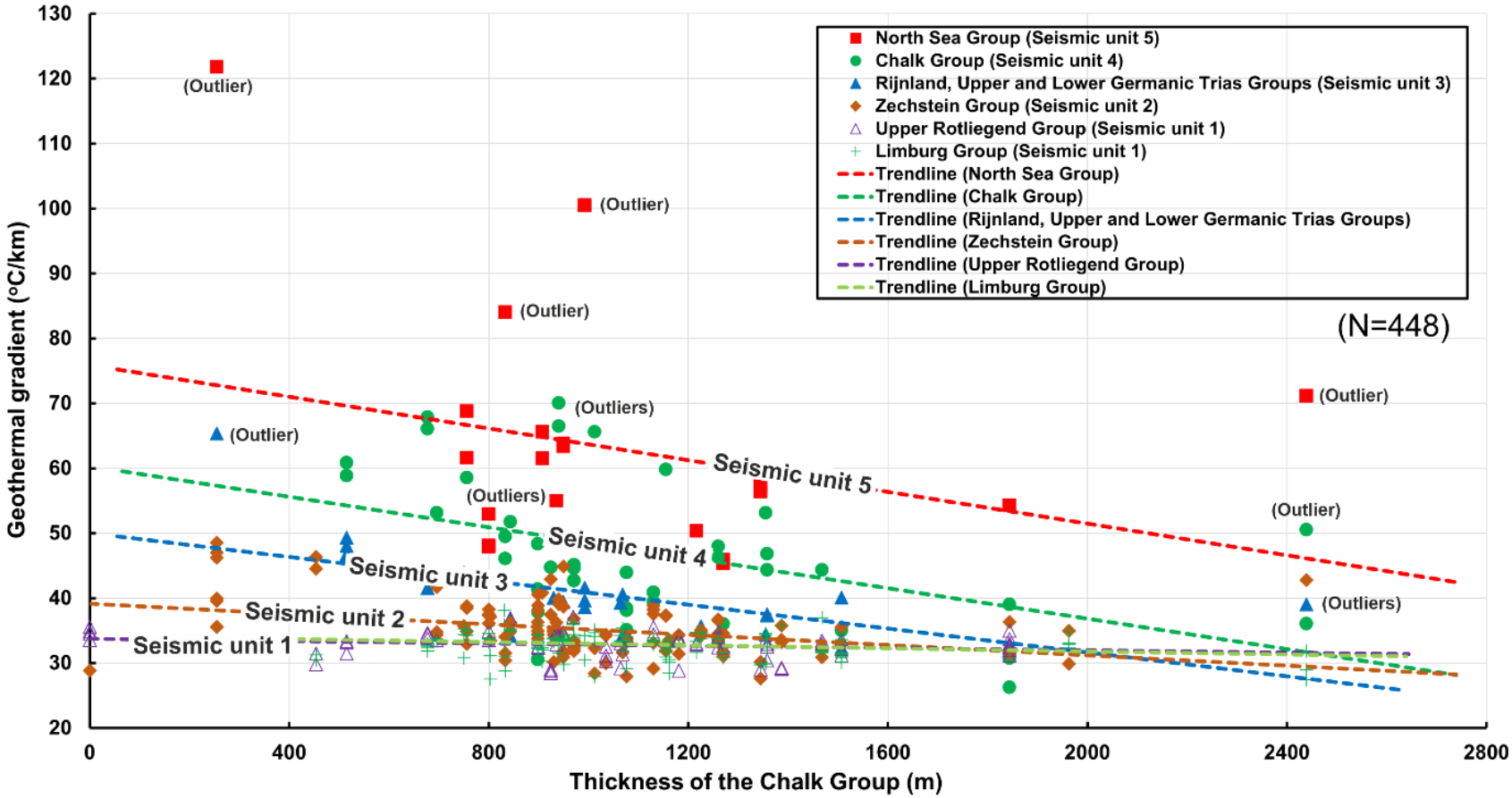

Fig. 6.13. Plot of geothermal gradient for different seismic-stratigraphic units vs. thickness of the Chalk Group. Geothermal gradients in the North Sea Group (Seismic unit 5), Chalk Group (Seismic unit 4), Rijnland, Upper and Lower Germanic Trias Groups (Seismic unit 3) and Zechstein Group (Seismic unit 2) show a negative correlation with the thickness of the Chalk Group. This can be explained by the low permeability of the Chalk Group, hindering the transfer of heat from underlying strata. Conversely, geothermal gradients in the Upper Rotliegend and Limburg Groups do not correlate with the thickness of the Chalk Group.

Well Name	Position	Distance to the fault (m)	Thickness of the Zechstein salt (m)	North Sea Group		Chalk Group		Rijnland, Upper and Lower Germanic Trias Groups		Zechstein Group		Upper Rotliegend Group		Limburg Group	
				Corrected BHT (°C)	Gradient (°C/km)	Corrected BHT (°C)	Gradient (°C/km)	Corrected BHT (°C)	Gradient (°C/km)	Corrected BHT (°C)	Gradient (°C/km)	Corrected BHT (°C)	Gradient (°C/km)	Corrected BHT (°C)	Gradient (°C/km)
K11-10	Footwall	2450	1283	46.9	121.8	-	-	78.4	65.4	104.7	48.5	-	-	128.0	33.8
K11-02	Footwall	9526	899	-	-	67.1	67.9	82.3	44.1	-	-	116.4	34.6	118.8	33.0
K11-07	Hanging wall	566	722	-	-	88.1	48.0	-	-	81.0	36.6	101.0	34.1	119.8	34.3
K11-01	Footwall	2623	1493	-	-	77.5	60.9	89.1	49.3	-	-	-	-	-	-
K08-11	Footwall	2586	132	52.8	84.0	87.9	49.5	-	-	117.5	34.0	-	-	119.8	31.1
K11-11	Hanging-wall	3472	396	-	-	-	-	-	-	109.5	33.5	-	-	123.6	31.2
K11-08	Hanging-wall	806	77	65.0	54.3	67.4	39.0	-	-	113.8	32.0	121.4	33.0	124.0	31.8
K12-12	Hanging-wall	2373	83	71.2	45.9	101.0	36.0	-	-	95.0	31.8	125.0	32.4	122.0	30.8
K09-06	Footwall	-	1709	-	-	-	-	-	-	87.4	44.6	117.3	31.5	125.0	31.3
K12-04	Hanging-wall	5501	182	-	-	73.4	46.8	119.8	37.5	-	-	128.0	33.0	131.1	33.8
K09-10	Footwall	-	1781	-	-	54.8	44.7	-	-	98.9	42.9	115.4	29.0	-	-
K09-07	Footwall	6093	486	-	-	80.3	44.4	-	-	113.4	32.3	115.0	32.9	132.8	37.0
Average values for foot-wall		4656	1112	49.9	102.9	73.5	53.5	83.3	52.9	104.4	40.5	116.0	32.0	124.9	33.2
Average values for hang-ing-wall		2544	292	68.1	50.1	82.5	42.5	119.8	37.5	99.8	33.4	118.9	33.1	124.1	32.4
Difference (%) for foot-wall to hanging-wall		83	281	-27	105	-11	26	-31	41	5	21	-2	-3	1	3

Table 6.2. Corrected BHTs and geothermal gradients recorded from twelve (12) wells located next to Fault A, highlighting the influence of this fault on local geothermal gradient. The highest geothermal gradient and its corresponding corrected BHT are listed below when there is more than one temperature measurement for a seismic-stratigraphic unit. Well locations are shown in Figs. 6.1-6.4.

Well Name	Position	Distance to the fault (m)	Thickness of the Zechstein salt (m)	North Sea Group		Chalk Group		Rijnland, Upper and Lower Germanic Trias Groups		Zechstein Group		Upper Rotliegend Group		Limburg Group	
				Corrected BHT (°C)	Gradient (°C/km)	Corrected BHT (°C)	Gradient (°C/km)	Corrected BHT (°C)	Gradient (°C/km)	Corrected BHT (°C)	Gradient (°C/km)	Corrected BHT (°C)	Gradient (°C/km)	Corrected BHT (°C)	Gradient (°C/km)
K07-01	Structural high	-	954	65.3	100.5	-	-	87.0	41.6	-	-	-	-	123.8	34.2
K07-FD-105	Structural high	-	1192	26.7	72.8	47.0	50.5	77.3	39.1	107.0	42.8	-	-	117.0	31.8
K10-03	Salt with-drawal basin	-	650	67.1	68.8	98.0	58.6	-	-	98.0	38.5	-	-	121.1	34.9
K09-03	Next to fluid path	-	182	-	-	-	-	129.0	40.6	134.0	31.6	116.0	31.4	139.7	35.4
K07-13	West of Fault B	4274	1365	-	-	42.6	65.6	-	-	64.3	32.3	-	-	125.0	35.1
K07-02	East of Fault B	1751	228	-	-	-	-	83.0	33.7	-	-	108.7	33.1	120.9	34.3

Table 6.3. Corrected BHTs and geothermal gradients measured from wells located next to two large NW-striking crestal faults, a fluid path and a large hard-linked fault. The highest geothermal gradient and its corresponding corrected BHT are listed below when there is more than one temperature measurement for a seismic-stratigraphic unit. Well locations are shown in Figs. 6.1-6.4.

as heat can be quickly rebalanced (Pruess, 2005; Pruess, 2008; Li et al., 2018). The direct influence of faults on geothermal gradients is introduced below by using Fault A as an example.

Fault A is a growth fault propagating upwards from the Zechstein Group into the Upper North Sea Group (Fig. 6.2). It was formed during the Early Triassic, as shown by the thickening of the Upper and Lower Germanic Trias Groups on its hanging-wall block (Fig. 6.2a). It is also a part of a large NE-striking fault zone across the Southern North Sea (See Fig. 1 in Ten Veen et al., 2012). In supra-salt strata, geothermal gradients on the footwall of Fault A are much higher than on its immediate hanging-wall block (Table 6.2). Average geothermal gradients on the footwalls of Fault A are respectively 105.36%, 25.94% and 41.11% in the North Sea Group (Seismic Unit 5), Chalk Group (Seismic Unit 4) and Rijnland, Upper and Lower Germanic Trias Groups (Seismic Unit 3), values that are higher than on its immediate hanging-wall block (Table 6.2). In more detail, geothermal gradients recorded in well K11-10 - located on the footwall of Fault A - are the highest in all supra-salt strata, excluding the Chalk Group due to the lack of BHT data for this interval, which are respectively 121.8^{o}C/km in the North Sea Group (Seismic Unit 5), 65.4^{o}C/km in the Rijnland, Upper and Lower Germanic Trias Groups (Seismic Unit 3) and 48.5^{o}C/km in the Zechstein Group (Seismic Unit 2) (Fig. 6.2a; Table 6.2). Comparatively, geothermal gradients recorded in wells K11-08 and K12-12, i.e. on the hanging-wall block of Fault A, approach the lowest values in each of the supra-salt units considered in this work (Table 6.2).

Such an observation suggests the footwalls of large supra-salt faults to be favourable geothermal exploration targets, a character justified by the fact that salt in these footwalls is also thicker when compared to their hanging-wall blocks (Fig. 6.2; Table 6.2). Thicker salt is likely to cause 'chimney effects' near the largest faults. More importantly, it is related to fluid migration along Fault A into shallow strata, as multiple low-amplitude trails of fluid are observed in the hanging-wall of Fault A in Fig. 6.2a. This can also be confirmed by the distinct differences between modelled present-day temperatures and corrected BHTs for wells K11-10 and K11-02 that are located on the footwall of Fault A, as their corrected BHTs are much higher than their modelled present-day temperatures (Figs. 6.10b and d). In contrast, modelled well K12-12 that is located on the hanging wall of Fault A is almost free of perturbations caused by salt structures and faults, showing that its corrected BHTs relatively fit well with modelled present-day temperatures (Fig. 6.10f). In addition, the depth differences between the footwall of large supra-salt faults and their corresponding hanging-wall can also partly account for this observation, as geothermal gradient has a negative correlation with depth (Fig. 6.8b). Footwalls

are also effective structural traps for fluid, so the fluid accumulated by diffusion and focused fluid migrations are more likely to be preserved in the footwalls of faults (Fig. 6.14). This has already been proven by the hydrocarbon accumulations thus far encountered near some of the wells drilled in the study area.

The relative distance from the largest faults influences the geothermal gradients recorded in supra-salt strata (Fig. 6.2; Table 6.2). Geothermal gradient in the Rijnland, Upper and Lower Germanic Trias Groups (Seismic Unit 3) gathered from well K11-10 is 65.4^{o}C/km, a higher value than the 44.1^{o}C/km recorded in well K11-02 (Fig. 6.2a; Table 6.2). These two wells are located on the footwall of Fault A, but well K11-10 is located much closer to this fault (Fig. 6.2a; Table 6.2). This explains why the difference between modelled present-day temperatures and corrected BHTs is larger for well K11-10 than for well K11-02 (Figs. 10 b and d). These data prove that large supra-salt faults significantly increase the local geothermal gradients in their vicinity, but their influence decreases as one moves away from them. Furthermore, large NW-striking crestal faults can influence the geothermal gradients around salt structures (Figs. 6.4 and 6.14; Table 6.3). These faults propagate into the Upper North Sea Group from the Zechstein Group (Figs. 6.4, 6.5 and 6.7), and high geothermal gradients are recorded next to these faults (Table 3). In detail, the second highest geothermal gradient (100.5^{o}C/km), recorded in well K07-01 within the North Sea Group, is located next to the crestal faults in Fig. 6.4 (also see Table 6.3). The presence of this high geothermal gradient is likely associated with the influence of these crestal faults, though the underlying thick salt may have also contributed in part (Fig. 6.11). It is important to note that the development of crestal faults above salt structures is usually associated with underlying salt movement, so halokinesis can indirectly influence the geothermal potential by controlling the development of crestal faults above salt structures.

Sub-salt faults impose a direct influence on the geothermal potential of the Cleaver Bank High. This usually occurs in the areas where the Zechstein salt is very thin (<100 ms; or ~230 m), or even absent, promoting fluid flow along sub-salt faults into supra-salt strata (Figs. 6.2c-e and 6.14). As a key example, well K09-03 was drilled next to a low-amplitude trail of fluid located above a salt weld (Fig. 6.2c). A relatively high geothermal gradient (40.58^{o}C/km) is recorded in well K09-03 in the Rijnland, Upper and Lower Germanic Trias Groups (Seismic Unit 3; Table 6.3), suggesting fluid flow into supra-salt strata. The presence, near this well, of a relatively high geothermal gradient implies very recent, if not active, fluid flow.

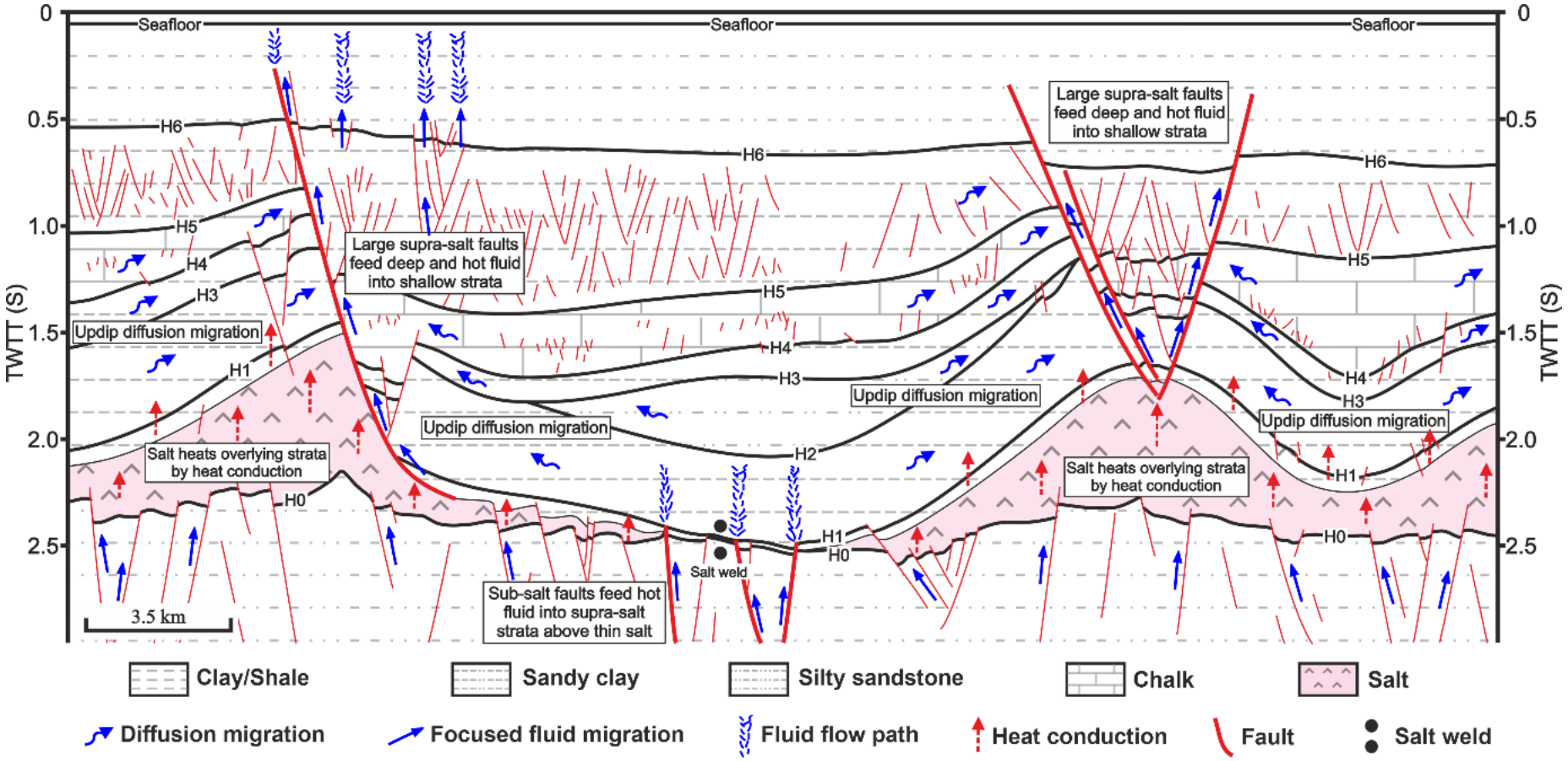

Fig. 6.14. Summary of the influence of salt structures and faults on geothermal potential, highlighting three potential geothermal exploration targets in the study area. The Zechstein salt heats the overlying strata by heat conduction, causing higher geothermal gradients above salt strata. Large supra-salt and sub-salt faults act as fluid paths to deep and hot fluid into shallow strata, resulting in the presence of the high geothermal gradients in shallow strata. Three potential geothermal exploration targets are located at the footwall of large supra-salt fault, above thick Zechstein salt, or areas with salt welds and dense sub-salt faults. This section is modified from Figs. 6.2a and 6.4.

6.8.2.2 Indirect influence of faults on geothermal potential

An indirect influence of faults on geothermal potential is recorded where higher geothermal gradients occur in supra-salt strata, but lower geothermal gradients are observed in sub-salt strata (Figs. 6.11, 6.12 and 6.14). In the study area, faults control the geometry, position and spatial pattern of salt structures, showing they have an indirect influence on the Cleaver Bank's geothermal potential.

Supra-salt faults are the most common faults in the study area, but most are restricted to Cenozoic strata. Only a few large Mesozoic supra-salt faults propagated upward into the North Sea Group (Figs. 6.2-6.4). These large supra-salt faults exerted an effective control on the geometry of salt structures, but not on their spatial distribution (Fig. 6.7). Sub-salt faults are mainly NW- or NE-striking in the study area and experienced multiple episodes of reactivation. They control the strike and thickness of salt structures, creating the necessary accommodation space on their hanging-wall blocks for thick Zechstein salt (Fig. 6.7). In parallel, large hard-linked faults can influence the distribution of salt structures. In the study area, a large strike-slip fault (Fault B) located in the western sector of the study area resulted in the formation of a ~20 km long salt wall (Fig. 6.3). The thickness of Zechstein salt changes on both sides of Fault B, generating contrasting geothermal gradients in supra-salt strata (Figs. 6.3 and 6.12; Table 6.3). These exert large-scale and long-lasting controls on geothermal gradients and subsurface temperatures when compared with the direct influence of faults on geothermal potential.

On the Cleaver Bank High, the greatest geothermal energy potential occurs at the footwall of large supra-salt faults, especially near Fault A. The area near such faults records high geothermal gradients due to the combined presence of thick Zechstein salt at depth and the migration of hot fluid along these same faults. Another potential geothermal exploration target is located above thick salt intervals in the Zechstein Group, as thick salt can heat supra-salt strata up due to its good thermal conductivity. The last potential geothermal exploration target on the Cleaver Bank High coincides with the sector where thin salt (<100 ms) is observed above dense sub-salt faults. Here, sub-salt fluid can flow upwards along the sub-salt faults, resulting in the migration of deep and hot fluid across salt welds.

6.9 Chapter-specific conclusions

Chapter 6 aimed at understanding the influence of salt structures and faults on the geothermal potential of the Cleaver Bank High, Southern North Sea. Salt structures and faults were analysed, and subsurface temperature and geothermal gradient maps were compiled. The influence of salt structures and faults on the geothermal potential of the study area was discussed. The main conclusions of this work can be summarised as follows:

a) Salt structures developed on the Cleaver Bank High include multiple salt diapirs, salt pillows and a salt wall, all of which have experienced multiple phases of growth. Their relative positions, geometries and distributions are significantly controlled by sub-salt faults and large NE-striking supra-salt faults.

b) The presence of salt structures has an important influence on the geothermal potential of the study area. In more detail, strata deposited above the Zechstein Group show higher geothermal gradients proportionally to the thickness of Zechstein salt. In contrast, the strata buried below this Group show a minor decreasing trend in geothermal gradients with an increasing thickness of salt. This proves the large-scale, long-lasting influence of salt on geothermal gradients and sub-surface temperatures.

c) Faults developed on the Cleaver Bank High also play an important role in influencing the geothermal potential. Large supra-salt faults can act as migration paths for deep and hot fluid, resulting in the presence of the high geothermal gradients in shallow strata. Geothermal gradients on footwall blocks are usually higher than that on the corresponding hanging-walls of large supra-salt faults. However, it decreases with the distance away from these faults, and their influence merely lasts for short periods, if no new hot fluid is transmitted through faults, as heat can be quickly rebalanced.

d) Sub-salt faults influence the geothermal gradient of supra-salt strata in the sector where there is very thin, or even absent, salt (<100 ms), forming distinct low-amplitude trails of fluid above these same faults. They indirectly influence geothermal gradient by controlling the position, geometry and distribution pattern of salt structures.

e) Faults and salt structures present a contrasting influence on temperatures and geothermal gradients. As a result, three potential geothermal exploration targets are summarised in the study area, located at the footwall of large supra-salt fault, above thick Zechstein salt, or areas with salt welds and dense sub-salt faults.

As a corollary, this work classifies the influence of tectonic faults on the geothermal potential of the Cleaver Bank High as: a) direct, and b) indirect. This highlights the contrasting influence on geothermal gradients between faults and salt structures on the Cleaver Bank High.

Chapter 7

Summary and discussion

7 Summary and discussion

7.1 Preamble

The results chapters (Chapters 4-6) in this thesis aim at addressing the size, geometry and distribution of fault families around salt structures, at illustrating the formation and development of these fault families under the local stress field associated with halokinesis, and at exploring their implications for fluid flow, carbon and energy storage, and geothermal potential. The main findings of results chapters are summarised and presented in this chapter. It indicates that multiple fault families are observed around salt structures in the Espírito Santo Basin, SE Brazil and the Cleaver Bank High, Southern North Sea, with different size, geometry and distribution. Their formation and development are usually associated with halokinesis, and they have implications for fluid flow, storage and production. This chapter aims to discuss the wider implications of the results in this thesis, outline the limitations of the research and propose themes for further work.

7.2 Summary of scientific results

7.2.1 Chapter 4: Fault analysis of a salt minibasin offshore Espírito Santo, SE Brazil

The first result chapter in this thesis (Chapter 4) aimed at understanding the distribution, evolution history and significance of different fault families in a salt minibasin, at the same time identifying any favourable fluid pathways offshore Espírito Santo Basin, SE Brazil (Fig. 7.1). High-quality 3D seismic data were used to interpret faults in the study area, and these faults were separated into four fault families based on their geometry, orientation, distribution and relationship with main salt structures. Three principal stratigraphic units were defined based on their internal seismic reflection characters, bounding reflection terminations, and their relationship with main structural features. Well profile correlations were plotted to identify lithological variations in the seismic-stratigraphic units, and a chronostratigraphic framework was established based on the work of Ze and Alves (2021).

Displacement analyses for representative faults showed that lateral tip linkage and dip linkage were commonly observed to explain the growth of faults, except for listric faults.

Listric faults have distinctly higher displacements when compared to other fault families, accommodating significant extensions in the minibasin during the Cenozoic. The development of listric faults can indicate the existence of sub-surface overpressure in strata. Moreover, the intervals into which listric faults sole out comprise soft and ductile strata, which is likely associated with source rocks. Additionally, three stages of halokinesis occurred during the Cenozoic, controlling the formation and development of surrounding fault families. Finally, normalised leakage factor analyses reveal keystone faults to be the most favourable pathways to fluid migrating in the investigated salt minibasin, whereas listric faults are likely to form barriers and baffles to fluid in their lower parts.

7.2.2 Chapter 5: Palaeostress state around a rising salt diapir inferred from seismic reflection data

The main aim of the second result chapter in this thesis (Chapter 5) was to understand the palaeostress state around a rising triangular salt diapir on the Cleaver Bank High, Southern North Sea. High-quality 3D seismic data were used to interpreted faults around the diapir of interest (Fig. 7.2). Interpreted faults include radial, polygonal and keystone faults, which are separated into eight zones based on their geometry, strike and overall distribution. Eight (8) key seismic-stratigraphic horizons are interpreted and correlated with borehole data, revealing the main chronostratigraphic framework of the study area. In addition, graphs recording the number of faults offsetting the interpreted seismic horizons were compiled, showing the presence of two distinct polygonal fault tiers in the study area. Well profile correlations were plotted to identify lithological variations and establish a chronostratigraphic framework for the interpreted seismic-stratigraphic units.

Displacement analyses for selected faults indicated that dip linkage is the common fault growth process in the study area. Fault nucleation and growth were mainly controlled by halokinesis in three structural stages during the Cenozoic. Stress inversions for interpreted faults revealed that palaeostresses in flanking zones of the salt diapir show marked differences when compared with corner zones, with the combination of minimum principal palaeostresses from all flanking and corner zones formed a triangular stress ring around the salt diapir. The width of this stress ring was not only associated with the rise of the salt diapir, but also largely influenced by adjacent salt structures. This work has important implications to the analysis of salt diapirs, and their adjacent strata, in areas posed for carbon sequestration, gas storage, and

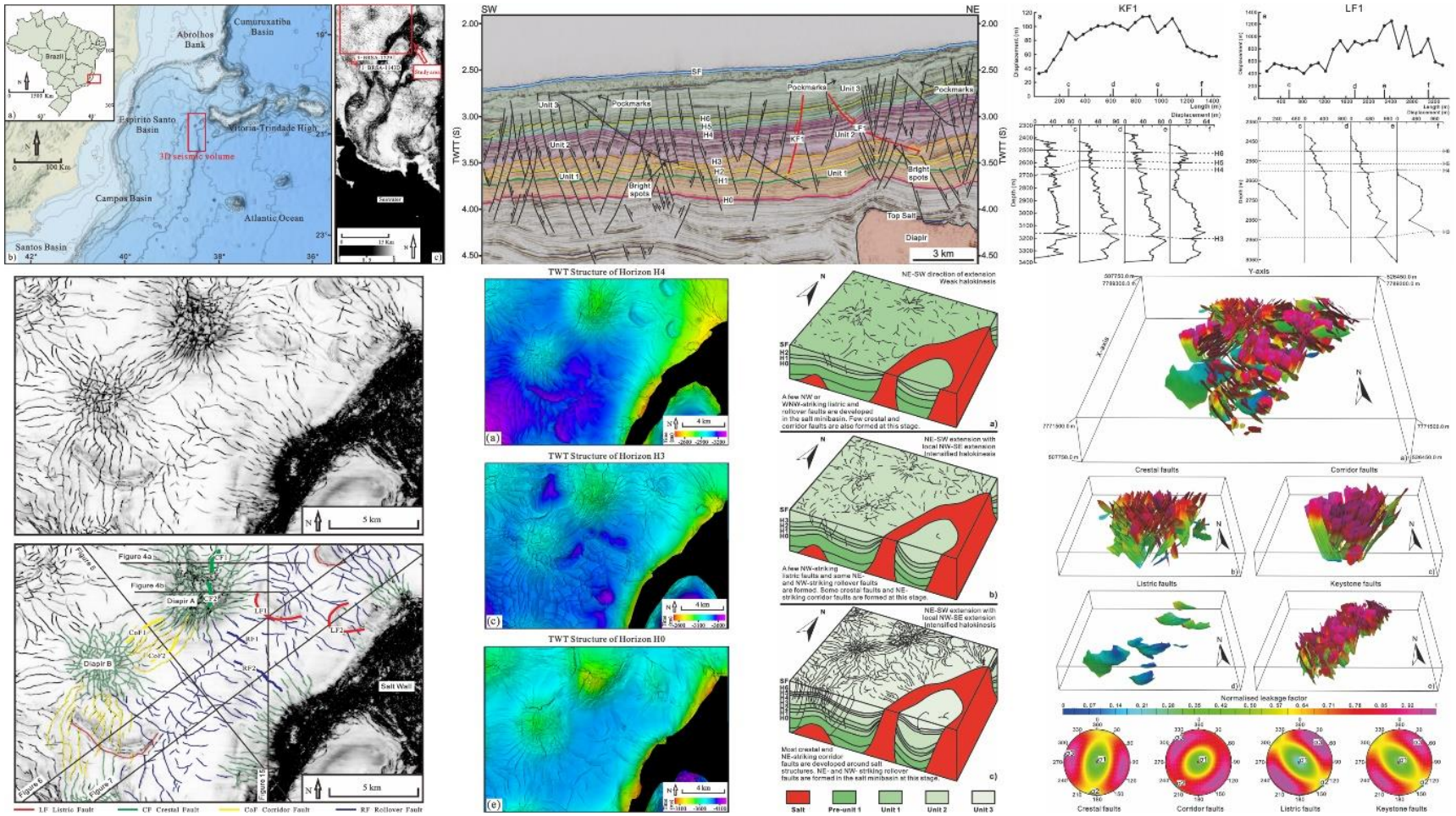

Fig. 7.1. Diagram summarising the key results from Chapter 4. It shows that seismic profiles, variance and TWT structural maps were used to understand fault families, and fault displacement-length (D_{max}-L) and displacement-depth (D-Z) for selected faults were compiled. The evolution history of fault families was summarised in three stages, and fault leakage analyses were implemented for four fault families.

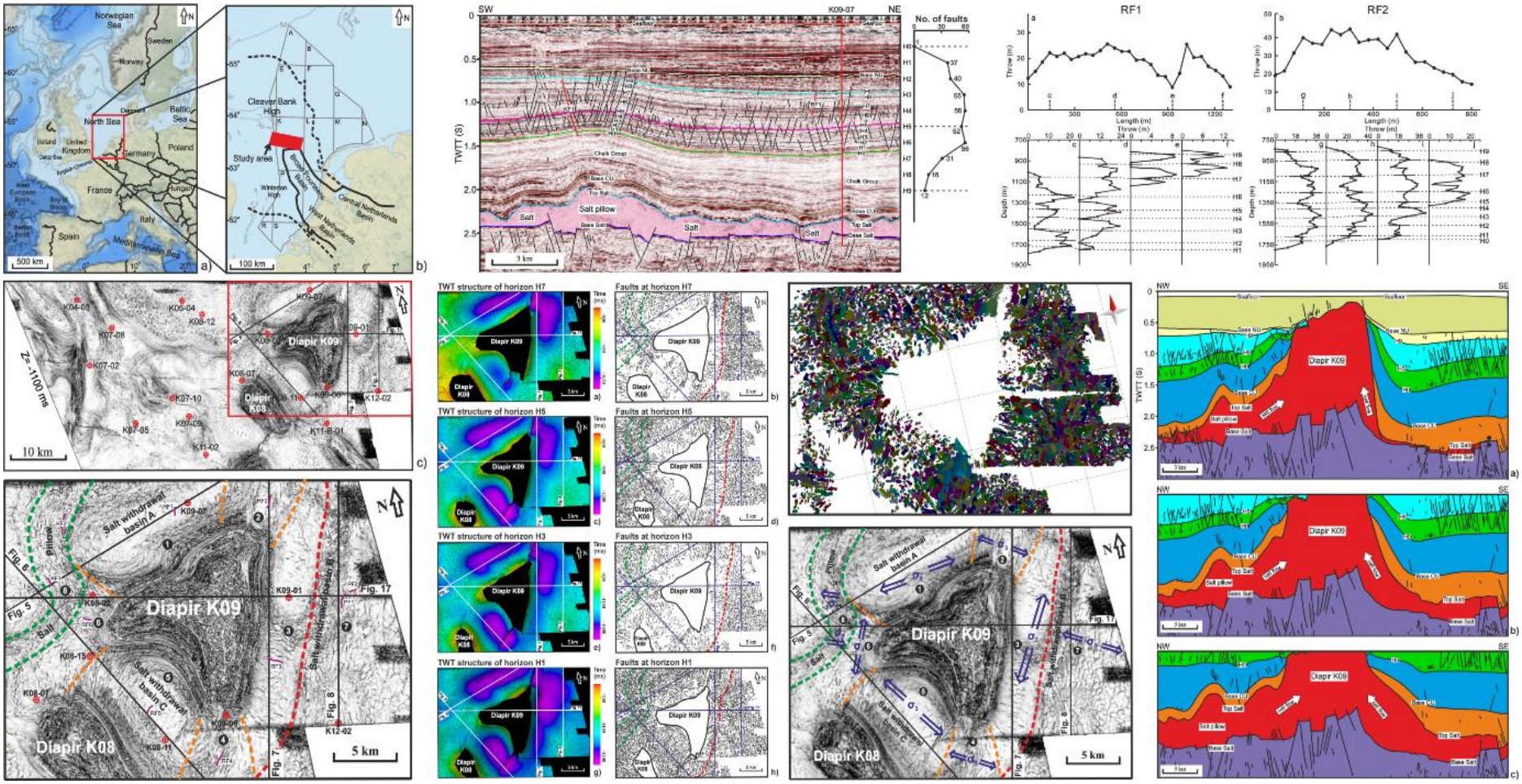

Fig. 7.2. Diagram summarising the key results from Chapter 5. It shows that seismic profiles, variance and TWT structural maps were used to understand fault families around the salt diapir of interest, and fault throw-length (T_{max}-L) and throw-depth (T-Z) for selected faults were compiled for selected faults. Palaeostress state around this salt diapir were studied by using the stress inversion for the interpreted faults. The evolution of salt diapir in the Cenozoic was summarised in three stages.

the production of oil and gas.

7.2.3 Chapter 6: The influence of salt structures and faults on geothermal potential on the Cleaver Bank High

The key aims of the third result chapter in this thesis (Chapter 6) were to investigate the influence of salt structures and faults on the geothermal potential of the Cleaver Bank High (Fig. 7.3). High-quality 3D seismic data showed multiple salt diapirs, salt pillows and a salt wall were developed on the Cleaver Bank High, and these salt structures have experienced multiple phases of growth. Three groups of faults were separated based on their spatial distribution and stratigraphic position relative to the Zechstein Group. The distribution of faults and salt structures in the study area indicates that sub-salt faults and large NE-striking supra-salt faults control the relative positions, geometries and distributions of salt structures. In addition, 448 bottom-hole temperatures (BHTs) measured from 48 wells show the distribution of subsurface temperature and geothermal gradient. Temperature has a near-linear positive correlation with depth, with the slope of temperature trendline of 38.5ºC/km, whereas geothermal gradients show a negative power law relationship with depth.

Strata deposited above the Zechstein Group record geothermal gradients that are enhanced proportionally to the thickness of this salt unit. Conversely, strata buried below the Zechstein Group reveal a moderate decreasing trend in geothermal gradients with increasingly thick salt. In parallel, large supra-salt faults can act as fluid paths to deep and hot fluid into shallow strata, resulting in the presence of the high geothermal gradients in shallow strata. Geothermal gradients on footwall blocks are usually higher than that on the corresponding hanging-walls of large supra-salt faults. However, it decreases with the distance away from these faults. In more detail, average geothermal gradients on the footwall of the largest supra-salt fault (Fault A) are, relative to its immediate hanging-wall, 105% higher in the North Sea Group, 26% higher in the Chalk Group, and 41% higher in the Rijnland, Upper and Lower Germanic Trias Groups. Additionally, sub-salt faults influence the geothermal gradient of supra-salt strata in parts of the study area where there is very thin, or even absent, salt (<100 ms; or ~230 m), forming distinct low-amplitude trails of fluid above these same faults. They also indirectly influence geothermal gradient by controlling the position, geometry and distribution pattern of salt structures.

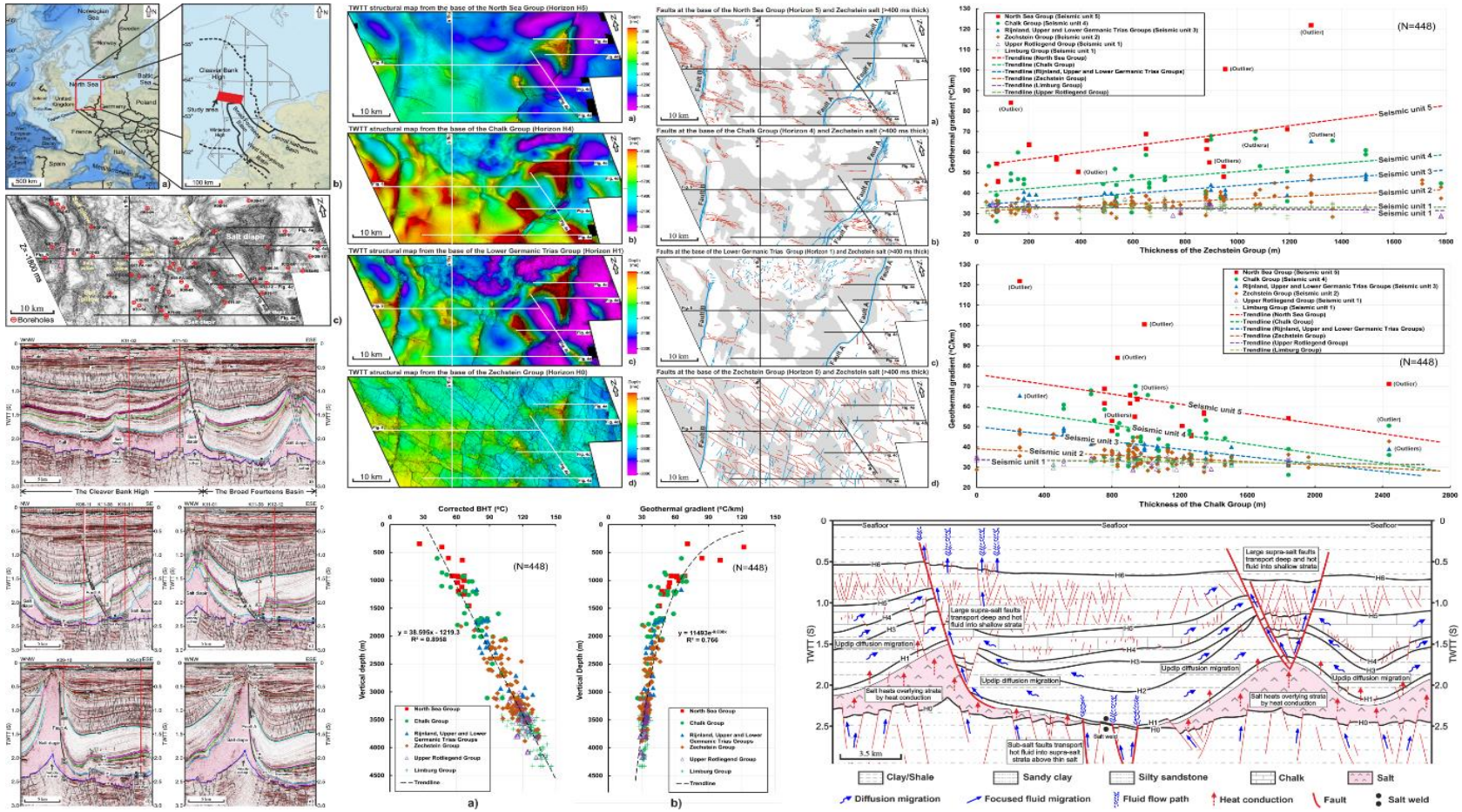

Fig. 7.3. Diagram summarising the key results from Chapter 6. It shows that seismic profiles, variance and TWT structural maps were used to study fault families on the Cleaver Bank High. Subsurface temperature and geothermal gradients were investigated by using bottom-hole temperatures, and the relationship between geothermal gradients vs. Zechstein Group thickness and Chalk Group thickness is studied. The influence of salt and fault on geothermal potential is summarised in a schematic diagram.

In summary, faults and salt structures present a contrasting influence on temperatures and geothermal gradients. As a result, three potential geothermal exploration targets are summarised in the study area, located at the footwall of large supra-salt faults, above thick Zechstein salt, or areas with salt welds and dense sub-salt faults.

7.3 Scales and styles of faulting in areas affected by halokinesis

In order to understand the scales and styles of faulting in the Espírito Santo Basin, SE Brazil and the Cleaver Bank High, Southern North Sea, this thesis randomly selected 110 faults from the former and 93 faults from the latter to compile displacement-length (D_{max}-L) and their corresponding throw-length (T-L) plots (See Appendix C and D).

Such plots are shown in Figs. 7.4 to 7.6 and reveal that crestal, corridor and keystone faults measured from the Espírito Santo Basin are clustered, as they have shown similar dimensions of maximum displacement and length in D_{max}-L plot (Fig. 7.5). Similarly, radial, polygonal and keystone faults recorded from the Cleaver Bank High are also clustered, showing similar dimensions of maximum displacement and length in D_{max}-L plot (Fig.7.6). Interestingly, the areas where these fault families clustered in D_{max}-L plots seem to overlap, especially for the faults with the length of ~1000 m in two study areas (Figs. 7.4-7.6). These faults clustered in D_{max}-L data are salt-related faults, as their growth and development are closely associated with halokinesis. Conversely, sub-salt and listric faults are scattered away from these clustered faults, showing larger maximum displacements and lengths than the latter (Figs. 7.4-7.6).

As a result, this thesis divides fault families around salt structures into two different types based on their distributions in D_{max}-L plots: 1) clustered salt-related faults with small displacements and 2) scattered sub-salt and listric faults. Note that two large faults, named Faults A and B described in Chapter 6 are not classified into these two types, as they are a part of two large fault zones crosscutting the entire seismic volume.

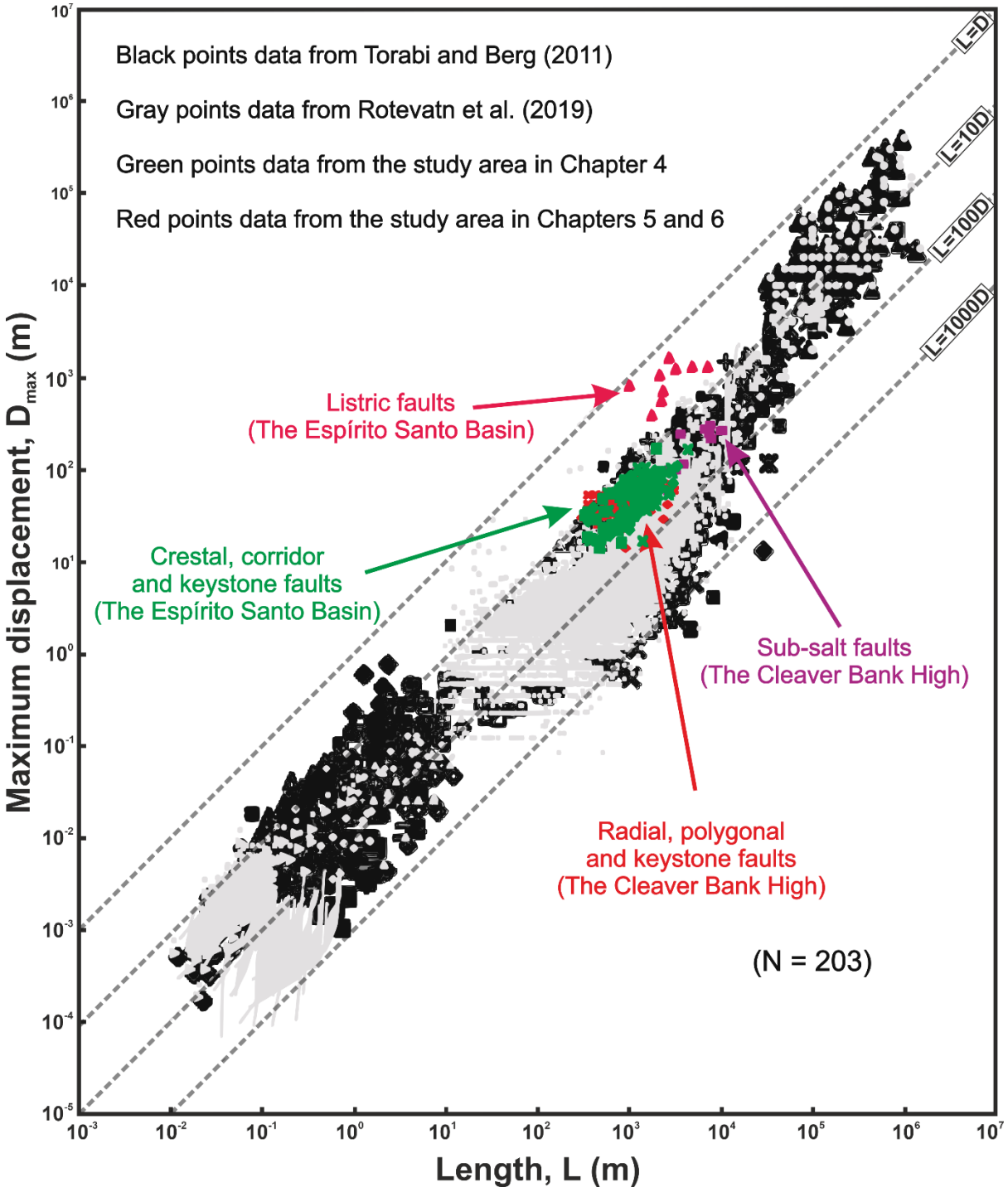

Fig. 7.4. Relationship between maximum displacement and length (D_{max}-L) for faults plotted in log-log space - data plotted as black points from Torabi and Berg (2011) and data plotted as grey points from Rotevatn et al. (2019). A total number of 203 maximum displacement and length data from the Espírito Santo Basin, SE Brazil in Chapter 4 and from the Cleaver Bank High, Southern North Sea in Chapters 5 and 6 are plotted as different colour points.

7.3.1 Clustered salt-related faults with small displacements

7.3.1.1 Clustered salt-related faults in the Espírito Santo Basin, SE Brazil

Clustered salt-related faults in the Espírito Santo Basin represent crestal, corridor and keystone faults. These faults are commonly planar faults, and their dips vary from 23º to 64º (Fig. 4.7). A total number of 101 salt-related faults in the Espírito Santo Basin were measured, with maximum displacement ranging from 14 to 168 m, throw ranging from 4 to 91 m, and length ranging from 325 to 4283 m (Fig. 7.5; Table 7.1; See Appendix C). Among these three fault families, keystone faults record the largest average value of length, maximum displacement and throw, which respectively are 1537, 60 and 30 m (Table 7.1). Conversely, crestal faults have the smallest average value of length, maximum displacement and throw, which respectively are 1008, 47 and 17 m (Table 7.1). The average value of length, maximum displacement and throw for corridor faults are 1294, 57 and 23 m, respectively (Table 7.1).

The displacement-length relationships of three fault families are similar in D_{max}-L plot (Fig. 7.5a). The length of these faults is about 10 to 100 times their maximum displacement. The throw-length relationship of three fault families are also similar in T-L plot, with the length of faults around 60 to 110 times their throw (Fig. 7.5b). Their maximum displacement and throw have shown positive correlations with length in log-log plots, indicating that fault's maximum displacement and corresponding throw increase with length (Fig. 7.5).

7.3.1.2 Clustered salt-related faults on the Cleaver Bank High, Southern North Sea

On the Cleaver Bank High, clustered salt-related faults refer to radial, polygonal and keystone faults, and their growth and development are associated with halokinesis. Polygonal faults mentioned here concern the aligned polygonal faults in Chapter 5, as they were influenced by the local stress field produced due to the growth of salt diapir K09. Polygonal faults in D_{max}-L plots overlap with radial and keystone faults (Fig. 7.6), so this thesis have classified them into salt-related faults.

Salt-related faults on the Cleaver Bank high are typical planar faults, with dips varying from 46º to 68º (Table 5.1). A total number of 82 salt-related faults were measured, showing that they have the maximum displacement ranging from 14 to 90 m, throw ranging from 10 to 16 m, and length ranging from 150 to 3061 m (Fig. 7.6; Table 7.1; See Appendix D). Measured radial and keystone faults have similar average lengths that are respectively 1068 and 1024 m,

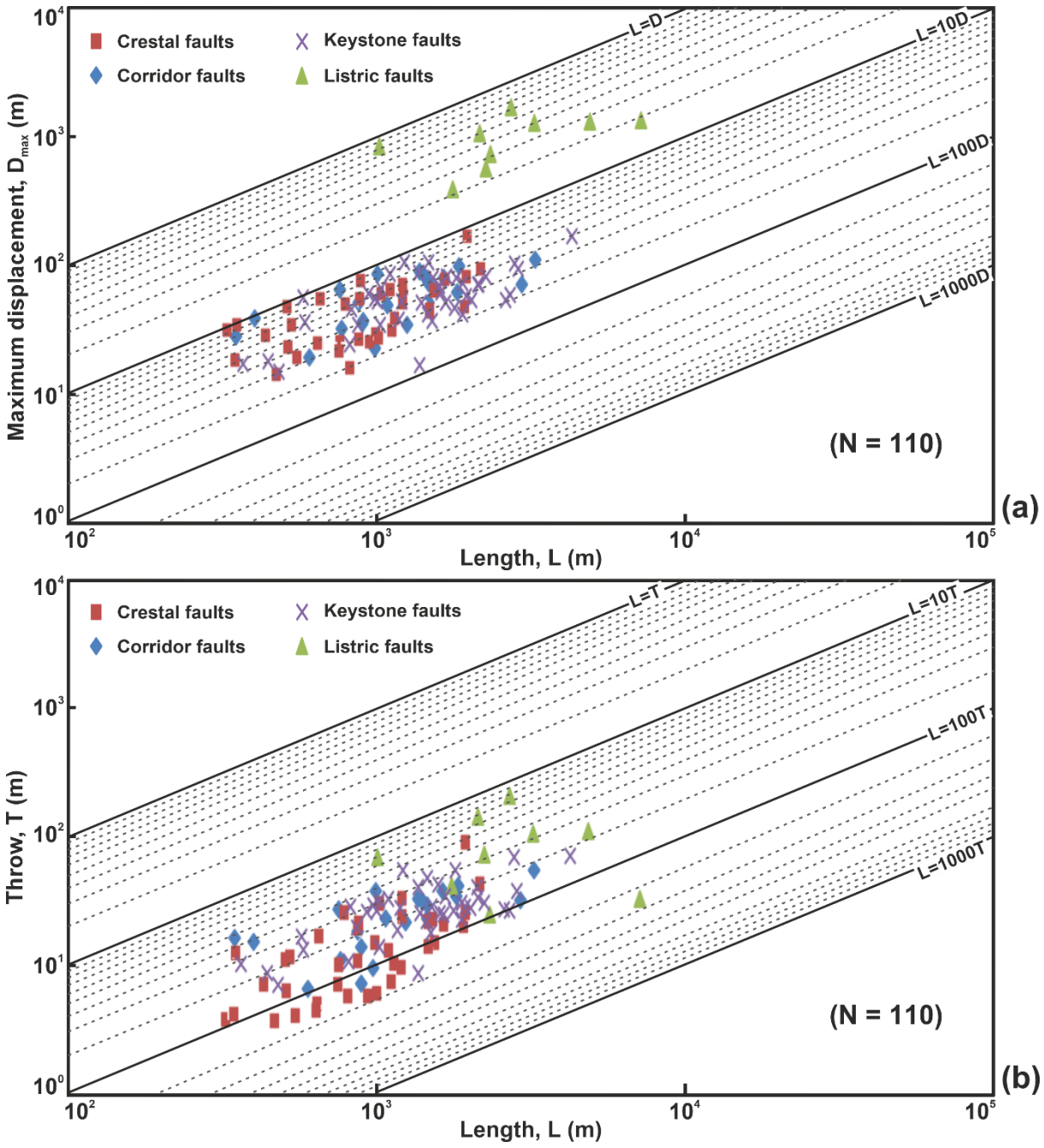

Fig. 7.5. A total number of 110 crestal, corridor, keystone and listric faults from the Espírito Santo Basin, SE Brazil, showing a) the relationship between their maximum displacement and length (D_{max}-L) and b) the relationship between their corresponding throw and length (T-L) in log-log plots.

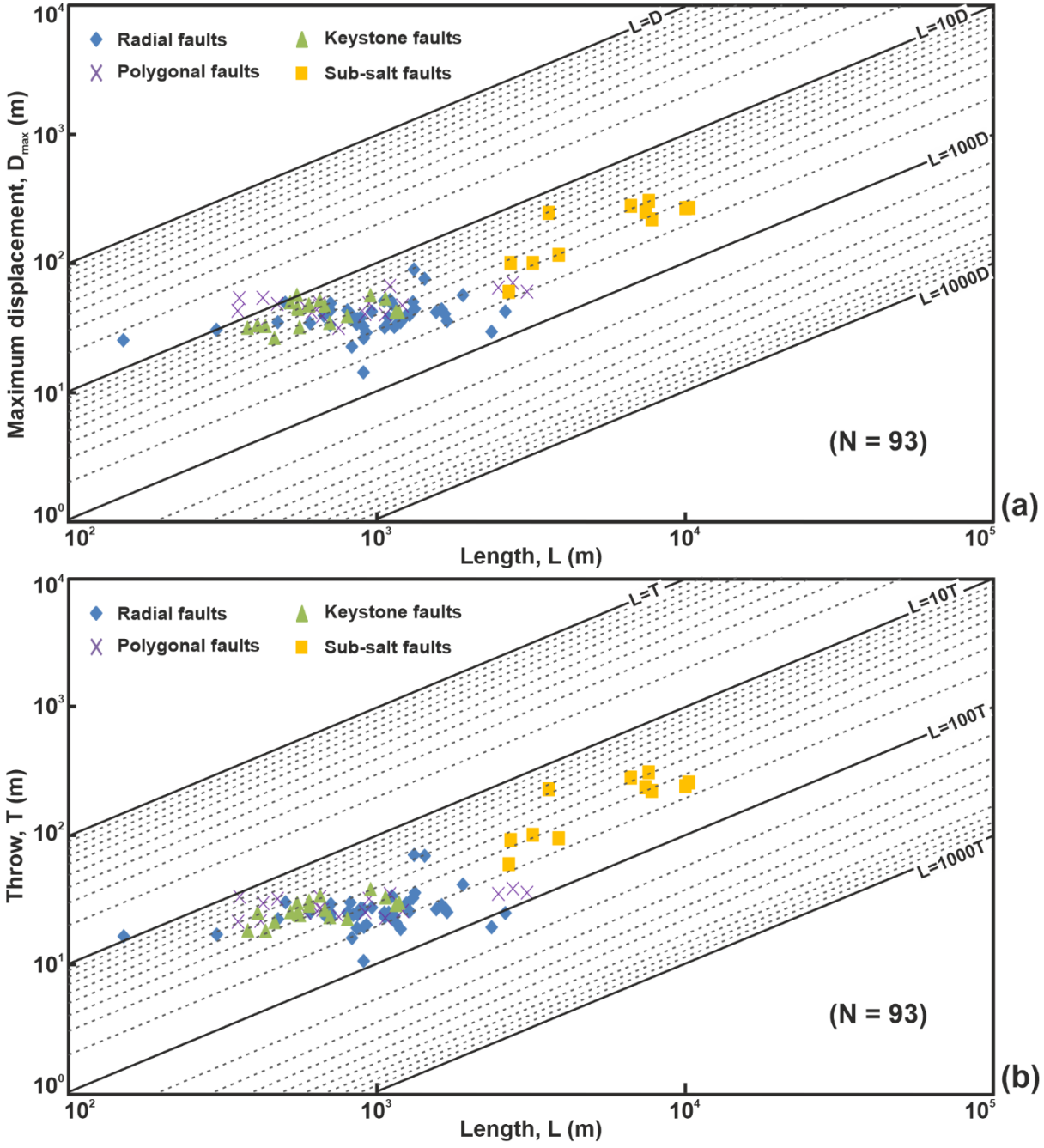

Fig. 7.6. A total number of 93 radial, polygonal, keystone and sub-salt faults from the Cleaver Bank High, Southern North Sea, showing a) the relationship between their maximum displacement and length (D_{max}-L) and b) the relationship between their corresponding throw and length (T-L) in log-log plots.

Area	Fault family	Fault number (N)	Length (L/m)	Average length (m)	Maximum dis-placement (D_{max}/m)	Average maximum displacement (m)	Throw (T/m)	Average throw (m)
The Espírito Santo Basin	Crestal faults	38	325 - 2166	1008	14.3 - 168	46.9	3.8 - 91.3	16.5
	Corridor faults	21	350 - 3275	1294	19.4 - 109.3	57.6	6.6 - 55.5	23.4
	Keystone faults	42	368 - 4283	1537	14.8 - 165.6	59.9	7.2 - 71.8	29.5
	Listric faults	9	1019 - 7211	3066	386.3 – 1658.0	1006.5	25.1 – 210.9	91.1
	Clustered salt-related faults	101	325 – 4283	1288	14.3 – 168.0	54.6	3.8 – 91.3	23.8
The Cleaver Bank High	Radial faults	44	150 - 2605	1068	14.3 - 89.8	40.1	10.3 - 69.1	26.4
	Polygonal faults	19	380 - 1178	674	26. 4 - 57.3	43.0	17.7 - 37.3	26.1
	Keystone faults	19	353 - 3061	1024	31.6 - 79.9	48.8	20.9 - 37.8	28.5
	Basement faults	11	2676 - 10269	5987	60.4 - 306.3	202.1	58.5 - 303.7	189.8
	Clustered salt-related faults	82	150 - 3061	966	14.3 – 89.8	42.8	10.3 - 16.0	26.8
Two study area	Clustered salt-related faults	183	150 - 4283	1144	14.3 - 168	49.3	3.8 - 91.3	25.1

Table 7.1. Fault data obtained from the Espírito Santo Basin and the Cleaver Bank High. The data show two different types of faults: 1) clustered salt-related faults with small displacements and 2) scattered sub-salt and listric faults.

whereas polygonal faults record the shortest average length of 674 m (Table 7.1). Measured polygonal faults have higher average value of the maximum displacement (43 m) than that (40 m) of radial faults, but lower than that (49 m) of keystone faults (Table 7.1).

The displacement-length relationships for radial and polygonal faults are similar in D_{max}-L plot, but are different from that for keystone faults (Fig. 7.6a). The length of radial and polygonal faults is about 9 to 100 times their maximum displacement, whereas the length of keystone faults is around 10 to 75 times their maximum displacement. This may be related to the fact that radial and polygonal faults are usually constrained to the Paleogene strata, resulting in that these faults are more likely to propagate laterally rather than vertically (Figs. 7.6 and 7.7). Similarly to the growth of a fault in layered sequence illustrated in Fig. 7.7, it shows that a fault expands horizontally when reaching to the upper and lower stratigraphic boundaries, resulting in the presence of low D_{max}/L ratio (Fossen, 2016). In parallel, the throw-length relationships for radial and polygonal faults are also similar in T-L plot, showing obvious differences with keystone faults (Fig. 7.6b). The length of radial and polygonal faults is around 10 to 105 times their throw, whereas the length of keystone faults is about 50 to 90 times their throw. The maximum displacement and throw for three fault families have shown positive correlations with length in log-log plots, indicating that their maximum displacement and corresponding throw increase with length (Fig. 7.6).

7.3.1.3 Clustered salt-related faults

Clustered salt-related faults measured in two study areas are all planar faults, with dips ranging from 23^o to 68^o. They have the maximum displacement ranging from 14 to 168 m, throw varying from 4 to 91 m, and length ranging from 150 to 168 m (Fig. 7.8; Table 7.1). Average values of length, maximum displacement and throw for these faults are 1144, 49 and 25 m, respectively (Table 7.1). The displacement-length relationships for clustered salt-related faults are similar to the throw-length relationships. The length of clustered salt-related faults is about 9 to 100 times their maximum displacement, and the throw of these same faults is about 10 to 110 times their throw (Fig. 7.8). The maximum displacement and throw for these faults show positive correlations with length in log-log plots, indicating that their maximum displacement and corresponding throw increase with length (Fig. 7.8). This correlates with the scaling laws of faults proposed by previous researchers (e.g. Ferrill and Morris, 2008; Ferrill et al., 2017; Kim and Sanderson, 2005; Schultz et al., 2008; Walsh et al., 2002).

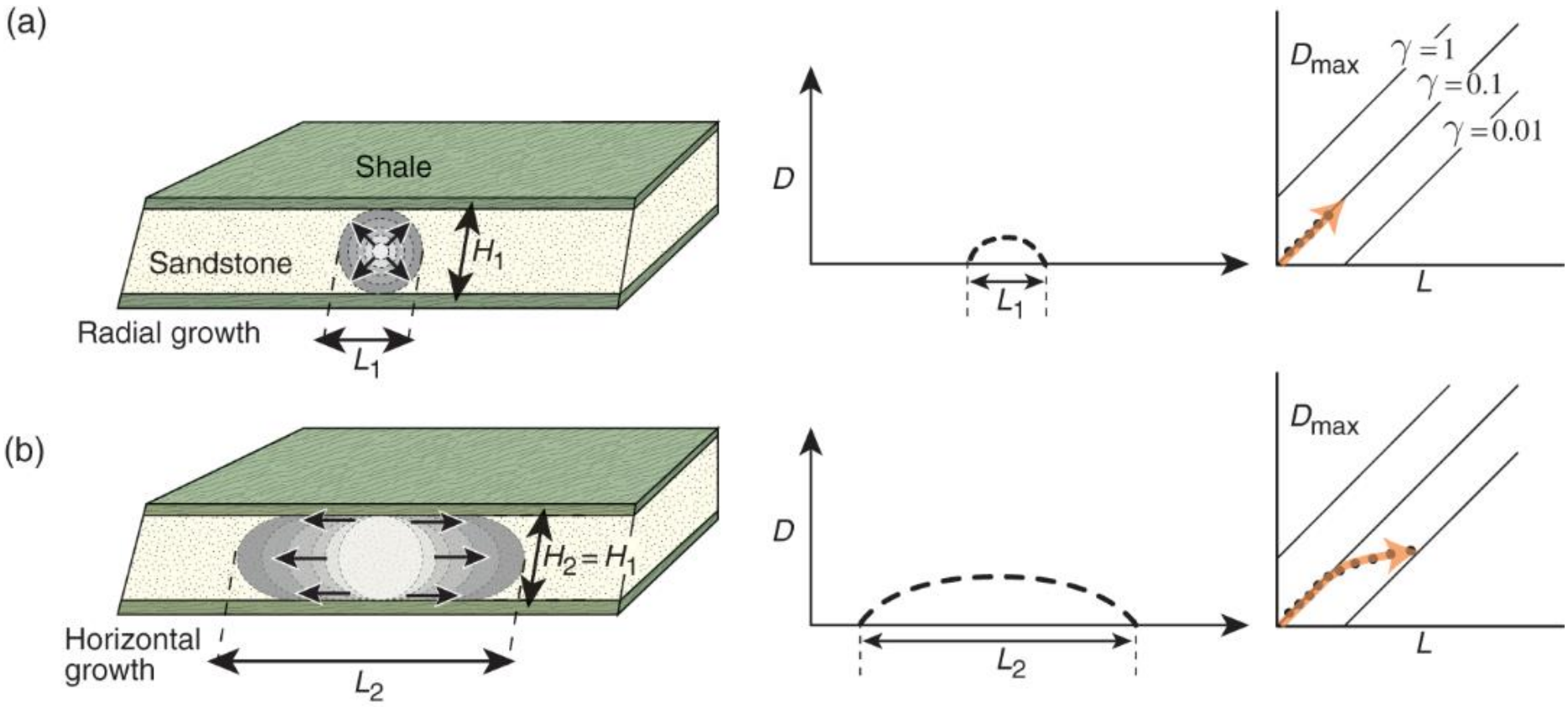

Fig. 7.7. Diagram illustrating the growth of a fault in a layered sequence, with displacement profile and displacement-length evolution shown to the right (logarithmic axes). The fault nucleates in a sandstone layer (a) with a normal displacement profile and expands horizontally when hitting the upper and lower boundaries (b). Figure from Fossen (2016).

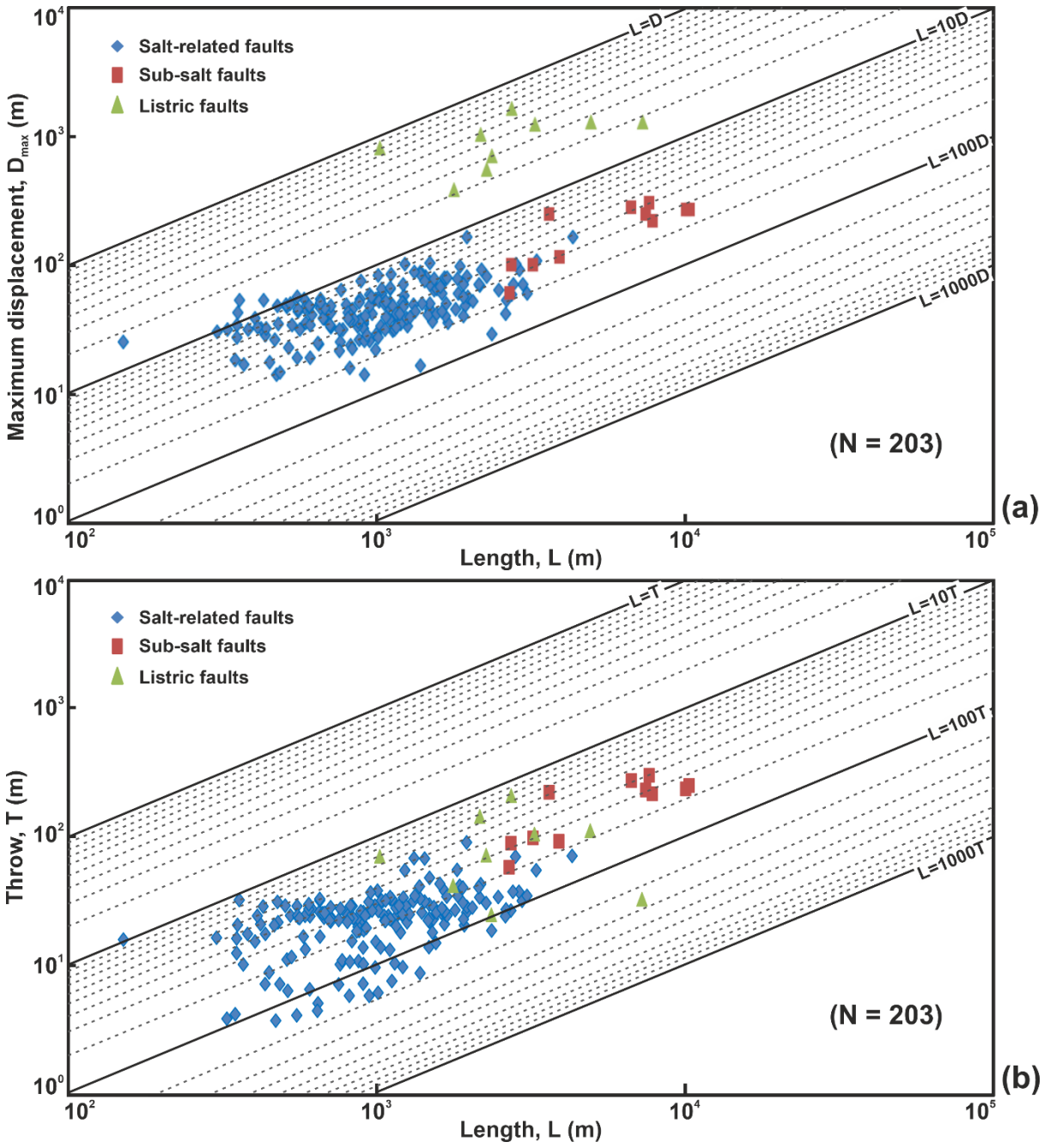

Fig. 7.8. A total number of 203 clustered salt-related, sub-salt and listric faults from the Espírito Santo Basin, SE Brazil and the Cleaver Bank High, Southern North Sea, showing a) the relationship between their maximum displacement and length (D_{max}-L) and b) the relationship between their corresponding throw and length (T-L) in log-log space.

Clustered salt-related faults from two study areas in D_{max}-L or T-L plots overlap with faults documented from the previous publications in literature, which were developed in different tectonic settings and mechanical stratigraphy (Fig. 7.4). For example, normal faults offset Carboniferous to early Permian coal measures deposits in the Lorraine coal field, NE France (Villemin et al., 1995) and in the East Pennine Coalfield, United Kingdom (Childs et al., 1990; Nicol et al., 1996), which records the faults length ranging from ~350 to ~20,000 m with the throw ranging from ~10 to ~300 m and length varying from ~100 to 10,000 m with maximum throw ranging from ~20 to ~800 m, respectively. Normal faults developed in Jurassic strata affected by end-Jurassic extension in the northern North Sea, with fault length ranging from ~300 to ~20,000 and maximum throw ranging from ~8 to ~1500 m (Yielding, 1996). Crestal faults developed in the Mesozoic strata above the Samson Dome, Northern Norway, with the fault length from 2776 to 19801 m and displacement from 23 to 82 m (Mattos et al., 2016). Crestal and radial faults intersect the Late Cretaceous to Paleogene strata around salt diapirs in Espírito Santo Basin, showing the length of faults from 751 to 9512 m and displacement from 36 to 83 m (Mattos and Alves, 2018). This indicates that clustered salt-related faults from two study areas are normal faults in nature, which can have the same displacement/throw-length relationships with other normal faults formed in different tectonic settings and mechanical stratigraphy.

7.3.2 Scattered sub-salt and listric faults

7.3.2.1 Sub-salt faults on the Cleaver Bank High, Southern North Sea

Sub-salt faults on the Cleaver Bank High are covered by thick overlying Zechstein Group, and they are decoupled from supra-salt strata for the tectonic deformation. These faults usually have experienced multiple phases of reactivation since the Upper Palaeozoic, resulting in their high length-throw ratios (Ligtenberg et al., 2011; Van Ojik et al., 2020; Alves et al., 2022). Sub-salt faults are usually high angle planar faults, with dips varying from 71º to 89º (Figs. 6.2-6.4). A total of 11 sub-salt faults were measured on the Cleaver Bank High, and most measured sub-salt faults have the lower tips reaching out the lower boundary of seismic volume. This may cause the wrong measurements of maximum displacement for these faults. Measured sub-salt faults have the maximum displacement ranging from 60 to 306 m, throw ranging from 59 to 304 m, and length ranging from 2676 to 10,269 m (Fig. 7.8; Table 7.1). The average value of length, maximum displacement and throw of sub-salt faults are respectively

5987, 202 and 189 m, values that are much higher than those of clustered salt-related faults. The displacement-length relationships for sub-salt faults are almost the same with their throw-length relationships (Fig. 7.8). The length of sub-salt faults is about 30 to 90 times their displacement, and the length of these same faults is also about 30 to 90 times their throw. This indicates that sub-salt faults mainly accrue vertical displacement rather than horizontal displacement with the increase of length. It correlates with the fact that sub-salt faults have high dip angles (71^o to 89^o). Similarly to clustered salt-related faults, the maximum displacement and throw of sub-salt faults have shown positive correlation with the length (Fig. 7.8).

Sub-salt faults measured in this thesis have distinct differences with sub-salt faults documented by Alves et al. (2022) in the Central Offshore Platform, Southern North Sea, though their study area is next to the Cleaver Bank High. Their sub-salt faults have the length ranging from 325 to 4725 m (Alves et al., 2022), which is much shorter than sub-salt faults measured in this thesis. However, the maximum throws of their sub-salt faults vary from 15 to 320 m, having similar dimension of throws with sub-salt faults measured in this thesis. It indicates that their sub-salt faults are likely to have larger displacement than sub-salt faults recorded in this thesis with the same fault length. This may be related to the difference of faults reactivation histories for sub-salt faults between the Central Offshore Platform and the Cleaver Bank High.

7.3.2.2 Listric faults in the Espírito Santo Basin, SE Brazil

Listric faults developed in the Espírito Santo Basin are highly curved in plan view, and their dips vary greatly with depth in seismic profiles, with dips varying from 2.3^o to 22.9^o (Fig. 4.7). Their formation was related to the presence of underlying local overpressure based on the mechanism proposed by Yuan et al. (2020). A total number of 9 listric faults were measured in the Espírito Santo Basin, with the maximum displacements varying from 386 to 1658 m, throw varying from 25 to 211 m, and length varying from 1019 to 7211 m (Fig. 7.8; Table 7.1). The average value of length and throw for listric faults are 3066 and 91 m, which are higher than clustered salt-related faults but lower than sub-salt faults mentioned above (Fig. 7.8; Table 7.1). However, average value of the maximum displacement for listric faults is 1002 m, which is much higher than sub-salt and salt-related faults (Fig. 7.8; Table 7.1). This indicates that listric faults have large horizontal displacement - heave, which is mainly attributed to their lower dip angles in their lower parts. The length of listric faults is about 2 to 10 times their displacement, but the length of these same faults is about 12 to 120 times their throw (Figs. 7.5 and 7.8). It

means that listric faults mainly accrue horizontal displacement rather than vertical displacement with the increase of length. Additionally, their maximum displacement and throw have shown positive correlation with length (Fig. 7.8). In literature, there are rarely faults overlapping with these listric faults in D_{max}-L plot (Fig. 7.4), as little research has focused on the relationships between the maximum displacement and length for listric faults by using seismic data.

Apart from faults mentioned above, two NE-striking large faults named Faults A and B in Chapter 6 were also developed on the Cleaver Bank High, Southern North Sea, and their formations mainly relate to the regional NW-SE extension in the Mesozoic. Fault A is a large growth normal fault with the maximum displacement over 1647 m, and its length measured in this 3D seismic volume is 36,678 m (Fig. 6.2). It is a large planar fault at its lower part but is separated into two fault segments at its upper part (Figs. 6.5 and 6.7), indicating the variation of regional tectonic stress directions during the Cenozoic. Fault A propagated upwards from the Zechstein Group into the Upper North Sea Group, and it was formed during the Early Triassic due to the thickening of the Upper and Lower Germanic Trias Groups on its hanging-wall block. Fault B is a large dextral strike-slip fault with a length of 19.4 km in the study area, and its lateral maximum offset is ~9.1 km based on the distance between two equivalent NW-striking faults that were offset by it (Figs. 6.5-6.7). It is nearly vertical and propagates from the subsalt Rotliegend Group into the relatively shallow North Sea Group (Fig. 6.3).

7.4 Implications for fluid flow, storage and production

Fault families around salt structures play an important role in controlling the fluid flow, storage and production in salt-rich basins, as faults are capable of acting as barriers or conduits to fluid flow (e.g. Cox et al., 2001a; Gartrell et al., 2004). However, it is usually hard to distinguish whether a fault acted as barrier or conduit to fluid flow. This is because faults sealing competence are affected by multiple geological factors, such as the lithology of the strata crossed by the fault, fault displacement, fault-gouge geometry, fault geometry in relation to local stress fields, post-deformation cementation and interactions between fluids and host rock (Caine et al., 1996; Fisher and Knipe, 2001; Koledoye et al., 2003; Manzocchi et al., 2010). In this section, this thesis discusses the importance of fault families around salt structures for fluid

flow and trapping based on fluid flow features and geothermal gradient anomalies. Later, their implications for carbon and energy storage are also discussed, highlighting that salt-related faults can be useful palaeostress indicators around salt structures.

7.4.1 Importance of fault families around salt structures to fluid flow and trapping

In this thesis, multiple fluid flow features are observed around faults in seismic data, including pockmarks, bright spots and gas pipes (Fig. 7.9). Although these fluid flow features are subtle in seismic data, they have a key significance to hydrocarbon and geothermal energy exploration. In more detail, pockmarks and gas pipes around faults indicate that these faults have acted as effective fluid migration pathways, which are associated with fluid leakage along faults. Conversely, bright spots around faults indicate that faults have been acting as barriers to fluid flow, showing the position of hydrocarbon traps around salt structures.

Pockmarks are usually recognised as circular to elliptical depressions at the (paleo) sea-floor, and their formation relates to the expulsive fluid venting (Hovland and Judd, 1988; Hovland et al., 2002; Judd et al., 2007; Cathles et al., 2010; Marcon et al., 2014). In the Espírito Santo Basin, many large pockmarks are observed at the upper part of listric faults with different geometries and sizes (Fig. 7.9). These pockmarks occur on the hanging-wall of listric faults and directly or indirectly lie above the footwall (Fig. 7.9), proving that their formation are associated with fluid flow along these faults. This can also be confirmed by the fact that many bright spots are found at the lower part of listric faults. Many pockmarks directly overlie the footwall of listric faults, whereas a few pockmarks indirectly overlie the footwall of listric faults (Fig. 7.9). This is associated with the position in which fluid escape from listric faults. Previous research has reported the formation of pockmarks associated with listric faults in the Ebro Delta, Spain and the West African continental margin (e.g. Maestro et al., 2002; Pilcher and Argent, 2007), indicating that pockmarks occurred above the footwall cut-offs of the organic-rich unit or overpressured interval (Fig. 7.10). It is because the minimum effective stress is usually located at the point of the footwall cut-off of the overpressured layer where it is the most likely to cause the vertical fluid leakage to the seabed and the formation of a pockmark (Pilcher and Argent, 2007). This can also explain the formation of pockmarks associated with listric faults in the Espírito Santo Basin, though fluid in the latter were transported through

listric faults from deep potential source rock into shallow strata, rather than transported from the organic-rich unit or overpressured intervals offset by listric faults.

Bright spots are known for the indicators of hydrocarbons, and their formation usually relates to gas within clastic reservoirs (e.g. Cox et al., 2020). In the Espírito Santo Basin, many bright spots are found around faults, especially listric faults (Fig. 7.9). This indicates that these faults act as barriers to the hydrocarbon, showing the position of hydrocarbon traps. The distribution of bright spots shows that hydrocarbon traps are not only located around faults above salt diapirs, but also founded around faults in the salt minibasin. Moreover, bright spots are founded at different depths around faults in the Espírito Santo Basin (Fig. 7.9), showing that they were transported from deep strata into shallow strata. Bright spots are mainly observed around faults propagating into the interval that listric faults sole out into, implying that these intervals are potential source rocks. Furthermore, for listric faults, bright spots are mainly located at their lower parts, which may be related to the dips of faults. It is because faults with lower dips are subjected to larger sediment loading from the overburden than faults with higher dips at the same depth, a fact related to the resolving of loading forces on fault's plane. In this way, faults with low dips are more likely to trap fluid than faults with high dips, which has also been proved by fault leakage factor analyses in Chapter 4. This explains why many bright spots are mainly observed at the lower part of listric faults and many large pockmarks are formed at the upper part of listric faults. Additionally, most listric faults are growth faults, so they are more likely to transport fluids during their growth when compared with salt-related faults. That explains that many fluid flow features are usually observed around listric faults rather salt-related faults.

Gas pipes are usually shown as vertical extensive either low- or high-amplitude anomalies in seismic data, mainly associated with vertically focused fluid flow (e.g. Løseth et al., 2009; Andresen, 2012; Cartwright and Santamarina, 2015; Wangen, 2020; Robinson et al., 2021). On the Cleaver Bank High, many gas pipes are observed at different depths, showing as vertical low-amplitude anomalies in seismic data. This indicates that these faults below gas pipes acted as effective fluid migration paths, transporting fluid from deep strata into shallow strata. Gas pipes above sub-salt faults are mainly developed around the areas where the Zechstein salt is very thin (<100 ms; or ~230 m), or even absent. It is mainly because the Zechstein salt is an effective seal, stopping fluid flow along sub-salt faults into the supra-salt strata. The fluid migrated through sub-salt faults consist mainly of wet and dry gas generated from the

Westphalian Coal Measures in the Limburg Group and Pre-Westphalian marine deposits (Fattah et al., 2012a). The pre-Westphalian source rocks entered the hydrocarbon generation window in the Late Carboniferous; the Westphalian source rocks started generating gas during the Upper Triassic, generating more gas during the Paleogene and continuing in present-day (Fattah et al., 2012a). Additionally, some salt-related faults have also acted as fluid migration paths, promoting the shallow fluid flow upward into the (paleo) seafloor (Fig. 7.9). The fluid may be mainly composed of biogenetic gas, as the temperature of supra-salt strata is not high enough to reach the hydrocarbon generation window since their depositions on the Cleaver Bank High (Fig. 6.10).

In addition to the fluid flow features mentioned above, geothermal gradient anomalies are also useful to indicate the existence of fluid flow along faults. Geothermal gradients measured from twelve (12) wells around Fault A discussed in Chapter 6, indicating that high geothermal gradients are recorded on the footwall of the Fault A. For example, well K11-10 recorded the extremely high geothermal gradient of 121.8ºC/km at the vertical depth of 404 m, though the temperature at this depth is merely 46.9ºC. This high geothermal gradient anomaly relates to fluid migration along Fault A into shallow strata, as multiple low-amplitude trails of fluid are observed on the hanging-wall of Fault A in Fig. 6.2a. This can also be confirmed by the distinct differences between its modelled present-day temperatures and corrected BHTs for well K11-10, as its corrected BHTs are much higher than modelled present-day temperatures (Fig. 6.10b). It proves that Fault A has acted as conduits to deep and hot fluid into shallow depth, resulting in the presence of high geothermal gradient anomalies around faults.

In summary, fluid flow features around salt-related faults indicate that salt-related faults can act as effective fluid conduits in the Espírito Santo Basin and the Cleaver Bank High, especially these faults propagating into the (potential) source rock. Sub-salt and listric faults are also useful fluid conduits, and they may have more important role in fluid flow than salt-related faults in two study areas. This is because most sub-salt and listric faults directly offset or detach the source rocks, and they are respectively growth and reactivated faults. This means that sub-salt and listric faults are more likely to transport fluid generated from the source rocks into shallow strata when source rocks enter the hydrocarbon generation windows. Additionally, the geometry of faults has influence on fluid flow, especially their dips, as steep faults are more favourable to fluid flow than gentle faults. Finally, large regional faults, such as Fault A, are important paths for fluid flow, proved by the geothermal gradient anomalies recorded around them.

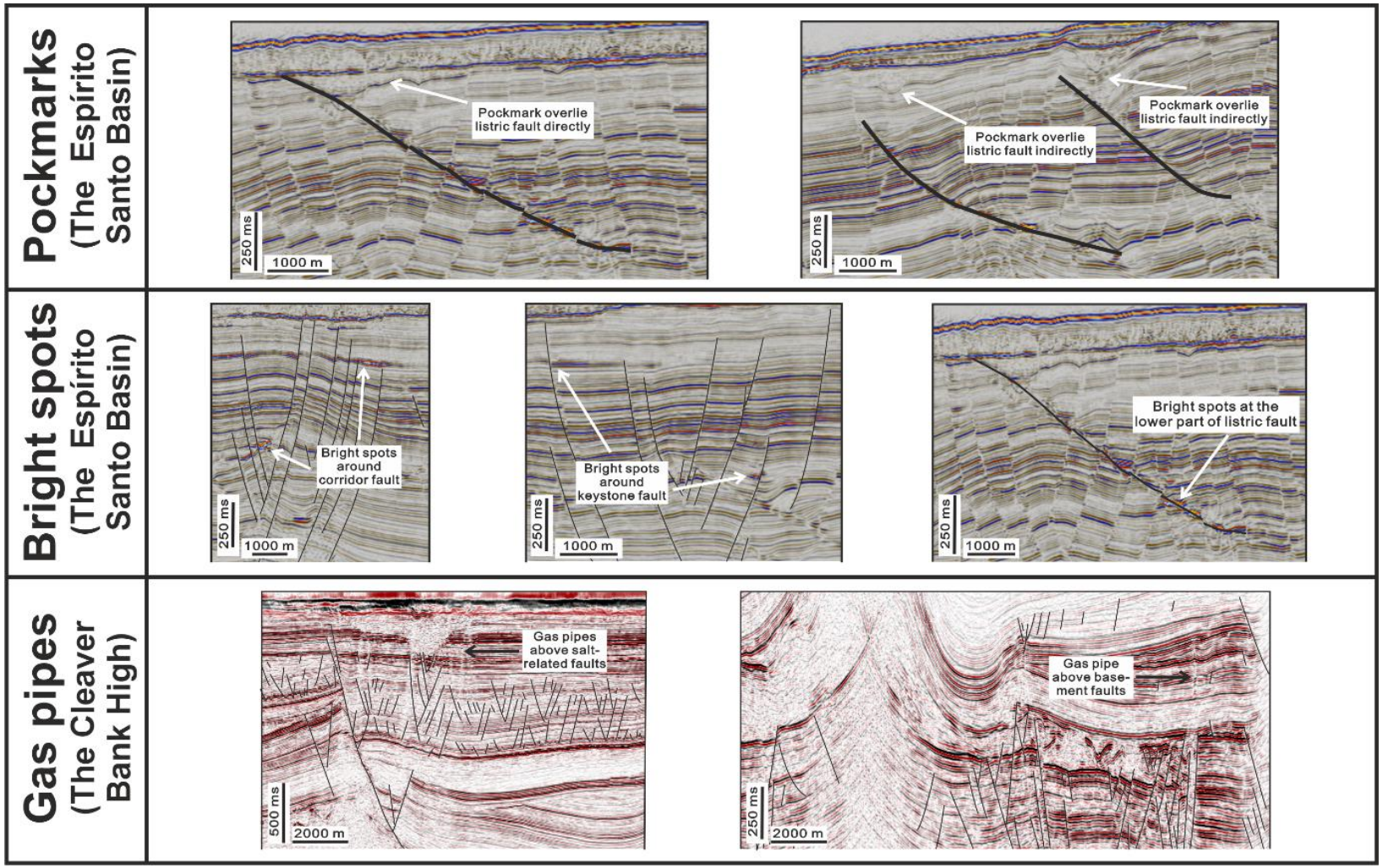

Fig. 7.9. Fluid flow features on seismic data observed around faults in the Espírito Santo Basin and the Cleaver Bank High. Pockmarks are mainly formed at the upper part of listric faults, whereas bright spots are found around corridor, keystone and listric faults in the Espírito Santo Basin. Gas pipes are developed above salt-related and sub-salt faults on the Cleaver Bank High.

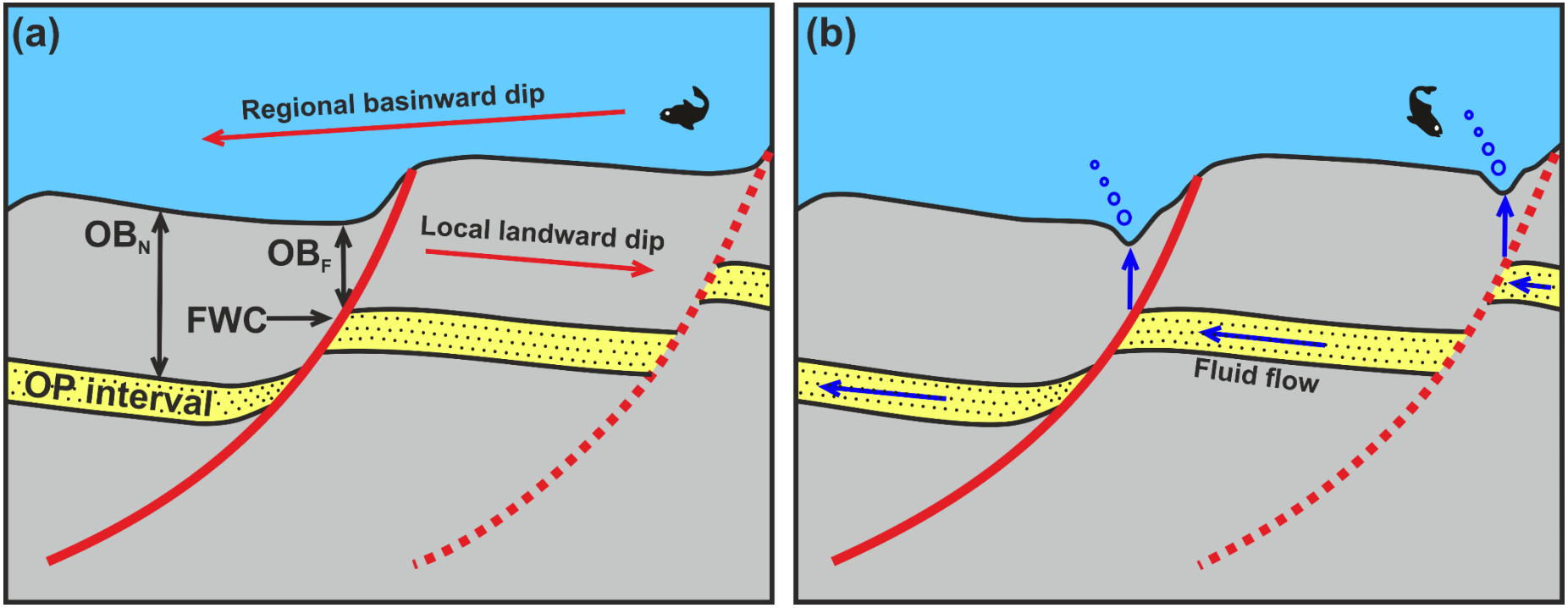

Fig. 7.10. Schematic illustration of the formation of pockmarks associated with listric faults. (a) An overpressured (OP) interval offset by listric faults and rotated to dip landward. The confining overburden above the overpressured interval is reduced from normal (OB_N) to a thinner amount related to the throw on the fault (OB_F). (b) An effective stress minimum at the point of the footwall cut-off (FWC) is created due to the local reduction of the overburden if the pressure magnitude in the overpressured interval is constant. With the increasing pore pressure or decreasing overburden pressure, the effective stress may reduce to zero, resulting in vertical fluid leakage to the seabed and the formation of pockmarks. Figure modified from Pilcher and Argent (2007).

7.4.2 Salt-related faults as palaeostress indicators around salt structures

Salt structures with different geometries and sizes are ubiquitous in salt-rich basins, and they have important significances from the geological and economic aspects (e.g. Jackson and Hudec, 2017). Understanding the stress state around salt structures is vital for conventional hydrocarbon exploration, carbon sequestration and gas storage around the former. However, the stress state around salt structures, especially irregular salt structures, varies with their position and distance relative to surrounding salt structures (Fredrich et al., 2003; Bowers, 2007; Sanz and Dasari, 2010b; Luo et al., 2012; Nikolinakou et al., 2012; Carruthers et al., 2013; Coleman et al., 2018; Zhang and Alves, 2023). In this thesis, salt-related faults are used to reveal the palaeostress state around salt structures in Chapters 4 and 5 by applying the stress inversion for interpreted salt-related faults, providing insights into their evolving stress states. This is based on the fact that salt-related faults were usually formed under the stress field produced by halokinesis. For example, crestal and corridor faults studied in Chapter 4 were developed above or around salt diapirs A and B, and their growth and development are mainly associated with the growth of these two salt diapirs (Fig. 4.15). Radial faults in Chapter 5 were developed around salt diapir K09, having accommodated the circumferential stress around this salt diapir (Fig. 5.12). The geometrical differences between the corners and the flanks of salt diapir K09 account for the different palaeostress states between flanking and corner zones. The corner shape of salt diapir K09 is convex in plan view, whereas the flank shape of this same salt diapir is concave (Fig. 5.12). This implies that salt diapir K09 is more likely to push the surrounding strata during salt rise in its corners when compared to its flanks. This means that the magnitude of intermediate stress (σ_2) from corner zones to flanking zones would decrease, as the salt pushing directions mainly represents the direction of intermediate stress (σ_2). As for the transition from the zones of radial faults to the zone of polygonal faults, it is mainly associated with the boundary of hoop stress produced due to salt growth around salt structures. Moreover, aligned polygonal faults in Chapter 5 developed in the outer part of diapir K09 flanks are also influenced by the stress field produced due to the underlying salt movement (Fig. 5. 15). Therefore, salt-related faults are capable of providing a relatively accurate record of the stress states associated with halokinesis (Quintà et al., 2012; Carruthers et al., 2013; Coleman et al., 2018). In other words, salt-related faults are effective palaeostress indicators around salt structures, a character with important implications to the hydrocarbon exploration, carbon and energy storage around salt structures.

In comparison with salt-related faults, sub-salt faults buried below the Zechstein salt in Chapters 5 and 6 were formed during the Upper Paleozoic by inheriting the pre-existing weakness zones in the Paleozoic basement (Ziegler, 1990; Schroot and Haan, 2003). They are not able to provide useful record of the stress states associated with halokinesis, though halokinesis may influence the reactivation of these sub-salt faults. The driving forces for the reactivation of sub-salt faults is likely to be associated with overlying salt movement above basement faults. As for listric faults in Chapter 4, they are not applicable to stress inversion used for salt-related faults, though they were also developed in the minibasin where keystone faults developed. It is mainly because the formation of listric faults related to the presence of underlying local overpressure, resulting in the presence of very low dip angle (2.3º to 22.9º) for listric faults, which cannot be correctly calculated during stress inversion on Move®. Hence, salt-related faults, including the aligned polygonal faults can be the useful palaeostress indicators around salt structures in the Espírito Santo Basin and the Cleaver Bank High, which can also be used in other salt-rich basins around the world.

7.5 Limitations of this research

High quality 3D seismic reflection volumes and well data are the primary data used in two study areas throughout this thesis; the Espírito Santo Basin, SE Brazil and the Cleaver Bank High, Southern North Sea. However, seismic resolution is the key limitation for 3D seismic reflection volumes in two study areas, as many small geological elements are not resolvable at the seismic scale. As for the limitation of well data, it is mainly associated with the depth of well logging. Except for the limitations mentioned above, there are also other limitations in three key result chapters (Chapters 4-6), so this section here discusses these limitations in three chapters, respectively.

The main limitations for Chapter 4 included the vertical extent of 3D seismic reflection volume and the absence of well logging data, especially total organic carbon (TOC), pore fluid pressure and subsurface stress data. The 3D seismic volume of the Espírito Santo Basin is delimited by its bottom boundary at the depth of ~4600 ms. A greater depth range would have provided a better opportunity to map salt structures and sub-salt stratigraphic units, study the spatial and temporal evolution of salt structures, and analyse the development of sub-salt faults. Two (2) wells drilled in the Espírito Santo Basin do not include TOC, pore fluid pressure and subsurface stress data. These data could be useful to verify the formation mechanism of listric

faults, helping to understand the significance of listric faults and to analyse fault slip and leakage under the present geological conditions. Additionally, all interpreted faults for stress inversion analyses are assumed as dip-slip faults, as fault stria data cannot be obtained from the seismic data. This assumption would result in the differences between the palaeostress state calculated by stress inversions and the true palaeostress state around salt structures.

In Chapter 5, seismic resolution, the assumption of stress inversion and the assumption of fault formation timing were the key limitations. Seismic resolution in 3D seismic volume of the Cleaver Bank High ranges from 8 to 12 m in Cenozoic strata, limiting the interpretation of smaller faults that are not resolvable in seismic data. Similarly to Chapter 4, stress inversions for interpreted faults in Chapter 5 were applied by assuming that all interpreted faults are dip-slip faults, indicating that stress inversion results may not be the true palaeostress state around salt structures. All interpreted faults used for stress inversion were assumed to form in the Paleogene rather than in sequence, which may result in the incorrect result obtained from stress inversion.

The key limitations for Chapter 6 consisted of seismic resolution, the depth of measured BHTs, and the incomplete information of BHTs. Seismic resolution in 3D seismic volume of the Cleaver Bank High is around 40 m below Zechstein salt, and ranges from 8 to 12 m in Cenozoic strata. It results in that many small geological structures that are not resolvable in seismic data, especially at deep depths. Furthermore, most BHTs were measured in the Upper Rotliegend or Limburg Groups, much more than BHTs measured in the North Sea and Chalk Groups. This may lead to the higher inaccuracy of the subsurface temperature and geothermal gradients in the North Sea and Chalk Groups than in the Upper Rotliegend or Limburg Groups. In addition, 191 BHTs are measured without recording the time since mud circulation, so they are simply corrected by adding 18^{o}C to the original temperatures. These BHT data have relative large uncertainties after corrections, causing the misunderstanding of the subsurface temperature and geothermal gradients on the Cleaver Bank High.

7.6 Further work

In this thesis, fault families around salt structures and their implications for fluid flow, storage and production have been investigated in two different study areas, including a passive margin setting (SE Brazil) and an inter-cratonic basin (Southern North Sea). The two study

areas are typical salt-rich areas with abundant salt structures, and multiple fault families have been developed around salt structures. Many fluid flow features are also observed around these faults in two study areas, implying that faults around salt structures have controlled fluid flow. Faults, especially salt-related faults, in two study areas are significantly affected by the halokinesis, indicating that the growth of salt structures is vital to their surrounding fault families. However, salt structures, developed in foreland basins of continental collision zones such as Tarim Basin, have distinctly different geometries and styles when compared with salt structures in this thesis. Consequently, faults around salt structures and their implications for fluid flow in the former may also be different with faults in this thesis. Hence, it is important in the future to study fault families around salt structures and their implications for fluid flow in foreland basins, which can compare and contrast with the results in this thesis. It helps us to have a better understanding of the relationship between fault families and salt structures in different tectonic settings.

In addition to studying fault families in foreland basins, it will be useful to obtain the present subsurface stress state around salt structures from drilling wells or numerical modelling. Using these stress data to implement fault slip tendency and leakage analyses would provide the robust evidence to predict effective fluid flow paths. With these stress data, it is possible to reconstruct the evolving stress state around salt structures. Moreover, fault seal competence analyses, such as fault juxtaposition, fault gouge smear and surrounding damage zone, would be helpful to have a better understanding of the implications of faults on fluid flow. Furthermore, the development of large pockmarks above listric faults mentioned in Chapter 4 can be further studied to understand the relationship between pockmarks and listric faults. The stress inversion method introduced in Chapter 5 is likely useful to explore the palaeostress state around complex salt structures. These further work is of great importance to hydrocarbon exploration, carbon and energy storage around salt structures.

Chapter 8

Conclusions

8 Conclusions

This thesis provides a detailed analysis of fault families around salt structures and their implications for fluid flow, storage and production, covering two study areas in the Espírito Santo Basin, SE Brazil (Chapter 4) and the Cleaver Bank High, Southern North Sea (Chapters 5 and 6). A summary of the main conclusions from this thesis is listed below.

8.1 Conclusions from Chapter 4

- Ten (10) interpreted listric faults with dips ranging from 2.3^{o} to 22.9^{o} were analysed in a salt minibasin of the Espírito Santo Basin, SE Brazil. These listric faults sole out into the soft and ductile strata that has similar seismic, lithological and petrophysical characters to known Cenomanian to Turonian source rocks. It implies that listric faults can mark the presence of hydrocarbon source rocks in salt minibasins.
- Fault families around salt structures include crestal, corridor, keystone and listric faults, and their formation and evolution are strongly influenced by halokinesis in salt minibasins. It can be summarised into three structural stages during the Cenozoic.
- Leakage factor analyses for fault families around salt structures, indicating that keystone faults are the most favourable fluid pathways. Conversely, listric faults are likely to form barriers and baffles to fluid, especially in their lower parts.

8.2 Conclusions from Chapter 5

- Fault families, especially radial faults, around salt diapirs are capable of providing a relatively accurate record of the stress states associated with halokinesis.
- Halokinesis controlled the formation and development of fault families around salt structures in three structural stages during the Cenozoic.
- Stress inversions are useful to estimate palaeostress around irregular salt diapirs. It shows that palaeostresses in flanking and corner zones differ around irregular salt diapirs. The combination of minimum principal palaeostresses from all flanking and corner zones forms a triangle-shaped hoop.

8.3 Conclusions from Chapter 6

- Strata deposited above the Zechstein Group show higher geothermal gradients proportionally to the thickness of Zechstein salt. Conversely, the strata buried below this Group show a minor decreasing trend in geothermal gradients with an increasing thickness of salt.
- Large supra-salt faults can be effective fluid migration paths, resulting in the high geothermal gradients around them. Geothermal gradients on footwall blocks are usually higher than that on the corresponding hanging-walls of these large supra-salt faults, but it decreases with the distance away from these faults.
- Sub-salt faults can also be effective fluid migration paths, as long as its overlying Zechstein salt is very thin (<100 ms). It transports the sub-salt fluid into the supra-salt intervals, forming distinct gas pipes in seismic data.
- As a corollary of this thesis, three potential geothermal exploration targets are identified on the Cleaver Bank High.

References

Ackermann, R. V., Schlische, R. W., and Withjack, M. O., 2001, The geometric and statistical evolution of normal fault systems: an experimental study of the effects of mechanical layer thickness on scaling laws: Journal of Structural Geology, v. 23, no. 11, p. 1803-1819.

Alaei, B., and Torabi, A., 2017, Seismic imaging of fault damaged zone and its scaling relation with displacement: Interpretation-a Journal of Subsurface Characterization, v. 5, no. 4, p. Sp83-Sp93.

Alberts, M. A., Underhill, J. R., and Spencer, A., 1991, The effect of Tertiary structuration on Permian gas prospectivity, Cleaver Bank area, southern North Sea, UK: Generation, accumulation, and production of Europe's hydrocarbons. European Association of Petroleum Geoscientists Special Publication, v. 1, p. 161-173.

Alsop, G., Brown, J., Davison, I., and Gibling, M., 2000, The geometry of drag zones adjacent to salt diapirs: Journal of the Geological Society, v. 157, no. 5, p. 1019-1029.

Alsop, G. I., 1996, Physical modelling of fold and fracture geometries associated with salt diapirism: Geological Society, London, Special Publications, v. 100, no. 1, p. 227-241.

Alsop, G. I., Weinberger, R., Levi, T., and Marco, S., 2016, Cycles of passive versus active diapirism recorded along an exposed salt wall: Journal of Structural Geology, v. 84, p. 47-67.

Alves, T., Fetter, M., Busby, C., Gontijo, R., Cunha, T. A., and Mattos, N. H., 2020, A tectono-stratigraphic review of continental breakup on intraplate continental margins and its impact on resultant hydrocarbon systems: Marine and Petroleum Geology, v. 117, p. 104341.

Alves, T. M., 2012, Scale-relationships and geometry of normal faults reactivated during gravitational gliding of Albian rafts (Espirito Santo Basin, SE Brazil): Earth and Planetary Science Letters, v. 331, p. 80-96.

Alves, T. M., and Cartwright, J. A., 2009, Volume balance of a submarine landslide in the Espirito Santo Basin, offshore Brazil: Quantifying seafloor erosion, sediment accumulation and depletion: Earth and Planetary Science Letters, v. 288, no. 3-4, p. 572-580.

Alves, T. M., and Cunha, T., 2018, A phase of transient subsidence, sediment bypass and deposition of regressive–transgressive cycles during the breakup of Iberia and Newfoundland: Earth and Planetary Science Letters, v. 484, p. 168-183.

Alves, T. M., and Elliott, C., 2014, Fluid flow during early compartmentalisation of rafts: A North Sea analogue for divergent continental margins: Tectonophysics, v. 634, p. 91-96.

Alves, T. M., Mattos, N. H., Newnes, S., and Goodall, S., 2022, Analysis of a basement fault zone with geothermal potential in the Southern North Sea: Geothermics, v. 102, p. 102398.

Andresen, K., and Clausen, O., 2014, An integrated subsurface analysis of clastic remobilization and injection; a case study from the Oligocene succession of the eastern North Sea: Basin Research, v. 26, no. 5, p. 641-674.

Andresen, K. J., 2012, Fluid flow features in hydrocarbon plumbing systems: What do they tell us about the basin evolution?: Marine Geology, v. 332, p. 89-108.

Andresen, K. J., Huuse, M., and Clausen, O., 2008, Morphology and distribution of Oligocene and Miocene pockmarks in the Danish North Sea–implications for bottom current activity and fluid migration: Basin Research, v. 20, no. 3, p. 445-466.

Andresen, K. J., Huuse, M., Schødt, N. H., Clausen, L. F., and Seidler, L., 2011, Hydrocarbon plumbing systems of salt minibasins offshore Angola revealed by three-dimensional seismic analysis: AAPG bulletin, v. 95, no. 6, p. 1039-1065.

Angelier, J., 1990, Inversion of field data in fault tectonics to obtain the regional stress—III. A new rapid direct inversion method by analytical means: Geophysical Journal International, v. 103, no. 2, p. 363-376.

Asmus, H., Gomes, J., and Pereira, A., 1971, Integração geológica regional da bacia do Espírito Santo: Relatório Interno, PETROBRAS.

Atwater, G. I., and Forman, M. J., 1959, Nature of growth of southern Louisiana salt domes and its effect on petroleum accumulation: AAPG Bulletin, v. 43, no. 11, p. 2592-2622.

Bally, A., Bernoulli, D., Davies, G., and Montadert, L., 1981, Listric normal faults: Oceanologica Acta: Proceedings of the 26th International Geological Congress. Geology of Continental Margins Colloque C3. Paris, July (1981), p. 87-101.

Barker, P., Buffler, R., and Gambôa, L., 1983, A SEISMIC-REFLECTION STUDY OF THE RIO-GRANDE RISE: Initial Reports of the Deep Sea Drilling Project, v. 72, no. DEC, p. 499-517.

Baudon, C., and Cartwright, J., 2008a, Early stage evolution of growth faults: 3D seismic insights from the Levant Basin, Eastern Mediterranean: Journal of Structural Geology, v. 30, no. 7, p. 888-898.

Baudon, C., and Cartwright, J., 2008b, The kinematics of reactivation of normal faults using high resolution throw mapping: Journal of Structural Geology, v. 30, no. 8, p. 1072-1084.

Behlau, J., and Mingerzahn, G., 2001, Geological and tectonic investigations in the former Morsleben salt mine (Germany) as a basis for the safety assessment of a radioactive waste repository: Engineering Geology, v. 61, no. 2-3, p. 83-97.

Bergen, K. J., and Shaw, J. H., 2010, Displacement profiles and displacement-length scaling relationships of thrust faults constrained by seismic-reflection data: Bulletin, v. 122, no. 7-8, p. 1209-1219.

Berndt, C., 2005, Focused fluid flow in passive continental margins: Philosophical Transactions of the Royal Society A: Mathematical, Physical and Engineering Sciences, v. 363, no. 1837, p. 2855-2871.

Berndt, C., Bünz, S., Clayton, T., Mienert, J., and Saunders, M., 2004, Seismic character of bottom simulating reflectors: examples from the mid-Norwegian margin: Marine and Petroleum Geology, v. 21, no. 6, p. 723-733.

Biancardi, C. A., Alves, T. M., and Martins-Ferreira, M. A. C., 2020, Unpredictable geometry and depositional stacking patterns of mass-transport complexes in salt minibasins: Marine and Petroleum Geology, v. 120, p. 104522.

Boetius, A., Ravenschlag, K., Schubert, C. J., Rickert, D., Widdel, F., Gieseke, A., Amann, R., Jørgensen, B. B., Witte, U., and Pfannkuche, O., 2000, A marine microbial consortium apparently mediating anaerobic oxidation of methane: Nature, v. 407, no. 6804, p. 623-626.

Bonini, M., 2012, Mud volcanoes: indicators of stress orientation and tectonic controls: Earth-Science Reviews, v. 115, no. 3, p. 121-152.

Bonnet, E., Bour, O., Odling, N. E., Davy, P., Main, I., Cowie, P., and Berkowitz, B., 2001, Scaling of fracture systems in geological media: Reviews of Geophysics, v. 39, no. 3, p. 347-383.

Bose, S., and Mitra, S., 2009, Deformation along oblique and lateral ramps in listric normal faults: Insights from experimental models: Aapg Bulletin, v. 93, no. 4, p. 431-451.

Bowers, G. L., 2007, Effect of inelastic sediment behavior on near-salt stresses and pore pressures: The Leading Edge, v. 26, no. 11, p. 1462-1465.

Bradley, W. B., Bore hole failure near salt domes, *in* Proceedings SPE Annual Fall Technical Conference and Exhibition1978, OnePetro.

Brennan, C., Preiss, A., and Adam, J., 2023, Three-dimensional seismic classification of salt structure morphologies across the Southern North Sea: AAPG Bulletin, v. 107, no. 12, p. 2141-2167.

Brown, A. R., 2011, Interpretation of three-dimensional seismic data, Society of Exploration Geophysicists and American Association of Petroleum Geology.

Brown, K. M., 1990, The nature and hydrogeologic significance of mud diapirs and diatremes for accretionary systems: Journal of Geophysical Research: Solid Earth, v. 95, no. B6, p. 8969-8982.

Bruce, C. H., 1984, Smectite dehydration—its relation to structural development and hydrocarbon accumulation in northern Gulf of Mexico basin: AAPG bulletin, v. 68, no. 6, p. 673-683.

Bruhn, C. H., Pinto, A. C., Johann, P. R., Branco, C. C., Salomão, M. C., and Freire, E. B., Campos and Santos basins: 40 Years of reservoir characterization and management of shallow-to ultra-deep water, post-and pre-salt reservoirs-Historical overview and future challenges, *in* Proceedings Offshore Technology Conference Brasil2017, OTC, p. D011S006R001.

Bruhn, C. H., and Walker, R. G., 1997, Internal architecture and sedimentary evolution of coarse-grained, turbidite channel-levee complexes, Early Eocene Regencia Canyon, Espirito Santo Basin, Brazil: Sedimentology, v. 44, no. 1, p. 17-46.

Brun, J.-P., and Mauduit, T. P.-O., 2008, Rollovers in salt tectonics: the inadequacy of the listric fault model: Tectonophysics, v. 457, no. 1-2, p. 1-11.

Bürgmann, R., Pollard, D. D., and Martel, S. J., 1994, Slip distributions on faults: effects of stress gradients, inelastic deformation, heterogeneous host-rock stiffness, and fault interaction: Journal of Structural Geology, v. 16, no. 12, p. 1675-1690.

Burkhard, M., 1993, Calcite twins, their geometry, appearance and significance as stress-strain markers and indicators of tectonic regime: a review: Journal of structural geology, v. 15, no. 3-5, p. 351-368.

Busby, J., 2014, Geothermal energy in sedimentary basins in the UK: Hydrogeology journal, v. 22, no. 1, p. 129-141.

Caine, J. S., Evans, J. P., and Forster, C. B., 1996, Fault zone architecture and permeability structure: Geology, v. 24, no. 11, p. 1025-1028.

Cainelli, C., and Mohriak, W. U., 1999, Some remarks on the evolution of sedimentary basins along the Eastern Brazilian continental margin: Episodes, v. 22, no. 3, p. 206-216.

Canova, D. P., Fischer, M. P., Jayne, R. S., and Pollyea, R. M., 2018, Advective heat transport and the salt chimney effect: A numerical analysis: Geofluids, v. 2018.

Carruthers, D., Cartwright, J., Jackson, M. P., and Schutjens, P., 2013, Origin and timing of layer-bound radial faulting around North Sea salt stocks: New insights into the evolving stress state around rising diapirs: Marine and Petroleum Geology, v. 48, p. 130-148.

Cartwright, J., 2007, The impact of 3D seismic data on the understanding of compaction, fluid flow and diagenesis in sedimentary basins: Journal of the Geological Society, v. 164, no. 5, p. 881-893.

Cartwright, J., 2011, Diagenetically induced shear failure of fine-grained sediments and the development of polygonal fault systems: Marine and Petroleum Geology, v. 28, no. 9, p. 1593-1610.

Cartwright, J., Huuse, M., and Aplin, A., 2007, Seal bypass systems: AAPG bulletin, v. 91, no. 8, p. 1141-1166.

Cartwright, J., James, D., and Bolton, A., 2003, The genesis of polygonal fault systems: a review: Geological Society, London, Special Publications, v. 216, no. 1, p. 223-243.

Cartwright, J., James, D., Huuse, M., Vetel, W., and Hurst, A., 2008, The geometry and emplacement of conical sandstone intrusions: Journal of Structural Geology, v. 30, no. 7, p. 854-867.

Cartwright, J., Kirkham, C., Foschi, M., Hodgson, N., Rodriguez, K., and James, D., 2021, Quantitative reconstruction of pore-pressure history in sedimentary basins using fluid escape pipes: Geology.

Cartwright, J., and Lonergan, L., 1996, Volumetric contraction during the compaction of mudrocks: A mechanism for the development of regional-scale polygonal fault systems: Basin Research, v. 8, no. 2, p. 183-193.

Cartwright, J., and Mansfield, C., 1998, Lateral displacement variation and lateral tip geometry of normal faults in the Canyonlands National Park, Utah: Journal of Structural Geology, v. 20, no. 1, p. 3-19.

Cartwright, J., and Santamarina, C., 2015, Seismic characteristics of fluid escape pipes in sedimentary basins: Implications for pipe genesis: Marine and Petroleum Geology, v. 65, p. 126-140.

Cartwright, J. A., 1994, Episodic basin-wide hydrofracturing of overpressured Early Cenozoic mudrock sequences in the North Sea Basin: Marine and Petroleum Geology, v. 11, no. 5, p. 587-607.

Cartwright, J. A., 1996, Polygonal fault systems: a new type of fault structure revealed by 3-D seismic data from the North Sea Basin.

Cartwright, J. A., Mansfield, C., and Trudgill, B., 1996, The growth of normal faults by segment linkage: Geological Society, London, Special Publications, v. 99, no. 1, p. 163-177.

Cartwright, J. A., Trudgill, B. D., and Mansfield, C. S., 1995, Fault growth by segment linkage: an explanation for scatter in maximum displacement and trace length data from the Canyonlands Grabens of SE Utah: Journal of Structural Geology, v. 17, no. 9, p. 1319-1326.

Cathles, L., Su, Z., and Chen, D., 2010, The physics of gas chimney and pockmark formation, with implications for assessment of seafloor hazards and gas sequestration: Marine and petroleum Geology, v. 27, no. 1, p. 82-91.

Chang, C., Zoback, M. D., and Khaksar, A., 2006, Empirical relations between rock strength and physical properties in sedimentary rocks: Journal of Petroleum Science and Engineering, v. 51, no. 3-4, p. 223-237.

Chang, H. K., Kowsmann, R. O., Figueiredo, A. M. F., and Bender, A. A., 1992, Tectonics and Stratigraphy of the East Brazil Rift System - an Overview: Tectonophysics, v. 213, no. 1-2, p. 97-138.

Chang, K. W., Hesse, M. A., Nicot, J.-P., and Hovorka, S. D., 2011, Effects of adjacent mud rocks on CO2 injection pressure: model case based on a typical US Gulf Coast salt diapir field under injection: Energy Procedia, v. 4, p. 4567-4574.

Chapman, D. S., Keho, T., Bauer, M. S., and Picard, M. D., 1984, Heat flow in the Uinta Basin determined from bottom hole temperature (BHT) data: Geophysics, v. 49, no. 4, p. 453-466.

Chapman, T. J., and Williams, G. D., 1984, Displacement-distance methods in the analysis of fold-thrust structures and linked-fault systems: Journal of the Geological Society, v. 141, no. 1, p. 121-128.

Chen, P., 2016, Fault reactivation analysis of the Cleaver Bank High based on 3D seismic data.

Chiaramonte, L., Zoback, M. D., Friedmann, J., and Stamp, V., 2008, Seal integrity and feasibility of CO 2 sequestration in the Teapot Dome EOR pilot: Geomechanical site characterization: Environmental Geology, v. 54, p. 1667-1675.

Childs, C., Easton, S., Vendeville, B., Jackson, M., Lin, S., Walsh, J., and Watterson, J., 1993, Kinematic analysis of faults in a physical model of growth faulting above a viscous salt analogue: Tectonophysics, v. 228, no. 3-4, p. 313-329.

Childs, C., Holdsworth, R. E., Jackson, C. A.-L., Manzocchi, T., Walsh, J. J., and Yielding, G., 2017, Introduction to the geometry and growth of normal faults: Geological Society, London, Special Publications, v. 439, no. 1, p. 1-9.

Childs, C., Manzocchi, T., Walsh, J. J., Bonson, C. G., Nicol, A., and Schopfer, M. P. J., 2009, A geometric model of fault zone and fault rock thickness variations: Journal of Structural Geology, v. 31, no. 2, p. 117-127.

Childs, C., Nicol, A., Walsh, J. J., and Watterson, J., 1996a, Growth of vertically segmented normal faults: Journal of Structural Geology, v. 18, no. 12, p. 1389-1397.

Childs, C., Nicol, A., Walsh, J. J., and Watterson, J., 2003, The growth and propagation of synsedimentary faults: Journal of Structural Geology, v. 25, no. 4, p. 633-648.

Childs, C., Watterson, J., and Walsh, J., 1995, Fault overlap zones within developing normal fault systems: Journal of the Geological Society, v. 152, no. 3, p. 535-549.

Childs, C., Watterson, J., and Walsh, J. J., 1996b, A model for the structure and development of fault zones: Journal of the Geological Society, v. 153, p. 337-340.

Cladouhos, T. T., and Marrett, R., 1996, Are fault growth and linkage models consistent with power-law distributions of fault lengths?: Journal of Structural Geology, v. 18, no. 2-3, p. 281-293.

Cloetingh, S., van Wees, J. D., Ziegler, P., Lenkey, L., Beekman, F., Tesauro, M., Förster, A., Norden, B., Kaban, M., and Hardebol, N., 2010, Lithosphere tectonics and thermo-mechanical properties: an integrated modelling approach for Enhanced Geothermal Systems exploration in Europe: Earth-Science Reviews, v. 102, no. 3-4, p. 159-206.

Cobbold, P. R., Meisling, K. E., and Mount, V. S., 2001, Reactivation of an obliquely rifted margin, Campos and Santos basins, southeastern Brazil: Aapg Bulletin, v. 85, no. 11, p. 1925-1944.

Coleman, A. J., Jackson, C. A.-L., Duffy, O. B., and Nikolinakou, M. A., 2018, How, where, and when do radial faults grow near salt diapirs?: Geology, v. 46, no. 7, p. 655-658.

Collettini, C., and Sibson, R. H., 2001, Normal faults, normal friction?: Geology, v. 29, no. 10, p. 927-930.

Collignon, M., Schmid, D. W., Galerne, C., Lupi, M., and Mazzini, A., 2018, Modelling fluid flow in clastic eruptions: Application to the Lusi mud eruption: Marine and Petroleum Geology, v. 90, p. 173-190.

Cooke, M. L., and Underwood, C. A., 2001, Fracture termination and step-over at bedding interfaces due to frictional slip and interface opening: Journal of structural geology, v. 23, no. 2-3, p. 223-238.

Corrigan, J., 1997, Correcting Bottom Hole Temperature Data, AEPT Research Memo RM 97-0007.

Corrigan, J., 2003, Correcting Bottom Hole Temperature Data.

Cowie, P. A., 1998, Normal fault growth in three dimensions in continental and oceanic crust: Geophysical Monograph-American Geophysical Union, v. 106, p. 325-348.

Cowie, P. A., and Roberts, G. P., 2001, Constraining slip rates and spacings for active normal faults: Journal of Structural Geology, v. 23, no. 12, p. 1901-1915.

Cowie, P. A., and Scholz, C. H., 1992a, Displacement-length scaling relationship for faults: data synthesis and discussion: Journal of Structural Geology, v. 14, no. 10, p. 1149-1156.

Cowie, P. A., and Scholz, C. H., 1992b, Physical explanation for displacement-length relationship of faults using a post-yield fracture mechanics model: Journal of Structural Geology, v. 14, p. 1133-1133.

Cowley, R., and O'brien, G., 2000, Identification and interpretation of leaking hydrocarbons using seismic data: A comparative montage of examples from the major fields in Australia's northwest shelf and Gippsland Basin: The APPEA Journal, v. 40, no. 1, p. 119-150.

Cox, S., Knackstedt, M., and Braun, J., 2001a, Principles of structural control on permeability and fluid flow in hydrothermal systems.

Cox, S. F., Knackstedt, M. A., and Braun, J., 2001b, Principles of structural control on permeability and fluid flow in hydrothermal systems.

Dando, P., Aliani, S., Arab, H., Bianchi, C., Brehmer, M., Cocito, S., Fowlers, S., Gundersen, J., Hooper, L., and Kölbh, R., 2000, Hydrothermal studies in the Aegean Sea: Physics and Chemistry of the Earth, Part B: Hydrology, Oceans and Atmosphere, v. 25, no. 1, p. 1-8.

Daniilidis, A., and Herber, R., 2017, Salt intrusions providing a new geothermal exploration target for higher energy recovery at shallower depths: Energy, v. 118, p. 658-670.

Davies, R. J., 2005, Differential compaction and subsidence in sedimentary basins due to silica diagenesis: A case study: Geological Society of America Bulletin, v. 117, no. 9-10, p. 1146-1155.

Davies, R. J., and Cartwright, J. A., 2007, Kilometer-scale chemical reaction boundary patterns and deformation in sedimentary rocks: Earth and Planetary Science Letters, v. 262, no. 1-2, p. 125-137.

Davison, I., 1987, Normal fault geometry related to sediment compaction and burial: Journal of Structural Geology, v. 9, no. 4, p. 393-401.

Davison, I., 2007, Geology and tectonics of the South Atlantic Brazilian salt basins: Geological Society, London, Special Publications, v. 272, p. 15.

Davison, I., 2009, Faulting and fluid flow through salt: Journal of the Geological Society, v. 166, no. 2, p. 205-216.

Davison, I., Alsop, G., Evans, N., and Safaricz, M., 2000a, Overburden deformation patterns and mechanisms of salt diapir penetration in the Central Graben, North Sea: Marine and Petroleum Geology, v. 17, no. 5, p. 601-618.

Davison, I., Alsop, I., Birch, P., Elders, C., Evans, N., Nicholson, H., Rorison, P., Wade, D., Woodward, J., and Young, M., 2000b, Geometry and late-stage structural evolution of Central Graben salt diapirs, North Sea: Marine and Petroleum Geology, v. 17, no. 4, p. 499-522.

Davison, I., Anderson, L., and Nuttall, P., 2012, Salt deposition, loading and gravity drainage in the Campos and Santos salt basins: Geological Society, London, Special Publications, v. 363, no. 1, p. 159-174.

Davison, I., Bosence, D., Alsop, G. I., and Al-Aawah, M. H., 1996, Deformation and sedimentation around active Miocene salt diapirs on the Tihama Plain, northwest Yemen: Geological Society, London, Special Publications, v. 100, no. 1, p. 23-39.

Davison, I., Insley, M., Harper, M., Weston, P., Blundell, D., Mcclay, K., and Quallington, A., 1993, Physical Modeling of Overburden Deformation around Salt Diapirs: Tectonophysics, v. 228, no. 3-4, p. 255-274.

Dawers, N. H., and Anders, M. H., 1995, Displacement-length scaling and fault linkage: Journal of Structural Geology, v. 17, no. 5, p. 607-614.

Dawers, N. H., Anders, M. H., and Scholz, C. H., 1993, Growth of normal faults: Displacement-length scaling: Geology, v. 21, no. 12, p. 1107-1110.

De Jager, J., 2003, Inverted basins in the Netherlands, similarities and differences: Netherlands Journal of Geosciences, v. 82, no. 4, p. 339-349.

De Jager, J., 2007, Geological development: Geology of the Netherlands, v. 5, p. 26.

De Lugt, I., Van Wees, J., and Wong, T. E., 2003, The tectonic evolution of the southern Dutch North Sea during the Palaeogene: basin inversion in distinct pulses: Tectonophysics, v. 373, no. 1-4, p. 141-159.

De Lugt, I. R., 2007, Stratigraphical and structural setting of the Palaeogene siliciclastic sediments in the Dutch part of the North Sea Basin, UU Dept. of Earth Sciences.

Deckers, J., Rombaut, B., Broothaers, M., Dirix, K., and Debacker, T., 2022, New 3D fault model for eastern Flanders (Belgium) providing insights on the major deformation phases in the region since the late Paleozoic: Journal of Structural Geology, p. 104779.

Deckers, J., and van der Voet, E., 2018, A review on the structural styles of deformation during Late Cretaceous and Paleocene tectonic phases in the southern North Sea area: Journal of Geodynamics, v. 115, p. 1-9.

Defant, A., 1961, Physical oceanography, Pergamon.

Demercian, S., Szatmari, P., and Cobbold, P., 1993, Style and pattern of salt diapirs due to thin-skinned gravitational gliding, Campos and Santos basins, offshore Brazil: Tectonophysics, v. 228, no. 3-4, p. 393-433.

Deming, D., 1989, Application of bottom-hole temperature corrections in geothermal studies: Geothermics, v. 18, no. 5-6, p. 775-786.

Despinois, F., 2013, Intra-Salt Stringer Play in Oman, Angola Salt Conference: Luanda, ANGOLA.

Deville, É., Guerlais, S. H., Lallemant, S., and Schneider, F., 2010, Fluid dynamics and subsurface sediment mobilization processes: an overview from Southeast Caribbean: Basin Research, v. 22, no. 4, p. 361-379.

Di Naccio, D., Boncio, P., Cirilli, S., Casaglia, F., Morettini, E., Lavecchia, G., and Brozzetti, F., 2005, Role of mechanical stratigraphy on fracture development in carbonate reservoirs: Insights from outcropping shallow water carbonates in the Umbria-Marche Apennines, Italy: Journal of Volcanology and Geothermal Research, v. 148, no. 1-2, p. 98-115.

Diegel, F. A., Karlo, J., Schuster, D., Shoup, R., and Tauvers, P., 1995, Cenozoic structural evolution and tectono-stratigraphic framework of the northern Gulf Coast continental margin.

Dimitrov, L. I., 2002, Mud volcanoes—the most important pathway for degassing deeply buried sediments: Earth-Science Reviews, v. 59, no. 1-4, p. 49-76.

Donath, F. A., 1970, Rock deformation apparatus and experiments for dynamic structural geology: Journal of Geological Education, v. 18, no. 1, p. 3-12.

Doornenbal, H., and Stevenson, A., 2010, Petroleum geological atlas of the Southern Permian Basin area, EAGE.

Dow, W. G., 1984, Oil source beds and oil prospect definition in the upper Tertiary of the Gulf Coast.

Dula Jr, W. F., 1991, Geometric models of listric normal faults and rollover folds: AAPG bulletin, v. 75, no. 10, p. 1609-1625.

Dunn, D. E., LaFountain, L. J., and Jackson, R. E., 1973, Porosity dependence and mechanism of brittle fracture in sandstones: Journal of Geophysical Research, v. 78, no. 14, p. 2403-2417.

Duranti, D., Hurst, A., Bell, C., Groves, S., and Hanson, R., 2002, Injected and remobilized Eocene sandstones from the Alba Field, UKCS: core and wireline log characteristics: Petroleum Geoscience, v. 8, no. 2, p. 99-107.

Durogbitan, A. A., 2016, Investigating fault propagation and segment linkage using throw distribution analysis within the Agbada formation of Ewan and Oloye fields, northwestern Niger delta: Journal of African Earth Sciences, v. 120, p. 248-265.

Dusseault, M. B., Maury, V., Sanfilippo, F., and Santarelli, F. J., Drilling around salt: risks, stresses, and uncertainties, *in* Proceedings Gulf Rocks 2004, the 6th North America Rock Mechanics Symposium (NARMS)2004, OnePetro.

Ebrahimi, P., Razavi, S., Ismaeili, S., and Azarpour, M., 2013, Gas-Chimney detection in 3D seismic by neural network: Petroleum science and technology, v. 31, no. 11, p. 1188-1195.

Elger, J., Berndt, C., Rüpke, L., Krastel, S., Gross, F., and Geissler, W. H., 2018, Submarine slope failures due to pipe structure formation: Nature communications, v. 9, no. 1, p. 1-6.

Ellis, M. A., and Dunlap, W. J., 1988, Displacement variation along thrust faults: Implications for the development of large faults: Journal of Structural Geology, v. 10, no. 2, p. 183-192.

Erdlac Jr, R., Armour, L., Lee, R., Snyder, S., Sorensen, M., Matteucci, M., and Horton, J., Ongoing resource assessment of geothermal energy from sedimentary basins in Texas, *in* Proceedings Proceedings of Thirty-second Workshop on Geothermal Reservoir Engineering, Stanford University, Stanford, California2007.

Erickson, S. G., 1996, Influence of mechanical stratigraphy on folding vs faulting: Journal of Structural Geology, v. 18, no. 4, p. 443-450.

Estrella, G., Mello, M. R., Gaglianone, P., Azevedo, R., Tsubone, K., Rossetti, E., Concha, J., and Bruning, I., 1984, The Espirito Santo Basin (Brazil) source rock characterization and petroleum habitat.

Evans, J. P., 1990, Thickness-displacement relationships for fault zones: Journal of structural geology, v. 12, no. 8, p. 1061-1065.

Evans, T. R., and Coleman, N., 1974, North Sea geothermal gradients: Nature, v. 247, no. 5435, p. 28-30.

Fattah, A., Verweij, J., and Witmans, N., 2012a, Reconstruction of burial history, temperature, source rock maturity and hydrocarbon generation for the NCP-2D area, Dutch Offshore.

Fattah, R. A., Verweij, J., Witmans, N., and Ten Veen, J., 2012b, Reconstruction of burial history, temperature, source rock maturity and hydrocarbon generation in the northwestern Dutch offshore: Netherlands Journal of Geosciences, v. 91, no. 4, p. 535-554.

Ferrill, D. A., 1998, Critical re-evaluation of differential stress estimates from calcite twins in coarse-grained limestone: Tectonophysics, v. 285, no. 1-2, p. 77-86.

Ferrill, D. A., and Groshong Jr, R. H., 1993, Kinematic model for the curvature of the northern Subalpine Chain, France: Journal of structural Geology, v. 15, no. 3-5, p. 523-541.

Ferrill, D. A., McGinnis, R. N., Morris, A. P., Smart, K. J., Sickmann, Z. T., Bentz, M., Lehrmann, D., and Evans, M. A., 2014, Control of mechanical stratigraphy on bed-restricted jointing and normal faulting: Eagle Ford Formation, south-central Texas: Aapg Bulletin, v. 98, no. 11, p. 2477-2506.

Ferrill, D. A., and Morris, A. P., 2001, Displacement gradient and deformation in normal fault systems: Journal of Structural Geology, v. 23, no. 4, p. 619-638.

Ferrill, D. A., and Morris, A. P., 2003, Dilational normal faults: Journal of Structural Geology, v. 25, no. 2, p. 183-196.

Ferrill, D. A., and Morris, A. P., 2008, Fault zone deformation controlled by carbonate mechanical stratigraphy, Balcones fault system, Texas: AAPG bulletin, v. 92, no. 3, p. 359-380.

Ferrill, D. A., Morris, A. P., and McGinnis, R. N., 2012, Extensional fault-propagation folding in mechanically layered rocks: The case against the frictional drag mechanism: Tectonophysics, v. 576, p. 78-85.

Ferrill, D. A., Morris, A. P., McGinnis, R. N., Smart, K. J., Wigginton, S. S., and Hill, N. J., 2017, Mechanical stratigraphy and normal faulting: Journal of Structural Geology, v. 94, p. 275-302.

Ferrill, D. A., Morris, A. P., Sims, D. W., Waiting, D. J., and Hasegawa, S., 2005, Development of synthetic layer dip adjacent to normal faults, v. AAPG Special Volumes, p. 125-138.

Fiduk, J. C., Brush, E. R., Anderson, L. E., Gibbs, P. B., and Rowan, M. G., 2004, Salt Deformation, Magmatism, and Hydrocarbon Prospectivity in the Espirito Santo Basin, Offshore Brazil.

Figueiredo, A., and Mohriak, W., A tectonica salifera e as acumulacoes de Petroleo da Bacia de Campos, *in* Proceedings Proceedings of the 33rd Brazilian Geological Congress, Sociedada Brasileira de Geologia, Rio de Janeiro1984, Volume 3, p. 1380-1394.

Fisher, Q., and Knipe, R., 2001, The permeability of faults within siliciclastic petroleum reservoirs of the North Sea and Norwegian Continental Shelf: Marine and Petroleum Geology, v. 18, no. 10, p. 1063-1081.

Fossen, H., and Hesthammer, J., 1997, Geometric analysis and scaling relations of deformation bands in porous sandstone: Journal of Structural Geology, v. 19, no. 12, p. 1479-1493.

Fossen, H., and Rotevatn, A., 2016, Fault linkage and relay structures in extensional settings-A review: Earth-Science Reviews, v. 154, p. 14-28.

Fossum, A. F., and Fredrich, J. T., 2002, Salt mechanics primer for near-salt and sub-salt deepwater Gulf of Mexico field developments, Sandia National Laboratories Albuquerque, New Mexico, and Livermore, California.

Fowler, S., Mildenhall, J., Zalova, S., Riley, G., Elsley, G., Desplanques, A., and Guliyev, F., 2000, Mud volcanoes and structural development on Shah Deniz: Journal of Petroleum Science and Engineering, v. 28, no. 4, p. 189-206.

França, R. L., Del Rey, A. C., Tagliari, C. V., Brandão, J. R., and Fontanelli, P. d. R., 2007, Bacia do espírito Santo: Boletim de Geociencias da PETROBRAS, v. 15, p. 2.

Fredrich, J. T., Coblentz, D., Fossum, A. F., and Thorne, B. J., Stress perturbations adjacent to salt bodies in the deepwater Gulf of Mexico, *in* Proceedings SPE Annual Technical Conference and Exhibition?2003, SPE, p. SPE-84554-MS.

Gaitan, G., and Adam, J., 2023, Extent and variability of Mesozoic-Cenozoic multi-stage salt diapirs in the Southern Permian Basin, Southern North Sea: Basin Research.

Gale, J. F. W., Lander, R. H., Reed, R. M., and Laubach, S. E., 2010, Modeling fracture porosity evolution in dolostone: Journal of Structural Geology, v. 32, no. 9, p. 1201-1211.

Gallup, D. L., 2009, Production engineering in geothermal technology: a review: Geothermics, v. 38, no. 3, p. 326-334.

Gamboa, D., Alves, T., Cartwright, J., and Terrinha, P., 2010, MTD distribution on a 'passive' continental margin: The Espirito Santo Basin (SE Brazil) during the Palaeogene: Marine and Petroleum Geology, v. 27, no. 7, p. 1311-1324.

Gamboa, D., Alves, T. M., and Cartwright, J., 2012, A submarine channel confluence classification for topographically confined slopes: Marine and Petroleum Geology, v. 35, no. 1, p. 176-189.

Gamboa, D. A., 2011, An integrated seismic-scale analysis of reservoir compartmentalisation on continental margins: the Espirito Santo Basin, SE Brazil: Cardiff University.

Gartrell, A., Zhang, Y., Lisk, M., and Dewhurst, D., 2004, Fault intersections as critical hydrocarbon leakage zones: integrated field study and numerical modelling of an example from the Timor Sea, Australia: Marine and petroleum geology, v. 21, no. 9, p. 1165-1179.

Gasanzade, F., Pfeiffer, W. T., Witte, F., Tuschy, I., and Bauer, S., 2021, Subsurface renewable energy storage capacity for hydrogen, methane and compressed air–A performance

assessment study from the North German Basin: Renewable and Sustainable Energy Reviews, v. 149, p. 111422.

Gawthorpe, R. L., Leeder, M. R., Kranis, H., Skourtsos, E., Andrews, J. E., Henstra, G. A., Mack, G. H., Muravchik, M., Turner, J. A., and Stamatakis, M., 2018, Tectono-sedimentary evolution of the Plio-Pleistocene Corinth rift, Greece: Basin Research, v. 30, no. 3, p. 448-479.

Gay, A., Lopez, M., Cochonat, P., Séranne, M., Levaché, D., and Sermondadaz, G., 2006, Isolated seafloor pockmarks linked to BSRs, fluid chimneys, polygonal faults and stacked Oligocene–Miocene turbiditic palaeochannels in the Lower Congo Basin: Marine Geology, v. 226, no. 1-2, p. 25-40.

Gay, A., Lopez, M., Cochonat, P., and Sermondadaz, G., 2004, Polygonal faults-furrows system related to early stages of compaction - upper Miocene to recent sediments of the Lower Congo Basin: Basin Research, v. 16, no. 1, p. 101-116.

Ge, H., and Jackson, M. P., 1996, Salt structures, hydrocarbon traps and mineral deposits: JOURNAL OF NAIJING UNIVERSITY (NATURAL SCIENCES), no. 4.

Ge, Z., Nemec, W., Gawthorpe, R. L., Rotevatn, A., and Hansen, E. W., 2018, Response of unconfined turbidity current to relay-ramp topography: Insights from process-based numerical modelling: Basin Research, v. 30, no. 2, p. 321-343.

Gerling, P., Geluk, M., Kockel, F., Lokhorst, A., Lott, G., and Nicholson, R., 'NW European Gas Atlas'–new implications for the Carboniferous gas plays in the western part of the Southern Permian Basin, *in* Proceedings Geological Society, London, Petroleum Geology Conference Series1999, Volume 5, The Geological Society of London, p. 799-808.

Gevantman, L., and Lorenz, J., 1981, Physical properties data for rock salt, US Department of Commerce, National Bureau of Standards.

Gibbs, P. B., Brush, E. R., and Fiduk, J. C., The evolution of the syn rift and transition phases of the central/southern Brazilian and W. African conjugate margins: the implications for source rock distribution in time and space, and their recognition on seismic data, *in* Proceedings 8th International Congress of the Brazilian Geophysical Society2003.

Giles, K. A., and Lawton, T. F., 2002, Halokinetic sequence stratigraphy adjacent to the El Papalote diapir, northeastern Mexico: AAPG bulletin, v. 86, no. 5, p. 823-840.

Gillespie, P., Walsh, J. t., and Watterson, J., 1992, Limitations of dimension and displacement data from single faults and the consequences for data analysis and interpretation: Journal of Structural Geology, v. 14, p. 1157-1157.

Glaas, C., Genter, A., Girard, J., Patrier, P., and Vidal, J., 2018, How do the geological and geophysical signatures of permeable fractures in granitic basement evolve after long periods of natural circulation? Insights from the Rittershoffen geothermal wells (France): Geothermal Energy, v. 6, no. 1, p. 1-25.

Glennie, K., 1997, History of exploration in the southern North Sea: Geological Society, London, Special Publications, v. 123, no. 1, p. 5-16.

Groshong Jr, R. H., 1988, Low-temperature deformation mechanisms and their interpretation: Geological Society of America Bulletin, v. 100, no. 9, p. 1329-1360.

Groshong, R. H., and Groshong, R., 2006, 3-D structural geology, Springer.

Gross, M. R., GutierrezAlonso, G., Bai, T. X., Wacker, M. A., Collinsworth, K. B., and Behl, R. J., 1997, Influence of mechanical stratigraphy and kinematics on fault scaling relations: Journal of Structural Geology, v. 19, no. 2, p. 171-183.

Gudmundsson, A., 1992, Formation and growth of normal faults at the divergent plate boundary in Iceland: Terra Nova, v. 4, no. 4, p. 464-471.

Gudmundsson, A., De Guidi, G., and Scudero, S., 2013, Length–displacement scaling and fault growth: Tectonophysics, v. 608, p. 1298-1309.

Gupta, A., and Scholz, C. H., 2000, A model of normal fault interaction based on observations and theory: Journal of Structural Geology, v. 22, no. 7, p. 865-879.

Halbouty, M. T., 1979, Salt Domes, Gulf Region, United States & Mexico, Gulf Publishing.

Hanks, C. L., Lorenz, J., Teufel, L., and Krumhardt, A. P., 1997, Lithologic and structural controls on natural fracture distribution and behavior within the Lisburne Group, northeastern Brooks Range and North Slope subsurface, Alaska: AAPG bulletin, v. 81, no. 10, p. 1700-1720.

Harding, R., and Huuse, M., 2015, Salt on the move: multi stage evolution of salt diapirs in the Netherlands North Sea: Marine and Petroleum Geology, v. 61, p. 39-55.

Harding, T. P., and Lowell, J. D., 1979, Structural styles, their plate-tectonic habitats, and hydrocarbon traps in petroleum provinces: AAPG bulletin, v. 63, no. 7, p. 1016-1058.

Hart, B. S., 1999, Definition of subsurface stratigraphy, structure and rock properties from 3-D seismic data: Earth-Science Reviews, v. 47, no. 3-4, p. 189-218.

Heggland, R., 2005, Using gas chimneys in seal integrity analysis: A discussion based on case histories.

Heggland, R., 2013, Hydrocarbon trap classification based on associated gas chimneys.

Henstra, G. A., Gawthorpe, R. L., Helland-Hansen, W., Ravnås, R., and Rotevatn, A., 2017, Depositional systems in multiphase rifts: seismic case study from the Lofoten margin, Norway: Basin Research, v. 29, no. 4, p. 447-469.

Henstra, G. A., Rotevatn, A., Gawthorpe, R. L., and Ravnås, R., 2015, Evolution of a major segmented normal fault during multiphase rifting: The origin of plan-view zigzag geometry: Journal of Structural Geology, v. 74, p. 45-63.

Hernandez, K., Mitchell, N. C., and Huuse, M., 2018, Deriving relationships between diapir spacing and salt-layer thickness in the Southern North Sea: Geological Society, London, Special Publications, v. 469, no. 1, p. 119-137.

Higgs, R., 1991, The Bude Formation (Lower Westphalian), SW England: siliciclastic shelf sedimentation in a large equatorial lake: Sedimentology, v. 38, no. 3, p. 445-469.

Hillis, R. R., 2003, Pore pressure/stress coupling and its implications for rock failure: Geological Society, London, Special Publications, v. 216, no. 1, p. 359-368.

Hinz, N. H., Faulds, J. E., and Coolbaugh, M. F., 2014, Association of fault terminations with fluid flow in the Salt Wells geothermal field, Nevada, USA: Geothermal Resources Council Transactions, v. 38, p. 3-10.

Holgate, F. L., 2005, Exploration and evaluation of the Australian geothermal resource.

Hooghvorst, J. J., Harrold, T. W., Nikolinakou, M. A., Fernandez, O., and Marcuello, A., 2020, Comparison of stresses in 3D v. 2D geomechanical modelling of salt structures in the Tarfaya Basin, West African coast: Petroleum Geoscience, v. 26, no. 1, p. 36-49.

Hovland, M., 2007, Discovery of prolific natural methane seeps at Gullfaks, northern North Sea: Geo-Marine Letters, v. 27, no. 2-4, p. 197-201.

Hovland, M., Gardner, J. V., and Judd, A., 2002, The significance of pockmarks to understanding fluid flow processes and geohazards: Geofluids, v. 2, no. 2, p. 127-136.

Hovland, M., and Judd, A. G., 1988, Seabed pockmarks and seepages: impact on geology, biology and the marine environment, Graham & Trotman London.

Hovland, M., Svensen, H., Forsberg, C. F., Johansen, H., Fichler, C., Fosså, J. H., Jonsson, R., and Rueslåtten, H., 2005, Complex pockmarks with carbonate-ridges off mid-Norway: Products of sediment degassing: Marine geology, v. 218, no. 1-4, p. 191-206.

Hudec, M. R., and Jackson, M. P., 2007, Terra infirma: Understanding salt tectonics: Earth-Science Reviews, v. 82, no. 1-2, p. 1-28.

Hurst, A., Cartwright, J., and Duranti, D., 2003a, Fluidization structures produced by upward injection of sand through a sealing lithology: Geological Society, London, Special Publications, v. 216, no. 1, p. 123-138.

Hurst, A., Cartwright, J., Huuse, M., Jonk, R., Schwab, A., Duranti, D., and Cronin, B., 2003b, Significance of large-scale sand injectites as long-term fluid conduits: evidence from seismic data: Geofluids, v. 3, no. 4, p. 263-274.

Hurst, A., and Cartwright, J. A., 2007, Sand Injectites: Implications for Hydrocarbon Exploration and Production, AAPG Memoir 87, AAPG, v. 87.

Hurst, A., Huuse, M., Silcock, S., and Lovelock, C., Subsurface Sand Remobilization and Injection2021, Geological Society of London.

Hustoft, S., Bünz, S., and Mienert, J., 2010, Three-dimensional seismic analysis of the morphology and spatial distribution of chimneys beneath the Nyegga pockmark field, offshore mid-Norway: Basin Research, v. 22, no. 4, p. 465-480.

Huuse, M., Cartwright, J., Gras, R., and Hurst, A., Kilometre-scale sandstone intrusions in the Eocene of the Outer Moray Firth (UK North Sea): migration paths, reservoirs and potential drilling hazards, *in* Proceedings Geological Society, London, Petroleum Geology Conference Series2005, Volume 6, The Geological Society of London, p. 1577-1594.

Huuse, M., Cartwright, J., Hurst, A., and Steinsland, N., 2007, Seismic characterization of large-scale sandstone intrusions.

Huuse, M., Jackson, C. A. L., Van Rensbergen, P., Davies, R. J., Flemings, P. B., and Dixon, R. J., 2010, Subsurface sediment remobilization and fluid flow in sedimentary basins: an overview: Basin Research, v. 22, no. 4, p. 342-360.

Imber, J., Childs, C., Nell, P. A. R., Walsh, J. J., Hodgetts, D., and Flint, S., 2003, Hanging wall fault kinematics and footwall collapse in listric growth fault systems: Journal of Structural Geology, v. 25, no. 2, p. 197-208.

Istadi, B. P., Wibowo, H. T., Sunardi, E., Hadi, S., Sawolo, N., and Dar, I. A., 2012, Mud volcano and its evolution: Earth Sciences, Dr. Imran Ahmad Dar (Ed.), p. 375-434.

Jackson, C. A.-L., Bell, R. E., Rotevatn, A., and Tvedt, A. B., 2017, Techniques to determine the kinematics of synsedimentary normal faults and implications for fault growth models: Geological Society, London, Special Publications, v. 439, no. 1, p. 187-217.

Jackson, C. A.-L., Huuse, M., and Barber, G. P., 2011, Geometry of winglike clastic intrusions adjacent to a deep-water channel complex: Implications for hydrocarbon exploration and production: AAPG bulletin, v. 95, no. 4, p. 559-584.

Jackson, C. A. L., and Rotevatn, A., 2013, 3D seismic analysis of the structure and evolution of a salt-influenced normal fault zone: A test of competing fault growth models: Journal of Structural Geology, v. 54, p. 215-234.

Jackson, L., Brown, F., and Neil, S., 1987, Major and minor elements requiring individual determination, classical whole rock analysis: Methods for Geochemical Analysis, v. 1770, p. G1-G23.

Jackson, M., and Seni, S., 1983, Geometry and evolution of salt structures in a marginal rift basin of the Gulf of Mexico, east Texas: Geology, v. 11, no. 3, p. 131-135.

Jackson, M. P., 1997, Conceptual Breakthroughs in Salt Tectonics: A Historical Review, 1856-1993, Bureau of Economic Geology, University of Texas at Austin.

Jackson, M. P., and Hudec, M. R., 2017, Salt tectonics: Principles and practice, Cambridge University Press.

Jackson, M. P., and Talbot, C. J., 1986, External shapes, strain rates, and dynamics of salt structures: Geological Society of America Bulletin, v. 97, no. 3, p. 305-323.

Jackson, M. P. A., and Vendeville, B. C., 1990, The rise and fall of diapirs during thin-skinned extension, AAPG Bulletin (American Association of Petroleum Geologists); (USA); Journal Volume: 74:5; Conference: Annual convention and exposition of the American Association of Petroleum Geologists, San Francisco, CA (USA), 3-6 Jun 1990, Medium: X; Size: Pages: 683.

Jackson, M. P. A., and Vendeville, B. C., 1994, Regional Extension as a Geologic Trigger for Diapirism: Geological Society of America Bulletin, v. 106, no. 1, p. 57-73.

Jackson, M. P. A., Vendeville, B. C., and Schultzela, D. D., 1994, Structural Dynamics of Salt Systems: Annual Review of Earth and Planetary Sciences, v. 22, p. 93-117.

James, D., 2003, The millennium atlas: Petroleum geology of the central and northern North Sea: Geological Magazine, v. 140, no. 4, p. 487.

Jamison, W. R., 1979, Laramide deformation of the Wingate Sandstone, Colorado National Monument: A study of cataclastic flow, Texas A&M University.

Jensen, P., 1983, Calculations on the thermal conditions around a salt diapir: Geophysical Prospecting, v. 31, no. 3, p. 481-489.

Jensen, P. K., 1990, Analysis of the temperature field around salt diapirs: Geothermics, v. 19, no. 3, p. 273-283.

Jenssen, A., Bergslien, D., Rye-Larsen, M., and Lindholm, R., Origin of complex mound geometry of Paleocene submarine-fan sandstone reservoirs, Balder Field, Norway, *in* Proceedings Geological Society, London, Petroleum Geology Conference Series1993, Volume 4, The Geological Society of London, p. 135-143.

Jianfeng, H., Yukui, L., Minghui, Y., Duoming, Z., Hu, L., Ganglin, L., and Li, Z., 2004, Salt structure characteristics and its relation to hydrocarbon accumulation in the Kuqa depression, Tarim Basin: Chinese Journal of Geology, v. 39, no. 4, p. 580-588.

Johri, M., Zoback, M. D., and Hennings, P., 2014, A scaling law to characterize fault-damage zones at reservoir depths: Aapg Bulletin, v. 98, no. 10, p. 2057-2079.

Jolly, R. J., and Lonergan, L., 2002, Mechanisms and controls on the formation of sand intrusions: Journal of the Geological Society, v. 159, no. 5, p. 605-617.

Judd, A., Croker, P., Tizzard, L., and Voisey, C., 2007, Extensive methane-derived authigenic carbonates in the Irish Sea: Geo-Marine Letters, v. 27, p. 259-267.

Karstens, J., and Berndt, C., 2015, Seismic chimneys in the Southern Viking Graben–Implications for palaeo fluid migration and overpressure evolution: Earth and Planetary Science Letters, v. 412, p. 88-100.

Katz, B., and Mello, M., 2000, Petroleum systems of South Atlantic Marginal basins-an overview: MEMOIRS-AMERICAN ASSOCIATION OF PETROLEUM GEOLOGISTS, p. 1-14.

Kim, Y.-S., Andrews, J. R., and Sanderson, D. J., 2001, Reactivated strike–slip faults: examples from north Cornwall, UK: Tectonophysics, v. 340, no. 3-4, p. 173-194.

Kim, Y. S., and Sanderson, D. J., 2005, The relationship between displacement and length of faults: a review: Earth-Science Reviews, v. 68, no. 3-4, p. 317-334.

King, L. H., and Maclean, B., 1970, Pockmarks on the Scotian Shelf: GSA Bulletin, v. 81, no. 10, p. 3141-3148.

Knai, T., and Knipe, R., 1998, The impact of faults on fluid flow in the Heidrun Field: Geological Society, London, Special Publications, v. 147, no. 1, p. 269-282.

Koh, C. A., Sloan, E. D., Sum, A. K., and Wu, D. T., 2011, Fundamentals and applications of gas hydrates: Annual review of chemical and biomolecular engineering, v. 2, p. 237-257.

Koledoye, B. A., Aydin, A., and May, E., 2003, A new process-based methodology for analysis of shale smear along normal faults in the Niger Delta: AAPG bulletin, v. 87, no. 3, p. 445-463.

Kolyukhin, D., and Torabi, A., 2012, Statistical analysis of the relationships between faults attributes: Journal of Geophysical Research-Solid Earth, v. 117.

Kopf, A. J., 2002, Significance of mud volcanism: Reviews of geophysics, v. 40, no. 2, p. 2-1-2-52.

Kvenvolden, K. A., 1988, Methane hydrate—a major reservoir of carbon in the shallow geosphere?: Chemical geology, v. 71, no. 1-3, p. 41-51.

Kvenvolden, K. A., 1993, Gas hydrates—geological perspective and global change: Reviews of geophysics, v. 31, no. 2, p. 173-187.

Langer, M., and Heusermann, S., 2001, Geomechanical stability and integrity of waste disposal mines in salt structures: Engineering geology, v. 61, no. 2-3, p. 155-161.

Larsen, B. D., Ben-Avraham, Z., and Shulman, H., 2002, Fault and salt tectonics in the southern Dead Sea basin: Tectonophysics, v. 346, no. 1-2, p. 71-90.

Laubach, S. E., Olson, J. E., and Gross, M. R., 2009, Mechanical and fracture stratigraphy: Aapg Bulletin, v. 93, no. 11, p. 1413-1426.

Li, W., Li, X., Peng, Y., Wang, Y., and Tu, J., 2018, Experimental and numerical investigations on heat transfer in stratified subsurface materials: Applied Thermal Engineering, v. 135, p. 228-237.

Ligtenberg, H., Okkerman, J., and De Keijzer, M., 2011, Fractures in the Dutch Rotliegend—An Overview.

Lisle, R. J., and Srivastava, D. C., 2004, Test of the frictional reactivation theory for faults and validity of fault-slip analysis: Geology, v. 32, no. 7, p. 569-572.

Lohr, T., Krawczyk, C. M., Oncken, O., and Tanner, D. C., 2008, Evolution of a fault surface from 3D attribute analysis and displacement measurements: Journal of Structural Geology, v. 30, no. 6, p. 690-700.

Lopez, J. A., 1990, Structural styles of growth faults in the US Gulf Coast Basin: Geological Society, London, Special Publications, v. 50, no. 1, p. 203-219.

Løseth, H., Gading, M., and Wensaas, L., 2009, Hydrocarbon leakage interpreted on seismic data: Marine and Petroleum Geology, v. 26, no. 7, p. 1304-1319.

Løseth, H., Wensaas, L., Arntsen, B., Hanken, N.-M., Basire, C., and Graue, K., 2011, 1000 m long gas blow-out pipes: Marine and Petroleum Geology, v. 28, no. 5, p. 1047-1060.

Luo, G., Nikolinakou, M. A., Flemings, P. B., and Hudec, M. R., 2012, Geomechanical modeling of stresses adjacent to salt bodies: Part 1—Uncoupled modelsStress Around Salt Bodies: AAPG bulletin, v. 96, no. 1, p. 43-64.

Maestro, A., Barnolas, A., Somoza, L., Lowrie, A., and Lawton, T., 2002, Geometry and structure associated to gas-charged sediments and recent growth faults in the Ebro Delta (Spain): Marine Geology, v. 186, no. 3-4, p. 351-368.

Magalhães, V. H., Pinheiro, L. M., Ivanov, M. K., Kozlova, E., Blinova, V., Kolganova, J., Vasconcelos, C., McKenzie, J. A., Bernasconi, S. M., and Kopf, A. J., 2012, Formation processes of methane-derived authigenic carbonates from the Gulf of Cadiz: Sedimentary Geology, v. 243, p. 155-168.

Maia da Costa, A., V. M da Costa, P., D. Udebhulu, O., Cabral Azevedo, R., FF Ebecken, N., CO Miranda, A., M. de Eston, S., de Tomi, G., R. Meneghini, J., and Nishimoto, K., 2019, Potential of storing gas with high CO2 content in salt caverns built in ultra-deep water in Brazil: Greenhouse Gases: Science and Technology, v. 9, no. 1, p. 79-94.

Makogon, Y. F., 2010, Natural gas hydrates–A promising source of energy: Journal of natural gas science and engineering, v. 2, no. 1, p. 49-59.

Malthe-Sørenssen, A., Walmann, T., Jamtveit, B., Feder, J., and Jøssang, T., 1999, Simulation and characterization of fracture patterns in glaciers: Journal of Geophysical Research: Solid Earth, v. 104, no. B10, p. 23157-23174.

Mandl, G., 1999, Faulting in brittle rocks: an introduction to the mechanics of tectonic faults, Springer, Berlin.

Manighetti, I., King, G., and Sammis, C. G., 2004, The role of off-fault damage in the evolution of normal faults: Earth and Planetary Science Letters, v. 217, no. 3-4, p. 399-408.

Mansfield, C., and Cartwright, J., 1996, High resolution fault displacement mapping from three-dimensional seismic data: evidence for dip linkage during fault growth: Journal of Structural Geology, v. 18, no. 2-3, p. 249-263.

Mansfield, C., and Cartwright, J., 2001, Fault growth by linkage: observations and implications from analogue models: Journal of Structural Geology, v. 23, no. 5, p. 745-763.

Manzocchi, T., Childs, C., and Walsh, J., 2010, Faults and fault properties in hydrocarbon flow models: Geofluids, v. 10, no. 1-2, p. 94-113.

Marcon, Y., Ondréas, H., Sahling, H., Bohrmann, G., and Olu, K., 2014, Fluid flow regimes and growth of a giant pockmark: Geology, v. 42, no. 1, p. 63-66.

Marrett, R., and Allmendinger, R. W., 1991, Estimates of strain due to brittle faulting: sampling of fault populations: Journal of Structural Geology, v. 13, no. 6, p. 735-738.

Mattos, N. H., and Alves, T. M., 2018, Corridors of crestal and radial faults linking salt diapirs in the Espirito Santo Basin, SE Brazil: Tectonophysics, v. 728, p. 55-74.

Mayolle, S., Soliva, R., Caniven, Y., Wibberley, C., Ballas, G., Milesi, G., and Dominguez, S., 2019, Scaling of fault damage zones in carbonate rocks: Journal of Structural Geology, v. 124, p. 35-50.

Mazzini, A., Svensen, H., Akhmanov, G., Aloisi, G., Planke, S., Malthe-Sørenssen, A., and Istadi, B., 2007, Triggering and dynamic evolution of the LUSI mud volcano, Indonesia: Earth and Planetary Science Letters, v. 261, no. 3-4, p. 375-388.

Mazzini, A., Svensen, H., Planke, S., Guliyev, I., Akhmanov, G., Fallik, T., and Banks, D., 2009, When mud volcanoes sleep: Insight from seep geochemistry at the Dashgil mud volcano, Azerbaijan: Marine and Petroleum Geology, v. 26, no. 9, p. 1704-1715.

McGinnis, R. N., Ferrill, D. A., Morris, A. P., and Smart, K. J., 2016, Insight on mechanical stratigraphy and subsurface interpretation.

McLean, K., McDowell, J., Sepulveda, F., Seastres, J., Zarrouk, S. J., and Alcaraz, S., Upflow along a basement fault revealed by geothermal numerical pressure transient analysis, *in* Proceedings Proceedings 40th New Zealand Geothermal Workshop2018, Volume 14, p. 16.

McNeill, L. C., Piper, K. A., Goldfinger, C., Kulm, L. D., and Yeats, R. S., 1997, Listric normal faulting on the Cascadia continental margin: Journal of Geophysical Research-Solid Earth, v. 102, no. B6, p. 12123-12138.

Meisling, K. E., Cobbold, P. R., and Mount, V. S., 2001, Segmentation of an obliquely rifted margin, Campos and Santos basins, southeastern Brazil: Aapg Bulletin, v. 85, no. 11, p. 1903-1924.

Mello, M., and Maxwell, J., 1990, Organic Geochemical and Biological Marker Characterization of Source Rocks and Oils Derived from Lacustrine Environments in the Brazilian Continental Margin: Chapter 5.

Mello, M., Peres, W., Rostirolla, S., Pedrosa Jr, O., Piquet, A., Becker, S., and Yilmaz, P., 2021, The Santos Basin pre-salt super giant petroleum system: An incredible journey from failure to success.

Mellors, R., Kilb, D., Aliyev, A., Gasanov, A., and Yetirmishli, G., 2007, Correlations between earthquakes and large mud volcano eruptions: Journal of Geophysical Research: Solid Earth, v. 112, no. B4.

Mijnlieff, H. F., 2020, Introduction to the geothermal play and reservoir geology of the Netherlands: Netherlands Journal of Geosciences, v. 99.

Milkov, A., 2000, Worldwide distribution of submarine mud volcanoes and associated gas hydrates: Marine Geology, v. 167, no. 1-2, p. 29-42.

Mitchell, T., and Faulkner, D., 2009, The nature and origin of off-fault damage surrounding strike-slip fault zones with a wide range of displacements: A field study from the

Atacama fault system, northern Chile: Journal of Structural Geology, v. 31, no. 8, p. 802-816.

Mitchell, T. M., and Faulkner, D. R., 2012, Towards quantifying the matrix permeability of fault damage zones in low porosity rocks: Earth and Planetary Science Letters, v. 339, p. 24-31.

Mohriak, W., Nemčok, M., and Enciso, G., 2008, South Atlantic divergent margin evolution: rift-border uplift and salt tectonics in the basins of SE Brazil: Geological Society, London, Special Publications v. 294.

Mohriak, W., and Rosendahl, B., 2003, Transform zones in the South Atlantic rifted continental margins: Geological Society, London, Special Publications, v. 210, no. 1, p. 211-228.

Mohriak, W. U., Szatmari, P., and Anjos, S., 2012, Salt: geology and tectonics of selected Brazilian basins in their global context: 363, p. 28.

Molyneux, S., Cartwright, J., and Lonergan, L., 2002, Conical sandstone injection structures imaged by 3D seismic in the central North Sea, UK: First Break, v. 20, no. 6.

Morley, C. K., 1999, Patterns of displacement along large normal faults: Implications for basin evolution and fault propagation, based on examples from east Africa: Aapg Bulletin, v. 83, no. 4, p. 613-634.

Morris, A., Ferrill, D. A., and Henderson, D. B., 1996, Slip-tendency analysis and fault reactivation: Geology, v. 24, no. 3, p. 275-278.

Morris, A. P., Ferrill, D. A., and McGinnis, R. N., 2009, Mechanical stratigraphy and faulting in Cretaceous carbonates: Aapg Bulletin, v. 93, no. 11, p. 1459-1470.

Müller, S., Reinhardt, L., Franke, D., Gaedicke, C., and Winsemann, J., 2018, Shallow gas accumulations in the German North Sea: Marine and Petroleum Geology, v. 91, p. 139-151.

Muraoka, H., and Kamata, H., 1983, Displacement distribution along minor fault traces: Journal of Structural Geology, v. 5, no. 5, p. 483-495.

Murray, G. E., 1966, Salt structures of Gulf of Mexico Basin--a review: AAPG Bulletin, v. 50, no. 3, p. 439-478.

Neagu, R. C., Cartwright, J., Davies, R., and Jensen, L., 2010, Fossilisation of a silica diagenesis reaction front on the mid-Norwegian margin: Marine and Petroleum Geology, v. 27, no. 10, p. 2141-2155.

Newton, S., and Flanagan, K., The Alba Field: evolution of the depositional model, *in* Proceedings Geological Society, London, Petroleum Geology Conference Series1993, Volume 4, The Geological Society of London, p. 161-171.

Ngeri, A., Tamunobereton-Ari, I., and Amakiri, A., 2015, Ant-tracker attributes: an effective approach to enhancing fault identification and interpretation: Journal of VLSI and Signal Processing, v. 5, p. 67-73.

Nicol, A., Childs, C., Walsh, J. J., Manzocchi, T., and Schöpfer, M. P. J., 2017, Interactions and growth of faults in an outcrop-scale system: Geological Society, London, Special Publications, v. 439, no. 1, p. 23.

Nicol, A., Walsh, J., Berryman, K., and Nodder, S., 2005, Growth of a normal fault by the accumulation of slip over millions of years: Journal of Structural Geology, v. 27, no. 2, p. 327-342.

Nicol, A., Walsh, J., Childs, C., and Manzocchi, T., 2020, The growth of faults, Understanding faults, Elsevier, p. 221-255.

Nicol, A., Walsh, J., Villamor, P., Seebeck, H., and Berryman, K., 2010, Normal fault interactions, paleoearthquakes and growth in an active rift: Journal of Structural Geology, v. 32, no. 8, p. 1101-1113.

Nikolinakou, M. A., Flemings, P. B., and Hudec, M. R., 2014, Modeling stress evolution around a rising salt diapir: Marine and Petroleum Geology, v. 51, p. 230-238.

Nikolinakou, M. A., Luo, G., Hudec, M. R., and Flemings, P. B., 2012, Geomechanical modeling of stresses adjacent to salt bodies: Part 2—Poroelastoplasticity and coupled overpressures: AAPG bulletin, v. 96, no. 1, p. 65-85.

Nolan, C., 2021, Geothermal Energy and Ice an unlikely alliance? Insights from temperature data on the Norwegian Continental Shelf.

Ojeda, H. A. O., 1982, Structural Framework, Stratigraphy, and Evolution of Brazilian Marginal Basins: AAPG Bulletin-American Association of Petroleum Geologists, v. 66, no. 6, p. 732-749.

Omosanya, K. O., 2020, Cenozoic tectonic inversion in the Naglfar Dome, Norwegian North Sea: Marine and Petroleum Geology, v. 118, p. 104461.

Omosanya, K. O., Johansen, S. E., and Harishidayat, D., 2015, Evolution and character of supra-salt faults in the Easternmost Hammerfest Basin, SW Barents Sea: Marine and Petroleum Geology, v. 66, p. 1013-1028.

Oudmayer, B., and De Jager, J., Fault reactivation and oblique-slip in the Southern North Sea, *in* Proceedings Geological Society, London, Petroleum Geology Conference Series1993, Volume 4, The Geological Society of London, p. 1281-1290.

Ouellet, A., Bérard, T., Desroches, J., Frykman, P., Welsh, P., Minton, J., Pamukcu, Y., Hurter, S., and Schmidt-Hattenberger, C., 2011, Reservoir geomechanics for assessing containment in CO2 storage: a case study at Ketzin, Germany: Energy Procedia, v. 4, p. 3298-3305.

Ozarslan, A., 2012, Large-scale hydrogen energy storage in salt caverns: International journal of hydrogen energy, v. 37, no. 19, p. 14265-14277.

Peacock, D., and Sanderson, D., 1991, Displacements, segment linkage and relay ramps in normal fault zones: Journal of Structural Geology, v. 13, no. 6, p. 721-733.

Peacock, D. C. P., 1991, Displacements and Segment Linkage in Strike-Slip-Fault Zones: Journal of Structural Geology, v. 13, no. 9, p. 1025-1035.

Peacock, D. C. P., and Mann, A., 2005, Evaluation of the controls on fracturing in reservoir rocks: Journal of Petroleum Geology, v. 28, no. 4, p. 385-396.

Peacock, D. C. P., Nixon, C. W., Rotevatn, A., Sanderson, D. J., and Zuluaga, L. F., 2017, Interacting faults: Journal of Structural Geology, v. 97, p. 1-22.

Peacock, D. C. P., and Sanderson, D. J., 1996, Effects of propagation rate on displacement variations along faults: Journal of structural geology, v. 18, no. 2-3, p. 311-320.

Peryt, T. M., Halas, S., and Petrivna Hryniv, S., 2010, Sulphur and oxygen isotope signatures of late Permian Zechstein anhydrites, West Poland: seawater evolution and diagenetic constraints: Geological Quarterly, v. 54, p. 387-400.

Piedade, A., and Alves, T. M., 2017, Structural styles of Albian rafts in the Espirito Santo Basin (SE Brazil): Evidence for late raft compartmentalisation on a 'passive' continental margin: Marine and Petroleum Geology, v. 79, p. 201-221.

Pilcher, R., and Argent, J., 2007, Mega-pockmarks and linear pockmark trains on the West African continental margin: Marine Geology, v. 244, no. 1, p. 15-32.

Pilcher, R. S., Kilsdonk, B., and Trude, J., 2011, Primary basins and their boundaries in the deep-water northern Gulf of Mexico: Origin, trap types, and petroleum system implications: AAPG bulletin, v. 95, no. 2, p. 219-240.

Planke, S., Svensen, H., Hovland, M., Banks, D., and Jamtveit, B., 2003, Mud and fluid migration in active mud volcanoes in Azerbaijan: Geo-Marine Letters, v. 23, p. 258-268.

Pollard, D., Saltzer, S., and Rubin, A. M., 1993, Stress inversion methods: are they based on faulty assumptions?: Journal of Structural Geology, v. 15, no. 8, p. 1045-1054.

Popescu, I., Lericolais, G., Panin, N., De Batist, M., and Gillet, H., 2007, Seismic expression of gas and gas hydrates across the western Black Sea: Geo-Marine Letters, v. 27, p. 173-183.

Powell, J., Chisholm, J., Bridge, D., Rees, J., Glover, B., and Besly, B., 2000, Stratigraphical framework for Westphalian to Early Permian red-bed successions of the Pennine Basin: Geological Survey (Keyworth) (Research Report No. R/00/01).

Powell, J. W., 1875, Exploration of the Colorado River of the West and its Tributaries.

Preiss, A. D., and Adam, J., 2021, Basement fault trends in the Southern North Sea Basin: Journal of Structural Geology, v. 153, p. 104449.

Pruess, K., 2005, Numerical studies of fluid leakage from a geologic disposal reservoir for CO2 show self-limiting feedback between fluid flow and heat transfer: Geophysical research letters, v. 32, no. 14.

Pruess, K., 2008, On CO 2 fluid flow and heat transfer behavior in the subsurface, following leakage from a geologic storage reservoir: Environmental Geology, v. 54, p. 1677-1686.

Qin, Y. P., Alves, T. M., Constantine, J., and Gamboa, D., 2016, Quantitative seismic geomorphology of a submarine channel system in SE Brazil (Espirito Santo Basin): Scale comparison with other submarine channel systems: Marine and Petroleum Geology, v. 78, p. 455-473.

Quintà, A., Tavani, S., and Roca, E., 2012, Fracture pattern analysis as a tool for constraining the interaction between regional and diapir-related stress fields: Poza de la Sal Diapir (Basque Pyrenees, Spain): Geological Society, London, Special Publications, v. 363, no. 1, p. 521-532.

Quirk, D., Interpreting the Upper Carboniferous of the Dutch Cleaver Bank High, *in* Proceedings Geological Society, London, Petroleum Geology Conference Series1993, Volume 4, The Geological Society of London, p. 697-706.

Rafavich, F., Kendall, C. S. C., and Todd, T., 1984, The relationship between acoustic properties and the petrographic character of carbonate rocks: Geophysics, v. 49, no. 10, p. 1622-1636.

Räss, L., Simon, N. S., and Podladchikov, Y. Y., 2018, Spontaneous formation of fluid escape pipes from subsurface reservoirs: Scientific reports, v. 8, no. 1, p. 11116.

Ratcliff, D. W., Gray, S. H., and Whitmore Jr, N., 1992, Seismic imaging of salt structures in the Gulf of Mexico: The Leading Edge, v. 11, no. 4, p. 15-31.

Raymond, J., Langevin, H., Comeau, F.-A., and Malo, M., 2022, Temperature dependence of rock salt thermal conductivity: Implications for geothermal exploration: Renewable Energy, v. 184, p. 26-35.

Reinecker, J., Gutmanis, J., Foxford, A., Cotton, L., Dalby, C., and Law, R., 2021, Geothermal exploration and reservoir modelling of the United Downs deep geothermal project, Cornwall (UK): Geothermics, v. 97, p. 102226.

Reinecker, J., Hochschild, T., Kraml, M., Löschan, G., and Kreuter, H., Experiences and challenges in geothermal exploration in the Upper Rhine Graben, *in* Proceedings Proceedings of European Geothermal Congress2019, p. 11-12.

Remmelts, G., 1995, Fault-related salt tectonics in the southern North Sea, the Netherlands.

Remmelts, G., Salt tectonics in the southern North Sea, the Netherlands, *in* Proceedings Geology of Gas and Oil under the Netherlands: Selection of papers presented at the 1983 Iternational Conference of the American Association of Petroleum Geologists, held in The Hague1996, Springer, p. 143-158.

Rippon, J., 1984, Contoured patterns of the throw and hade of normal faults in the Coal Measures (Westphalian) of north-east Derbyshire: Proceedings of the Yorkshire Geological Society, v. 45, no. 3, p. 147-161.

Robinson, A. H., Callow, B., Böttner, C., Yilo, N., Provenzano, G., Falcon-Suarez, I. H., Marín-Moreno, H., Lichtschlag, A., Bayrakci, G., and Gehrmann, R., 2021, Multiscale characterisation of chimneys/pipes: Fluid escape structures within sedimentary basins: International Journal of Greenhouse Gas Control, v. 106, p. 103245.

Roche, V., Homberg, C., and Rocher, M., 2012, Fault displacement profiles in multilayer systems: from fault restriction to fault propagation: Terra Nova, v. 24, no. 6, p. 499-504.

Roche, V., Homberg, C., and Rocher, M., 2013, Fault nucleation, restriction, and aspect ratio in layered sections: Quantification of the strength and stiffness roles using numerical modeling: Journal of Geophysical Research: Solid Earth, v. 118, no. 8, p. 4446-4460.

Rogers, A. D., Tyler, P. A., Connelly, D. P., Copley, J. T., James, R., Larter, R. D., Linse, K., Mills, R. A., Garabato, A. N., and Pancost, R. D., 2012, The discovery of new deep-sea hydrothermal vent communities in the Southern Ocean and implications for biogeography: PLoS biology, v. 10, no. 1, p. e1001234.

Rotevatn, A., and Jackson, C. A. L., 2014, 3D structure and evolution of folds during normal fault dip linkage: Journal of the Geological Society, v. 171, no. 6, p. 821-829.

Rotevatn, A., Jackson, C. A. L., Tvedt, A. B. M., Bell, R. E., and Blaekkan, I., 2019, How do normal faults grow?: Journal of Structural Geology, v. 125, p. 174-184.

Rouby, D., Guillocheau, F., Robin, C., Bouroullec, R., Raillard, S., Castelltort, S., and Nalpas, T., 2003, Rates of deformation of an extensional growth fault/raft system (offshore Congo, West African margin) from combined accommodation measurements and 3-D restoration: Basin Research, v. 15, no. 2, p. 183-200.

Rowan, M. G., Jackson, M. P. A., and Trudgill, B. D., 1999, Salt-related fault families and fault welds in the northern Gulf of Mexico: AAPG Bulletin-American Association of Petroleum Geologists, v. 83, no. 9, p. 1454-1484.

Rowan, M. G., Urai, J. L., Fiduk, J. C., and Kukla, P. A., 2019, Deformation of intrasalt competent layers in different modes of salt tectonics: Solid Earth, v. 10, no. 3, p. 987-1013.

Rutter, N., 1976, MULTIPLE GLACIATION IN THE CANADIAN ROCKY MOUNTAINS WITH SPECIAL EMPHASIS ON NORTHEASTERN BRITISH COLUMBIA.

Sanz, P., and Dasari, G., Controls on in-situ stresses around salt bodies, *in* Proceedings 44th US Rock Mechanics Symposium and 5th US-Canada Rock Mechanics Symposium2010a, OnePetro.

Sanz, P. F., and Dasari, G. R., Controls on in-situ stresses around salt bodies, *in* Proceedings ARMA US Rock Mechanics/Geomechanics Symposium2010b, ARMA, p. ARMA-10-169.

Savage, H. M., and Brodsky, E. E., 2011, Collateral damage: Evolution with displacement of fracture distribution and secondary fault strands in fault damage zones: Journal of Geophysical Research: Solid Earth, v. 116, no. B3.

Schlische, R. W., Young, S. S., Ackermann, R. V., and Gupta, A., 1996, Geometry and scaling relations of a population of very small rift-related normal faults: Geology, v. 24, no. 8, p. 683-686.

Scholz, C., and Cowie, P. A., 1990, Determination of total strain from faulting using slip measurements: Nature, v. 346, no. 6287, p. 837-839.

Scholz, C. H., Dawers, N. H., Yu, J. Z., and Anders, M. H., 1993, Fault Growth and Fault Scaling Laws - Preliminary-Results: Journal of Geophysical Research-Solid Earth, v. 98, no. B12, p. 21951-21961.

Schopfer, M. P. J., Childs, C., and Walsh, J. J., 2006, Localisation of normal faults in multilayer sequences: Journal of Structural Geology, v. 28, no. 5, p. 816-833.

Schroot, B. M., and Haan, H. B. D., 2003, An improved regional structural model of the Upper Carboniferous of the Cleaver Bank High based on 3D seismic interpretation: Geological Society, London, Special Publications, v. 212, no. 1, p. 23-37.

Schultz, R. A., and Fossen, H., 2002, Displacement–length scaling in three dimensions: the importance of aspect ratio and application to deformation bands: Journal of Structural Geology, v. 24, no. 9, p. 1389-1411.

Schultz, R. A., Soliva, R., Fossen, H., Okubo, C. H., and Reeves, D. M., 2008, Dependence of displacement-length scaling relations for fractures and deformation bands on the volumetric changes across them: Journal of Structural Geology, v. 30, no. 11, p. 1405-1411.

Schultzela, D. D., Jackson, M. P. A., and Vendeville, B. C., 1993, Mechanics of Active Salt Diapirism: Tectonophysics, v. 228, no. 3-4, p. 275-312.

Seni, S., and Jackson, M., 1983, Evolution of salt structures, east Texas diapir province, part 1: Sedimentary record of halokinesis: AAPG bulletin, v. 67, no. 8, p. 1219-1244.

Seymour, K., Rae, G., Peden, J., and Ormston, K., Drilling close to salt diapirs in the North Sea, *in* Proceedings SPE Offshore Europe1993, OnePetro.

Shelton, J. W., 1984, Listric Normal Faults - an Illustrated Summary: AAPG Bulletin-American Association of Petroleum Geologists, v. 68, no. 7, p. 801-815.

Shenyan, L., Xiaolin, H., and Jinbo, L., 2011, Great discovery and its significance for exploration in subsalt reservoir in Santos Basin, Brazil: China Petroleum Exploration, v. 16, no. 4, p. 74.

Shipton, Z. K., and Cowie, P. A., 2003, A conceptual model for the origin of fault damage zone structures in high-porosity sandstone: Journal of Structural Geology, v. 25, no. 3, p. 333-344.

Sloan Jr, E. D., 2003, Fundamental principles and applications of natural gas hydrates: Nature, v. 426, no. 6964, p. 353-359.

Sone, H., and Zoback, M., Strength, creep and frictional properties of gas shale reservoir rocks, *in* Proceedings ARMA US Rock Mechanics/Geomechanics Symposium2010, ARMA, p. ARMA-10-463.

Stanton-Yonge, A., Cembrano, J., Griffith, W. A., Jensen, E., and Mitchell, T. M., 2020, Self-similar length-displacement scaling achieved by scale-dependent growth processes: Evidence from the Atacama Fault System: Journal of Structural Geology, v. 133, p. 103993.

Stewart, S., 2006, Implications of passive salt diapir kinematics for reservoir segmentation by radial and concentric faults: Marine and petroleum geology, v. 23, no. 8, p. 843-853.

Stewart, S., Harvey, M., Otto, S., and Weston, P., 1996, Influence of salt on fault geometry: examples from the UK salt basins: Geological Society, London, Special Publications, v. 100, no. 1, p. 175-202.

Stewart, S. A., 2007, Salt tectonics in the North Sea Basin: a structural style template for seismic interpreters: Geological Society, London, Special Publications, v. 272, no. 1, p. 361-396.

Stewart, S. A., and Coward, M. P., 1995, Synthesis of salt tectonics in the southern North Sea, UK: Marine and Petroleum Geology, v. 12, no. 5, p. 457-475.

Suppe, J., 1985, Principles of structural geology, Prentice Hall.

Suppe, J., 2014, Fluid overpressures and strength of the sedimentary upper crust: Journal of Structural Geology, v. 69, p. 481-492.

Talbot, C., and Jackson, M., 1987a, Internal kinematics of salt diapirs: AAPG Bulletin, v. 71, no. 9, p. 1068-1093.

Talbot, C. J., 2005, "Evidence for Triassic salt domes in the Tunisian Atlas from gravity and geological data" by C. Jallouli et al., Tectonophysics 396 (2005) 209–225: Tectonophysics, v. 406, no. 3-4, p. 249-254.

Talbot, C. J., and Jackson, M. P., 1987b, Salt tectonics: Scientific American, v. 257, no. 2, p. 70-79.

Tao, Z., 2018, Crestal fault reactivation on rising salt diapirs: An integrated analysis from large to small scales of observation: Cardiff University.

Tao, Z., and Alves, T. M., 2017, The role of gravitational collapse in controlling the evolution of crestal fault systems (Espírito Santo Basin, SE Brazil)–Reply: Journal of Structural Geology, v. 98, p. 12-14.

Tao, Z., and Alves, T. M., 2019, Impacts of data sampling on the interpretation of normal fault propagation and segment linkage: Tectonophysics, v. 762, p. 79-96.

Taylor, J., 1998, Upper Permian—Zechstein: Petroleum Geology of the North Sea: Basic concepts and recent advances, p. 174-211.

Ten Veen, J., Van Gessel, S., and Den Dulk, M., 2012, Thin-and thick-skinned salt tectonics in the Netherlands; a quantitative approach: Netherlands Journal of Geosciences, v. 91, no. 4, p. 447-464.

Teófilo, F. A. F., Junior, E. P., Roehl, D., and Martha, L. F., 2018, A numerical approach for investigation of stress states induced by salt structures: International Journal of Rock Mechanics and Mining Sciences, v. 106, p. 223-233.

Thigpen, J. R., Roberts, D., Snow, J. K., Walker, C. D., and Bere, A., 2019, Integrating kinematic restoration and forward finite element simulations to constrain the evolution of salt diapirism and overburden deformation in evaporite basins: Journal of Structural Geology, v. 118, p. 68-86.

Torabi, A., Alaei, B., and Libak, A., 2019, Normal fault 3D geometry and displacement revisited: Insights from faults in the Norwegian Barents Sea: Marine and Petroleum Geology, v. 99, p. 135-155.

Torabi, A., and Berg, S. S., 2011, Scaling of fault attributes: A review: Marine and Petroleum Geology, v. 28, no. 8, p. 1444-1460.

Underwood, C. A., Cooke, M. L., Simo, J. A., and Muldoon, M. A., 2003, Stratigraphic controls on vertical fracture patterns in Silurian dolomite, northeastern Wisconsin: AAPG bulletin, v. 87, no. 1, p. 121-142.

van-der-Zee, W., Ozan, C., Brudy, M., and Holland, M., 3D geomechanical modeling of complex salt structures, *in* Proceedings SIMULIA customer conference2011, p. 1-16.

van den Berg, A., Weimer, P., and Bouroullec, R., 2004, Structural evolution of the mensa minibasin, mississippi canyon, northern deep gulf of mexico.

Van Gent, H., Urai, J. L., and De Keijzer, M., 2011, The internal geometry of salt structures–a first look using 3D seismic data from the Zechstein of the Netherlands: Journal of Structural Geology, v. 33, no. 3, p. 292-311.

Van Ojik, K., Silvius, A., Kremer, Y., and Shipton, Z., 2020, Fault seal behaviour in Permian Rotliegend reservoir sequences: case studies from the Dutch Southern North Sea: Geological Society, London, Special Publications, v. 496, no. 1, p. 9-38.

Van Rensbergen, P., Hillis, R. R., Maltman, A. J., and Morley, C. K., 2003, Subsurface sediment mobilization: Introduction: Geological Society, London, Special Publications, v. 216, no. 1, p. 1-8.

Van Wees, J.-D., Kronimus, A., Van Putten, M., Pluymaekers, M., Mijnlieff, H., Van Hooff, P., Obdam, A., and Kramers, L., 2012, Geothermal aquifer performance assessment for direct heat production–Methodology and application to Rotliegend aquifers: Netherlands Journal of Geosciences, v. 91, no. 4, p. 651-665.

Van Wees, J.-D., Stephenson, R., Ziegler, P., Bayer, U., McCann, T., Dadlez, R., Gaupp, R., Narkiewicz, M., Bitzer, F., and Scheck, M., 2000, On the origin of the southern Permian Basin, Central Europe: Marine and Petroleum Geology, v. 17, no. 1, p. 43-59.

Van Wees, J., Van Bergen, F., David, P., Nepveu, M., Beekman, F., Cloetingh, S., and Bonté, D., 2009, Probabilistic tectonic heat flow modeling for basin maturation: Assessment method and applications: Marine and Petroleum Geology, v. 26, no. 4, p. 536-551.

Vendeville, B. C., 2005, Salt tectonics driven by sediment progradation: Part I - Mechanics and kinematics: Aapg Bulletin, v. 89, no. 8, p. 1071-1079.

Vendeville, B. C., and Jackson, M. P. A., 1992a, The Fall of Diapirs during Thin-Skinned Extension: Marine and Petroleum Geology, v. 9, no. 4, p. 354-371.

Vendeville, B. C., and Jackson, M. P. A., 1992b, The Rise of Diapirs during Thin-Skinned Extension: Marine and Petroleum Geology, v. 9, no. 4, p. 331-353.

Vidal, J., and Genter, A., 2018, Overview of naturally permeable fractured reservoirs in the central and southern Upper Rhine Graben: Insights from geothermal wells: Geothermics, v. 74, p. 57-73.

Vieira, R. A., Mendes, M. P., Vieira, P. E., Costa, L. A., Tagliari, C. V., Bacellar, L. d. A. P., and Feijó, F. J., 1994, Bacias do Espírito Santo e Mucuri.

Volozh, Y., Talbot, C., and Ismail-Zadeh, A., 2003, Salt structures and hydrocarbons in the Pricaspian basin: AAPG bulletin, v. 87, no. 2, p. 313-334.

Waghorn, K. A., Pecher, I., Strachan, L. J., Crutchley, G., Bialas, J., Coffin, R., Davy, B., Koch, S., Kroeger, K. F., and Papenberg, C., 2018, Paleo-fluid expulsion and contouritic drift formation on the Chatham Rise, New Zealand: Basin Research, v. 30, no. 1, p. 5-19.

Walsh, J. J., Bailey, W. R., Childs, C., Nicol, A., and Bonson, C. G., 2003, Formation of segmented normal faults: a 3-D perspective: Journal of Structural Geology, v. 25, no. 8, p. 1251-1262.

Walsh, J. J., Nicol, A., and Childs, C., 2002, An alternative model for the growth of faults: Journal of Structural Geology, v. 24, no. 11, p. 1669-1675.

Walsh, J. J., and Watterson, J., 1988, Analysis of the relationship between displacements and dimensions of faults: Journal of Structural geology, v. 10, no. 3, p. 239-247.

Waltham, D., 1997, Why does salt start to move?: Tectonophysics, v. 282, no. 1-4, p. 117-128.

Wangen, M., 2020, A 3D model for chimney formation in sedimentary basins: Computers & Geosciences, v. 137, p. 104429.

Warren, J. K., 2017, Salt usually seals, but sometimes leaks: Implications for mine and cavern stabilities in the short and long term: Earth-science reviews, v. 165, p. 302-341.

Watterson, J., 1986, Fault dimensions, displacements and growth: Pure and Applied Geophysics, v. 124, no. 1-2, p. 365-373.

Weijermars, R., Jackson, M. P. A., and Vendeville, B., 1993, Rheological and Tectonic Modeling of Salt Provinces: Tectonophysics, v. 217, no. 1-2, p. 143-174.

Welch, M. J., Davies, R. K., Knipe, R. J., and Tueckmantel, C., 2009, A dynamic model for fault nucleation and propagation in a mechanically layered section: Tectonophysics, v. 474, no. 3-4, p. 473-492.

Wells, D. L., and Coppersmith, K. J., 1994, New empirical relationships among magnitude, rupture length, rupture width, rupture area, and surface displacement: Bulletin of the seismological Society of America, v. 84, no. 4, p. 974-1002.

Wenau, S., and Alves, T. M., 2020, Salt-induced crestal faults control the formation of Quaternary tunnel valleys in the southern North Sea: Boreas, v. 49, no. 4, p. 799-812.

Westaway, R., 1999, The mechanical feasibility of low-angle normal faulting: Tectonophysics, v. 308, no. 4, p. 407-443.

Wilkins, S. J., and Gross, M. R., 2002, Normal fault growth in layered rocks at Split Mountain, Utah: influence of mechanical stratigraphy on dip linkage, fault restriction and fault scaling: Journal of Structural Geology, v. 24, no. 9, p. 1413-1429.

Willemse, E. J., 1997, Segmented normal faults: Correspondence between three-dimensional mechanical models and field data: Journal of Geophysical Research: Solid Earth, v. 102, no. B1, p. 675-692.

Willemse, E. J., Pollard, D. D., and Aydin, A., 1996, Three-dimensional analyses of slip distributions on normal fault arrays with consequences for fault scaling: Journal of Structural Geology, v. 18, no. 2-3, p. 295-309.

Wilson, A., and Ruppel, C., 2007, Salt tectonics and shallow subseafloor fluid convection: Models of coupled fluid-heat-salt transport: Geofluids, v. 7, no. 4, p. 377-386.

Wiltschko, D., and Chapple, W., 1977, Flow of weak rocks in Appalachian Plateau folds: AAPG Bulletin, v. 61, no. 5, p. 653-670.

Wojtal, S. F., 1994, Fault Scaling Laws and the Temporal Evolution of Fault Systems: Journal of Structural Geology, v. 16, no. 4, p. 603-612.

Wojtal, S. F., 1996, Changes in fault displacement populations correlated to linkage between faults: Journal of Structural Geology, v. 18, no. 2-3, p. 265-279.

Wood, C. P., Brathwaite, R. L., and Rosenberg, M. D., 2001, Basement structure, lithology and permeability at Kawerau and Ohaaki geothermal fields, New Zealand: Geothermics, v. 30, no. 4, p. 461-481.

Worden, R. H., Benshatwan, M. S., Potts, G. J., and Elgarmadi, S. M., 2016, Basin-scale fluid movement patterns revealed by veins: Wessex Basin, UK: Geofluids, v. 16, no. 1, p. 149-174.

Wynn, R. B., Huvenne, V. A., Le Bas, T. P., Murton, B. J., Connelly, D. P., Bett, B. J., Ruhl, H. A., Morris, K. J., Peakall, J., and Parsons, D. R., 2014, Autonomous Underwater Vehicles (AUVs): Their past, present and future contributions to the advancement of marine geoscience: Marine geology, v. 352, p. 451-468.

Xiao, H.-B., and Suppe, J., 1989, Role of compaction in listric shape of growth normal faults: AAPG bulletin, v. 73, no. 6, p. 777-786.

Yang, K., Huntington, J. F., Browne, P. R., and Ma, C., 2000, An infrared spectral reflectance study of hydrothermal alteration minerals from the Te Mihi sector of the Wairakei geothermal system, New Zealand: Geothermics, v. 29, no. 3, p. 377-392.

Yao, Z., Zhang, M., Zeng, L., Wang, R., and He, T., 2003, Salt structures and exploration of oil and gas: Petroleum Exploration and Development, v. 30, no. 2.

Yin, H., and Groshong, R. H., 2007, A three-dimensional kinematic model for the deformation above an active diapir: AAPG bulletin, v. 91, no. 3, p. 343-363.

Yixin, Y., Liangjie, T., Wenjing, Y., Wenzheng, J., Gengxin, P., and Ganglin, L., 2008, Thick-skinned contractional salt structures in the Kuqa depression, the northern Tarim basin: constraints from physical experiments: Acta Geologica Sinica-English Edition, v. 82, no. 2, p. 327-333.

Young, C., Patti, N. C., and Trent, B. C., 1982, Stratigraphic variations in oil-shale fracture properties: Stratigraphic variations in oil-shale fracture properties DOE.

Younger, P. L., Gluyas, J. G., and Stephens, W. E., 2012, Development of deep geothermal energy resources in the UK: Proceedings of the Institution of Civil Engineers-Energy, v. 165, no. 1, p. 19-32.

Yu, Y., Tang, L., Yang, W., Huang, T., Qiu, N., and Li, W., 2014, Salt structures and hydrocarbon accumulations in the Tarim Basin, northwest China: AAPG Bulletin, v. 98, no. 1, p. 135-159.

Yu, Y., Zhou, X., Peng, W., Wei, G., and Lv, D., 2011, An overview on salt structures: Geotectonica et Metallogenia, v. 35, p. 169-182.

Yuan, X. P., Leroy, Y. M., and Maillot, B., 2020, Control of fluid pressures on the formation of listric normal faults: Earth and Planetary Science Letters, v. 529.

Ze, T., and Alves, T. M., 2016, The role of gravitational collapse in controlling the evolution of crestal fault systems (Espirito Santo Basin, SE Brazil): Journal of Structural Geology, v. 92, p. 79-98.

Ze, T., and Alves, T. M., 2021, Localized strata-bound domino faulting offshore Espírito Santo Basin (southeastern Brazil): The case for sudden release of fluid in salt-withdrawal basins: AAPG Bulletin, v. 105, no. 8, p. 1535-1562.

Zhang, Q., and Alves, T., 2023, Palaeostress state around a rising salt diapir inferred from seismic reflection data: Marine and Petroleum Geology, p. 106385.

Zhang, Q., Alves, T. M., and Martins-Ferreira, M. A. C., 2022, Fault analysis of a salt minibasin offshore Espírito Santo, SE Brazil: Implications for fluid flow, carbon and energy storage in regions dominated by salt tectonics: Marine and Petroleum Geology, v. 143, p. 105805.

Zhuo, Q., Meng, F., Zhao, M., Li, Y., Lu, X., and Ni, P., 2016, The salt chimney effect: delay of thermal evolution of deep hydrocarbon source rocks due to high thermal conductivity of evaporites: Geofluids, v. 16, no. 3, p. 440-451.

Ziegler, P., 1990, Collision related intra-plate compression deformations in Western and Central Europe: Journal of Geodynamics, v. 11, no. 4, p. 357-388.

Appendix A: Interpreted faults around the salt diapir in Chapter 5

Panoramic views of the 10,401 faults interpreted in this work. a) Top view of all interpreted faults on Petrel®. b) and c) Top and oblique views of all interpreted faults on Move®.

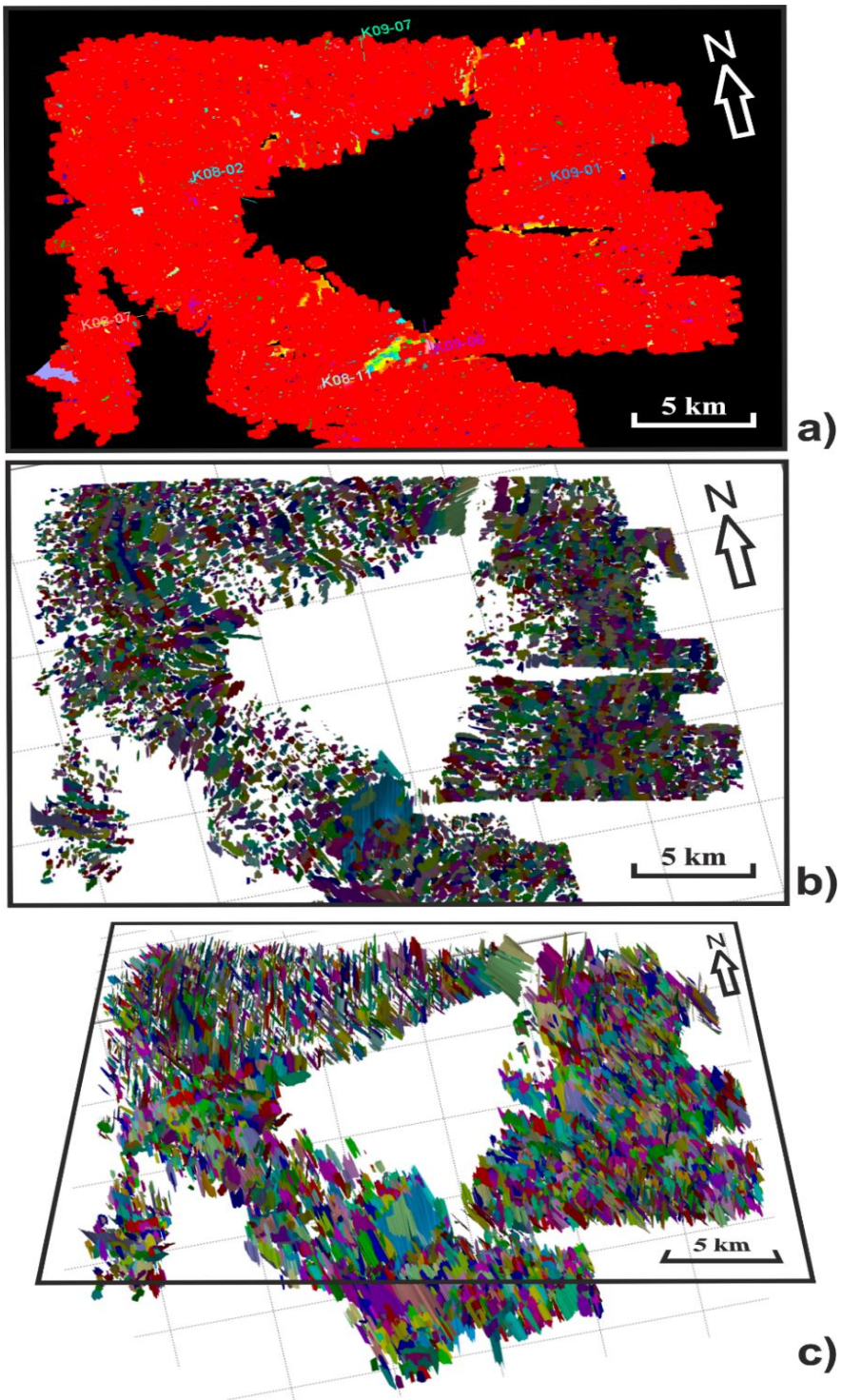

Appendix B: Geothermal data analysed in Chapter 6

Number	Well name	True vertical depth (m)	Measured BHT (ºC)	Time since mud circulation (h)	Duration of mud circulation (h)	Corrected BHT (ºC)	True vertical depth relative to the Sea-floor (m)	Geothermal gradient (ºC/km)
1	K04-01	1243.2	60.0			78.0	1173.7	59.8
2	K04-01	1247.8	45.0			63.0	1178.3	46.8
3	K04-01	2590.0	84.0			102.0	2520.5	37.4
4	K04-01	3322.0	111.0			129.0	3252.2	37.3
5	K04-01	3333.0	96.0			114.0	3263.5	32.5
6	K04-01	3336.0	94.0			112.0	3266.5	31.9
7	K04-01	3336.0	97.0			115.0	3266.5	32.8
8	K04-01	3600.0	99.0			117.0	3530.5	30.9
9	K04-01	3602.0	103.0			121.0	3532.5	32.0
10	K04-01	3708.0	110.0			128.0	3638.5	33.0
11	K04-01	3711.5	105.0			123.0	3642.0	31.6
12	K04-01	3711.5	110.0			128.0	3642.0	33.0
13	K04-01	3712.0	108.0			126.0	3642.5	32.5
14	K04-01	3712.0	111.0			129.0	3642.5	33.3
15	K04-03	1250.0	44.0	4.5		66.9	1173.6	50.4
16	K04-03	3066.0	82.0	8.0		102.4	2989.6	31.6
17	K04-03	3440.0	104.0	17.3		118.9	3363.6	33.0
18	K04-03	3524.0	101.0	8.2		121.2	3447.6	32.9

19	K04-03	3940.0	123.0	10.0		142.0	3863.6	34.7
20	K04-03	3981.0	123.0	17.3		137.9	3904.6	33.3
21	K04-04	1261.5	51.0	8.3		71.1	1191.2	53.2
22	K04-04	2972.0	88.0	9.0		107.7	2901.7	34.4
23	K04-04	3545.0	104.0	7.7		124.6	3474.7	33.6
24	K04-04	3698.0	115.0			133.0	3627.7	34.5
25	K04-04	3700.3	112.2	20.0	3.0	116.4	3630.0	29.9
26	K04-04	3702.0	112.3	17.9	3.0	116.4	3631.7	29.9
27	K04-04	3703.0	107.2	7.8	3.0	116.4	3632.7	29.9
28	K05-04	3725.0	115.0			133.0	3650.0	34.3
29	K05-04	3740.0	118.0	14.4		134.4	3665.0	34.5
30	K07-01	639.0	42.0	4.0		65.3	572.0	100.5
31	K07-01	1971.0	69.0			87.0	1904.0	41.6
32	K07-01	2097.0	65.0	4.0		88.3	2030.0	39.7
33	K07-01	2101.0	63.0	4.0		86.3	2034.0	38.6
34	K07-01	3455.0	93.0			111.0	3388.0	30.5
35	K07-01	3459.0	102.0	6.0		123.8	3392.0	34.2
36	K07-02	2296.5	74.0	6.5		95.4	2229.2	39.3
37	K07-02	2299.5	65.0			83.0	2232.2	33.7
38	K07-02	3119.5	85.0	3.5		108.7	3052.2	33.1
39	K07-02	3122.0	79.0			97.0	3054.7	29.2
40	K07-02	3367.5	97.0	3.3		120.9	3300.2	34.3
41	K07-02	3370.0	100.0			118.0	3302.7	33.4
42	K07-03	944.5	44.0			62.0	881.0	61.5
43	K07-03	955.2	43.0	4.0		66.3	891.7	65.6

44	K07-03	2344.0	78.0	4.5		100.9	2280.5	40.8
45	K07-03	3395.0	99.0			117.0	3331.5	32.8
46	K07-03	3436.3	98.0	12.0		115.8	3372.8	32.0
47	K07-03	3437.0	92.0			110.0	3373.5	30.3
48	K07-03	3437.0	99.0			117.0	3373.5	32.4
49	K07-04	1105.5	25.0	6.0		46.8	1029.0	37.9
50	K07-04	2227.5	77.0	11.5		95.1	2151.0	40.6
51	K07-04	2230.0	73.5			91.5	2153.5	38.9
52	K07-04	3167.5	94.0	18.5		108.3	3091.0	32.5
53	K07-04	3172.5	90.0			108.0	3096.0	32.4
54	K07-04	3371.5	93.0	6.0		114.8	3295.0	32.5
55	K07-04	3377.5	104.0	6.0		125.8	3301.0	35.7
56	K07-04	3488.5	104.0	12.5		121.5	3412.0	33.3
57	K07-04	3491.5	100.0			118.0	3415.0	32.3
58	K07-04	3491.5	107.0			125.0	3415.0	34.3
59	K07-04	3492.0	103.0			121.0	3415.5	33.1
60	K07-05	901.0	32.0	9.5		51.4	841.7	51.7
61	K07-05	2201.5	69.0	12.0		86.8	2142.2	36.9
62	K07-05	2202.7	63.0			81.0	2143.4	34.2
63	K07-05	2870.0	93.0	16.0		108.5	2810.7	35.8
64	K07-05	2877.5	88.0			106.0	2818.2	34.8
65	K07-05	2878.0	92.0			110.0	2818.7	36.3
66	K07-05	3011.0	104.0	22.0		116.7	2951.7	36.9
67	K07-05	3161.0	102.0	18.5		116.3	3101.7	35.0
68	K07-05	3163.0	98.0			116.0	3103.7	34.9

69	K07-05	3163.0	99.0			117.0	3103.7	35.2
70	K07-08	1020.7	51.0	4.0		74.3	949.4	70.0
71	K07-08	1021.7	53.0			71.0	950.4	66.5
72	K07-08	2199.0	70.0	5.0		92.5	2127.7	39.8
73	K07-08	2200.0	73.0			91.0	2128.7	39.1
74	K07-08	3241.5	99.0			117.0	3170.2	34.4
75	K07-08	3242.0	101.0	17.0		116.0	3170.7	34.1
76	K07-08	3735.0	110.0			128.0	3663.7	32.8
77	K07-08	3739.0	112.0	11.5		130.1	3667.7	33.3
78	K07-08	3745.5	102.0	6.0		123.8	3674.2	31.6
79	K07-08	3748.0	106.0			124.0	3676.7	31.6
80	K07-09	2226.0	89.0	16.0		104.5	2155.7	44.9
81	K07-09	2808.0	99.0	17.5		113.8	2737.7	38.7
82	K07-09	3741.0	113.0			131.0	3670.7	33.6
83	K07-09	3750.0	111.0	43.0		117.2	3679.7	29.7
84	K07-09	3750.0	116.0			134.0	3679.7	34.3
85	K07-09	3812.0	116.0	14.0		132.6	3741.7	33.4
86	K07-10	2012.0	80.0	21.0		93.1	1941.7	43.9
87	K07-10	3150.0	102.0	15.5		117.8	3079.7	35.7
88	K07-10	3412.0	106.0	51.0		110.8	3341.7	30.8
89	K07-10	3420.0	105.0			123.0	3349.7	34.4
90	K07-10	3420.0	108.0			126.0	3349.7	35.3
91	K07-13	606.8	37.5	49.0		42.6	530.4	65.6
92	K07-13	1826.0	63.0	90.5		64.3	1749.6	32.3
93	K07-13	3111.0	94.0	233.0		94.0	3034.6	28.4

94	K07-13	3417.0	107.0			125.0	3340.6	35.1
95	K07-13	3421.0	101.0	145.0		101.2	3344.6	27.9
96	K07-13	3455.8	107.0			125.0	3379.4	34.7
97	K07-13	3455.8	107.0			125.0	3379.4	34.7
98	K07-13	3455.8	107.0			125.0	3379.4	34.7
99	K07-13	3455.8	117.0	69.0		119.6	3379.4	33.1
100	K07-13	3514.0	107.0			125.0	3437.6	34.1
101	K07-	2623.0	72.0	8.0		92.4	2545.2	33.2
102	K07-	3192.0	98.8	8.0		119.2	3114.2	35.8
103	K07-	3412.0	107.0	8.0		127.4	3334.2	35.9
104	K07-	4063.2	106.5			124.5	3985.4	29.3
105	K07-	4080.8	106.5			124.5	4003.0	29.2
106	K07-	4094.0	106.5			124.5	4016.2	29.1
107	K07-	345.8	16.0	27.2		26.7	259.1	72.8
108	K07-	862.0	44.0	65.0		47.0	775.3	50.5
109	K07-	1784.0	69.0	220.0		69.0	1697.3	36.1
110	K07-	1867.0	76.0	89.0		77.3	1780.3	39.0
111	K07-	2406.5	107.0	230.0		107.0	2319.8	42.8
112	K07-	3254.0	114.0	143.0		114.2	3167.3	33.6
113	K07-	3517.3	99.0	65.0		102.0	3430.6	27.5
114	K07-	3517.3	99.0			117.0	3430.6	31.8
115	K07-	3517.3	107.0	179.0		107.1	3430.6	28.9
116	K08-01	997.0	49.0			67.0	927.6	63.8
117	K08-01	1001.7	49.0			67.0	932.3	63.5
118	K08-01	1003.5	49.0			67.0	934.1	63.4

119	K08-01	2155.0	72.0			90.0	2085.6	39.4
120	K08-01	2156.5	72.0			90.0	2087.1	39.4
121	K08-01	3228.0	89.0			107.0	3158.2	31.4
122	K08-01	3233.7	89.0			107.0	3163.9	31.4
123	K08-01	3282.8	89.0			107.0	3213.0	30.9
124	K08-01	3282.8	92.0			110.0	3213.0	31.8
125	K08-01	3283.0	92.0			110.0	3213.2	31.8
126	K08-01	3287.0	92.0			110.0	3217.2	31.8
127	K08-01	3287.5	92.0			110.0	3217.7	31.8
128	K08-01	3445.0	107.0			125.0	3375.2	34.7
129	K08-01	3446.0	106.0			124.0	3376.2	34.4
130	K08-01	3446.0	107.0			125.0	3376.2	34.7
131	K08-01	3627.5	110.0			128.0	3557.7	33.8
132	K08-01	3632.8	110.0			128.0	3563.0	33.7
133	K08-01	3664.5	110.0			128.0	3594.7	33.4
134	K08-01	3694.5	113.0			131.0	3624.7	34.0
135	K08-01	3695.8	113.0			131.0	3626.0	34.0
136	K08-01	3696.5	113.0			131.0	3626.7	34.0
137	K08-02	1193.7	44.0			62.0	1126.7	48.1
138	K08-02	1196.6	44.0			62.0	1129.6	48.0
139	K08-02	1198.2	44.0	3.5		67.7	1131.2	52.9
140	K08-02	1198.2	44.0			62.0	1131.2	47.9
141	K08-02	2399.2	72.0	4.0		95.3	2332.2	37.5
142	K08-02	2399.4	74.0			92.0	2332.4	36.1
143	K08-02	2400.0	79.0			97.0	2333.0	38.2

144	K08-02	2401.2	77.0			95.0	2334.2	37.4
145	K08-02	3323.1	99.0	5.0		121.5	3256.1	34.9
146	K08-02	3325.8	99.0			117.0	3258.8	33.5
147	K08-02	3600.0	112.0			130.0	3533.0	34.6
148	K08-02	3690.5	110.0			128.0	3623.5	33.2
149	K08-02	3690.5	112.0			130.0	3623.5	33.7
150	K08-02	3690.5	112.0	11.0		130.4	3623.5	33.8
151	K08-02	3691.0	112.0			130.0	3624.0	33.7
152	K08-02	3691.5	112.0			130.0	3624.5	33.7
153	K08-03	1797.3	61.0	10.5		79.7	1736.5	41.4
154	K08-03	1802.0	61.0	Sonic cement bond logging			61.0	1741.2
155	K08-03	2050.0	86.0			104.0	1989.2	48.4
156	K08-03	2711.5	86.0			104.0	2650.7	36.3
157	K08-03	2712.7	85.0	19.0		99.0	2651.9	34.4
158	K08-03	2714.5	82.5			100.5	2653.7	34.9
159	K08-03	2715.7	79.4			97.4	2654.9	33.7
160	K08-03	3115.0	106.0			124.0	3054.2	38.0
161	K08-03	3451.0	105.0	23.5		117.1	3390.2	32.2
162	K08-03	3454.5	106.0			124.0	3393.7	34.2
163	K08-03	3457.0	102.0			120.0	3396.2	33.0
164	K08-03	3458.0	100.0			118.0	3397.2	32.4
165	K08-07	2008.0	76.0	Sonic cement bond logging			76.0	1941.4
166	K08-07	2012.0	64.0			82.0	1945.4	38.1
167	K08-07	2013.5	66.0	14.0		82.6	1946.9	38.4
168	K08-07	3263.0	97.0	Sonic cement bond logging			97.0	3196.4

169	K08-07	3268.0	99.0	16.5		114.3	3201.4	33.3
170	K08-07	3269.0	98.0	12.0		115.8	3202.4	33.7
171	K08-07	3269.5	95.0	7.0		116.1	3202.9	33.8
172	K08-07	3540.0	109.0	12.0		126.8	3473.4	34.3
173	K08-07	3558.5	101.0	7.5		121.7	3491.9	32.6
174	K08-07	3559.5	109.0			127.0	3492.9	34.1
175	K08-07	3571.6	110.0	Sonic cement bond logging			110.0	3505.0
176	K08-07	3635.0	108.0	9.0		127.7	3568.4	33.6
177	K08-08	1896.5	62.0			80.0	1831.5	39.4
178	K08-08	1904.0	65.0			83.0	1839.0	40.9
179	K08-08	2477.0	87.7	Sonic cement bond logging			87.7	2412.0
180	K08-08	2495.0	79.0	6.0		100.8	2430.0	38.3
181	K08-08	2495.0	81.0	9.0		100.7	2430.0	38.2
182	K08-08	2646.0	84.0	7.5		104.7	2581.0	37.5
183	K08-08	2663.0	88.0	7.5		108.7	2598.0	38.8
184	K08-08	3298.0	84.0			102.0	3233.0	29.1
185	K08-08	3471.5	108.0	7.5		128.7	3406.5	35.5
186	K08-08	3473.0	104.0	7.0		125.1	3408.0	34.4
187	K08-08	3577.0	105.0	8.5		125.0	3512.0	33.4
188	K08-08	3578.0	109.0	18.8		123.2	3513.0	32.8
189	K08-08	3582.0	105.0	5.5		127.1	3517.0	33.9
190	K08-08	3590.0	108.0	11.5		126.1	3525.0	33.6
191	K08-09	2498.0	70.0	5.0		92.5	2419.0	35.0
192	K08-09	2927.0	104.0			122.0	2848.0	40.1
193	K08-09	2936.0	82.0			100.0	2857.0	32.3

194	K08-09	3104.0	95.0	8.0		115.4	3025.0	35.6
195	K08-09	3552.0	102.0	8.0		122.4	3473.0	33.0
196	K08-09	3553.0	104.0	11.5		122.1	3474.0	32.9
197	K08-09	3700.0	106.0			124.0	3621.0	32.1
198	K08-09	3700.0	106.0			124.0	3621.0	32.1
199	K08-09	3746.0	104.0			122.0	3667.0	31.1
200	K08-09	3747.0	108.0			126.0	3668.0	32.2
201	K08-09	3800.0	115.0			133.0	3721.0	33.6
202	K08-09	3800.0	115.0			133.0	3721.0	33.6
203	K08-09	3828.0	121.0	22.0		133.7	3749.0	33.6
204	K08-09	3875.5	116.0	12.5		133.5	3796.5	33.1
205	K08-09	4047.0	112.0			130.0	3968.0	30.8
206	K08-09	4047.0	115.0			133.0	3968.0	31.6
207	K08-09	4130.5	118.0			136.0	4051.5	31.6
208	K08-09	4146.0	124.0			142.0	4067.0	33.0
209	K08-09	4204.0	114.0			132.0	4125.0	30.1
210	K08-09	4204.0	118.0			136.0	4125.0	31.1
211	K08-09	4206.0	119.0			137.0	4127.0	31.3
212	K08-09	4206.0	123.0			141.0	4127.0	32.3
213	K08-11	602.0	32.0	7.3		52.8	535.8	84.0
214	K08-11	1681.0	70.0	23.0		82.3	1614.8	46.1
215	K08-11	1684.0	66.0	5.8		87.9	1617.8	49.5
216	K08-11	3282.0	90.0	16.0		105.5	3215.8	30.4
217	K08-11	3292.0	102.0	16.0		117.5	3225.8	34.0
218	K08-11	3293.0	94.0	16.0		109.5	3226.8	31.5

219	K08-11	3667.0	105.0	41.8		111.5	3600.8	28.8
220	K08-11	3672.0	99.0	7.4		119.8	3605.8	31.1
221	K08-14	3673.5	117.0	14.0		133.6	3598.5	35.0
222	K08-14	3689.0	117.0	14.0		133.6	3614.0	34.8
223	K08-14	3694.0	116.0	Sonic cement bond logging			116.0	3619.0
224	K08-14	4006.8	120.7	12.8		138.0	3931.8	33.1
225	K08-14	4013.0	120.7	12.8		138.0	3938.0	33.1
226	K08-14	4031.0	120.7	12.8		138.0	3956.0	32.9
227	K08-14	4031.5	123.0	22.0		135.7	3956.5	32.3
228	K08-15	3513.0	113.0			131.0	3434.0	35.9
229	K08-15	3513.5	113.0	36.0		120.9	3434.5	32.9
230	K08-15	3511.0	112.0	0.0		138.7	3432.0	38.1
231	K08-15	3511.0	113.0	36.0		120.9	3432.0	33.0
232	K08-	2398.1	70.0	7.0		91.1	2333.2	35.7
233	K08-	3178.0	99.0			117.0	3113.1	35.1
234	K08-	3178.0	99.0			117.0	3113.1	35.1
235	K08-	3178.5	99.0	16.5		114.3	3113.6	34.2
236	K08-	3447.0	107.0			125.0	3382.1	34.7
237	K08-	3447.3	107.0	13.0		124.2	3382.4	34.4
238	K08-	3447.5	104.0			122.0	3382.6	33.8
239	K08-	1041.9	43.0			61.0	967.4	55.0
240	K08-	3224.0	104.0			122.0	3149.5	36.3
241	K08-	3225.5	101.0			119.0	3151.0	35.3
242	K08-	3229.3	99.0			117.0	3154.8	34.6
243	K08-	3453.0	101.0			119.0	3378.5	32.9

244	K08-	3453.0	106.0			124.0	3378.5	34.4
245	K08-	3453.0	107.0			125.0	3378.5	34.7
246	K08-	3454.0	104.0			122.0	3379.5	33.8
247	K09-01	921.0	38.0			56.0	854.0	56.4
248	K09-01	927.0	38.0	10.0		57.0	860.0	57.2
249	K09-01	3474.5	91.0	9.0		110.7	3407.5	30.2
250	K09-01	3478.5	84.0			102.0	3411.5	27.6
251	K09-01	3783.0	93.0	5.0		115.5	3716.0	29.0
252	K09-01	4076.2	106.0	7.0		127.1	4009.2	29.7
253	K09-01	4079.2	109.0			127.0	4012.2	29.7
254	K09-03	3050.0	111.0			129.0	2986.7	40.6
255	K09-03	3486.0	116.0	Sonic cement bond logging			116.0	3422.7
256	K09-03	3511.0	111.0	8.5		116.0	3447.7	31.4
257	K09-03	3788.1	112.0	18.5		126.3	3724.8	31.8
258	K09-03	3791.4	116.0	3.5		139.7	3728.1	35.4
259	K09-03	3791.5	116.0	15.0		132.1	3728.2	33.3
260	K09-03	3791.7	112.0			130.0	3728.4	32.8
261	K09-06	1848.0	68.0	9.5		87.4	1786.4	44.5
262	K09-06	2457.0	107.0	24.0		118.9	2395.4	46.4
263	K09-06	3542.0	100.0	12.9		117.3	3480.4	31.4
264	K09-06	3752.0	101.0	14.0		117.6	3685.4	29.8
265	K09-06	3807.0	101.0	7.0		122.1	3745.4	30.5
266	K09-06	3808.0	107.0			125.0	3746.4	31.3
267	K09-07	1713.9	58.0	5.3		80.3	1633.2	44.4
268	K09-07	3352.4	95.0	19.2		108.9	3271.7	30.9

269	K09-07	3352.9	95.0	11.1		113.4	3272.2	32.3
270	K09-07	3460.0	115.0	12.0		132.8	3379.3	37.0
271	K09-07	3827.8	115.0			133.0	3747.1	33.4
272	K09-07	3827.9	115.0	14.8		131.2	3747.2	32.9
273	K09-07	3828.5	115.0			133.0	3747.8	33.4
274	K09-07	4121.0	121.0	15.9		136.6	4040.3	31.9
275	K09-07	4123.0	125.0	27.8		135.4	4042.3	31.6
276	K09-07	4137.7	118.0	10.5		136.7	4057.0	31.8
277	K09-07	4139.1	121.0	15.9		136.6	4058.4	31.7
278	K09-07	4139.5	123.0	21.0		136.1	4058.8	31.6
279	K09-10	1126.0	54.8	Sonic cement bond logging			54.8	1050.5
280	K09-10	1897.6	61.2	17.3		76.1	1822.1	37.5
281	K09-10	2197.0	80.8	11.5		98.9	2121.5	42.9
282	K09-10	3782.0	96.5	10.3		115.4	3706.5	29.0
283	K09-10	3804.0	96.5	10.3		115.4	3728.5	28.8
284	K09-10	3805.0	99.3	17.8		113.9	3729.5	28.5
285	K09-11	3688.8	114.0			132.0	3613.2	34.4
286	K09-11	3788.0	117.0			135.0	3712.4	34.3
287	K09-11	3883.0	104.0			122.0	3807.4	30.0
288	K09-11	4145.1	122.0			140.0	4069.5	32.5
289	K09-11	4159.8	117.0			135.0	4084.2	31.1
290	K09-11	4173.5	114.0			132.0	4097.9	30.3
291	K09-12	3819.0	120.0	19.2		134.0	3749.0	33.6
292	K09-12	3825.0	120.0	19.2		134.0	3755.0	33.6
293	K09-12	4328.0	126.0	65.5		128.9	4258.0	28.4

294	K09-12	4331.7	120.0	14.9		136.1	4261.7	30.1
295	K09-12	4332.0	120.0			138.0	4262.0	30.5
296	K09-12	4333.0	127.0	10.5		145.7	4263.0	32.3
297	K10-03	922.0	43.0	3.0		67.1	862.1	68.8
298	K10-03	923.5	43.0			61.0	863.6	61.6
299	K10-03	1600.0	80.0			98.0	1540.1	58.6
300	K10-03	2404.5	73.0	14.0		89.6	2344.6	34.9
301	K10-03	2404.5	80.0			98.0	2344.6	38.5
302	K10-03	2405.0	67.0			85.0	2345.1	32.9
303	K10-03	3300.7	101.0			119.0	3240.8	34.3
304	K10-03	3301.0	100.0	7.0		121.1	3241.1	34.9
305	K10-03	3301.3	101.0			119.0	3241.4	34.3
306	K10-14	2828.5	101.0	19.3		114.9	2761.5	38.8
307	K10-14	3037.0	101.0	13.3		118.0	2970.0	37.1
308	K10-14	3077.0	98.0	10.6		116.6	3010.0	36.2
309	K10-14	3079.0	102.0	17.5		116.8	3012.0	36.2
310	K10-14	3082.0	101.0	17.0		116.0	3015.0	35.9
311	K10-16	1194.0	45.0	4.8		67.7	1127.1	53.2
312	K10-16	2111.0	73.0	8.5		93.0	2044.1	41.7
313	K10-16	3141.0	95.5			113.5	3074.1	34.4
314	K10-16	3141.0	95.8	10.2		114.7	3074.1	34.8
315	K10-16	3380.0	99.0	8.8		118.8	3313.1	33.5
316	K10-16	3393.0	102.0			120.0	3326.1	33.7
317	K10-16	3410.0	102.0	12.8		119.3	3343.1	33.4
318	K10-16	3540.0	104.0	7.8		124.5	3473.1	33.6

319	K10-16	3540.0	106.0			124.0	3473.1	33.5
320	K11-01	1203.6	54.0	7.0		75.1	1142.6	58.9
321	K11-01	1205.7	54.0	3.8		77.5	1144.7	60.9
322	K11-01	1703.7	65.0	6.0		86.8	1642.7	48.1
323	K11-01	1705.7	65.0	9.0		84.7	1644.7	46.7
324	K11-01	1708.8	65.0	3.0		89.1	1647.8	49.3
325	K11-01	3383.8	97.0	6.0		118.8	3322.8	33.4
326	K11-01	3384.0	100.0	23.0		112.3	3323.0	31.4
327	K11-01	3386.0	100.0			118.0	3325.0	33.1
328	K11-01	3386.5	100.0			118.0	3325.5	33.1
329	K11-02	933.2	43.0	5.0		65.5	873.5	66.1
330	K11-02	933.5	43.0	3.0		67.1	873.8	67.9
331	K11-02	1748.2	60.0			78.0	1688.5	41.6
332	K11-02	1749.3	59.0	4.0		82.3	1689.6	44.1
333	K11-02	3193.0	93.0	5.0		115.5	3133.3	34.4
334	K11-02	3193.0	96.0	8.0		116.4	3133.3	34.6
335	K11-02	3233.0	97.0			115.0	3173.3	33.8
336	K11-02	3422.0	97.0	8.0		117.4	3362.3	32.6
337	K11-02	3424.0	97.0			115.0	3364.3	31.9
338	K11-02	3424.5	97.0			115.0	3364.8	31.9
339	K11-02	3425.0	97.0	6.0		118.8	3365.3	33.0
340	K11-02	3425.0	97.0	6.0		118.8	3365.3	33.0
341	K11-02	3425.5	100.0			118.0	3365.8	32.7
342	K11-02	3426.0	97.0	9.0		116.7	3366.3	32.3
343	K11-06	1720.0	64.0			82.0	1663.9	44.6

344	K11-06	1721.5	61.0			79.0	1665.4	42.8
345	K11-06	1723.0	61.0			79.0	1666.9	42.7
346	K11-06	1723.0	65.0			83.0	1666.9	45.1
347	K11-06	2604.0	73.0			91.0	2547.9	32.7
348	K11-06	2605.0	72.0			90.0	2548.8	32.3
349	K11-06	2605.5	71.0			89.0	2549.4	31.9
350	K11-06	2606.0	73.0			91.0	2549.9	32.6
351	K11-06	3234.5	96.0			114.0	3178.4	33.4
352	K11-06	3237.2	95.0			113.0	3181.1	33.1
353	K11-06	3238.7	96.0			114.0	3182.6	33.4
354	K11-06	3239.0	94.0			112.0	3182.9	32.7
355	K11-06	3239.0	96.0			114.0	3182.9	33.4
356	K11-06	3239.0	107.0			125.0	3182.9	36.8
357	K11-06	3425.9	106.0			124.0	3369.8	34.5
358	K11-06	3428.7	105.0			123.0	3372.6	34.2
359	K11-06	3429.0	104.0			122.0	3372.9	33.9
360	K11-07	1734.0	66.0	9.5		85.4	1674.5	46.3
361	K11-07	1735.0	66.0	5.5		88.1	1675.5	47.9
362	K11-07	2627.0	83.5	10.8		102.1	2567.5	36.7
363	K11-07	2628.0	81.0	7.5		101.7	2568.5	36.6
364	K11-07	3322.0	98.0			116.0	3262.5	33.2
365	K11-07	3322.5	103.5	13.5		120.4	3263.0	34.5
366	K11-07	3322.5	98.0			116.0	3263.0	33.2
367	K11-07	3325.0	98.0	10.0		117.0	3265.5	33.4
368	K11-07	3325.5	98.0	6.0		119.8	3266.0	34.3

369	K11-07	3403.0	104.5	15.0		120.6	3343.5	33.7
370	K11-07	3403.0	101.0	7.5		121.7	3343.5	34.1
371	K11-07	3403.0	106.0			124.0	3343.5	34.8
372	K11-07	3403.0	107.5	20.0		121.1	3343.5	33.9
373	K11-07	3492.0	101.0			119.0	3432.5	32.4
374	K11-08	1119.0	47.0			65.0	1053.5	54.3
375	K11-08	1591.4	47.0	8.0		67.4	1525.9	39.0
376	K11-08	3111.9	86.0	16.0		101.5	3046.4	30.8
377	K11-08	3112.4	76.0	24.0		87.9	3046.9	26.3
378	K11-08	3374.8	104.0	3.0		128.1	3309.3	36.4
379	K11-08	3380.5	96.0	12.0		113.8	3315.0	32.0
380	K11-08	3381.1	91.0	7.5		111.7	3315.6	31.3
381	K11-08	3508.0	102.0	6.0		123.8	3442.5	33.7
382	K11-08	3509.5	102.0	9.5		121.4	3444.0	33.0
383	K11-08	3513.0	108.0	8.0		128.4	3447.5	35.0
384	K11-08	3570.6	104.0	15.0		120.1	3505.1	32.0
385	K11-08	3653.0	102.0	12.0		119.8	3587.5	31.2
386	K11-08	3650.0	103.0	7.0		124.1	3584.5	32.4
387	K11-08	3653.0	106.0	10.0		125.0	3587.5	32.7
388	K11-08	3720.0	106.0			124.0	3654.5	31.8
389	K11-10	403.5	23.0	3.3		46.9	320.9	121.8
390	K11-10	1161.8	58.0	8.0		78.4	1079.2	65.4
391	K11-10	2076.3	83.5	11.6		101.5	1993.7	47.0
392	K11-10	2077.2	84.0	15.2		100.0	1994.6	46.2
393	K11-10	2078.0	82.0	4.8		104.7	1995.4	48.5

394	K11-10	2395.0	78.0	6.7		99.2	2312.4	39.5
395	K11-10	2397.0	81.0	9.7		100.2	2314.4	39.9
396	K11-10	3303.1	102.0	7.8		122.5	3220.5	35.6
397	K11-10	3305.0	105.0	12.7		122.4	3222.4	35.6
398	K11-10	3634.5	106.0	5.8		128.0	3551.9	33.8
399	K11-10	3636.2	110.0	13.7		126.8	3553.6	33.5
400	K11-10	3636.5	108.0	10.3		126.8	3553.9	33.5
401	K11-11	3108.0	89.0	7.7		109.5	3038.9	33.5
402	K11-11	3319.0	107.0	6.5		128.4	3249.8	37.1
403	K11-11	3612.0	84.0	6.5		105.4	3542.8	27.6
404	K11-11	3783.0	113.0	28.0		123.4	3713.8	31.1
405	K11-11	3785.0	112.0	24.7		123.6	3715.8	31.2
406	K11-	3127.0	96.0	Sonic cement bond logging			96.0	3057.4
407	K11-	3243.0	102.0	14.5		118.3	3173.4	34.8
408	K11-	3247.0	103.0	12.0		120.8	3177.4	35.6
409	K11-	3249.0	100.0	18.0		114.5	3179.4	33.6
410	K11-	3249.0	103.0	18.0		117.5	3179.4	34.5
411	K12-02	2708.0	96.0	12.0	4.0	113.8	2646.4	40.0
412	K12-02	3025.0	93.0	7.5		97.2	2963.4	30.2
413	K12-02	3026.6	93.0			111.0	2965.0	34.8
414	K12-02	3026.6	93.0	10.5		111.7	2965.0	35.0
415	K12-02	3097.0	96.0	15.0		112.1	3035.4	34.4
416	K12-02	3794.0	114.0	8.5		134.0	3732.4	33.8
417	K12-02	3796.0	117.0	13.0		134.2	3734.4	33.8
418	K12-02	3797.0	118.0	16.0	3.3	133.5	3735.4	33.7

419	K12-02	3797.3	114.0			132.0	3735.7	33.2
420	K12-03	3508.2	116.0	Sonic cement bond logging			116.0	3446.8
421	K12-03	3515.3	106.0	8.0		126.4	3453.9	34.3
422	K12-03	3779.8	115.0	Sonic cement bond logging			115.0	3718.4
423	K12-03	3796.0	116.0	16.5		131.3	3734.6	33.1
424	K12-03	3803.0	114.0	7.5		134.7	3741.6	33.9
425	K12-03	3803.0	115.0	11.5	5.0	133.1	3741.6	33.5
426	K12-03	3803.0	116.0			134.0	3741.6	33.7
427	K12-04	1463.5	52.0	6.5		73.4	1401.2	46.8
428	K12-04	1465.2	52.0			70.0	1402.9	44.3
429	K12-04	3048.0	104.0	15.5		119.8	2985.7	37.5
430	K12-04	3079.5	104.0	14.4		120.4	3017.2	37.3
431	K12-04	3556.1	114.0	Sonic cement bond logging			114.0	3493.8
432	K12-04	3561.0	102.0	9.0		121.7	3498.7	32.5
433	K12-04	3710.9	110.0			128.0	3648.6	32.9
434	K12-04	3710.9	114.0	19.0		128.0	3648.6	33.0
435	K12-04	3712.6	114.0	15.0	4.5	130.1	3650.3	33.5
436	K12-04	3713.0	110.0	7.0		131.1	3650.7	33.8
437	K12-04	3750.0	115.0	24.0		126.9	3687.7	32.3
438	K12-12	1453.3	53.0	11.3		71.2	1381.3	45.9
439	K12-12	1463.0	53.0			71.0	1391.0	45.4
440	K12-12	2659.0	83.0			101.0	2587.0	36.0
441	K12-12	2679.0	83.0	10.0		102.0	2607.0	36.1
442	K12-12	3390.0	95.0			113.0	3318.0	31.7
443	K12-12	3400.0	95.0	14.8		111.2	3328.0	31.1

444	K12-12	3400.5	95.0	14.8		111.2	3328.5	31.1
445	K12-12	3468.0	107.0	11.5		125.1	3396.0	34.5
446	K12-12	3688.0	106.0	10.0		125.0	3616.0	32.4
447	K12-12	3766.0	106.0	11.5		124.1	3694.0	31.5
448	K12-12	3777.1	107.0	17.0		122.0	3705.1	30.8

Appendix C: Fault attribute data from the Espírito Santo Basin, SE Brazil (Chapter 7)

Fault types	Length (m)	Throw (m)	Heave (m)	Maximum displacement (m)
Crestal fault	758	10.3	23.4	25.6
Crestal fault	812	5.9	14.9	16.0
Crestal fault	1475	22.2	38.2	44.2
Crestal fault	1028	30.7	52.3	60.6
Crestal fault	750	7.2	20.7	21.9
Crestal fault	875	19.6	51.5	55.1
Crestal fault	1473	14.1	43.3	45.5
Crestal fault	1216	34.0	47.2	58.2
Crestal fault	2166	43.1	83.3	93.8
Crestal fault	790	26.0	42.9	50.2
Crestal fault	990	15.4	25.2	29.5
Crestal fault	1524	23.3	59.7	64.1
Crestal fault	1652	21.1	74.8	77.7
Crestal fault	1916	20.8	43.9	48.6
Crestal fault	469	3.8	13.8	14.3
Crestal fault	942	5.9	25.3	26.0
Crestal fault	643	5.1	24.0	24.5
Crestal fault	1212	24.3	67.8	72.0
Crestal fault	880	21.4	73.4	76.5
Crestal fault	1951	91.3	141.0	168.0
Crestal fault	513	6.4	22.4	23.3
Crestal fault	1550	15.1	64.0	65.8
Crestal fault	1007	6.2	26.9	27.6
Crestal fault	1117	7.7	30.4	31.3
Crestal fault	510	11.2	46.7	48.0
Crestal fault	1210	9.8	51.0	51.9
Crestal fault	1100	13.4	64.2	65.6
Crestal fault	325	3.9	31.7	31.9
Crestal fault	548	4.1	18.9	19.3
Crestal fault	640	4.5	24.7	25.1
Crestal fault	653	17.0	52.3	55.0

Crestal fault	346	4.2	18.0	18.5
Crestal fault	350	12.6	32.3	34.7
Crestal fault	871	10.9	24.4	26.7
Crestal fault	1141	10.5	37.8	39.2
Crestal fault	527	11.8	32.9	34.9
Crestal fault	433	7.3	27.8	28.7
Crestal fault	1948	26.0	78.6	82.8
Corridor fault	1825	35.0	50.0	61.0
Corridor fault	1474	29.9	65.6	72.1
Corridor fault	1650	38.4	70.3	80.1
Corridor fault	1082	23.6	42.1	48.3
Corridor fault	1851	42.0	88.5	98.0
Corridor fault	1003	38.6	75.4	84.7
Corridor fault	3275	55.5	94.1	109.3
Corridor fault	2951	32.2	63.6	71.3
Corridor fault	760	28.0	58.4	64.7
Corridor fault	1426	31.8	76.8	83.1
Corridor fault	1377	33.4	83.1	89.6
Corridor fault	1475	23.4	44.9	50.6
Corridor fault	350	16.4	22.3	27.7
Corridor fault	985	9.8	20.2	22.4
Corridor fault	873	18.7	47.9	51.4
Corridor fault	604	6.6	18.2	19.4
Corridor fault	900	13.9	32.1	35.0
Corridor fault	1250	22.0	25.9	34.0
Corridor fault	402	15.5	35.6	38.8
Corridor fault	769	11.1	30.1	32.1
Corridor fault	901	7.3	36.0	36.7
Keystone fault	2879	37.9	84.9	93.0
Keystone fault	4283	71.8	149.2	165.6
Keystone fault	1477	48.7	93.2	105.1
Keystone fault	939	26.2	54.2	60.2
Keystone fault	1955	28.9	49.7	57.5
Keystone fault	2713	26.9	52.7	59.2
Keystone fault	1026	13.9	31.3	34.3
Keystone fault	446	8.9	15.6	18.0
Keystone fault	2253	30.8	75.6	81.6
Keystone fault	982	29.4	46.7	55.2

Keystone fault	585	13.4	33.5	36.1
Keystone fault	1814	55.8	55.8	78.9
Keystone fault	1510	18.3	31.6	36.5
Keystone fault	368	10.3	13.6	17.1
Keystone fault	1613	25.9	55.0	60.8
Keystone fault	1596	43.5	53.9	69.2
Keystone fault	2148	34.1	61.5	70.3
Keystone fault	1903	23.1	33.9	41.0
Keystone fault	1204	28.0	44.0	52.2
Keystone fault	483	7.2	12.9	14.8
Keystone fault	1008	26.8	45.4	52.7
Keystone fault	1461	22.6	34.4	41.1
Keystone fault	1372	41.4	75.4	86.0
Keystone fault	830	29.2	35.2	45.7
Keystone fault	867	20.1	28.3	34.7
Keystone fault	1033	32.4	56.9	65.5
Keystone fault	1377	8.8	14.3	16.8
Keystone fault	816	10.8	21.7	24.2
Keystone fault	1180	18.9	32.2	37.3
Keystone fault	1680	34.7	73.4	81.2
Keystone fault	1395	26.1	43.6	50.8
Keystone fault	1789	27.1	37.5	46.3
Keystone fault	1897	31.1	64.6	71.7
Keystone fault	1104	33.1	79.0	85.6
Keystone fault	576	16.9	52.7	55.3
Keystone fault	1228	55.4	87.7	103.7
Keystone fault	2617	27.5	46.5	54.0
Keystone fault	2131	40.9	58.0	70.9
Keystone fault	2033	28.5	44.9	53.2
Keystone fault	2806	70.9	75.4	103.5
Keystone fault	1525	28.7	73.0	78.5
Keystone fault	1667	25.2	44.4	51.1
Listric fault	3236	106.3	1243.2	1247.7
Listric fault	2257	72.9	554.3	559.1
Listric fault	2342	25.1	715.4	715.8
Listric fault	4900	112.7	1294.7	1299.6
Listric fault	2152	145.7	1043.0	1053.1
Listric fault	1019	71.1	822.9	826.0

Listric fault	7211	33.0	1312.8	1313.2
Listric fault	2717	210.9	1644.5	1658.0
Listric fault	1762	42.0	384.0	386.3

Appendix D: Fault attribute data from the Cleaver Bank High, Southern North Sea (Chapter 7)

Fault types	Length (m)	Throw (m)	Heave (m)	Maximum displace-ment (m)
Radial fault	1555	26.1	32.8	41.9
Radial fault	2605	24.4	34.6	42.4
Radial fault	1088	24.5	29.1	38.1
Radial fault	1896	40.7	39.7	56.9
Radial fault	1136	23.1	22.4	32.2
Radial fault	2350	23.8	20.9	31.7
Radial fault	903	10.3	9.9	14.3
Radial fault	150	16.0	19.6	25.3
Radial fault	301	16.6	25.6	30.5
Radial fault	1242	29.0	26.7	39.4
Radial fault	1190	18.3	29.9	35.1
Radial fault	1053	24.5	44.9	51.1
Radial fault	1057	22.7	22.4	31.9
Radial fault	961	27.0	32.8	42.5
Radial fault	828	15.6	16.3	22.6
Radial fault	802	24.7	35.6	43.3
Radial fault	902	26.3	19.2	32.5
Radial fault	1685	24.8	25.9	35.8
Radial fault	1152	20.4	26.2	33.2
Radial fault	904	18.9	18.3	26.3
Radial fault	706	22.3	37.1	43.3
Radial fault	606	24.5	24.4	34.5
Radial fault	859	18.6	28.3	33.9
Radial fault	864	23.7	28.5	37.1
Radial fault	884	26.5	27.1	37.9
Radial fault	704	24.5	22.6	33.3
Radial fault	818	29.4	28.5	40.9
Radial fault	477	21.9	27.3	35.0

Radial fault	504	29.5	40.0	49.7
Radial fault	1424	68.2	33.7	76.1
Radial fault	836	23.6	30.3	38.4
Radial fault	704	23.7	23.8	33.6
Radial fault	1317	69.1	57.4	89.8
Radial fault	1307	31.9	38.8	50.3
Radial fault	1657	26.6	30.5	40.5
Radial fault	1324	35.1	27.4	44.5
Radial fault	922	19.7	21.3	29.0
Radial fault	1102	23.1	46.6	52.0
Radial fault	707	28.6	40.0	49.2
Radial fault	812	23.5	29.7	37.8
Radial fault	1118	32.9	35.8	48.7
Radial fault	672	23.7	31.5	39.4
Radial fault	1620	28.1	33.8	44.0
Radial fault	1273	25.2	31.0	40.0
Keystone fault	2471	34.4	55.3	65.1
Keystone fault	2753	37.8	60.0	70.9
Keystone fault	751	22.8	21.9	31.6
Keystone fault	357	32.7	42.8	53.8
Keystone fault	3061	35.0	49.4	60.6
Keystone fault	650	26.5	41.6	49.3
Keystone fault	475	31.5	37.0	48.6
Keystone fault	426	29.1	45.8	54.3
Keystone fault	1062	22.3	33.2	40.0
Keystone fault	914	24.7	32.2	40.6
Keystone fault	583	24.5	39.5	46.5
Keystone fault	614	27.9	30.9	41.6
Keystone fault	940	31.5	37.6	49.1
Keystone fault	419	21.1	25.0	32.7
Keystone fault	651	32.4	33.6	46.7
Keystone fault	1100	34.3	57.7	67.1
Keystone fault	665	25.8	29.4	39.1
Keystone fault	353	20.9	37.6	43.0
Keystone fault	1207	25.3	40.0	47.3
Polygonal	676	25.8	39.5	47.2
Polygonal	523	24.7	43.8	50.3
Polygonal	1150	28.2	31.6	42.4

Polygonal	434	17.7	27.6	32.8
Polygonal	550	29.3	49.2	57.3
Polygonal	651	33.3	39.8	51.9
Polygonal	701	22.6	26.3	34.7
Polygonal	600	27.8	38.4	47.4
Polygonal	600	30.3	37.8	48.5
Polygonal	380	17.8	26.3	31.8
Polygonal	554	23.9	37.5	44.5
Polygonal	552	24.6	38.6	45.8
Polygonal	1178	29.4	30.0	42.0
Polygonal	1065	32.3	42.5	53.4
Polygonal	409	24.6	22.5	33.3
Polygonal	464	20.8	16.3	26.4
Polygonal	800	22.0	32.2	39.0
Polygonal	952	37.3	42.8	56.8
Polygonal	560	23.5	21.7	32.0
Sub-salt fault	6661	276.6	44.7	280.2
Sub-salt fault	7795	217.6	34.8	220.4
Sub-salt fault	2712	90.3	44.4	100.6
Sub-salt fault	2676	58.5	14.9	60.4
Sub-salt fault	3199	99.0	19.4	100.9
Sub-salt fault	7612	303.7	39.9	306.3
Sub-salt fault	3609	224.5	103.6	247.2
Sub-salt fault	10269	253.6	95.2	270.9
Sub-salt fault	10008	237.6	125.8	268.8
Sub-salt fault	7429	233.2	94.0	251.4
Sub-salt fault	3885	93.1	70.0	116.5